

---

Electronic Thesis and Dissertation Repository

---

7-17-2024 2:15 PM

# Birds of the ancient Nile: Species identification in Egyptian animal mummies using multi-resolution computed tomography and deep learning image segmentation

Maris A. Schneider, *Western University*

Supervisor: Nelson, Andrew J., *The University of Western Ontario*

A thesis submitted in partial fulfillment of the requirements for the Master of Arts degree in Anthropology

© Maris A. Schneider 2024

Follow this and additional works at: <https://ir.lib.uwo.ca/etd>



Part of the [Archaeological Anthropology Commons](#), and the [Biological and Physical Anthropology Commons](#)

---

## Recommended Citation

Schneider, Maris A., "Birds of the ancient Nile: Species identification in Egyptian animal mummies using multi-resolution computed tomography and deep learning image segmentation" (2024). *Electronic Thesis and Dissertation Repository*. 10215.

<https://ir.lib.uwo.ca/etd/10215>

This Dissertation/Thesis is brought to you for free and open access by Scholarship@Western. It has been accepted for inclusion in Electronic Thesis and Dissertation Repository by an authorized administrator of Scholarship@Western. For more information, please contact [wlsadmin@uwo.ca](mailto:wlsadmin@uwo.ca).

## Abstract

Using multi-resolution CT techniques, this project examined the visibility of identifiable skeletal traits in mummified avian bundles from ancient Egypt and the specificity with which avian taxa can be identified with digital 3D scans. Six mummified birds were scanned and processed with a deep learning segmentation algorithm. Three raptors were successfully identified as *Falco tinnunculus*, a species associated with the Egyptian goddess Isis. Analyses revealed that low-resolution (~110-80  $\mu\text{m}$ ) micro-CTs are sufficient for visualizing the bird skeleton (specifically the accessory pygostyle bones and distal wing sesamoid bones), while high-resolution (~30-20  $\mu\text{m}$ ) is necessary only for minute cranial details (the scleral ossicle). Clinical CT scans did not provide sufficient resolution to visualize skeletal traits; long bone measurements were found to be accurate with these scans. This research demonstrates the effectiveness of 3D imaging techniques for studying mummified birds and contributes to the growing body of research on ancient Egyptian animal mummies.

## Keywords

Animal Mummies, Ancient Egypt, Computed Tomography, Micro-Computed Tomography, Multi-Resolution, Image Segmentation, Deep Learning, Avian Osteology, Raptors, Ibises

## Summary for Lay Audience

Egyptian animal mummies have long fascinated researchers and archaeologists, but studying them typically involves unwrapping and damaging the bundles. This thesis uses non-destructive imaging methods to examine six mummified bird bundles (four raptors and two ibises) from ancient Egypt. The goal was to identify the bird species inside using their skeletons and propose interpretations of the bundles' roles in ancient Egyptian religion.

Three imaging techniques were used to assess how different resolutions would impact the ability to identify the birds from their skeletons. Clinical CT scans, which are common and easily accessible, provided the lowest resolution images. A dental cone-beam CT scanner gave medium-resolution images, while a micro-CT scanner offered high-resolution scans. A deep learning algorithm (an advanced form of machine learning) was trained and used to digitally separate the skeletons from the mummified bundles.

Using the lowest (~110-80  $\mu\text{m}$ ) and highest (~30-20  $\mu\text{m}$ ) resolution micro-CT scans, three of the raptors were successfully identified as belonging to the species *Falco tinnunculus* (common kestrel) by examining their whole skeletons and cranial features, respectively. This species identification can then be used to interpret the importance of certain bird species. For example, the common kestrel was associated with the goddess Isis, revered for her powers of fertility and healing. Identifying bird skeletons allows for their interpretation in their original context and enhances our understanding of ancient Egyptian beliefs.

Although clinical and dental cone-beam CT scans did not produce clear enough 3D images for species identification, clinical CTs provided accurate skeletal measurements, and the dental cone-beam CT showed good contrast resolution, indicating potential for future studies of bird mummies.

This thesis demonstrates the effectiveness of non-destructive digital imaging techniques for studying mummified birds from ancient Egypt. While micro-CT analysis is ideal, they are expensive, time-consuming, and produce very large data sets (~90 GB) that require significant processing power. Thus, even though clinical and cone-beam CT scans may not produce the best 3D images, they still provide valuable information that can aid in narrowing down a species identification of a mummified bird.

*This thesis is dedicated to my Opa, Wilhem Schneider. Your love and support for me and my pursuits of education never went unnoticed. I know you would be proud of all I have accomplished.*

## Acknowledgments

Words cannot convey how truly thankful I am to everyone who supported me and this research. First and foremost, my thanks go out to my incredible supervisor, Dr. Andrew Nelson. Without you, I would have never known animal mummies existed or become obsessed with birds. Your unwavering support and tolerance of my random ideas and interrupting office visits have not gone unnoticed. I am profoundly grateful for the opportunities you have provided me over the past two years and the impact you have had on me as a researcher.

To Dr. Natalie Reznikov, I am so appreciative for the time spent learning about CT scanning and Dragonfly with you and your students. Your passion for science and learning is truly inspiring. Thank you to the Bioengineering at McGill, specifically Dr. Daniel Buss, for sharing your knowledge and taking the time to teach me all things Dragonfly.

Thank you, Shumeng Jia and Dr. Salah Brika, for your dedication and assistance in collecting data for my research. 100+ hours of scanning is no small feat; I'm grateful for every moment.

Special thanks to those who helped facilitate my research: Lydia Burggraaf and Stephanie Saunders from the Chatham-Kent Museum; Annie Lussier and Anthony Howell from the Redpath Museum; Vladimir Brailovski from École de technologie supérieure; Kevin Hockley and Cheryl Sorenson from the Schulich School of Medicine and Dentistry; and Hatem Mehrez from Canon Medical Systems Canada.

I am thankful to my defence committee, Dr. Jay Stock, Dr. Lisa Hodgetts, and Dr. Scott MacDougall-Shackleton, for your time and thoughtful feedback and to Dr. Andrew Waters-Rist for chairing my defence.

I am deeply grateful to my undergraduate supervisor, Dr. Rebecca Gilmour, for her unwavering support and invaluable guidance throughout my academic journey. Your invaluable assistance, from helping me publish my first paper to taking me to my first conference, has significantly shaped my academic career. Thank you for inspiring me to strive for excellence.

Thank you to the Western Anthropology Department for their invaluable guidance, encouragement, and support throughout this process. Thank you to my funding bodies, the Western Graduate Research Scholarship, the Canadia Graduate Scholarship-Master's, and the New Frontiers in Research Fund (awarded to Dr. Reznikov, Dr. Dagdeviren, Dr. McKee, and Dr. Nelson). Without these resources, none of this work would have been possible. I would also like to thank Comet Technologies Canada Inc. (formerly ORS) for providing the academic license for Dragonfly software free of charge and all the folks at Dragonfly who were quick to help when I ran into technical difficulties.

This thesis would never have been completed without the invaluable support and encouragement from my friends. To Charmaine, Maddie, Kate, Emily, and Sarah, your friendship, encouragement, love for life and laughter remind me how truly fortunate I am to have such caring and supportive friends. To my friends back home, Charlee, Jill, Maddi, and Renee, I could not have done this without your friendship, laughter, and belief in me. Thank you for reminding me to maintain perspective amidst the challenges I have faced and reminding me not to take life too seriously.

I am incredibly grateful to Brodie for his support and understanding throughout this project. Your patience and skill in resolving all of my tech-related problems were invaluable (and saved me many tears). I am thankful for your love and encouragement, which have been a constant source of strength and motivation.

Finally, I extend my deepest gratitude to my family for their unwavering support throughout this journey. Your love, encouragement, and understanding have been the foundation upon which I built this academic pursuit. To my parents, Mary, Chris, Kara, and Dan, thank you for instilling in me the value of education and for always believing in my abilities, even when I doubted myself. Your sacrifices and guidance have shaped me into the person I am today. To my siblings, Kira and Kelly, thank you for cheering me on and for always reminding me what true strength looks like. *You both truly inspire me.* I am truly fortunate to have such a supportive and loving family, and I dedicate this accomplishment to each of you.

# Table of Contents

|   |      |
|---|------|
| Abstract.....   | ii   |
| Summary for Lay Audience.....                         | iii  |
| Dedication.....                                       | iv   |
| Acknowledgments.....                                  | v    |
| Table of Contents.....                                | vii  |
| List of Tables.....                                   | ix   |
| List of Figures.....                                  | x    |
| List of Appendices.....                               | xvii |
| Chapter 1.....  | 1    |
| 1 Introduction.....                                   | 1    |
| 1.1 Background.....                                   | 1    |
| 1.2 Research questions.....                           | 2    |
| 1.2.1 Methodological research questions.....          | 3    |
| 1.2.2 Anthropological research question.....          | 4    |
| 1.3 Organization of this thesis.....                  | 5    |
| Chapter 2.....  | 7    |
| 2 Literature Review.....                              | 7    |
| 2.1 A <i>brief</i> introduction to ancient Egypt..... | 7    |
| 2.1.1 Chronology of ancient Egypt.....                | 7    |
| 2.1.2 Maps of ancient Egypt.....                      | 8    |
| 2.1.3 Animal mummies: an introduction.....            | 10   |
| 2.1.4 Late Period onward.....                         | 10   |
| 2.2 Animals in ancient Egypt.....                     | 13   |
| 2.2.1 The importance of animals in ancient Egypt..... | 13   |
| 2.2.2 Animal mummies of ancient Egypt.....            | 14   |
| 2.2.3 Animal mummification.....                       | 21   |
| 2.2.4 Birds of ancient Egypt.....                     | 22   |
| 2.3 Avian osteology.....                              | 24   |
| 2.3.1 Axial skeleton.....                             | 26   |
| 2.3.2 Appendicular skeleton.....                      | 28   |
| 2.4 Imaging and deep learning.....                    | 32   |
| 2.4.1 X-rays.....                                     | 32   |
| 2.4.2 Clinical computed tomography.....               | 33   |
| 2.4.3 Cone-beam computed tomography.....              | 35   |
| 2.4.4 Micro-computed tomography.....                  | 36   |
| 2.4.5 Resolution.....                                 | 38   |
| 2.4.6 Image segmentation.....                         | 39   |
| Chapter 3.....  | 43   |
| 3 Materials and Methods.....                          | 43   |
| 3.1 Materials.....                                    | 43   |
| 3.1.1 Chatham Falcon.....                             | 43   |
| 3.1.2 Redpath Museum mummies.....                     | 45   |
| 3.1.3 IMPACT.....                                     | 49   |
| 3.2 Methods.....                                      | 50   |
| 3.2.1 Clinical CT.....                                | 50   |
| 3.2.2 Micro-CT.....                                   | 52   |

|                  |   |     |
|------------------|---|-----|
| 3.2.3            | Dental CBCT .....                                     | 53  |
| 3.2.4            | Image processing and Dragonfly .....                  | 56  |
| 3.2.5            | Avian identification .....                            | 60  |
| 3.2.6            | Effects of resolution .....                           | 69  |
| Chapter 4        | .....   | 71  |
| 4                | Results .....   | 71  |
| 4.1              | Chatham Falcon .....                                  | 71  |
| 4.2              | Redpath Museum raptors .....                          | 83  |
| 4.2.1            | Faucon 2726.02 .....                                  | 83  |
| 4.2.2            | Faucon 5731 .....                                     | 88  |
| 4.3              | Additional observations with micro-CT scans .....     | 95  |
| 4.4              | Redpath Museum ibises .....                           | 95  |
| 4.4.1            | Ibis 2727.01 .....                                    | 95  |
| 4.4.2            | Ibis 2727.02 .....                                    | 96  |
| 4.5              | IMPACT and the CMH Falcon 1 .....                     | 97  |
| 4.6              | Summary .....   | 102 |
| Chapter 5        | .....   | 104 |
| 5                | Discussion .....                                      | 104 |
| 5.1              | Chatham Falcon, Faucon 2726.02, and Faucon 5731 ..... | 104 |
| 5.2              | CMH Falcon 1 .....                                    | 108 |
| 5.3              | Ibis 2727.01 .....                                    | 110 |
| 5.4              | Ibis 2727.02 .....                                    | 111 |
| 5.5              | The effects of resolution .....                       | 112 |
| 5.5.1            | Why were the scans of Faucon 5731 so poor? .....      | 113 |
| 5.5.2            | Micro-CT scans .....                                  | 113 |
| 5.5.3            | Clinical CT .....                                     | 115 |
| 5.5.4            | Dental CBCT .....                                     | 116 |
| 5.6              | Tangential thoughts on deep learning .....            | 118 |
| Chapter 6        | .....   | 119 |
| 6                | Conclusion .....                                      | 119 |
| 6.1              | Summary .....   | 119 |
| 6.2              | Limitations .....                                     | 121 |
| 6.3              | Future directions .....                               | 122 |
| 6.4              | Conclusion .....                                      | 124 |
| References       | .....   | 126 |
| Appendices       | .....   | 142 |
| Curriculum Vitae | .....   | 211 |



## List of Tables

|   |    |
|---|----|
| <i>Table 2.1 Chronological periods of ancient Egypt, as presented in Shaw (2004, pg.197-199).</i><br>.....  | 7  |
| <i>Table 3.1 External measurements of the mummified bird bundles used for micro-CT scanning.</i> .....  | 49 |
| <i>Table 3.2 CT scan specifications from IMPACT (Wade &amp; Nelson, 2015) and the Roberts facility (including date, location, scanner, kV, mA, pixel spacing, slice thickness, and conduction kernel) of the mummified birds studied in this thesis.</i> .....              | 51 |
| <i>Table 3.3 The synthesized micro-CT parameters for the Chatham Falcon and the four mummified birds from the Redpath. Details include scanning resolution, anatomical position of the scan, scanning parameters, micro-CT scanners, and reconstruction software.</i> ..... | 54 |
| <i>Table 4.1 Reference of feature number to measured skeletal element in avian skeletons.</i> .....   | 74 |
| <i>Table 4.2 The long bone measurement standards and age classification of the Sacred Ibis (retrieved from von den Driesch et al., 2005) are compared to the long bone measurements of Ibis 2727.01.</i> .....  | 96 |
| <i>Table 4.3 Calculations of the percent error of long bone measurements taken on low resolution micro-CT scans compared to clinical CT scans for the Chatham Falcon, Faucon 2726.02, and Faucon 5731.</i> .....  | 98 |

## List of Figures

*Figure 1.1 Hieroglyphic depiction of the Long-legged Buzzard from Queen Hatshepsut's temple (left). Image retrieved from [http://www.griffith.ox.ac.uk/gri/carter\\_birds.html](http://www.griffith.ox.ac.uk/gri/carter_birds.html). Compared to a modern image of the Long-legged Buzzard (right). Image retrieved from <https://birdsoftheworld.org/bow/species/lolbuz1/cur/introduction>. .... 4*

*Figure 2.1 Map of ancient Egypt, highlighting the capital cities, Thebes and Memphis, and showcasing the geographic location of Upper versus Lower Egypt. Image retrieved from <https://carnegiemnh.org/egypt-and-the-nile/>. .... 8*

*Figure 2.2 Map of animal cemeteries in Egypt. Image drawn by Nicholas Warner and published in and retrieved from Ikram (2005a, p. xiiix). .... 9*

*Figure 2.3 Wooden funerary stela depicting the adoration of Ra-Horakhty-Atum (Third Intermediate Period). Animals feature prominently in this worship, notably the falcon-headed god Ra-Horakhty-Amun, a composite of the solar and sky gods Ra and Horus. Above this head is an Aten (sun disk), encircled by Uraeus (a depiction of the cobra-goddess Wadjet). The top of the stela is the winged sun disk, propelled by a scarab beetle. Two jackals symbolize Anubis and travel from the underworld. Plucked and eviscerated fowl are portrayed in the offerings. Image retrieved from [https://www.britishmuseum.org/collection/object/Y\\_EA27332](https://www.britishmuseum.org/collection/object/Y_EA27332). .... 14*

*Figure 2.4 Complete *Clumba palumbus* skeleton with accurate anatomical names. Image retrieved from Cohen and Serjeantson (1996, p. 4). .... 25*

*Figure 2.5 *Gallus gallus* skull with proper anatomical names. Image retrieved from Cohen and Serjeantson (1996, p. 10). .... 26*

*Figure 2.6 Example of the scleral ossicle. The top image is a 3D rendering of a modern *Accipiter cooperii*, scanned on the Yxlon FF35 CT (2023), at 13.5  $\mu\text{m}$  voxels. The blue bony ring indicates the location of the scleral ossicle within the bird's cranium. The bottom image is the same highlighted ossicle, digitally removed for visualization of the individual scales. Image processed and created by Maris Schneider in Dragonfly (v2022.2-1409). .... 27*

*Figure 2.7 Pelvic girdle of Buteo buteo with proper anatomical names. Image retrieved from <https://avesbiology.com/skeleton.html> ..... 28*

*Figure 2.8 Pectoral girdle of Gallus gallus with proper anatomical terms. Image retrieved from Cohen and Serjeantson (1996, p. 10). ..... 29*

*Figure 2.9 Bones of Gallus gallus wing with proper anatomical terms. Image retrieved from Cohen and Serjeantson (1996, p. 11). ..... 30*

*Figure 2.10 Image on the left: bones of the lower hind limb of Buteo buteo articulated with the pelvic girdle. Image retrieved from <https://avesbiology.com/skeleton.html>. Image on the right: hind limb of Gallus gallus, starting at the tarsometatarsus, with proper anatomical names. Image retrieved from Cohen and Serjeantson (1996, p. 11). ..... 31*

*Figure 2.11 Schematic diagram of fan beam X-ray production (left) versus cone beam X-ray production (right). Image adapted from <https://surgeryreference.aofoundation.org/cm/further-reading/cas-cone-beam-vs-fan-beam-ct>. ..... 35*

*Figure 2.12 Schematic diagram of a micro-computed tomography scanner. Image created by Maris Schneider in BioRender. .... 37*

*Figure 2.13 Schematic diagram of a deep learning network architecture with multiple layers. Image retrieved from <https://towardsdatascience.com/training-deep-neural-networks-9fdb1964b964>. ..... 40*

*Figure 3.1 Anterior view of the mummified falcon from the Chatham-Kent Museum. Photo taken by Maris Schneider. .... 44*

*Figure 3.2 Anterior view of the mummified falcons from the Redpath Museum. Faucon 2726.02 (left) and Faucon 5731 (right). Photos taken by Maris Schneider. .... 45*

*Figure 3.3 Anterior view of mummified ibises from the Redpath Museum. Ibis 2727.01 (right) and Ibis 2727.02 (left). Photos taken by Maris Schneider. .... 47*

*Figure 3.4 Taxonomic system for each mummified bird represented in Lortet and Gaillard (1905). Note, the names are listed as their current, valid taxonomic identification. The original names written by Lortet and Gaillard can be found in Appendix G. Image created by Maris Schneider. .... 61*

*Figure 3.5 Depiction of the sesamoid bones in the distal wing, present in the Genus Falco. Each sesamoid bone is identified by markers 10, 11, and 13. Image retrieved from Zucca and Cooper (2000, p. 198). .... 64*

*Figure 3.6 Example of scleral ossicle ring type and arrangement. Type A arraignment (2+ distinguished pairs) shown on the right. Type B arraignment (1 distinguished pair) shown in middle. Legend for distinguished scale reference on right. Reference drawing provided in Lemmrich (1931, p. 518). Image drawn by Maris Schneider. .... 67*

*Figure 4.1 Presence of the accessory pygostyle bones, ventral to the pygostyle bone, in the Chatham Falcon. Top image at 110  $\mu\text{m}$ ; bottom image at 50  $\mu\text{m}$ . .... 72*

*Figure 4.2 Identification of left and right sesamoid bones at metacarpophalangeal joints in the distal wing of the Chatham Falcon. Top image at 110  $\mu\text{m}$ ; bottom image at 50  $\mu\text{m}$ . ..... 73*

*Figure 4.3 Measurement deviation of skeletal features (Table 4.1) of known falcon species (Lortet & Gaillard, 1905) compared to the Chatham Falcon. Species with the least amount of deviation in skeletal trait measurements have a line running closest to 0 on the y-axis. .... 75*

*Figure 4.4 110  $\mu\text{m}$  3D deep learning segmentation rendering of the skull of the Chatham Falcon, showcasing the poor differentiation between bone and surrounding noise, thus obscuring the view of the individual scleral bones. .... 76*

*Figure 4.5 Visualization of the scleral ring in the Chatham Falcon. At 50  $\mu\text{m}$  (left) there is good visualization of the entire ring structure, and the shape of the individual scales can almost be discerned. At 25  $\mu\text{m}$  (left) individual ossicles are fully visible. Bottom yellow arrow indicates the first overlapping distinguished scale, and the topmost yellow arrow indicates the overlapped distinguished scale, confirming the 1:7 arrangement. .... 77*

*Figure 4.6 Scleral ossicle arrangement of the Chatham Falcon at 25  $\mu\text{m}$  using the molybdenum (left) target and the tungsten (right) target. No discernable differences between the targets were noted. .... 77*

*Figure 4.7 Diagram of the scleral scale arrangement for Falco tinnunculus, in accordance with the documenting style from Lemmrich (1931). Image drawn by Maris Schneider. .... 78*

*Figure 4.8 A 2D slice view of three scleral bones in the 50  $\mu\text{m}$  dataset of the Chatham Falcon. .... 78*

*Figure 4.9 Manually segmented left scleral ossicle of the Chatham Falcon at 50  $\mu\text{m}$ . .... 79*

*Figure 4.10 2D maximum intensity project view of a scleral ossicle in the Chatham Falcon at 50  $\mu\text{m}$ . .... 79*

*Figure 4.11 Identification of the accessory pygostyle bones in the Chatham Falcon on a 2D slice of a clinical CT scan (top) and the 50  $\mu\text{m}$  micro-CT scan (bottom) (yellow arrow indicating the pygostyle bone; pink arrows indicating the accessory bones). See figure 4.1 for 3D rendering of these bones. .... 80*

*Figure 4.12 Full dataset acquired of the Chatham Falcon using at dental CBCT scanner. ... 81*

*Figure 4.13 2D slice of the Chatham Falcon from a dental CBCT. Image on left shows the clear distinction between dense long bones and surrounding tissue/bandages. Image on the right identifies the scleral ossicle, which shows poor definition compared to the surrounding background noise. .... 82*

*Figure 4.14 Presence of the accessory pygostyle bones, ventral to the pygostyle bone, in Faucon 2726.02. Left image at 100  $\mu\text{m}$ ; right image at 50  $\mu\text{m}$ . Note, the datasets have been cropped, as the position the falcon is mummified in obstructs the view of the accessory bones. .... 83*

*Figure 4.15 Identification of left and right sesamoid bones at the metacarpophalangeal joint in the distal wing of Faucon 2726.02. Left image at 100  $\mu\text{m}$ ; right image at 50  $\mu\text{m}$ . .... 84*

*Figure 4.16 Measurement deviation of skeletal features (Table 4.1) of known falcon species (Lortet & Gaillard, 1905) compared to Faucon 2726.02. Species with the least amount of deviation in skeletal trait measurements have a line running closest to 0 on the y-axis. .... 84*

*Figure 4.17 100  $\mu\text{m}$  (left) and 50  $\mu\text{m}$  (right) 3D rendering of the skull of Faucon 2726.02, showcasing the scleral ring. While the bone is clearly present, there is no significant differentiation between the individual ossicles to determine ossicular arrangement. .... 85*

*Figure 4.18 2D maximum intensity project view of a scleral ossicle in Faucon 2726.02 at 50  $\mu\text{m}$ . .... 85*

*Figure 4.19 Visualization of the scleral ring in Faucon 2726.02 at 25  $\mu\text{m}$ . Bottommost yellow arrow indicates the first overlapping distinguished scale, and the topmost yellow arrow indicates the overlapped distinguished scale, confirming the 1:7 arrangement. .... 86*

*Figure 4.20 2D confirmation of the overlapping structure of ossicle 1 in Faucon 2726.02. 3D view (left) confirms which ossicle is being examined in 2D (right), with the placement of a 3D marker. Image on right shows the individual ossicle in question. Pink arrows indicate where the individual scale overlaps both of the neighbouring scales. Yellow arrows indicate where both of the neighbouring scales are overlapped by scale 1. .... 87*

*Figure 4.21 2D confirmation of the overlapped structure of ossicle 7 in Faucon 2726.02. 3D view (left) confirms which ossicle is being examined in 2D (right), with the placement of a 3D marker. Image on right shows the individual ossicle in question. Pink arrows indicate where the neighbouring scales overlap the middle scale. Yellow arrows indicate where the middle scale is overlapped by the neighbouring scales, confirming that scale 7 is a distinguished scale. .... 87*

*Figure 4.22 Depiction of the pygostyle bone showing the lost data due to poor image segmentation. The image on the left shows a pygostyle bone with no articulating accessory bones, whereas the image on the left shows the clear presence of accessory pygostyle bones, following new iterations of training to the deep learning algorithm. Both images are shown at 88  $\mu\text{m}$ . .... 88*

*Figure 4.23 Confirmation of the presence of the accessory pygostyle bones in Faucon 5731 at 44  $\mu\text{m}$ . ..... 89*

*Figure 4.24 Difference in visualization of the metacarpophalangeal sesamoid bone between 88  $\mu\text{m}$  (left) and 44  $\mu\text{m}$  (right) micro-CT scans of Faucon 5731. .... 90*

*Figure 4.25 Identification of a metacarpophalangeal sesamoid bone on a 2D slice of Faucon 5731, at 88  $\mu\text{m}$ . .... 90*

*Figure 4.26 Measurement deviation of skeletal features (Table 4.1) of known falcon species (Lortet & Gaillard, 1905) compared to Faucon 5731. Species with the least amount of deviation in skeletal trait measurements have a line running closest to 0 on the y-axis. .... 91*

*Figure 4.27 3D visualization of the scleral ring for Faucon 5731 at 88  $\mu\text{m}$  (left) and 44  $\mu\text{m}$  (right). .... 92*

*Figure 4.28 Image on the left highlights the scleral ring segmentation prior to retraining of the deep learning algorithm. Image on the right highlights the scleral ring at multiple additional iterations of deep learning training. Despite the more accurately segmented image, the arrangement of ossicles cannot be visualized. .... 92*

*Figure 4.29 2D maximum intensity project view of a scleral ossicle in Faucon 5731 at 22  $\mu\text{m}$ . .... 93*

*Figure 4.30 Examination of the scleral ossicles at 22  $\mu\text{m}$  in Faucon 5731 (right) and at 25  $\mu\text{m}$  in the Chatham Falcon (left). .... 94*

*Figure 4.31 3D rendering of Ibis 2727.01 at 27  $\mu\text{m}$  with indication of which bones were measured for aging. The bill is also identified, as it clearly differentiates between birds of prey and wading birds, such as ibises. .... 95*

*Figure 4.32 Lateral slice view of Ibis 2727.02 revealing intricately wrapped linens but no avian skeletal elements. .... 97*

*Figure 4.33 Linear regression comparing micro-CT measurements to clinical CT measurements of the Chatham Falcon (a), Faucon 2726.02 (b), and Faucon 5731 (c). Graph D presents all falcon data combined. .... 100*

*Figure 4.34 Measurement deviation of known raptor species (Lortet & Gaillard, 1905) compared to CMH Falcon 1. Species with the least deviation in skeletal trait measurements have a line running closest to the y-axis. .... 101*

*Figure 4.35 2D sagittal slice view of CMH Falcon 1 showing the size difference between the mummified bird and its coffin. Green arrow indicates the head of the bird; pink arrow indicates the talons; yellow arrow indicates tail feathers and mummification linens. .... 102*

*Figure 5.1 Arrows indicate the wings of Nephthys and Isis wrapped around the inner coffin of Tutankhamun. Image retrieved from <https://www.thecollector.com/ancient-egyptian-goddess-isis/>. .... 105*

*Figure 5.2 Comparison of modern common kestrels (female – right; male – left) to hieroglyph from the tomb of Sennedjem, Deir el-Medina, showing the goddess Isis in kestrel form (middle). Modern bird images retrieved from [https://en.wikipedia.org/wiki/Common\\_kestrel](https://en.wikipedia.org/wiki/Common_kestrel); hieroglyphic image retrieved from Houlihan & Goodman (1989, p. 45). .... 107*



## List of Appendices

|  |     |
|--|-----|
| Appendix A: Additional images of mummified birds .....   | 142 |
| Appendix B: Procedural guide for multi-image registration stitching in Dragonfly .....                                 | 162 |
| Appendix C: Procedural guide for training and applying a deep learning algorithm for 3D image segmentation .....       | 171 |
| Appendix D: Understanding the deep learning parameters in Dragonfly.....   | 183 |
| Appendix E: Procedural guide for cleaning up segmented images using the Connected Components feature in Dragonfly..... | 187 |
| Appendix F: Measuring bones in Dragonfly .....   | 192 |
| Appendix G: Raw measurements of known species of mummified birds.....  | 195 |
| Appendix H: Skeletal measurements and calculated differences from studied mummified birds.....                         | 198 |
| Appendix I: 3D renderings of studied mummified birds using clinical CTs.....   | 201 |
| Appendix J: Additional observations from mummified bundles .....   | 205 |
| Appendix K: Residual plots for clinical and micro-CT skeletal measurements.....  | 209 |

## Chapter 1

### 1 Introduction

Advanced imaging techniques have allowed researchers to peek beneath the wrappings of ancient Egyptian animal mummies without causing any physical damage. However, many questions remain unanswered. The motivations behind specific animal choices, the exact rituals involved, and the roles of different animals in religious ceremonies continue to intrigue historians and archaeologists. The allure of animal mummies persists as they stand as tangible connections to a civilization that venerated the natural world in profound and complex ways.

#### 1.1 Background

This thesis employs micro-Computed Tomography (micro-CT) and clinical Computed Tomography (CT) to identify ancient Egyptian animal mummy taxa non-destructively. In addition to the non-destructive imaging techniques, an advanced deep learning algorithm was trained to expedite the digital removal of internal objects (i.e., skeletal elements) from the surrounding noise (i.e., mummified tissue and bandages). Visualization of the skeletal elements within a mummy is essential to identify the taxonomic designation of the animal within the bundle. Identifying animals chosen for mummification offers unique insight into the context of animal use in ancient Egypt, especially regarding religious practices. Animal mummy identification presents a unique challenge to researchers because, unlike human mummies, the range of potential taxa varies extensively (McKnight et al., 2022). Traditionally, animal mummies are identified through a method known as "bone-in-hand" identification, which requires the destructive opening of a wrapped bundle to expose the skeletal elements and carry out comparative anatomy studies (McKnight et al., 2022). However, non-destructive imaging techniques have the capacity to reveal complex internal structures while preserving the integrity of these artifacts (Johnston et al., 2020). It has been suggested that clinical CT scans, although they can provide information beyond the capabilities of two-dimensional (2D) radiographs, are not able to achieve sufficient quality to accurately identify mummified

species (McKnight et al., 2022). Preliminary experimentation suggests, however, that micro-CT scanning will provide the necessary resolution to allow for species determination without relying on the "bone-in-hand" method.

Many animals in ancient Egypt were mummified, from cats to crocodiles to shrews, snakes, and birds (Hekkala et al., 2020; Ikram, 2005b; Ikram & Nicholson, 2005; Johnston et al., 2020; Richardin et al., 2017; Woodman et al., 2021). This project focuses on mummified bird bundles, which are available for study in Canadian museums or have been previously scanned and made available in an online database. Although the majority of faunal taxa in ancient Egypt were considered sacred, evidence suggests that birds occupied a position of elevated significance (McKnight, 2020; McKnight et al., 2022). Two-hundred and forty-three native and migratory bird species have been identified from ancient Egyptian hieroglyphic inscriptions, artistic representations, and excavated avian remains (McKnight et al., 2022). However, of that total, only 77 bird species have been identified from mummified remains (McKnight et al., 2022). Animal mummies are an element of Egyptian funerary rites that thus far have received limited attention and study. This project will provide methodological contributions to identifying avian taxa with multiple CT techniques and provide commentary regarding the importance and significance of certain avian species in the Egyptian ritual landscape.

## 1.2 Research questions

This thesis aims to answer the following three questions, explained in more detail below:

- (1) Using non-destructive Computed Tomography scans, what is the minimal resolution required to effectively visualize diagnostic skeletal traits for the most precise taxa identification of birds within mummy bundles?
- (2) To what level of specificity can taxa be identified within an avian bundle (i.e., Family, Order, Genus, or down to the species level)?
- (3) What comments can we make regarding the exploitation of certain birds in ancient Egypt and their religious importance?

### 1.2.1 Methodological research questions

Questions one and two address the applicability of studying mummified bird remains with digital imaging techniques. Previous research has sought to identify avian taxa through the use of 2D plane radiographs. While 2D plane radiographs are non-destructive and can quickly assess internal contents, 2D plane radiographs produce 2D images of a 3D object, where artifacts become superimposed and magnified. This leads to challenges in gauging the depth and perspective of the internal contents (Adams, 2015; McKnight et al., 2022).

Clinical CT scans have proved beneficial in demonstrating the shape of the long bones, and creating a 3D image facilitates the rotation of the digital mummy, thus allowing for a clearer understanding of the spatial placement of skeletal objects within a bundle (McKnight et al., 2022). Clinical CT scans, however, tend to have poor contrast resolution when imaging small objects, meaning that lower density elements (such as the sternum, cranium or smaller skeletal elements) may be lost when rendering a 3D object file or have extremely poor contrast in mummified remains. Poorer contrast resolution can also impact the ability to perform advanced forms of image segmentation necessary for digitally removing the bird skeleton from the surrounding noise.

In utilizing micro-CT, cone-beam scanners, and clinical CT scans, this thesis will examine the different resolutions achievable on these machines and identify skeletal features visible at specific resolutions. While micro-CT scans provide a higher resolution (voxel size  $< 100 \mu\text{m}$ ) (Clark & Badea, 2021) than clinical CT scans ( $\sim 500\text{-}650 \mu\text{m}$ ) (Conlogue et al., 2020), these scans are time-consuming, expensive, produce extensive datasets, and are not readily accessible to all researchers. Cone beam scanners (i.e., dental scanners) provide greater resolution ( $\sim 200\text{-}100 \mu\text{m}$ ) (Nemtoi et al., 2013) than a clinical CT, yet not as great as a micro-CT, thus representing an intermediate resolution. Cone beam scanners are also more accessible to researchers in various parts of the world. Therefore, their consideration in this thesis is essential when assessing the different resolutions in which certain skeletal features can be visualized, as they are more readily accessible. Regarding question one, the primary aim of this thesis is to investigate which skeletal features are visible at varying resolutions. Concurrently, by pinpointing the

skeletal traits visible at different resolutions, this study aims to discuss the potential taxa to which the mummified bird could belong. This exploration provides insights into the specificity with which birds can be identified at differing resolutions, which will address question two.

### 1.2.2 Anthropological research question

Answering question three and the broader anthropological interpretation of this thesis relies on the observations from questions one and two. Specific animals represented specific gods and goddesses in the ancient Egyptian pantheon and were typically depicted as human-animal hybrids. They also featured prominently in Egyptian hieroglyphic texts regarding gods and goddesses, as well as mortuary rites and rituals. Studies of birds in Egyptian culture have revealed that pictorial depictions of different avian species were represented with extreme accuracy. For example, the Long-legged Buzzard (*Buteo rufinus*) features prominently as an ornamental hieroglyph from the mortuary temple of Queen Hatshepsut at Deir el-Bahari (Houlihan & Goodman, 1986). Many accurate traits are noted in the morphological characteristics used to depict the buzzard. In the



Figure 1.1 Hieroglyphic depiction of the Long-legged Buzzard from Queen Hatshepsut's temple (left). Image retrieved from [http://www.griffith.ox.ac.uk/gri/carter\\_birds.html](http://www.griffith.ox.ac.uk/gri/carter_birds.html). Compared to a modern image of the Long-legged Buzzard (right). Image retrieved from <https://birdsoftheworld.org/bow/species/lolbuz1/cur/introduction>.

hieroglyph, the bird is pictured at rest, in an erect posture. The plumage and tail are a brownish-red hue (Houlihan & Goodman, 1986). At the same time, the cere (waxy

covering of the upper beak), legs, and feet are brownish-yellow, and the beak, talons, and primary feathers are dark brown, precisely mimicking the real-world observations of the Long-legged Buzzard (Houlihan & Goodman, 1986).

Long-legged buzzards have been discovered within avian mummy bundles. Like many other raptors mummified for ritual purposes, they are often associated with the solar nature of birds and, by extension, the solar gods in the Egyptian pantheon, such as the sun god Ra or Horus, the eternal king (Ikram, 2019a).

Considering that bird species can be identified with such accuracy in hieroglyphic inscriptions and artistic portrayals, the roles of certain birds are well documented (as shown in Chapter 2 and Chapter 5) and understood. Therefore, accurately identifying birds through their skeletal remains allows for better interpretation regarding the mummified bundle's role in Egyptian society.

### 1.3 Organization of this thesis

This thesis is organized into five chapters. Chapter Two is a literature review outlining key concepts regarding this thesis's anthropological and methodological background. The first third of the literature review covers ancient Egypt and the animal mummification industry. It provides insight into the current knowledge of animal mummies. The second third of the literature review covers the avian skeleton. This section offers a brief anatomical review of bird bones and some variations that could be examined between species. It is important to note that this is not an exhaustive review of bird variation but an introduction to the proper anatomical terms for studying birds. The last section of the literature review covers the methodological background, including 3D imaging and deep learning for 3D image segmentation with the program Dragonfly.

Chapter Three will discuss the materials and methods employed in this study. It will introduce the bird mummies studied in London (ON) and Montreal (QC), as well as those retrieved from the Internet Mummy Picture Archiving and Communication Technology (IMPACT) database (Nelson & Wade, 2015). This chapter will summarize the CT parameters used to acquire varying scans for each mummy. It will also describe the

stitching method in Dragonfly, employed to create a single mid-resolution scan from multiple micro-CTs. Regarding Dragonfly, this chapter will review the process for developing and training a deep learning algorithm capable of segmenting bird bones from surrounding mummified tissue. Finally, the section will conclude with a description of the methods employed to identify the species of birds based on their skeletal remains.

Chapter Four will present the results of the trained deep learning algorithm for segmenting the clinical and micro-CT scans through various images of digitally removed skeletal remains. The results of the morphological analysis of the bird's skeletal remains will also be presented. Finally, an outline of the visualization of specific skeletal elements on the clinical CT versus the micro-CT scans will be included.

Chapter Five will discuss the results of the CT image analysis. This will include identifying the bird species in the bundle or the most accurate taxonomic level that can be identified. Additionally, where possible, the gods/goddesses that the mummy bundle likely represented will be discussed. Finally, the discussion will examine the skeletal elements visible on the varying resolution scans and discuss the implications of employing clinical versus micro-CT scans for studying mummified birds.

Finally, Chapter Six will conclude with a summary of the overall aims of this study, addressing both the methodological and anthropological questions guiding this project and some insights for future directions for research on 3D imaging of avian mummies.

## Chapter 2

### 2 Literature Review

This chapter will provide an overview of the literature relevant to the aims of this thesis. It will begin with a timeline of ancient Egypt, followed by a discussion of the Late and Roman periods, as they witnessed the height of animal mummy production and animal cult following. This leads to the introduction of animal mummies, the current literature that seeks to understand their role and importance in ancient Egypt and methodological insights into the mummification industry. Next, this literature review will briefly review avian skeletons. The third section of this review will include detailed descriptions of the methods used to complete this thesis. This includes varying methods of CT (clinical, micro, and cone-beam) imaging and a discussion of image segmentation through deep learning, an essential concept to understanding how the CT scans in this study were processed for skeletal visualization.

#### 2.1 A *brief* introduction to ancient Egypt

##### 2.1.1 Chronology of ancient Egypt

*Table 2.1 Chronological periods of ancient Egypt, as presented in Shaw (2004, pg.197-199).*

| <b><i>Period</i></b>              | <b><i>Dates (BC)</i></b> |
|-----------------------------------|--------------------------|
| <b>Roman Period</b>               | 30-AD 311                |
| <b>Ptolemaic Period</b>           | 332-30                   |
| <b>Late Period</b>                | 644-332                  |
| <b>Third Intermediate Period</b>  | 1069-644                 |
| <b>New Kingdom</b>                | 1550-1069                |
| <b>Second Intermediate Period</b> | 1650-1550                |
| <b>Middle Kingdom</b>             | 2055-1650                |
| <b>First Intermediate Period</b>  | 2181-2055                |
| <b>Old Kingdom</b>                | 2686-2181                |
| <b>Early Dynastic Period</b>      | 3000-2686                |
| <b>Predynastic Period</b>         | 5300-3000                |



## 2.1.2 Maps of ancient Egypt

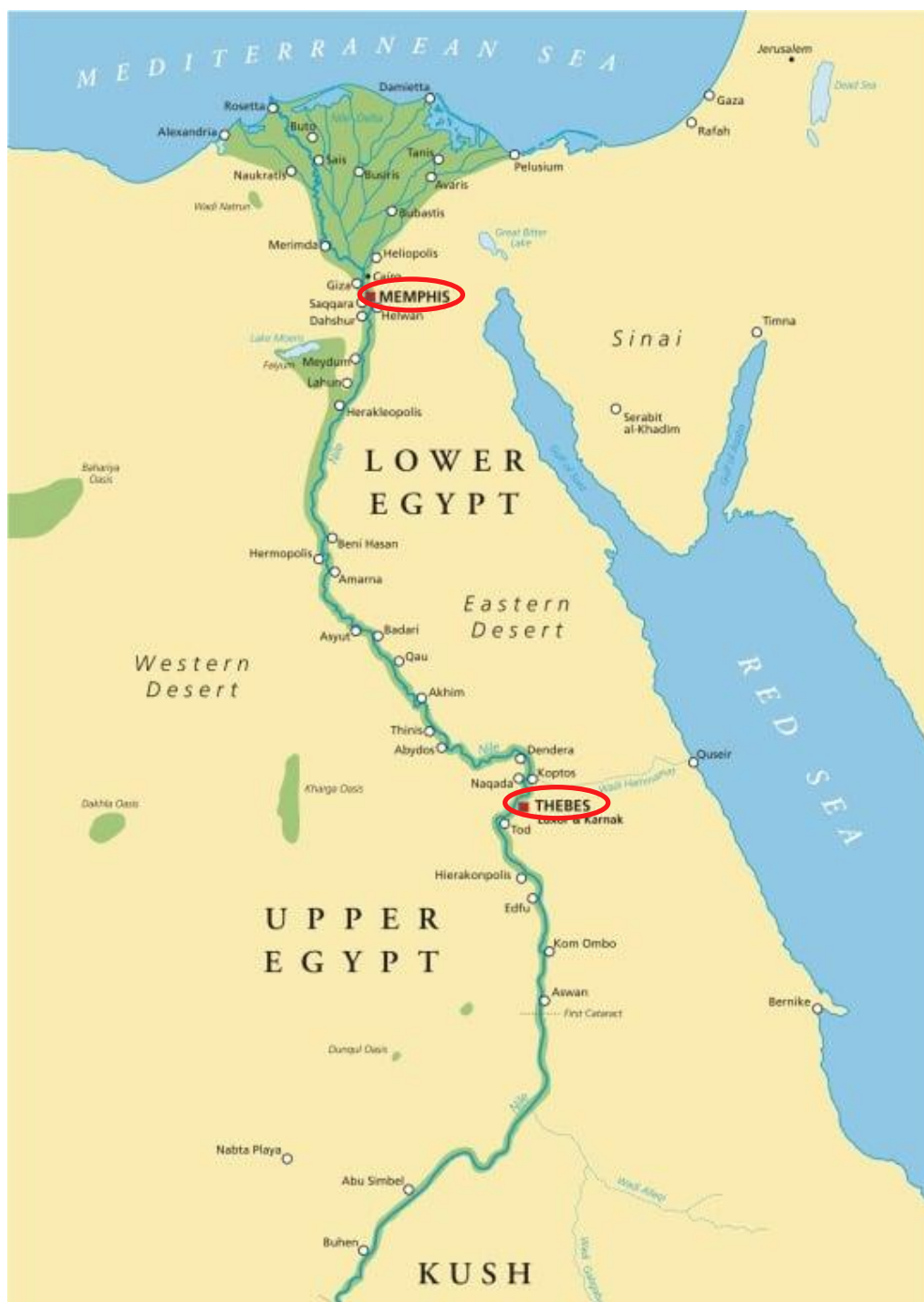


Figure 2.1 Map of ancient Egypt, highlighting the capital cities, Thebes and Memphis, and showcasing the geographic location of Upper versus Lower Egypt. Image retrieved from <https://carnegiennh.org/egypt-and-the-nile/>.

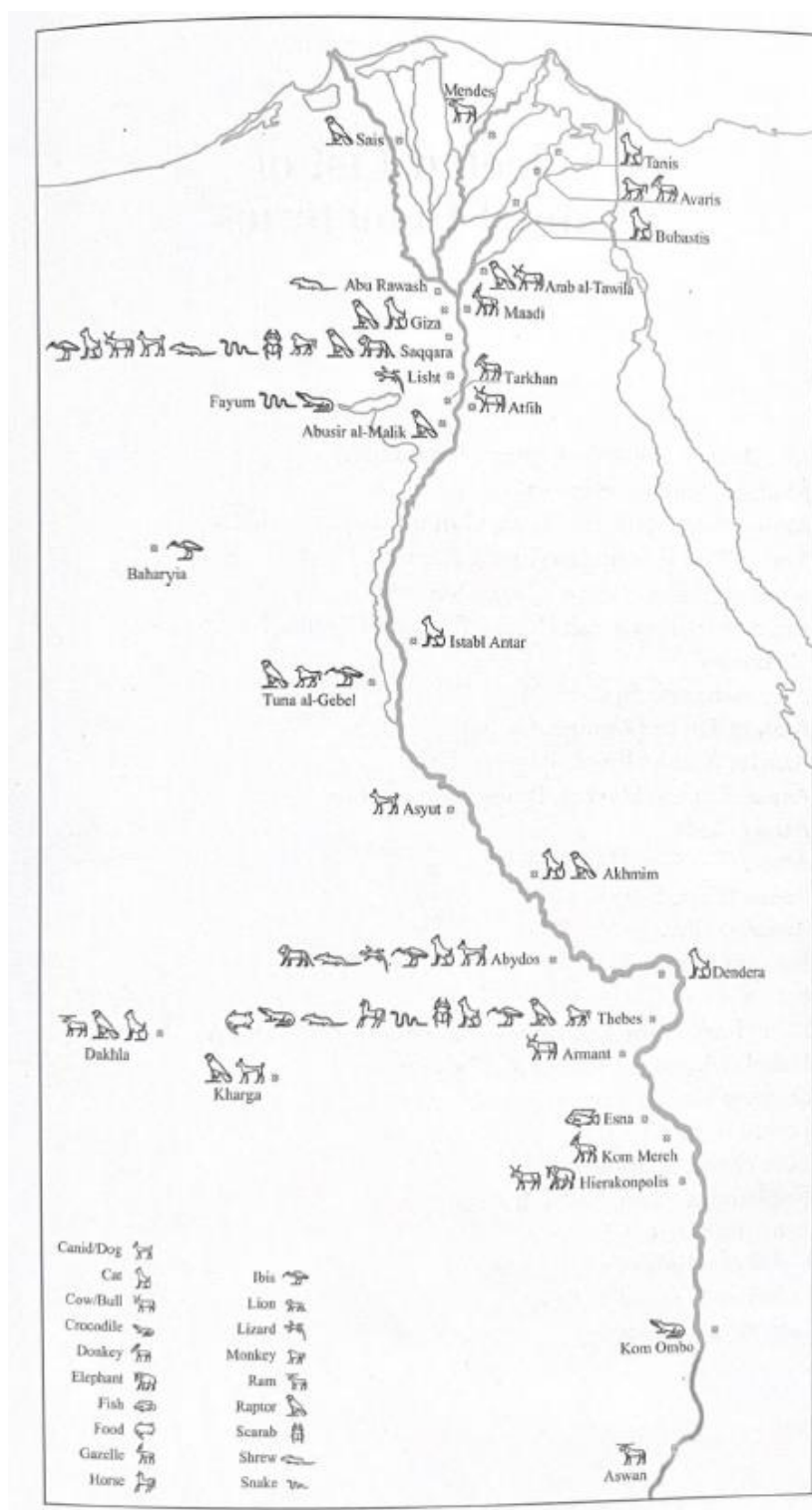


Figure 2.2 Map of animal cemeteries in Egypt. Image drawn by Nicholas Warner and published in and retrieved from Ikram (2005a, p. xiiix).

### 2.1.3 Animal mummies: an introduction

Animal mummies are among the most enigmatic and captivating artifacts from the ancient world, offering a fascinating window into ancient Egypt's beliefs, culture, and rituals. Animal mummies are defined as the artificially preserved/manipulated bodies of animals or parts (including eggs, feathers, fur, and pieces of bone) wrapped and deposited in a funerary context (Ikram, 2019b). These meticulously preserved animal remains, often wrapped in layers of linen bandages, reveal the profound reverence and spiritual significance that animals held in the hearts of the ancient Egyptians (Ikram, 2005a; McKnight, 2020; Scalf, 2012). The practice of mummifying animals in ancient Egypt dates back over 4,000 years, with evidence of its existence in the Pre-Dynastic period. The practice of mummifying animals grew significantly during the Late Period and continued throughout the subsequent Periods (Ikram, 2005a). This long history reflects the enduring importance of animals in Egyptian society. Their deeply rooted religious beliefs lay at the heart of the ancient Egyptian fascination with animal mummification. Animals were not seen merely as creatures of the physical world but as manifestations of divine forces (Ikram, 2005a). Various animals were associated with specific gods and goddesses, and the preservation of these creatures was a means of honouring and appeasing the deities (Hekkala et al., 2020; Ikram, 2005a; Johnston et al., 2020; Nicholson, 2022). Next, I explore the societal conditions that led to the boom of the animal mummy industry, followed by an in-depth review of the current literature surrounding animals and animal mummies in ancient Egypt.

### 2.1.4 Late Period onward

This literature review begins with the Late Period because the votive animal mummy industry became extremely popular during this time, and reached its peak production during the Ptolemaic and Roman periods. While animal mummies date back to the Predynastic period, votive mummies, those studied here, primarily date from the Late Period, the Ptolemaic Period, and the Roman Period.

Following the end of the New Kingdom and Third Intermediate period, religion in ancient Egypt was marked by significant developments owing to the changing political

landscape, including foreign rule and the integration of Greek and Egyptian beliefs (Franzmeier, 2022). Notably, the Late Period onward brought about the height of the animal mummification industry, which is believed to be an attempt to venerate the Egyptian religion during a time of significant change (Ikram, 2005a). Although animal cults existed from the Predynastic Period onwards (Budge, 2013; te Velde, 1980), animal cults became increasingly popular and abundant during the Late, Ptolemaic and Roman periods (Ikram, 2005a). The Late Period began at the end of the Third Intermediate Period with the collapse of the New Kingdom and the withdrawal of central authority following the death of Pharaoh Rameses XI. Egypt was subject to foreign rule during the Late Period, notably by the Assyrians and the Persians (Allen & Hill, 2018). These foreign rulers introduced their own religious beliefs and practices, leading to syncretism and the fusion of Egyptian deities with those from other cultures (Allen & Hill, 2018; Kitchen, 1991). Despite foreign influence, many Egyptians sought to preserve and revive their traditional religious practices. The towns around the Delta became the focus of significant development. The temples were restored or rebuilt, and local cults were reinvigorated (Zivie-Coche, 2008). For example, in the Kharga Oasis, the Temple of Hibis, dedicated to Amun, underwent several modifications, resulting in approximately 700 depictions of gods and divine statues throughout several rooms devoted to Osiris (Egyptian ruler of the underworld and judge of death) (Zelazko, 2023; Zivie-Coche, 2008).

The Ptolemaic Period was characterized by the rule of the Ptolemaic dynasty, which was of Greek origin. Despite foreign rule, the Egyptians could practice their local religion (or profess a religion of their choice). Mystery cults, such as the worship of Isis (goddess of healing and magic) and Osiris (god of the underworld), became increasingly popular during this period. However, Osiris was eventually replaced by the Greek-style god Serapis, who later formed a couple with Isis and succeeded the ancient couple of Osiris and Isis (Bommas, 2012; Vandrope, 2010). During the Ptolemaic period, Egypt has been referred to as the Age of Crisis, resulting from the integration of Greek and Egyptian beliefs. In response to the instability during the Ptolemaic Period, the animal mummy industry came to its apex, offering people promises of salvation, immortality, and

personal transformation, resonating with the people of the time (Ikram, 2005a; Mark, 2017; Vandrope, 2010).

Following the Ptolemaic Period, the Romans, known for their military prowess and imperial expansion, brought about a confluence of cultures that left an incredible mark on Egypt's traditional system during what is now called the Roman Period. Like the Greek rulers, Roman rule promoted an intertwining of Egyptian and Roman beliefs and deities. The polytheistic nature of both cultures allowed for a relatively seamless integration. Temples were often dedicated to a mix of Egyptian and Roman deities. One notable example is again the cult of Isis. The worship of Isis underwent a process of Romanization, adapting a Greco-Roman religious form (Bommas, 2012). Her cult, emphasizing salvation and an afterlife, resonated with the broader Roman religious milieu (Bommas, 2012).

The political landscape of ancient Egypt underwent significant transformations as well. With the defeat of Cleopatra VII and Mark Antony by Octavian (later known as Augustus) in 30 BC, Egypt became a Roman province (Bommas, 2012; Capponi, 2016). The annexation marked the end of the Ptolemaic rule and the beginning of a new administrative era. The Roman imperial system brought about a centralized administration that differed from the decentralized structure of the Pharaonic dynasties and periods (Capponi, 2016). This political shift was not without its challenges. While initially accepting Roman control, riots were common in Egypt as Egyptians voiced dissatisfaction with Roman rule and their rampage against pagan sanctuaries and religions (Wasson, 2016). Despite sporadic revolts, Roman influence remained dominant in Egypt for centuries, shaping its religious and political institutions.

From the Late Period onward, significant religious and political change saw a proliferation of animal cults due to the native Egyptians' desire to hold onto their religious beliefs in times of uncertainty. The animal cults reached their apex during these periods, which led to millions of animals being mummified (Ikram, 2005a, 2005b, 2015; O'Brien, 2011). Ultimately, ancient Egypt's animal cults and polytheistic religion ended

in AD 380, with the spread of Catholicism throughout the Roman Empire (Bailleul-LeSuer, 2019).

## 2.2 Animals in ancient Egypt

### 2.2.1 The importance of animals in ancient Egypt

Animals were profoundly multifaceted in ancient Egypt, integral to daily life, religion, culture, and the economy. One of the most striking aspects of ancient Egyptian culture was its deeply ingrained religious beliefs. Animals featured prominently in their pantheon of gods and goddesses. For example, the god Thoth had the head of an ibis (Houlihan & Goodman, 1986), while the goddess Bastet was represented as a lioness or cat (depending on time and region) (Ikram, 2007). All aspects of Egyptian life were connected to animals (Bodziony-Szweda, 2010).

The Egyptian economy relied heavily on animals. Cattle, goats, sheep, and pigs were domesticated for their milk, meat, and hides. At the same time, animals like donkeys and camels were essential for transportation and agriculture, helping to cultivate the fertile Nile floodplain (Scanes, 2018). Ancient Egyptians are also believed to be one of the first societies to use animal manure as compost to help crops grow year-round (Wetterstrom & Murray, 2001). Animal byproducts were also integral to the medicinal practices in ancient Egypt. For instance, honey was used as an antibiotic to prevent and treat infections, and substances like crocodile excrement were believed to prevent pregnancy. Organs were also used in early surgery, as the Egyptians believed that specific animal organs held curative powers (Metwaly et al., 2021).

Some animals, such as the sky goddess Nut, depicted as a cow, were associated with the Egyptian calendar and played a role in timekeeping. The rising of certain stars and constellations, often represented as animals, helped determine the timing of critical agricultural events, such as the flooding of the Nile (Mohamed, 2017). In ancient Egypt, animals also provided entertainment and sport. Hunting expeditions, particularly of wild animals like lions and hippos, were a common pastime for the elite; hieroglyphic depictions of hunting were prevalent among the pharaoh's tombs. These activities showcased their bravery and skills while also linking the elite to the divine by emulating

the prowess of goddesses like Sekhmet, the lion-headed goddess of war (Bodziony-Szweda, 2010).

In Egyptian art and hieroglyphs, animals were used extensively as symbols, each carrying its unique meaning. The scarab beetle, for instance, symbolized regeneration and transformation, while the hawk represented the god Horus and the protection of the pharaohs (Ikram, 2007). Animals also held significant roles in diverse cultural traditions and rituals, particularly evidenced in elaborate funeral ceremonies held for peoples' pets, believing that animals had souls that needed to be guided to the afterlife (Ikram, 2005a, 2005c, 2013; Mark, 2017). The reverence and respect with which the ancient Egyptians treated animals were fundamental to their civilization's identity and contributed to the enduring legacy of this remarkable civilization.

While using animals for religious and economic purposes was commonplace throughout human history (Alaica, 2018; Overton & Hamilakis, 2013), ancient Egyptians were unique in their practice of mummifying animals.

### 2.2.2 Animal mummies of ancient Egypt

Over the years, numerous archaeological discoveries have shed light on the extent of animal mummification in ancient Egypt (Ikram, 2015b; Nicholson, 2016, 2022). Vast cemeteries dedicated to specific animal species, such as cats, ibises, baboons, and more,



*Figure 2.3 Wooden funerary stela depicting the adoration of Ra-Horakhty-Atum (Third Intermediate Period). Animals feature prominently in this worship, notably the falcon-headed god Ra-Horakhty-Amun, a composite of the solar and sky gods Ra and Horus. Above this head is an Aten (sun disk), encircled by Uraeus (a depiction of the cobra-goddess Wadjet). The top of the stela is the winged sun disk, propelled by a scarab beetle. Two jackals symbolize Anubis and travel from the underworld. Plucked and eviscerated fowl are portrayed in the offerings. Image retrieved from [https://www.britishmuseum.org/collection/object/Y\\_EA27332](https://www.britishmuseum.org/collection/object/Y_EA27332).*

have been unearthed. For example, at the sacred falcon necropolis at Djedhor, a minimum of 391 mummified birds were unearthed (Rowland et al., 2013). Birds belonging to the Order of Falconiformes were most commonly found, accounting for 84% of the recovered avian remains (Rowland et al., 2013). At the Saqqara necropolis in Cairo, two embalming workshops were recently discovered, one used to mummify humans and the other to mummify animals, dating to 664-525 BC (Rageot et al., 2023; Tabikha, 2023). While research on the workshops is in its infancy, the co-existence of human and animal mummification practices demonstrates the entangled nature of the mummification industries and the equal importance of both humans and animals in the Egyptian worldview.

Additionally, it has been posited that specialized breeding and rearing practices were central to the animal mummification industry. While the domestication of cats and dogs for slaughter is probable, there are doubts about the domestication of birds considering modern DNA analysis and behavioural analysis. A study by Wasef et al. (2019) found that the mitochondrial genetic diversity of sampled mummified sacred ibis remains is not significantly different from modern wild populations. This means that the expected bottleneck from the mass sacrifice of birds and lack of external DNA influx, observed in domestication populations, is not observed in genetic samples from ibis mummies (Wasef et al., 2019). Due to their solitary nature, domestication of raptors also seems highly improbable. Raptors are unlikely to live in groups in a farm-like setting (Bailleul-LeSuer, 2019). Regardless, birds in ancient Egypt were mummified by the millions throughout the dynasties, perhaps alluding to some practices of wild animal “farming” or management, where populations were kept close to temples with the allure of food or safe breeding sites, in tandem with natural, seasonal migration patterns (Wasef et al., 2019).

Today, the study of animal mummies continues to provide valuable insights into ancient Egyptian culture, religion, and society (Atherton-Woolham & McKnight, 2014; Ikram, 2005a; McKnight, 2020; von den Driesch et al., 2005). Scientific analysis of the mummies’ contents has revealed details about the diet, health, and even the geographic origin of the animals (Hekkala et al., 2020; Johnston et al., 2020; Linglin et al., 2020).



Animal mummies are currently referred to in four distinct categories: pets, victual, sacred, and votive (Ikram, 2005a).

### 2.2.2.1 Pets

Pets served a religious and practical purpose in ancient Egypt. Pets were the most long lasting animal mummies, dating to the Predynastic Period and onward (Ikram, 2005a). Egyptians were pictured in their tombs with their pets, thus ensuring their continued joint existence in the Afterlife (Ikram, 2013; Ikram et al., 2013). Occasionally, a pet's name would be carved above its image, providing further insurance for their eternal life. Some pet lovers went so far as to bury their pets with them. A man called Hapy-man was buried with his pet dog curled up at his feet, much like medieval tomb carvings found in Europe featuring a knight and his hounds (Ikram, 2005c). In ancient Egypt, dogs were given care and respect as pets. Dogs played an essential role throughout Egyptian history, acting as guards, hunting aids, and companions. They also held a crucial position in Egyptian religion, being closely associated with the gods Anubis and Wepwawet, deities related to travel, either through the desert or between this world and the next (Ikram, 2013; Ikram et al., 2013). In some instances, the pets would be provided with their own coffins or sarcophagi and food offerings. Prince Djhutmose, the eldest son of Amenhotep III, had a unique limestone sarcophagus carved for his pet cat, Miao (Ikram, 2005c). Isetemkheb D was buried with her pet gazelle in her tomb, a gazelle that was mummified in the same manner as high-status humans from the 11<sup>th</sup> Dynasty (Ikram, 2005c). Baboon mummies from the Valley of the Kings show that they were eviscerated. Their canines had also been removed, likely so they would not harm anyone they had bitten. The presence of pet baboons in ancient Egypt indicates animal trade with neighbouring areas in Africa and raises questions regarding veterinary practices in ancient Egypt. No doubt, canine removal was an excruciating procedure for the baboons, best carried out with some form of anesthetic (Ikram, 2005c). Not to mention the danger it could pose to an individual pulling said teeth!

### 2.2.2.2 Victual

Sustaining the dead in the Afterlife was a crucial element of Egyptian society, a concept frequently depicted in tomb scenes of daily life and offerings, models of food and food processing, and evidenced by plant-based and animal offerings dating back to the Predynastic period (Brevick, 2019). While a wide range of food items was prepared to feed the dead in the afterlife, including food items such as bread, garlic, green onions, and dates (de Vartavan, 1990), victual mummies refer specifically to mummified animals intended as food for the afterlife. Victual mummies were food offerings placed in a human's tomb to ensure they could feast for eternity (Ikram, 2005a). These victual mummies were typically positioned within the tomb of the deceased, often alongside human remains or in dedicated chambers (Ikram, 1995).

Archaeological findings reveal various animals used for these victual offerings, including cattle, geese, pigeons, ovicaprids (domesticated goats and sheep), and possibly wild antelopes (Ikram, 2005a). These offerings often comprised diverse food elements, from ribs and steaks to entire legs and internal organs. Interestingly, although there is evidence of trichinella cysts in mummified remains, such as the remains of Nakht, indicating the consumption of inadequately cooked pork by ancient Egyptians (Millet et al., 1980), no victual pork mummies have been recovered (Brevick, 2019; Ikram, 2005a; O'Brien, 2011). This implies a possible devaluation or lack of preference for pork as a culinary offering in the afterlife (Brevick, 2019; Ikram, 2005a; O'Brien, 2011).

The preparation of victual mummies closely resembled how these animals would have appeared on the dinner table. For instance, fowl victual mummies, after being plucked and decapitated, typically had their wing tips and feet removed. The birds would then undergo evisceration and preservation in various oils, resins, and spices. Subsequently, they were meticulously wrapped in linen bandages, adopting a form closely mimicking a cooked fowl (Brevick, 2019).

### 2.2.2.3 Sacred

Sacred animals are meticulously preserved creatures that are more than just physical remains; they represent a sacred connection between humans and the divine. Sacred

animals were generally identified based on specific or unusual markings that were believed to represent the physical presence of a god. Central to the religious beliefs of ancient Egypt was the concept of animism (Budge, 2013; Oesterdiekhoff, 2008) – the belief that spirits inhabited both living beings and inanimate objects. For example, the Egyptians believed that part of the soul of the god Sobek (the crocodile-headed god responsible for fertility) entered the body of a crocodile (Hekkala et al., 2022). Specifically, sacred animals were believed to house a god's divine essence, thus transforming them into divinities (Ikram, 2005a). The animal was treated and worshipped as a god throughout life, buried with a grand ceremony, just as a pharaoh would have been treated and buried (Ikram, 2005a). Priests would adorn these animals with gold jewellery, feed them delicacies, and care for them until their natural death (Hekkala et al., 2022). Upon a sacred animal's death, its spirit found its way into another similarly marked animal, who would be worshipped and celebrated like the last. When the sacred animals died, the entirety of Egyptian society mourned. For example, the Apis Bull (the physical representation of Ptah and Osiris) was mourned for seventy days while the animal was mummified. Ceremonial, funerary rituals (observed by both priests and locals) included no cutting or washing of hair, public mourning, and a four-day fast, followed by the consumption of only bread and vegetables until the sacred Apis Bull was placed in its coffin and final rites were administered (Ikram, 2005a).

The Apis Bull is critical to Egyptologists seeking to understand animal mummification. Despite the vast written record of ancient Egypt, through translated hieroglyphs and countless recovered books and papyri, very few texts exist that provide a written record of the mummification process, especially for animals (Ikram, 2015a). Most of our understanding of animal mummification comes from experimental archaeology (e.g., Ikram, 2015a) or chemical analyses of embalming resins (e.g., Marković et al., 2022). However, The Apis Bull Papyrus is one of the only written records documenting the Apis' burial rites and embalming rituals (Vos, 1993).

#### 2.2.2.4 Votive

Votive mummies differed from sacred animals in that they were offerings of a specific animal to a particular divinity that locals or pilgrims could purchase as prayers to the

gods (Ikram, 2005a). Similar concepts exist in other religions, like lighting a candle in church (Ikram, 2005a, 2015b) or leaving terracotta tablets bearing Buddhist symbols at temples in Tibet (Reedy, 2006). In the case of ancient Egypt, mummified cats were offered to the goddess Bastet, the goddess of pleasure; ibises to Thoth, the god of learning and wisdom; and dogs to Anubis, the god of mummification and travel (Ikram, 2005a). Votive mummies dedicated to gods and goddesses differed from sacred animals because they were not unique. Instead, they acted as pilgrims' gifts to the gods; pilgrims purchased and offered votive mummies at shrines dedicated to the relevant gods. These mummies were presented as offerings to the gods in temples and shrines, symbolizing the devotion and piety of the individuals or communities who made these offerings. Pilgrims purchased animal mummies to seek favour or blessings from the gods (Ikram, 2005a). Votive mummies often bear a superficial likeness to animal representatives of the deity to whom they were dedicated (McKnight & Atherton-Woolham, 2016). A plea to the gods/goddesses may have also been written on papyrus or linens and wrapped around the mummified animal, as part of the votive offering (Cornelius, 2012; Ray, 2005).

Animals for votive offerings were killed before their natural death. For example, many cat mummies discovered at the Bubasteion in Saqqara were put to death at very young ages, either by breaking the neck (or strangulation?) or by smashing the skull with a blunt object (Ejsmond & Przewłocki, 2014). While not treated with the same funerary ceremony and rites as sacred animals, votive mummies were prepared in designated embalming houses and kept until purchased. Once a year, during a festival, the votive offerings would be taken in procession and buried in massive catacombs that were sealed with mud-brick walls for a year until the next celebration (Ikram, 2005a, 2015b). These catacombs were known as Houses of Rest and have been found at many significant ancient Egyptian sites such as Tuna al-Gebel, Armant, and Saqqara, where millions of votive mummies have been recovered through years of excavations (Ikram, 2005a).

In fact, animal mummies were produced in such high quantity that, in the nineteenth century, when archaeological expeditions were primarily consumed with the recovery of sarcophagi and artifacts for European museums, thousands of mummified animals were considered insignificant for scientific consideration (Ciliberti et al., 2020). An article

published in 1890 by Parisian doctor Gaston Camille Charles Maspero reported that 180,000 Egyptian cat mummies were brought to London and sold as fertilizer (Ciliberti et al., 2020). Additionally, Maspero accounts that an entire monkey mummy necropolis was sent to Germany to fertilize beet fields (Ciliberti et al., 2020). Animal mummies were also used for fuel, medicinal powder (both human and animal mummies were used for this purpose), and ballast for ships, which led to the destruction of hundreds of thousands of mummies throughout history (Ciliberti et al., 2020).

Votive animal mummies also played a significant role in the economy of ancient Egypt (Ikram 2012). Animal cults and their associated industries contributed to the economy in that they required personnel to maintain the functioning of the cult, acquire animals, care for the animals, fashion mummification materials, perform mummification, sell mummified animals, and build and maintain infrastructure for the ritual burial of animal mummies (Ikram, 2015; O'Brien, 2011).

As part of the *Ancient Egyptian Animal Bio Bank* project, 800 mummified animals stored in museums in the UK, Europe and the USA were imaged with varying radiographic techniques (McKnight & Atherton-Woolham, 2016). Researchers found that animal taxa varied significantly, documenting the discovery of birds, cats, and crocodiles. Notably, one-third of the votive mummies imaged were discovered to be pseudo mummies (McKnight & Atherton-Woolham, 2016). A pseudo mummy is a bundle containing either incomplete skeletal elements or non-skeletal materials (like mud, reeds, and eggshells) (Ikram, 2005a; McKnight et al., 2018; McKnight & Atherton-Woolham, 2016). It is important to note that pseudo mummies are not fake; fake implies a deliberate intention to misrepresent or mislead (McKnight et al., 2018). Instead, the ancient Egyptians believed that any material that came into contact with sacred animals could be considered equally effective as a votive offering (McKnight et al., 2018; von den Driesch et al., 2005). The concept of synecdoche, where a part symbolizes the whole, gained widespread acceptance in the context of votive offerings within ancient Greek and Roman cultures. It is plausible to extend this concept to Egypt, especially during the Late to Roman Periods, as these eras witnessed heightened interactions with Greco-Roman cultures alongside the rise of the votive cults (McKnight et al., 2018). In this context, materials gathered in

sacred settings could undergo a similar transformative process through mummification, fulfilling the donor's intent. The Egyptians, with their intricate connections to the natural world, including animals and the land intertwined with their religious beliefs, suggest that even partial elements such as materials or incomplete or co-mingled animal remains could attain votive status (Ikram, 2005a; McKnight et al., 2018; McKnight & Atherton-Woolham, 2016; von den Driesch et al., 2005).

### 2.2.3 Animal mummification

Throughout ancient Egypt, animals were mummified in diverse ways (Ikram, 2005b). Methods vary based on factors like the type of animal, available resources, and individual preferences. Few ancient texts highlight mummification methods for humans – some of these methods have been discovered in animal mummies. Other methods for animal mummification have been identified in modern archaeological research. Traditional practices, used for both humans and larger animals, involved desiccation using natron to draw out bodily fluids (Ikram, 2005b, 2010). Natron, abundant in ancient Egypt, possesses deodorizing and antibacterial properties crucial to mummification. Mummification quality peaked in the royal mummies of the New Kingdom, involving brain and organ removal, washing, and desiccation using dry natron for around 40 days (Ikram, 2005b, 2015a) to 70 days (Schjødt, 2020). The mummified body was then anointed with sacred oils and resin before being wrapped in linen bandages (Ikram, 2005b; Marković et al., 2022). This “evisceration and desiccation” method was prominent in the New Kingdom and closely associated with animals like dogs, gazelles, crocodiles, and baboons. By the Third Intermediate Period, mummification hastened, relying more on oils, resin, and bitumen, possibly leading to poorer desiccation. Reusing natron likely contributed to this decline (Ikram, 2005b).

The second method, “desiccation and anointment,” present in both human and animal mummies, involved cleaning the intestines, desiccating with natron, and anointing and wrapping the body. The wrapped bundle was then coated with vast amounts of black substances like resin, oil, or bitumen (Ikram, 2005b; Marković et al., 2022). Pouring substances like resin over minimally desiccated bodies inhibited bacterial growth and was a quick method essential to keep up with the demands of growing votive industries and

cult beliefs. However, this caused corporeal disintegration, as evidenced by skeletal disarticulation and black power residue (disintegrated flesh) (Ikram, 2005b).

“Immersion” is similar to the previous method. However, it has only been seen in votive mummies, particularly birds, and does not include any desiccation prior to mummification. Immersion involved submerging live birds in a hot resin vat, resulting in poorer mummification and preservation. Another variation called “encasement” has been observed in baboon mummies at Saqqara, involved placing baboons in squatting positions and encasing them in gypsum plaster, thus mimicking the living seated position of baboons (Ikram, 2005b).

“Enemas” were another commonly used method of mummification. This method bypassed incisions, using cedar or pine oil injected into the anus to liquefy internal organs. During this process, the body was also placed in natron. The best-known example of this method of mummification for animals includes the Buchis Bulls and the Mother of Buchis mummies, discovered at Armant (Ikram, 2005b). Recovered at this site are the actual enemas used on the animals, which are remarkably similar to those employed by modern-day veterinarians (Ikram, 2005b).

In the Ptolemaic and Roman Periods, “defleshing” appeared, evidenced by disarticulated skeletons wrapped in resin bandages. There are a few hypotheses as to why this practice would have occurred. For example, a proposed reasoning for defleshing a bovine concludes that the animals were used as a food source before mummification and burial (Ikram, 2005b). However, dog mummies found in similar conditions were much less likely to be used for consumption (Ikram, 2005b). Why this practice would have occurred remains unknown.

#### 2.2.4 Birds of ancient Egypt

Birds were profoundly significant in ancient Egyptian civilization, permeating various aspects of daily life, culture, religion, and symbolism (McKnight et al., 2022; McKnight et al., 2018). Avian creatures were not merely ornamental or casual elements in Egyptian

society; they played essential roles in shaping this ancient culture's belief system, artistic expressions, and daily rituals (McKnight et al., 2018).

One of the most significant roles of birds in ancient Egypt was their association with the soul and the afterlife (Mark, 2017). The Egyptians believed birds were intermediaries between earthly and divine realms. Birds, particularly the *ba*-bird (often represented as a human-headed bird), were thought to carry the deceased's soul to the afterlife (Assmann, 2005; Mark, 2017; McKnight et al., 2022). This symbolic journey was depicted in art and funerary texts, emphasizing the essential role of birds in facilitating the soul's transition to the next world. Various bird hieroglyphs represented not only the animals but also carried symbolic meanings associated with concepts such as flight, freedom, the soul, and the divine, thus conveying both practical and spiritual messages (McKnight et al., 2022).

Many bird species were associated with specific deities in the Egyptian pantheon. For instance, the falcon was closely linked to the god Horus. The story of Horus, one of the most recognized mythologies in ancient Egypt, illustrated the eternal fight between the virtuous and the sinful (ReFaey et al., 2019). Horus served many functions in the pantheon, notable as the god of kingship, healing, protection, the sun and the sky (Houlihan & Goodman, 1986; ReFaey et al., 2019). The ibis was associated with Thoth, the god of wisdom and writing (Houlihan & Goodman, 1986). The vulture, often depicted as a nurturing and protective mother, was connected with the goddess Nekhbet. Nekhbet was frequently portrayed on sarcophagi as spreading her wings over the pharaoh while grasping in her claw the cartouche symbol (a symbol representing good luck and protection from evil) (Graham, 2020; Houlihan & Goodman, 1986).

Mummified remains of ibises and birds of prey continue to emerge from catacombs and be discovered in tombs and necropoli specifically dedicated to house these birds for eternity (Ikram, 2005a; Rowland et al., 2013). The Upper Egyptian site of Edfu is notable for the abundance and quality of scenes portraying coronation ceremonies. During these ceremonies, a live falcon played a significant role, sitting for a year on the throne beside the god Horus of Behdet. This falcon enjoyed a privileged existence within the temple precinct, receiving special meat dishes, including fowl and possibly donkey meat, which



symbolized the god's enemies who had been ritually terminated (Bailleul-LeSuer, 2019). After a phase of development during the Late Period, the cults of the ibis and of the falcon, in which live birds played a key role, reached their pinnacle during the Ptolemaic period. They continued to be revered during the Roman period but presumably came to an end with the spread of Christianity in the country and the Edict of Thessalonica in AD 380, which ordered the closing of all pagan temples in Egypt. (Bailleul-LeSuer, 2019).

## 2.3 Avian osteology

The study of bird bones is critical to archaeological research, shedding light on past ecosystems, human behaviour, and environmental changes. Archaeologists employ various techniques to identify and analyze bird bones found at archaeological sites, some of which are increasingly challenging or impossible when analyzing bird bones on a clinical CT scan. An extensive understanding of basic bird skeletal anatomy is needed to accurately identify and discuss skeletal elements within wrapped, mummified bird bundles. The primary method for identifying bird bones is morphological analysis (Cohen & Serjeantson, 1996). This includes looking at the size and proportions of bones, the shape and structure of bones, and the joint connections between bones (Cohen & Serjeantson, 1996). For example, beaks vary significantly due to dietary specialization between species (Csermely & Rossi, 2006). The tomial tooth is a specialized beak and dental structure found in birds of prey, which plays a critical role in their hunting and feeding behaviour (Bellairs & Jenkin, 1960; Csermely & Rossi, 2006). Comparatively, wading birds, like ibises, have a straighter, crescent-shaped beak, which is more versatile for searching through mud and weeds for prey (du Toit et al., 2022).

In order to study mummified birds with 3D imaging techniques and deep learning techniques (explained in Chapter 2.4), the evolutionary trajectory of the bird skeleton (Figure 2.4) must be considered, as it affects scanning parameters and subsequent visualization. The skeletons of birds and mammals show significant differences resulting from their disparate evolutionary pathways and ecological adaptations (Storer, 1960; Swinton, 1960). Birds have developed two modes of locomotion: walking and flying. The lower limbs and pelvic girdle have become powerful stress-bearing structures, capable of supporting the body on land and in the air (Bellairs & Jenkin, 1960), yet lack relatively

robust articulations, which decreases the weight of their bones (Bartosiewicz & Gal, 2007). Additional lightening of the bird skeleton has been achieved through evolutionary processes resulting in the thinning of the bone cortex, pneumatisation of some of the bone through air sacs, and loss of teeth (Bellairs & Jenkins, 1960; Cohen & Serjeantson, 1996).

Bird skeletons are extremely diverse, and the images used in this chapter are to introduce basic anatomical terms. Each image is labelled with the species name, but do not necessarily reflect birds which may have been found in ancient Egypt.

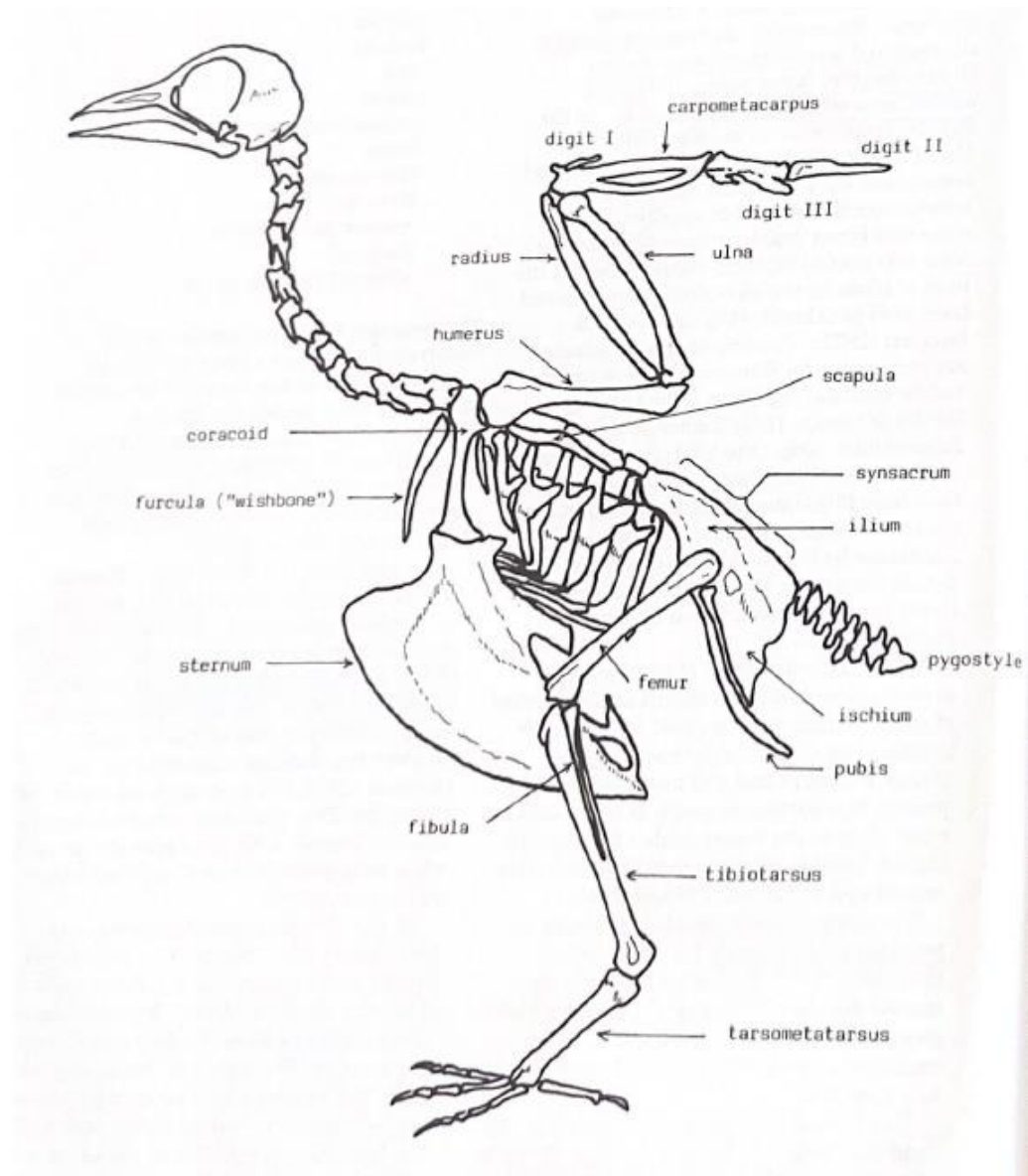


Figure 2.4 Complete *Clumba palumbus* skeleton with accurate anatomical names. Image retrieved from Cohen and Serjeantson (1996, p. 4).

### 2.3.1 Axial skeleton

The skull (Figure 2.5) is thin-walled with a large orbit and, like a reptile skull, has a quadrate bone from which the mandible or lower bill is suspended (Cohen & Serjeantson, 1996). The proportions of the avian skull reflect a much larger brain and eye in birds than in other reptiles and amphibians (Bellairs & Jenkin, 1960). The roof of the skull is formed by the parietals and larger frontals, which cover the orbits and articulate with the nasal bones at the back of the beak (Bellairs & Jenkin, 1960). In most bird species, the fused premaxillae form the majority of the skeleton of the upper beak and are encased by a horny rhamphotheca, which shapes the beak (Bellairs & Jenkin, 1960).

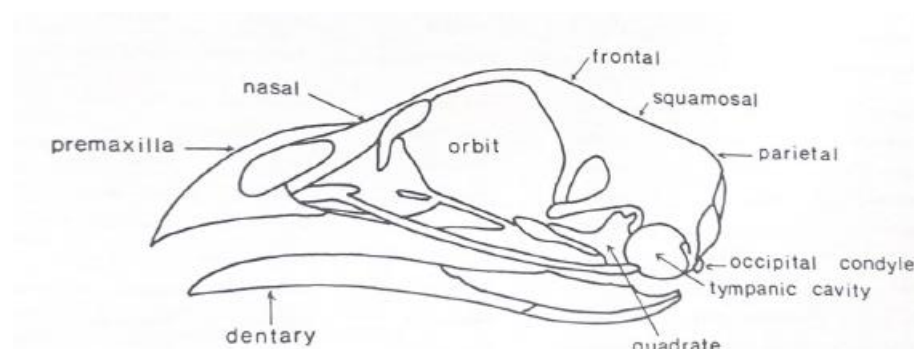


Figure 2.5 *Gallus gallus* skull with proper anatomical names. Image retrieved from Cohen and Serjeantson (1996, p. 10).

The bird skull also has a unique structure called the scleral ossicle (Figure 2.6), which is also found in some fish and reptiles. The scleral ossicle is not a single-ringed piece of bone but is formed by multiple individual scales of interlocking bone arranged in a ring (Lemrich, 1931), which stiffens the concavity of the eyeball at the corneoscleral junction (Bellairs & Jenkin, 1960). The number of individual scleral scales within an entire scleral ossicle varies between 10 to 18 in different species, with 14 to 15 being the most common (Bellairs & Jenkin, 1960).

There is high interspecies variation in the scleral ossicle as this structure is highly influenced by activity patterns (Franz-Odenaal, 2018; Hall, 2008), resulting in diverse morphologies owing to millions of years of evolution of the ocular skeleton (Franz-Odenaal, 2018). For example, nocturnal animals have larger corneal diameters that allow for more control over the amount of light let in to enhance night vision. This night-patterned activity is associated with larger, tubular shaped ossicular scales, whereas

diurnal animals have flatter ossicular scales (Franz-Odendaal, 2018; Otte, 2013). The scleral ossicle and scleral cartilage support the eye's sclera (outermost anatomy of the eyeball), which maintains the eyeball shape and protects the internal eye structures from injury (Franz-Odendaal & Hall, 2006). Between avian species, the scleral ossicles overlap in various ways, reflective of how the bones develop (see Franz-Odendaal, 2008; Franz-Odendaal, 2018), and the interspecies diversity for fish, reptiles, *and* birds is well documented (e.g., Lemmrich, 1931; Lima et al., 2009; Franz-Odendaal, 2008; Walls, 1942).

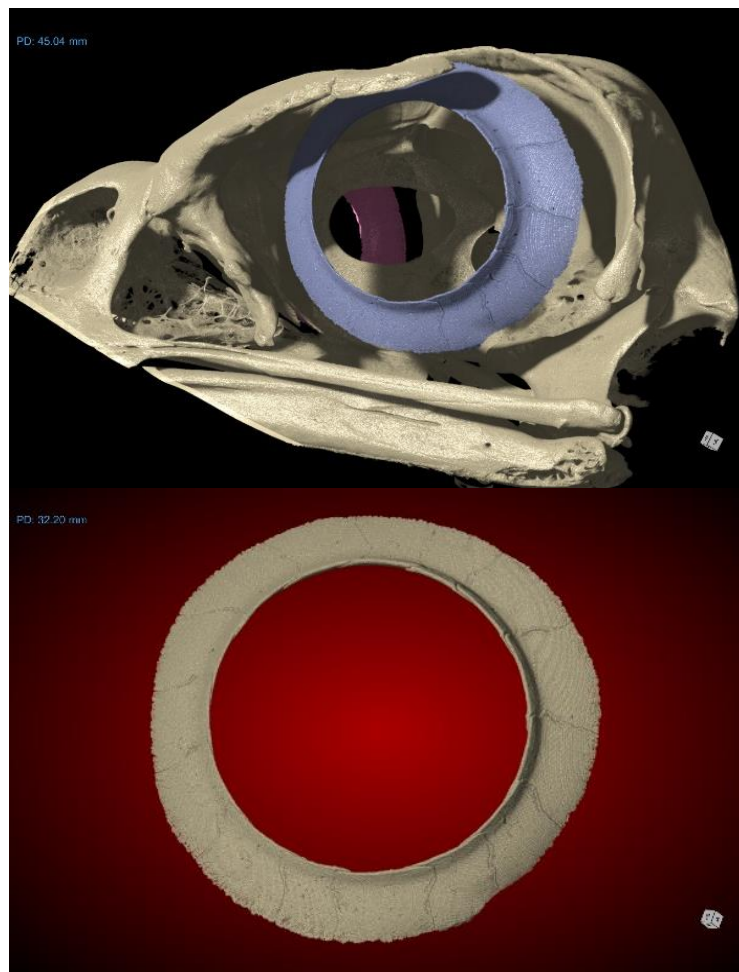


Figure 2.6 Example of the scleral ossicle. The top image is a 3D rendering of a modern *Accipiter cooperii*, scanned on the Yxlon FF35 CT (2023), at 13.5  $\mu\text{m}$  voxels. The blue bony ring indicates the location of the scleral ossicle within the bird's cranium. The bottom image is the same highlighted ossicle, digitally removed for visualization of the individual scales. Image processed and created by Maris Schneider in Dragonfly (v2022.2-1409).

The number of cervical vertebrae in a bird's neck varies from 8-25 (Cohen & Serjeantson, 1996). The atlas is a small ring-shaped bone articulating with the skull's occipital condyle (Bellairs & Jenkin, 1960). The upper thoracic vertebrae together form the notarium, and the lower thoracic vertebrae fuse to the lumbar vertebrae to form part of the synsacrum (Cohen & Serjeantson, 1996). The synsacrum comprises these and the sacral and anterior caudal vertebrae (Cohen & Serjeantson, 1996).

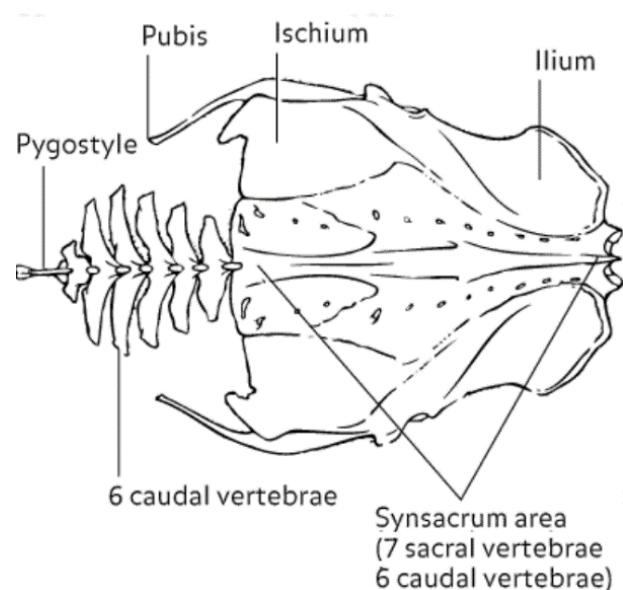


Figure 2.7 Pelvic girdle of *Buteo buteo* with proper anatomical names. Image retrieved from <https://avesbiology.com/skeleton.html>

The pelvis becomes ankylosed (fused) to the synsacrum in mature birds. There are five to eight caudal vertebrae, and the vertebral column terminates with the pygostyle (Cohen & Serjeantson, 1996; Smith & Smith, 1990), to which the primary tail feathers are attached (Figure 2.7). Some species of birds have accessory pygostyle bones, a bilateral pair of small bones attached to the base (ventral surface) and lateral edges of the pygostyle bone, responsible for transmitting the force of several major tail depressor and abductor muscles to the pygostyle (Richardson, 1972).

The thoracic ribs (Figure 2.4) are in two parts, connected by a movable joint. The dorsal part is two-headed and bears a backward point uncinat process, a feature that distinguishes bird ribs from those of small mammals. The sternum (Figure 2.4) is a triangular bone with a deep keel (Cohen & Serjeantson, 1996).

### 2.3.2 Appendicular skeleton

The coracoid, the scapula, and the pair of clavicles, which unite to form the furcula (wishbone), comprise the pectoral girdle (Figure 2.8). The scapula is very long, extending back over the ribs, to which it is firmly attached by ligaments (Bellairs & Jenkin, 1960). The scapula articulates with the coracoid and the acromion process on the clavicle (Bellairs & Jenkin, 1960). The large coracoids run downward and inward to articulate

with the sternum (Bellairs & Jenkin, 1960). The clavicles are characteristically fused ventrally to form the furcula and are united by cartilage. The angle of the furculum is closely tied to the flight patterns of birds; for example, strongly flying birds, like owls or raptors, have a wider furculum (Bellairs & Jenkin, 1960).

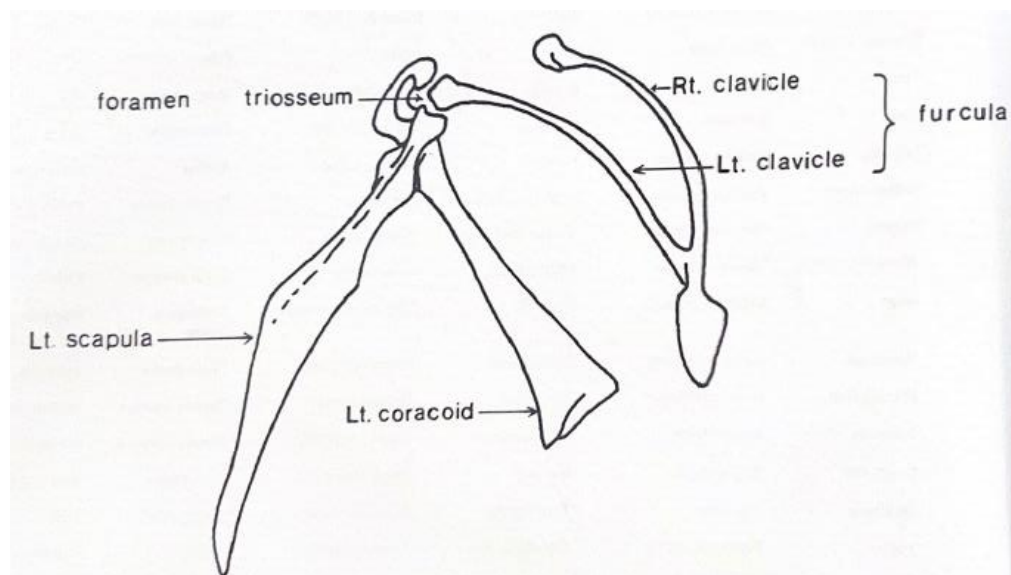


Figure 2.8 Pectoral girdle of *Gallus gallus* with proper anatomical terms. Image retrieved from Cohen and Serjeantson (1996, p. 10).

The forearm (Figure 2.9), or wing, comprises the humerus and ulna, which is a stouter bone than the radius in birds, a radius, a carpometacarpus, and the phalanges (Cohen & Serjeantson, 1996). Sesamoid bones may be present at the elbow, and in some species, these sesamoid bones fuse with the ulna at the olecranon process (Bellairs & Jenkin, 1960). Birds have two carpal bones, one at the end of the radius and one at the end of the ulna (Bellairs & Jenkin, 1960; Cohen & Serjeantson, 1996). Distal to the carpal bones is a compound structure, the carpometacarpus. This is formed by the fusion of some distal carpals with three metacarpals (Bellairs & Jenkin, 1960). The wing also contains a variable number of phalanges, of which the largest is the first phalanx of the major digit (Cohen & Serjeantson, 1996).

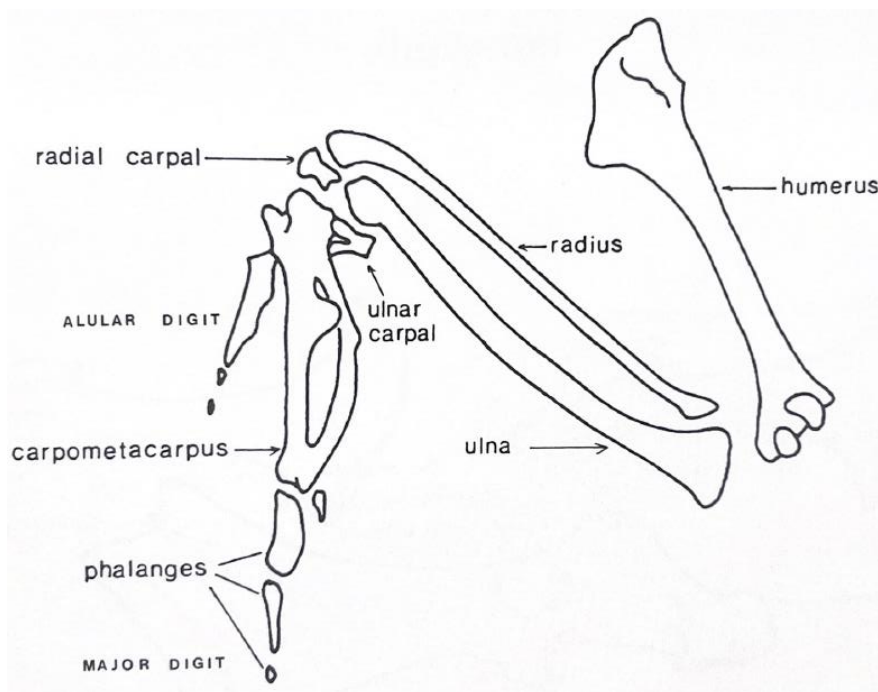


Figure 2.9 Bones of *Gallus gallus* wing with proper anatomical terms. Image retrieved from Cohen and Serjeantson (1996, p. 11).

In the hind limb (Figure 2.10), the femur has a prominent trochanter where the gluteal muscles attach (Bellairs & Jenkin, 1960). The tibiotarsus and the fibula articulate with the femur at the knee joint. The fibula is reduced to a narrow splint, which is generally only about two-thirds the length of the tibiotarsus (Bellairs & Jenkin, 1960; Cohen & Serjeantson, 1996). A patellar sesamoid bone is found in many bird species and is related to the tendon of the femoro-tibiales muscle (Bellairs & Jenkin, 1960). The avian foot is highly specialized owing to specific evolutionary mechanisms, such as the adaptive need to grasp prey or perch on trees (Backus et al., 2015). The fibula and tibiotarsus articulate with the tarso-metatarsus, a distal row of tarsals that has fused to the metatarsals II, III, and IV (Cohen & Serjeantson, 1996). Typically, the tibiotarsus and tarsometatarsus are the same length to help maintain a bird's centre of gravity over its feet while crouching (Storer, 1960). The articular ends of the distal tibiotarsus and the proximal tarsometatarsus are unfused or cartilaginous in immature birds. Digits II, III, and IV articulate with the trochlea of the tarsometatarsus and point forward in most species, and the first hind digit points backward. The number of foot phalanges varies (Cohen & Serjeantson, 1996); for example, a bird with an anisodactyl foot has four digits, with the

hallux (first digit) facing backward and the other three digits pointing forward. This is the most common arrangement of digits, specifically found within hawks (Tsang and McDonald, 2019). Other digit arrangements include zygodactyl, heterodactyl, syndactyl, pamprodactyl, didactyl, palmate, semipalmated, lobate, and totipalmate (see, Botelho et al., 2015 and Tokita et al. et al., 2020).

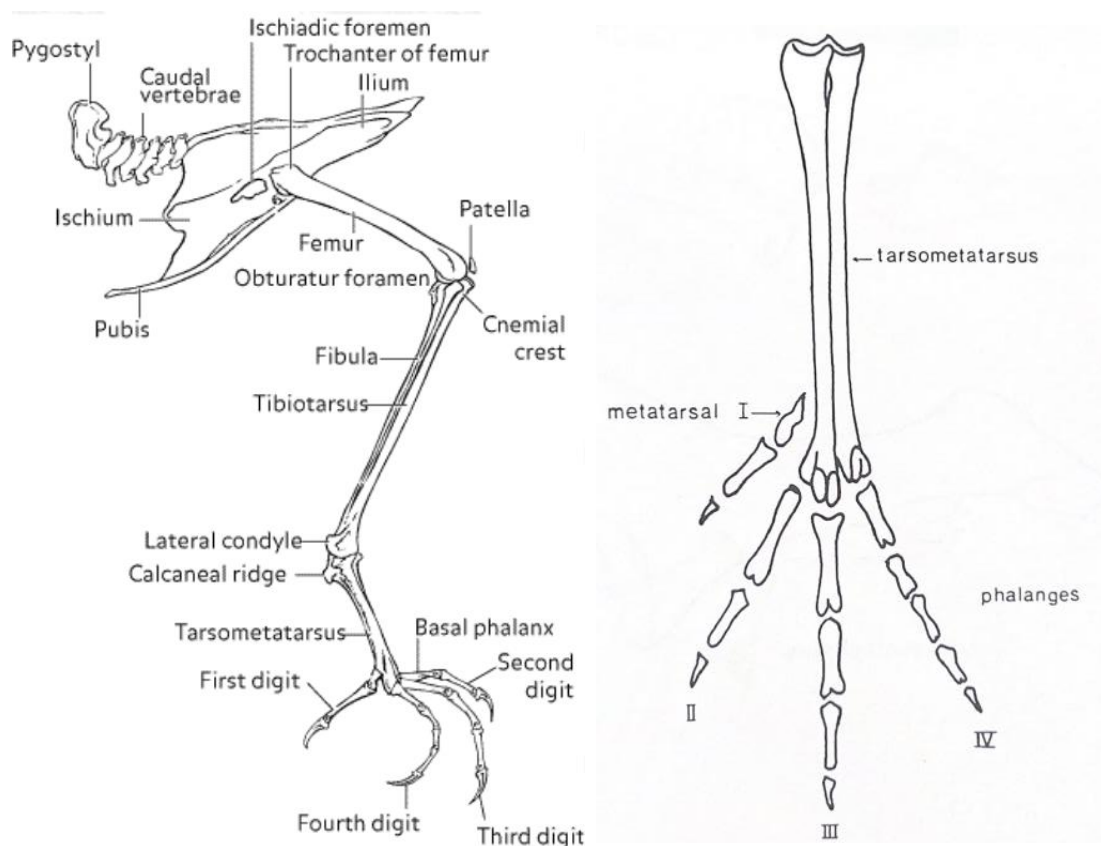


Figure 2.10 Image on the left: bones of the lower hind limb of *Buteo buteo* articulated with the pelvic girdle. Image retrieved from <https://avesbiology.com/skeleton.html>. Image on the right: hind limb of *Gallus gallus*, starting at the tarsometatarsus, with proper anatomical names. Image retrieved from Cohen and Serjeantson (1996, p. 11).

Understanding the proper anatomical terminology and relationality is crucial in forming the foundation for the accurate and systematic identification of bird skeletons. By delving into the intricate details of avian anatomies, such as the structural nuances of bones, variations in beak morphology, and the diverse arrangement of scleral ossicles, this overview lays the groundwork necessary for a multifaceted understanding of the skeletal features that distinguish one bird species from another.



## 2.4 Imaging and deep learning

### 2.4.1 X-rays

X-rays, a form of high-energy electromagnetic radiation, were discovered in 1895 by Wilhelm Conrad Roentgen (Farmelo, 1995). They have become crucial in medicine and industry for their ability to penetrate matter and generate images revealing internal structures (Farmelo, 1995). X-rays fall within the electromagnetic spectrum and have shorter wavelengths than ultraviolet light but longer than gamma rays. Their high energy penetrates most materials, including mummified tissues and skeletal remains (Conlogue et al., 2020; Tafti & Maani, 2023). An X-ray generator produces two kinds of X-rays: Bremsstrahlung radiation and characteristic X-rays. Bremsstrahlung and characteristic X-rays are generated simultaneously, and the overall X-ray spectrum results from the combined contribution of these two processes (Seibert, 2004).

Bremsstrahlung radiation involves high-energy electrons being deflected by atomic nuclei within a target material, emitting X-ray photons as electrons change directions (Seibert & Boone, 2005; Tafti & Maani, 2023). The energy of these X-rays depends on the incident electron energy and the atomic structure of the target material. Tungsten is often the usual anode target (Seibert, 2004; Tafti & Maani, 2023), although other material targets, such as molybdenum, are also employed. Molybdenum produces soft rays, which have a low penetrability yet create high contrast images, which makes this metal target beneficial in mammogram imaging for clinical breast exams (Su et al., 2020).

Characteristic X-rays are generated when high-energy electrons collide with inner-shell electrons of atoms in a target material, thus ejecting those inner-shell electrons. As outer-shell electrons fill these vacancies, they release energy in the form of X-ray photons specific to the target material's atomic structure (Redler et al., 2018).

X-ray generation typically occurs within specialized devices known as X-ray tubes. Essential components of an X-ray tube include a cathode and an anode positioned a short distance from each other, a vacuum enclosure, and high voltage cables forming the X-ray generator attached to the cathode and anode components (Tafti & Maani, 2023). In X-ray production, a cathode filament in a cathode cup is activated, causing intense heating of

the cathode filament. The heating of the filament causes the release of electrons through a process known as thermionic emission. The released electrons form an electron cloud at the filament surface, and repulsion forces prevent the ejection of electrons from this negatively charged cloud (Seibert, 2004; Tafti & Maani, 2023). When a high voltage is applied by an X-ray generator to both the cathode and the anode, electrons are accelerated towards the electrically positive anode. The filament and the focusing cup direct this path of acceleration. Once the high kinetic energy electrons reach the anode target, X-ray production begins. Some 3D imaging technology utilizes X-ray tubes (Comet Xylon, n.d.), whereas others use non-tube filaments (Nikon, 2021). The method of X-ray generation, whether tube or non-tube filament, does not impact the microfocus resolution; however, the non-tube filament has lower costs associated with maintenance and is therefore preferred in some machines (Nikon, 2021).

#### 2.4.2 Clinical computed tomography

Clinical computed tomography (CT) is a three-dimensional radiographic imaging technique. The image formation process begins with acquiring sequential radiographic projections captured over a range of angular positions through the object of interest (Burghardt et al., 2011; Conlogue et al., 2020). A computer then processes these images to create detailed, three-dimensional representations. The reconstructed image's intensity values represent the local radiographic attenuation, a material property related to the object's electron density (atomic number and mass density) (Conlogue et al., 2020). Attenuation refers to the diminishing intensity of an X-ray beam when it passes through a substance. The quantity of photons detected by the detector mirrors the degree of attenuation the beam undergoes while passing through an object (Conlogue et al., 2020; Friedman et al., 2012). The contrast between soft and mineralized tissue is high due to bone's relative electron-dense inorganic component (Burghardt et al., 2011). However, the contrast within mummified remains is less, owing to the process of tissue desiccation, creating a more relatively electron-dense organic component (Conlogue et al., 2020).

A clinical CT scanner consists of an X-ray source and a detector positioned on opposite sides of the patient/object. The X-ray source emits a fan beam of X-rays directed through the patient's/object's body towards the detector. In setting up a CT (clinical and micro),

we consider and manipulate the following X-ray parameters to create a desirable image. The kilovoltage (kV) of a scan denotes the electrical potential applied to accelerate an electron through the X-ray tube, which affects the ability of the X-ray beam to penetrate the sample (Frey, 2014). Additionally, the quantity of X-rays necessary to capture a satisfactory CT image is quantified in milliamperes (mA). This signifies the electron flow rate through the X-ray tube (Frey, 2014). These parameters are adjusted for each scan as different mediums being scanned require different parameters to allow electrons to penetrate the sample and hit the detector. The detector absorbs and counts the remaining photons that pass through the patient/object (Hermena & Young, 2023). The detector consists of two layers. The scintillator layer converts absorbed X-ray photons into visual light photons, and the photon tide layer converts the visual light photons into electrical signals (Hermena & Young, 2023).

These electrical signals are recorded as 2-dimensional (2D) projection data (Whiting et al., 2006). This 2D data can be reconstructed into a sinogram. A sinogram is the raw projection data organized into a 2-dimensional matrix. A sinogram has two axes, one representing the angles of projection and the other representing the position along the detector array. Each element in a sinogram corresponds to the intensity of the detected radiation at a specific angle and position (Whiting et al., 2006). While sinograms are not 3D reconstructions, they are convenient representations of 2D projection data, which can be used to quickly detect abnormalities or errors in a computed tomography scan, such as dead pixels in the detector, which cannot be easily seen on 3D renderings (Yamanaka et al., 2013). In addition, sinograms provide data about the attenuation of X-rays as they pass through an object from various angles.

To reconstruct a 3D image, all collected projection data are sent to a computer, which, generally, uses a mathematical technique called “filtered backprojection” (Willemink et al., 2014) to convert measured data into a 3D image. The first step in filtered back projection is to apply a filtering operation to the projection data. This filtering aims to enhance the quality of the reconstructed image by reducing certain artifacts and noise. These filters emphasize high-frequency components in the data while attenuating low-frequency components (Willemink & Noël, 2019). The next step involves taking the

filtered projection data and using it to construct an image. Filtered back projection is essentially the reverse of the X-ray projection process. It starts by assigning the attenuated X-ray measurements back to their corresponding location in the image matrix (Willeminck & Noël, 2019). For each angle or view used during the data acquisition, the filtered projection data is back-projected along the path the X-ray took through the object. This process is repeated for each angle, and the results are summed together (Willeminck & Noël, 2019). The result is a reconstructed image after all the back projection steps have been completed for all the angles. The reconstructed image represents two-dimensional slices of the object from each projection angle. When multiple slices are obtained at different positions along the object's axis, they can be stacked to create a three-dimensional volume image (Willeminck & Noël, 2019).

### 2.4.3 Cone-beam computed tomography

Clinical CT technologies primarily employ fan-beam tomography, wherein a fan-shaped array of X-rays is produced by positioning a collimator with an elongated and narrow slot in front of the X-ray source (Smith, 1990). By eliminating the collimator, a cone-shaped beam of X-rays is generated (Figure 2.11), enabling the X-rays to spread out from the X-ray source and form a solid angle resembling a cone (Smith, 1990).

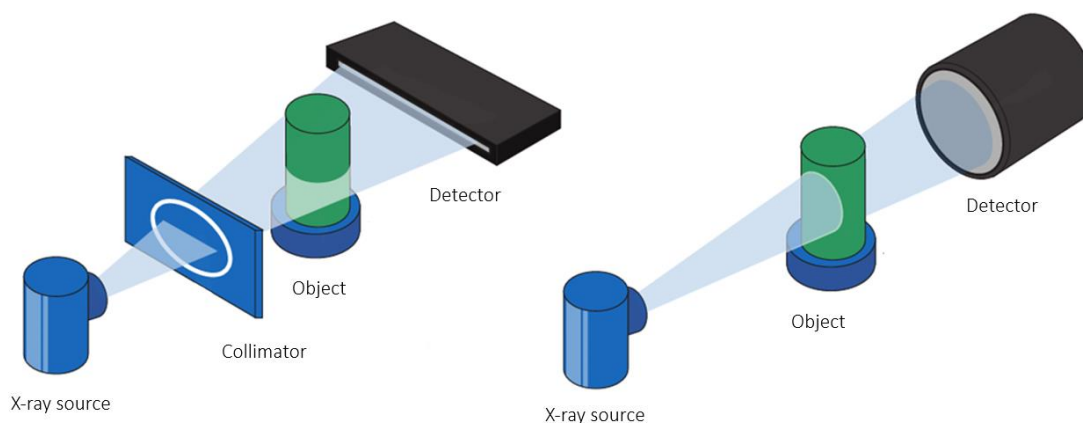


Figure 2.11 Schematic diagram of fan beam X-ray production (left) versus cone beam X-ray production (right). Image adapted from <https://surgeryreference.aofoundation.org/cmj/further-reading/cas-cone-beam-vs-fan-beam-ct>.

Cone-beam computed tomographs (CBCT) tend to have superior spatial resolution compared to clinical CT scans. However, clinical CT scans produce clearer and more

anatomically correct images, with better soft tissue differentiation (CBCTs are optimized for imaging bones and teeth), which is beneficial for the imaging of live patients (Lechuga & Weidlich, 2016; Lorenzoni et al., 2012). CBCT also has limited contrast resolution due to the highly scattered X-ray beam resulting from no collimator (Kiljunen et al., 2015). Cone beam technology was adopted in dental scanners because a cone beam CT creates larger fields of view and more detailed images than traditional radiographs. Additionally, the effective dose of radiation delivered to a patient with CBCT is far less than that of other conventional CT methods (Lorenzoni et al., 2012).

A dental CBCT machine consists of an X-ray source and a detector that rotates synchronously around a patient's head. The voxel size for a dental CBCT varies depending on the specific machine, but typically, they produce 3D images within 400-80  $\mu\text{m}$  (Conlogue et al., 2020; Spin-Neto et al., 2013), thus providing scans at a resolution between clinical and micro-CTs. Dental scanners are far more accessible than micro-CT scanners and require less time to complete a scan. For these reasons, using cone beam dental CT is considered in this thesis regarding identifiable skeletal features at small imaging volumes.

#### 2.4.4 Micro-computed tomography

Micro-computed tomography (micro-CT) is based on the same fundamental principles as conventional CT but is tailored for high-resolution imaging of small samples. Micro-CT begins with an X-ray source, which emits a focused cone beam of X-rays. This beam penetrates the sample, and its intensity decreases as it interacts with the object's internal structures (Conlogue et al., 2020; Kachelrieß, 2004). Unlike a clinical CT, where the X-ray source and detector rotate around the object, the sample in most micro-CT scanners is placed on a rotating stage (Figure 2.12) (Conlogue et al., 2020; Kachelrieß, 2004). The sample is rotated incrementally during the imaging process, typically through 360 degrees, while X-ray projections are acquired at each angular position (du Plessis et al., 2017; Kachelrieß, 2004). Multiple 2D X-ray projections are acquired from various angles around the sample as the sample rotates. The number of projections acquired depends on the desired level of detail and reconstruction quality (Heyndrickx et al., 2020).

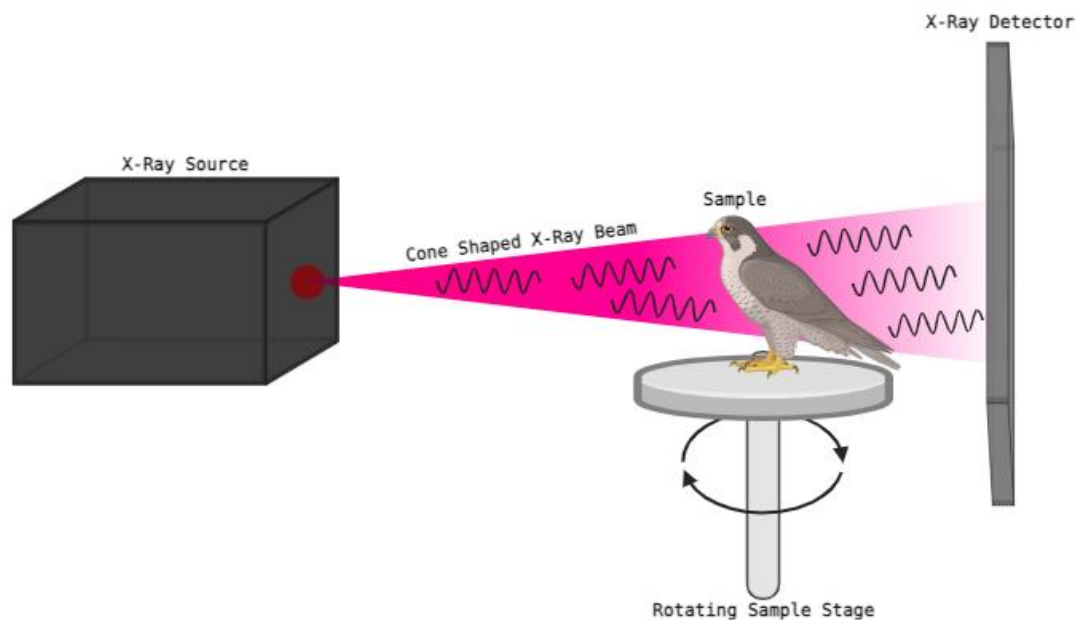


*Figure 2.12 Schematic diagram of a micro-computed tomography scanner. Image created by Maris Schneider in BioRender.*

While micro-CT scans create high-resolution images, one challenge is the object placement on the rotating sample stage. The object's rotation axis should generally be vertical in these scanners to ensure proper X-ray penetration at all angles (Kachelrieß, 2004). Take a bird for example. When placed vertically in a scanner, the bird's body creates a somewhat cylindrical shape, thus allowing for even X-ray penetration as the object rotates. However, if the bird were placed horizontally within the scanner, a much higher voltage (kV) would be required to ensure the X-ray beams penetrate the bird when the body rotates lengthwise (head to feet/tail). In contrast, a lower voltage would be required when the body rotates widthwise than when positioned sideways. Proper sample preparation and mounting are critical to ensuring clear, high-resolution scans.

### 2.4.5 Resolution

Resolution in 3D imaging is a critical concept that determines the level of detail and clarity in the three-dimensional representation of an object or scene. Resolution refers to the ability of an imaging system to distinguish between closely spaced objects or fine details within an image (Lin & Alessio, 2009). In 3D imaging, this concept extends to the ability to capture and represent fine details and structures in three-dimensional space. It is often quantified as the minimum distance or size between two distinct points or objects that can be distinguished in the 3D image (Lin & Alessio, 2009).

Resolution in 3D imaging can be categorized in five ways: spatial, temporal, spectral, contrast, and depth (Kalender, 2006; Lin & Alessio, 2009; Tuschel, 2020). Spatial and contrast resolution are essential to understanding the context of this thesis when discussing questions related to resolution. Spatial resolution defines the smallest distance between two points in a 3D image that can be distinguished as separate entities (Kalender, 2006; Lin & Alessio, 2009). Thus, this refers to the level of detail or clarity in depicting structures within a three-dimensional space (Kalender, 2006). Higher spatial resolution means smaller structures or features can be distinguished and represented more distinctly in the three-dimensional space. Spatial resolution is influenced by various factors, which depend on the imaging technology used, the size of the photoconductors in the detector, the size of the focal spot, and the capabilities of the imaging equipment (Conlogue et al., 2020; Kalender, 2006; Lin & Alessio, 2009).

In 3D imaging, contrast resolution refers to the ability of the imaging system to distinguish between slight differences in contrast or shades of gray between adjacent tissues or structures within an image (Lin & Alessio, 2009). It measures the capacity of the system to display and differentiate subtle variations in contrast, highlighting details and boundaries between different tissues and materials. A higher contrast resolution signifies the system's ability to depict fine density and composition variances. Increased contrast resolution can typically be achieved by increasing the voltage in the X-ray tube. However, radiation is a concern in clinical CTs; therefore, increasing contrast resolution through increased voltage cannot always be achieved (Lin & Alessio, 2009).

## 2.4.6 Image segmentation

Image segmentation in 3D imaging is a crucial step in analyzing three-dimensional data volumes. The process involves partitioning a 3D image into distinct regions or objects of interest based on specific criteria, making extracting meaningful information easier and performing subsequent analyses (Ramesh et al., 2021; Reznikov et al., 2020). With the increasing digitization of anthropological collections, artifacts, and individuals, image segmentation has become a prominent method to isolate and visualize specific structures and regions of interest, such as bones, teeth, or stone tool edges. While there are many methods for performing image segmentation, such as thresholding (e.g., Goh et al., 2018) or watershed transform (e.g., Beucher, 1992), this thesis will use deep learning (e.g., Reznikov et al., 2020) to achieve image segmentation.

### 2.4.6.1 Deep learning

Deep learning is a subset of machine learning, a broader field of artificial intelligence (AI) that has gained significant attention and transformed how AI systems process and understand data (González García et al., 2019). It has led to remarkable advancements in various domains, from image and speech recognition to natural language processing and autonomous driving. Deep learning uses artificial neural networks to model and solve complex problems. Unlike traditional machine learning algorithms that rely explicitly on defined rules and features, deep learning systems learn directly from data (LeCun et al., 2015; Reznikov et al., 2020). These systems are inspired by the structure and function of the human brain, specifically its neural networks.

Artificial neural networks consist of interconnected layers of artificial neurons or nodes (Figure 2.13). Neurons serve as the basic computation units within neural networks, receiving input signals, processing them, and generating an output signal. The connection between neurons, called weights, are adapted during training to enhance the network's effectiveness (Reznikov et al., 2020). A neural network is typically divided into three layers. The first is the input layer, which receives and processes raw data, such as images, text, or sensor data. The input layer has some form of human-led categorization to train the network. The second layer is the hidden layer(s). These intermediate layers perform



complex computation and feature extraction. Deep learning models are characterized by having multiple hidden layers, hence the term “deep” learning. Each layer refines the representation of the data. At these layers, activation functions inject non-linearity into neural networks, enabling them to discern intricate relationships within data (Reznikov et al., 2020). Finally, the output produces the final output or prediction based on the processed information from the hidden layers (Hussain, 2019; Reznikov et al., 2020).

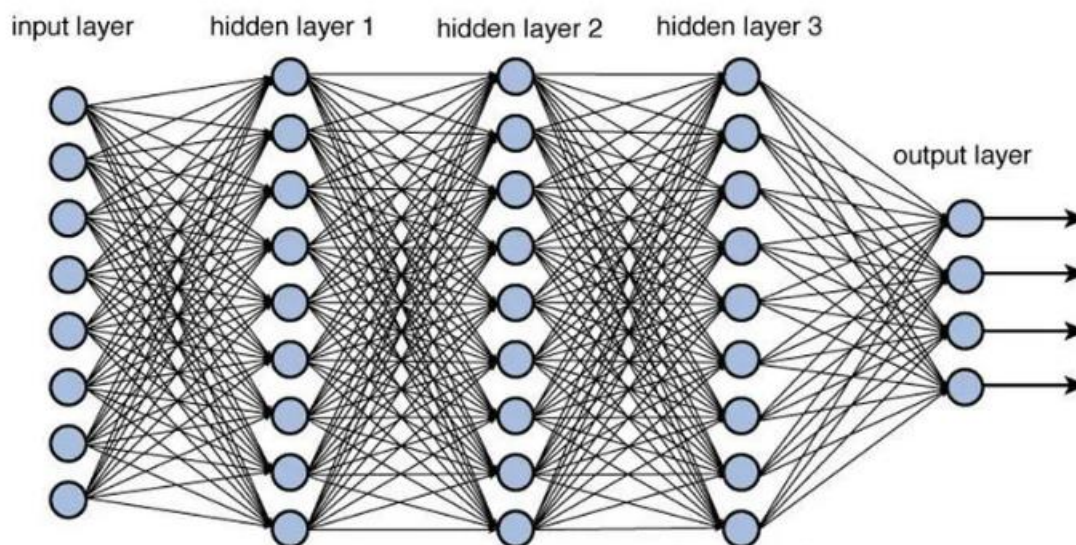


Figure 2.13 Schematic diagram of a deep learning network architecture with multiple layers. Image retrieved from <https://towardsdatascience.com/training-deep-neural-networks-9fdb1964b964>.

Training a deep learning algorithm involves utilizing labelled training data to adjust the model’s weights, minimizing disparities between predictions and actual values using optimization algorithms (Reznikov et al., 2020). A training network also utilizes backpropagation, which computes gradients of the loss function concerning the network’s weights, facilitating weight updates for improved performance (Reznikov et al., 2020).

Essential to understanding deep learning includes a basic understanding of the “black box” principle. The “black box” of deep learning refers to the internal workings of a complex neural network model that are not readily interpretable or explainable by humans (Hussain, 2019). Black box models are created directly from data by an algorithm, meaning that humans, even those who design said algorithms, cannot understand how variables are being combined to make predictions (Rudin & Radin, 2019). This lack of transparency has led to concerns about the trustworthiness and

accountability of AI systems. Deep neural networks can have thousands or even millions of parameters that determine their behaviour (Hussain, 2019). As data flows through the layers of these networks, complex transformation occurs, and the relationship between input and output becomes increasingly abstract and difficult to interpret. In traditional machine learning, feature engineering involves selecting and engineering relevant features from raw data to make models more interpretable (Rudin & Radin, 2019). In deep learning, features are learned automatically, making it challenging to pinpoint precisely which features or patterns the model uses to make predictions (Hussain, 2019; Rudin & Radin, 2019). Deep learning neural networks use activation functions that introduce non-linearity into the model. Non-linear transformations can make it difficult to understand how small changes in input data affect the output (Reznikov et al., 2020). The “black box” nature of deep learning models means that, while they can achieve remarkable accuracy in tasks like image recognition, it is often challenging to explain why they make a specific prediction.

#### 2.4.6.2 Dragonfly

Dragonfly 3D World, owned by the Swiss technology firm The Comet Group, is an image analysis platform specializing in visualizing and analyzing two-, three-, and four-dimension images (Comet Technologies Canada, 2024). This program incorporates artificial-intelligence-guided image segmentation features in its software, aiding image segmentation and visualization (Piche et al., 2017). Dragonfly has adopted deep learning computational models, which are Keras-format Python-encoded convolutional neural networks (CNNs) that can be trained by a user for image segmentation and visualization (Makovetsky et al., 2018). These CNNs connect human-given inputs to desired outputs and can be tuned and retrained for optimal results. Once trained, deep learning models can be applied to large datasets, like CT scans, which are incredibly tedious to segment manually (Makovetsky et al., 2018). Dragonfly also has pre-trained neural networks that can quickly identify regions of contrast (such as bone versus mummified tissue) by recognizing image pixel regions with the help of manual segmentation, undertaken using the paint tool to physically identify the feature to segment (Piche et al., 2017). By creating enhanced contrast, the image features can be segmented. In the case of a three-

dimensional scan, the features will be identified across all slices of the scan, while the supervised identification is carried out on just a few slices (Makovetsky et al., 2018; Piche et al., 2017; Reznikov et al., 2020).

The deep learning tool in Dragonfly will be used in this thesis to help process the CT scans. A few manually segmented slices in a scan will be utilized to train a deep learning algorithm, which will then be refined through more manual segmentation. A trained deep learning algorithm can then be applied to multiple sets of scans, essentially automating or semi-automating the segmentation and visualization process, thus allowing more time to study skeletal elements (see Chapter 3.2.2 for further details on the training process). In summary, this thesis employs 3D imaging techniques and advanced image processing and visualization techniques to study avian mummies from ancient Egypt and answer the questions posed in Chapter One.

## Chapter 3

### 3 Materials and Methods

This chapter will provide an overview of the animal mummies studied, a comprehensive overview of the scans collected on said mummies and the scans acquired from the Internet Mummy Picture and Archiving and Communication Technology (IMPACT) database (Wade & Nelson, 2015). In this, I will summarize the steps taken in completing the micro-CT scans, the use of image analysis software Dragonfly to stitch micro-CT scans together, and the training and use of a deep learning algorithm to perform semi-automatic segmentation in Dragonfly. Finally, the chapter will conclude by outlining features and methods used to identify the bird species based on the digitally segmented skeletons.

#### 3.1 Materials

This thesis examined one mummified bird from the Chatham-Kent Museum (Chatham-Kent, ON), four mummified birds from the Redpath Museum (Montreal, QC), and three scans of mummified birds obtained from the IMPACT database (Wade & Nelson, 2015). The physical mummies and their “provenance” from Chatham-Kent and Montreal are documented here. Table 3.1 presents physical measurements of all mummies from the Chatham-Kent Museum and the Redpath Museum; Table 3.1 also includes digital measurements of the external sarcophagus of a mummified falcon from the Canadian Museum of History (CMH). In addition to the physical descriptions of the mummies presented here, a collection of photo documentation can be found in Appendix A.

##### 3.1.1 Chatham Falcon

One mummified falcon was loaned to Dr. Nelson for scanning by the Chatham-Kent Museum.

##### *Chatham Falcon physical description*

The Chatham mummy (Figure 3.1) presents as a mummified raptor, wrapped symmetrically and in fair condition. Of all the raptor mummies studied in this thesis, the

Chatham mummy has the most external damage to the wrappings, exposing internal contents. This damage has led to the exposure of the tomial tooth, a segment of the sternum, the right foot and talons, and fractured tailed feathers. Despite the damage, the mummy remains tightly wrapped. The entirety of the mummy is a dark brown colour, excluding the exposed foot and feathers, which are lighter in colour.

#### *Chatham Falcon provenance*

In the early 1900s, George William Sulman travelled to Egypt and purchased a mummified hand, mummified fetal crocodiles, a mummified falcon, and a complete, mummified individual from the Cairo Museum (Chatham-Kent Museum, 2024; Gardner et al., 2004). In 1943, his son, C.D. Sulman, donated the collection of artifacts to the Chatham-Kent Museum, where they have remained since (Chatham-Kent Museum, 2024). The artifacts, including the mummified falcon, were showcased in the “Wonders of the World” exhibition until 1997, and the falcon now remains in the museum's exhibition galleries (Chatham-Kent Museum, 2024).

The falcon was purchased from the Cairo Museum in the early twentieth century, meaning there is no record of where it was found or the context in which it was found. Tuna-el-Gebel (Middle Egypt) and Saqqara (Memphis) are the most prolific of the raptor mass burial sites in Egypt; however, other sites, such as Giza, Sais, Arab el-Tawila, and Akhmim (to name a few) contain raptor mass burials (Ikram, 2005a; 2012). Therefore, narrowing down a possible falcon necropolis of origin is not possible. Additionally, there has been no carbon dating of the Chatham falcon. Thus, we have no context of the Dynasty or Period in which the falcon was manufactured, although it likely originates from the Ptolemaic or Roman Period, as judged by other votive mummies (Ikram, 2005a; 2015b).



*Figure 3.1 Anterior view of the mummified falcon from the Chatham-Kent Museum. Photo taken by Maris Schneider.*

### 3.1.2 Redpath Museum mummies

Two mummified falcons and two mummified ibises were loaned to Dr. Reznikov for scanning from the Redpath Museum.

#### 3.1.2.1 Mummified falcons

##### *Falcon<sup>1</sup> 2726.02 physical description*

Falcon 2726.02 (Figure 3.2) presents as a mummified raptor, displaying asymmetry in its bundling. Notably, the head and neck of the specimen are positioned over the left shoulder (leaving the right shoulder protruding), potentially indicating the cause of death is neck wringing. The majority of the wrappings along the body are a light brown colour, with exceptions including the head, the underside of the feet, and a section of the midsection, which appear blackened (Redpath Museum, 2023). The bandages used in the mummification process appear coarse in texture and tightly wound without observable damage. However, the bird's beak is exposed at the head end of the bundle and is damaged. No other internal elements are externally visible.



*Figure 3.2 Anterior view of the mummified falcons from the Redpath Museum. Falcon 2726.02 (left) and Falcon 5731 (right). Photos taken by Maris Schneider.*

---

<sup>1</sup> Note, the Redpath falcon bundles are spelled with the French spelling *falcon*, as this is how the artifact is categorized in the Redpath World Culture's archives (provided by Annie Lussier, Curator of Ethnology Redpath Museum).

### *Faucon 2726.02 provenance*

Faucon 2726.02 was donated to the Redpath Museum by the Natural History Society of Montreal (Redpath Museum, 2023). James Ferrier *likely* acquired this bird with other mummies during his 1859 visit to Egypt (Lawson, 2016). However, this is not confirmed. James Ferrier was a governor of McGill University and travelled throughout Europe and the Middle East, bringing many antiquities back to Canada. He donated these antiquities to the Natural History Society of Montreal (NHSM). In 1881, the move of the Geological Survey of Canada to Ottawa fragmented the NHSM, and in 1906, the society packed up all its artifacts to construct a more suitable facility (Lawson, 2016). Ultimately, the lack of funds for storage, the lack of a new facility, and the outbreak of war led the NHSM to close in 1925 (Lawson, 2016; MacLeod, 2012). The artifacts were dispersed to many museums and galleries, with James Ferrier's collection going to the Redpath Museum (MacLeod, 2012). The bird was first catalogued into the Redpath's collection in 1928 and is not currently on display. Again, there is no documentation on where or when this mummy was acquired in Egypt or when or how it made its way to Canada (Redpath Museum, 2023).

During the retrieval of Faucon 2726.02 from storage, a small piece of textile was damaged and fell off the mummified bundle. With permission from the Curator of Ethnology, Annie Lussier, at the Redpath Museum, this small piece of textile was sent to the Laboratoire de Radiochronologie in Laval, QC, for radiocarbon dating. The dates provided by the laboratory were calibrated by Dr. Nelson using the Calib 8.2 program using the INTCAL20 calibration curve (Reimer et al., 2020). Calibrated results date Faucon 2726.02 to 15BC cal (2 sigma range = 52BC-24AD). This date range places the origin of Faucon 2726.02 at the beginning of the Roman Period (or the end of the Ptolemaic Period). No other information regarding the mummy's provenience in Egypt or how it got to Canada is known.

### *Faucon 5731 physical description*

Faucon 5731 (Figure 3.2) is a mummified raptor wrapped tightly in a symmetrical bundle. While the overall condition of the textiles is fair, there are discernible areas

where the bandages have begun to loosen, particularly around the right shoulder region. Additionally, minor damage is observed at the foot end of the bundle, and superficial damage is evident on the top layer of wrappings near the head. Notably, the tomial tooth of the raptor is exposed. The missing bandages around the tomial tooth could have resulted from taphonomic factors during burial, improper handling before being in museum care, or both. The bundle is dark brown, with darker patches throughout the torso.

### *Falcon 5731 provenance*

Falcon 5731 is currently displayed at the Redpath Museum in Montreal, QC. As part of the collaborative project with the Redpath Museum, I was provided archival data from the World Cultures collection regarding the acquisition of mummified animals. Unfortunately, there is very little data regarding Falcon 5731, simply stating the mummified bird was acquired from the Redpath Library and was first catalogued in 1947 or 1949 (although it was likely acquired much earlier) (Redpath Museum, 2023). There is no description of who initially obtained the bird from Egypt or where it was sourced, and no carbon dating was approved for Falcon 5731.

### 3.1.2.2 Mummified ibises

#### *Ibis 2727.01 physical description*

Ibis 2727.01 (Figure 3.3), identified as an ibis mummy, as documented in previous clinical CT scans by Wade et al. (2012). The mummy bundle remains in good condition and exhibited small perforations in the outermost layer of linen wrappings. Additionally, there is localized damage near the upper left corner of the bundle. The



Figure 3.3 Anterior view of mummified ibises from the Redpath Museum. Ibis 2727.01 (right) and Ibis 2727.02 (left). Photos taken by Maris Schneider.



mummy is predominantly light brown, with isolated areas displaying a black residue, likely remnants of bitumen or resin from the mummification process. Notably, this bundle has a cartonnage plaque adorning the head end of the wrappings, featuring an illustration of an ibis. The ibis illustration is painted in white and black, portraying the bird wading in water, depicted with blue paint.

#### *Ibis 2727.02 physical description*

Ibis 2727.02 (Figure 3.3) is a suspected mummified ibis based on its conical shape. This mummy bundle is in poor condition, evident by the missing linens along the right-hand side of the bundle. A chunk of linen was damaged and detached from the head area of the bundle. It was noted that this detaching chunk would move while the bundling was being transported (this includes transportation from the museum to the scanner and in and out of the scanner). Therefore, Annie Lussier wrapped the mummified ibis in plastic to mitigate further damage during scanning and transportation. This plastic wrapping did not affect CT scanning. Furthermore, besides the damage at the head end, there is considerable damage at the foot end and numerous small perforations throughout the bundle's body.

#### *Ibis 2727.02 and Ibis 2727.02 provenance*

The Redpath Museum acquired both ibis bundles through the large dissemination of artifacts following the end of the N.H.S.M. The ibises are confirmed to have been purchased by James Ferrier in Thebes (Redpath Museum, 2023). It is important to note that while the ibis bundles were purchased in Thebes, it is possible that they are not originally from there. Although Thebes was a major falcon and ibis necropolis, the mummified ibises have also been found in mass burials at many sites, including Hermopolis, Abydos, Saqqara, Tuna el-Gebel and Kom Ombo (Ikram, 2012), to name a few. The mummified ibises could have come from the Thebes necropolis, or they could have been brought to Thebes from various locales with the intent of selling the artifacts. Based on the available archives, there is no way to confirm, with certainty, where the ibises were initially entombed. Like the falcon, the ibises were first catalogued by the

Redpath Museum in 1928 (Redpath Museum, 2023). Ibis 2727.02 is not currently on display in the museum due to poor preservation, and Ibis 2727.01 is presently on display.

Ibis 2727.02 was similarly damaged during handling at the museum, and a small piece of broken textile was sent to Laval for radiocarbon dating. Dr. Nelson again calibrated the laboratory's results with the Calib 8.2 program using the INTCAL20 calibration curve (Reimer et al., 2020). The calibrated results indicate Ibis 2727.02 dates to 278BC cal (2 sigma range = 295BC – 208BC), placing its origin in the Ptolemaic period. There was no dating for Ibis 2727.01.

*Table 3.1 External measurements of the mummified bird bundles used for micro-CT scanning.*

|                   | Total length (cm) | Width at head (cm) | Width at the broadest part of thorax (cm) | Width at feet (cm) |
|-------------------|-------------------|--------------------|---|--------------------|
| CMH Falcon 1*     | 38.9              | 6.9                | 9.9                                       | 3.9                |
| Chatham falcon    | 22.9              | 3.33               | 5.6                                       | 2.45               |
|                   |                   |                    |   |                    |
| RP Faucon 2726.02 | 30.8              | 3.5                | 6.5                                       | 4.0                |
| RP Faucon 5731    | 26.5              | 4.0                | 5.5                                       | 3.0                |
|                   |                   |                    |   |                    |
| RP Ibis 2727.01   | 26.0              | 9.7                | 8.7                                       | 4.0                |
| RP Ibis 2727.02   | 28.0              | 10.0               | 7.8                                       | 3.0                |

\*External measurements were acquired digitally, examining the clinical CT scan using the same technique as the long bone measurements (Appendix F).

### 3.1.3 IMPACT

The IMPACT database is a collaborative research initiative. Its primary focus is digitally preserving and scientifically investigating mummified remains alongside the mummification practices that shaped them. Leveraging non-invasive medical imaging technologies, IMPACT facilitates the study of mummified humans and animals (Nelson & Wade, 2015).

Clinical CT scans of mummified Egyptian birds, stored in various collections worldwide, were selected from IMPACT (Wade & Nelson, 2015) to compare resolution and

visualization. Fortunately, previous clinical CT scans have been acquired on Faucon 2726.02 and Faucon 5731 and are accessible through IMPACT (Wade & Nelson, 2015). Therefore, those scans will be compared to the micro-CT scans acquired of the same birds. An additional clinical CT scan of a mummified falcon housed at the CMH (Gatineau, QC) was examined for this thesis.

## 3.2 Methods

For each mummy studied in this thesis, the procedure was similar – (1) scanning, (2) image processing, and (3) osteological analysis. Here, I outline scanning procedures, followed by the image processing undertaken in Dragonfly, finishing with a discussion of the osteological investigation of the 3D-rendered bird skeletons.

### 3.2.1 Clinical CT

The mummified Redpath falcons and the mummified falcon from the CMH had accessible clinical CT scans through the IMPACT (Wade & Nelson, 2015) database. These scans were acquired by previous researchers and made available for academic use via the contributor's licence agreement between the Redpath Museum and Western University. The details of each scan are summarized in Table 3.2.

A Clinical CT of the Chatham Falcon was acquired at the Robarts Research Institute at Western University on March 13, 2023. A scan capturing the entire raptor body and head was acquired at 80kV, 400mA, using an Aquilion ONE/Prism edition by Canon Medical Systems helical scanner. The bird was placed on its dorsal side on a foam pad to lift it off the scanner bed. It was positioned at 90° to the scanner bed to allow for volumetric capture in a single rotation of the source and detector; no additional supports were needed. These parameters can also be found in Table 3.2.

#### *A note about computed tomography*

A 3D reconstruction is a volume that is made up of individual elements referred to as voxels (3D volumetric pixels). Large voxels yield lower resolution images, while smaller voxels yield higher resolution images. In clinical imaging, it is typically (although not

always) preferred to reconstruct isotropic voxels, which have uniform dimensions along all axes (Conlogue et al., 2020). Since the dimensions are all equal, the spatial resolution is uniform in all directions, which is advantageous for measuring distances and volumes accurately and for overall image analysis and interpretation (Conlogue et al., 2020). The scan of the Chatham Falcon, taken in 2023 at Western University, and all micro-CT scans have isotropic voxel sizes. However, the other clinical scans (e.g., clinical CT scans of the CMH Falcon 1) acquired from the IMPACT (Wade & Nelson, 2015) database have anisotropic voxels, as the X and Y dimensions of the pixels of the detector are different from the Z dimension of the voxels, which is determined by slice thickness. This creates a prismatic, anisotropic voxel (Conlogue et al., 2020; Wade et al., 2010). Anisotropic voxels can dramatically impact 3D reconstructions, possibly distorting the image along some axes, and, thus, have the potential to impact future image analyses (Conlogue et al., 2020; Wade et al., 2010).

*Table 3.2 CT scan specifications from IMPACT (Wade & Nelson, 2015) and the Robarts facility (including date, location, scanner, kV, mA, pixel spacing, slice thickness, and conduction kernel) of the mummified birds studied in this thesis.*

|                      | Faucon 2726.02                         | Faucon 5731                            | CMH Falcon 1                                     | Chatham Falcon                          |
|----------------------|--|--|--|---|
| Scan date            | 2011-04-30                             | 2011-04-30                             | 2009-08-31                                       | 2023-03-12                              |
| Scan location        | Montreal Neuro Hospital (Montreal, QC) | Montreal Neuro Hospital (Montreal, QC) | Ottawa Hospital Civic Emergency VCT (Ottawa, ON) | Robarts Research Institute (London, ON) |
| Scanner              | Aquilion ONE                           | Aquilion ONE                           | LightSpeed VCT                                   | Aquilion ONE/Prism                      |
| kV                   | 80                                     | 80                                     | 140  | 100                                     |
| mA                   | 400                                    | 400                                    | 460  | 400                                     |
| Pixel spacing (mm)   | 0.267/0.267                            | 0.238/0.238                            | 0.273/0.273                                      | 0.496/0.496                             |
| Slice thickness (mm) | 0.5                                    | 0.5                                    | 0.624  | 0.5                                     |

|                                  |                       |                       |                       |  |                           |
|----------------------------------|-----------------------|-----------------------|-----------------------|--|---------------------------|
| Voxel size<br>(mm <sup>3</sup> ) | 0.267x0.267x<br>0.300 | 0.238x0.238x<br>0.300 | 0.273x0.237x<br>0.363 |  | 0.496x0.496<br>x<br>0.500 |
| Convolution<br>kernel            | FC02                  | FC02                  | STANDARD              |  | FC30                      |

### 3.2.2 Micro-CT

The Chatham Falcon was scanned at the Museum of Ontario Archaeology (London, ON) using the Nikon Metris XT H 225 ST cabinet scanner. The bird was mounted vertically in a cardboard tube container and stabilized with floral foam. The mummy was scanned at various resolutions using a tungsten target, and one scan was taken using a molybdenum target. Details of the scans acquired, the anatomical location of scans, and scanning parameters are listed in Table 3.3.

The mummified bundles from the Redpath Museum were scanned at École de technologie supérieure (Montreal, QC), using the Yxlon FF35 CT scanner<sup>2</sup>. Following the loan agreement with the Redpath Museum, the mummies were not to be scanned vertically (to prevent the internal structures from disarticulating or moving). Therefore, the Redpath mummies were scanned at a 30° angle (see mounting images in Appendix A; Figures A.1, A.7, A.12, A.17). Since the mummies could not be mounted vertically, a custom-made stage was created by Shumeng Jia (Ph.D. student at McGill), which kept the mummies angled but also slid into the scanner apparatus to ensure that the internal contents of the bundle would remain in the center of rotation. Details of the scanning parameters for the Redpath mummies are also listed in Table 3.3. A mid-resolution and high-resolution scan of Ibis 2727.01 and a mid-resolution scan of Ibis 2726.02 were not

---

<sup>2</sup> The scans of the Redpath Museum birds were collected by a team of researchers in Montreal – Myself, Shumeng Jia (McGill University), Dr. Natalie Reznikov (McGill University), and Dr. Salah Brika (École de technologie supérieure).

acquired, as the initial X-ray projections did not indicate these scans were needed (Chapter 4 will explain why).

### 3.2.3 Dental CBCT

In addition to the micro-CT scans of the Chatham falcon, the mummified bird was brought to the Schulich School of Medicine and Dentistry at Western University on March 14, 2023, to acquire a scan on a dental scanner. A dental CBCT scan of the Chatham falcon's head was captured on a Sirona Orthophos XG 3D scanner. The scan was acquired at 85 kVp, 4mA, 14.4-second exposure, with 160  $\mu\text{m}$  slice thickness.

Table 3.3 The synthesized micro-CT parameters for the Chatham Falcon and the four mummified birds from the Redpath. Details include scanning resolution, anatomical position of the scan, scanning parameters, micro-CT scanners, and reconstruction software.

|                | Scan Date  | Body Part | Lowest Resolution ( $\mu\text{m}$ ) | Body Part             | Mid Resolution ( $\mu\text{m}$ ) | Body Part | Highest Resolution ( $\mu\text{m}$ ) | Scan Parameters     | Scanner                           | Reconstruction Software                          |
|----------------|------------|-----------|-------------------------------------|-----------------------|----------------------------------|-----------|--------------------------------------|---------------------|-----------------------------------|--|
| Chatham Falcon | 2024/02/24 | Full body | 110                                 | Head and upper torso* | 50*                              | Head      | 25                                   | 115kV<br>90uA       | Nikon<br>Metris<br>XT H<br>225 ST | X-Tec CT<br>Pro/CT Agent<br>3D Version 4.4       |
|                |            |           |                                     | Lower torso and leg*  |                                  |           |                                      |                     |                                   |  |
| Chatham Falcon | 2024/02/24 |           |                                     |                       |                                  | Head      | 25                                   | 115kV<br>90uA<br>** | Nikon<br>Metris<br>XT H<br>225 ST | X-Tec CT<br>Pro/CT Agent<br>3D Version 4.4       |
| Faucon 5731    | 2023/05/25 | Full body | 88                                  | Head and upper torso* | 44*                              | Head      | 22                                   | 80kV<br>380uA       | Yxlon<br>FF35<br>CT               | Yxlon<br>Reconstruction<br>Workspace<br>2206.4.0 |
|                |            |           |                                     | Lower torso and legs* |                                  |           |                                      |                     |                                   |  |
| Faucon 2726.02 | 2023/06/09 | Full body | 100                                 | Head and torso*       | 50*                              | Head      | 25                                   | 75kV<br>300uA       | Yxlon<br>FF35<br>CT               | Yxlon<br>Reconstruction                          |

|                 |            |              |    |       |  |      |    |               |                     |  |
|-----------------|------------|--------------|----|-------|--|------|----|---------------|---------------------|--|
|                 |            |              |    | Legs* |  |      |    |               |                     | Workspace<br>2206.4.0                            |
|                 |            |              |    |       |  |      |    |               |                     |  |
| Ibis<br>2727.01 | 2023/06/01 | Full<br>body | 90 |       |  | Head | 27 | 70kV<br>200uA | Yxlon<br>FF35<br>CT | Yxlon<br>Reconstruction<br>Workspace<br>2206.4.0 |
| Ibis<br>2727.02 | 2023/06/02 | Full<br>body | 94 |       |  |      |    | 80kV<br>380uA | Yxlon<br>FF35<br>CT | Yxlon<br>Reconstruction<br>Workspace<br>2206.4.0 |

\* Scans to be stitched together in Dragonfly

\*\* Scan taken with a molybdenum target. All other scans were taken on a tungsten target.



### 3.2.4 Image processing and Dragonfly

All micro-CT, CBCT, and clinical CT scans were uploaded and processed in Dragonfly 3D World (v2024.1-1579, Comet Technologies Canada Inc). First, some micro-CT scans were stitched together (Appendix B) (as identified in Table 3.3). Following the stitching, a deep learning algorithm (Appendix C) was trained for image segmentation. The final segmented images were then used to visualize the skeletal features for species identification.

The stitching method using Dragonfly was taught to me by Dr. Daniel Buss in Dr. Natalie Reznikov's BIEN 535 tutorial at McGill University. The deep learning protocols were also partially taught in this tutorial and further improved upon during my research period in Montreal (May 2023-July 2023) by Dr. Reznikov and Shumeng Jia. I also attribute a significant portion of the finalized methodological procedures to my own trial and error throughout this research.

#### 3.2.4.1 Stitching

One of the inherent challenges encountered when acquiring high-resolution micro-CT scans lies in the delicate balance between resolution and field of view. Opting for higher resolution inevitably sacrifices the breadth of the field of view, as attention is directed toward capturing finer details rather than visualizing the larger volume. To overcome this problem, multiple micro-CT scans of a singular object, referred to as subvolumes, were acquired at different locations on the object to address this limitation (Ji, 2010). These scans are then digitally aligned and stitched together to create one cohesive scan. The critical aspect of successfully stitching micro-CT scans together involves ensuring each scan has an overlapping area. The overlapping subvolumes are co-registered using image registration algorithms in Dragonfly (Dragonfly, 2020c).

Stitching micro-CT scans together entails manually aligning overlapping features by matching corresponding elements in adjacent scans to ensure a seamless transition. Subsequently, an image recognition algorithm is employed to automatically align the scans based on recognized features. Avian skeletal features and visible mummification

materials, such as bandages, served as features for manual alignment and were recognized by the algorithm within Dragonfly (Dragonfly, 2020c).

Creating a stitched 3D rendering involves uploading multiple scans of the same object into Dragonfly. For ease of processing, only two scans are manipulated simultaneously. Matching features are identified manually in both scans and once the scan is adjusted to overlap the other, the additional scans are then incorporated into the stitching dataset. While any number of scans can be stitched together, it is essential to note that a higher quantity necessitates increased processing power and time. A notable challenge with 3D stitching is that the matched alignment is performed manually on 2D slices, even though these slices collectively represent a 3D volume. When stitching scans together, it is essential to ensure proper alignment across all 2D planes (i.e., XY, XZ, ZY) for the image recognition software to identify superimposed features accurately (Dragonfly, 2020c). A comprehensive procedural guide to 3D imaging stitching in Dragonfly can be found in Appendix B.

#### 3.2.4.2 Deep learning and image segmentation

Typically, image segmentation of CT scans is a time-consuming process due to its reliance on manual segmentation. The time is extended further when considering the small features that need to be segmented within a bird mummy bundle. To expedite the process, a deep learning algorithm was trained. This algorithm can now automatically or semi-automatically segment images in new scans. The deep learning feature within Dragonfly is an artificial intelligence-guided image segmentation algorithm, processing classifiers within images to distinguish between various materials in a scan (Piche et al., 2017).

For this thesis, all scans were classified into three datasets: skeleton, mummified tissue/wrappings, and background. The first step of the process is to import the image volume into Dragonfly. The *Segmentation Wizard* was used for manual segmentations. Here, training frames are created, which are the manually segmented data provided to the algorithm for training (Dragonfly, 2020b). These serve as the ground truth for the training. “Ground truth” refers to the real data used to train machine learning output

models. It is the target used for training and validation of the model during the training process (Choy et al., 2018). Training frames were segmented into the three data classes, starting with mummified tissues/wrapping, then bones, and finally, all background pixels not assigned to a class were included in the background class. The process is repeated on multiple frames until approximately 1-2% of the data is manually segmented (e.g., a 3000-slice stack requires 30-60 slices to be manually segmented for optimal training). The stack of trained frames is then exported from the *Segmentation Wizard* back into Dragonfly as a Multi-ROI (i.e., multiple regions of interest).

The next step involves creating a *mask* ROI. During training, the mask ROI tells the algorithm which slices will be used for the training iterations. This is accomplished by creating a new ROI in Dragonfly and highlighting each slice that has been manually segmented. In this thesis, visual feedback was also utilized. It is not necessary for the training process; however, it provides real-time updates on how the algorithm segments data during the training process. The raw dataset, the Multi-ROI, the mask ROI, and the visual feedback were all imported into the *Deep Learning* plugin, and the algorithm was trained. A detailed procedural guide for deep learning training and application can be found in Appendix C.

There is a multitude of deep learning networks that can be trained in Dragonfly (Dragonfly, 2024); this thesis used a U-Net architecture. This network can process large datasets and apply the learned segmentation to the remaining 2900+ slices, which were not manually segmented. The U-Net architecture was first introduced by Ronneberger et al., and the architecture consists of an encoder path, a typical convolutional neural network used for segmentation (Ronneberger et al., 2015). The encoder path applies a series of convolutional and pooling layers to downsample the input image. Then, a decoder path uses a series of up-convolutional and concatenation layers to produce the segmented output (Ronneberger et al., 2015).

The training iterations can begin once the Multi-ROI and mask ROI have been input into the loaded U-Net architecture. The training data is split into patches, which are then randomly assigned as batches. The batch size parameters determine the quantity of

patches processed in a single batch. An epoch is completed when the training model passes over all data patches (Dragonfly, 2020b). As a model is being trained in Dragonfly, the user can watch in real-time as epochs of training are completed. In this instance, having the visual feedback visible is helpful, as you can watch how the training algorithm is learning and adjusting the borders of each data class after it passes through each epoch. The loss function captures the difference between the actual (manually trained) and predicted (algorithm output) values (Beason, 2021; Reznikov et al., 2020; Dragonfly, 2024). Training a deep learning architecture automatically stops when the value of the loss function fails to decrease for ten consecutive epochs (Dragonfly, 2020b). An in-depth discussion on deep learning parameters and how to adjust them in Dragonfly can be found in Appendix D.

Every machine learning algorithm, deep or not, is susceptible to overfitting, which occurs when the algorithm memorizes the training data but struggles to provide good results on new, previously unseen data (Dragonfly, 2024). To avoid this scenario, we employ validation data during the training process, which is distinct from the training data. In Dragonfly, the data provided to the algorithm is split into training and validation, specifying a percentage of data to be used for validation (20%), which is then used to monitor the model's progress as it passes through each epoch. It will stop the training if there is a validation error (a point when the validation error starts increasing) to prevent the algorithm from overfitting (Dragonfly, 2024).

Once the deep learning algorithm was successfully trained, it was applied to new datasets. It is important to note that while deep learning is incredibly efficient, it relies heavily on the quality of data it is fed. Meaning, good manual segmentation results in good output segmentation. Good data in, good data out!

### 3.2.4.3 Deep learning is not perfect! A quick fix for better visualization

In some instances, a deep learning algorithm will misidentify or mis-classify input data, regardless of the quality of training data. For example, there is a tendency for this trained deep learning algorithm to misidentify remnants of natron (or clay?) as skeletal elements. This results in many small spec-like artifacts which impact the visualization of the 3D

skeleton. The *Connected Components* feature can remove these small specs in Dragonfly. What results from a deep learning image segmentation is a dataset that has been separated into a pre-identified Multi-ROI. In Dragonfly, a Multi-ROI automatically groups labelled voxels into components based on their connectivity. Then, properties such as volume, surface area, aspect ratios, and centres of mass for each connected component can be calculated (Dragonfly, 2020a). The connected components can be sorted based on these specific characteristics, and certain elements, such as isolated voxels, can be removed at the user's request.

Following the image segmentations with the deep learning algorithm, the skeletal class was extracted from the resulting MultiROI. The connected components of this class were then mapped and sorted by voxel volume. Because natron artifacts were so small, the smallest volumes were removed, leaving the largest connected components, the connected voxels making up the bones; a detailed guide of the connected components feature can be found in Appendix E.

### 3.2.5 Avian identification

The identification of birds in this thesis is centred on identifying birds of prey within the studied bundles (Figure 3.4). The results presented in Chapter 4 indicate that one ibis contained no skeletal elements for analysis, and the other bundle contained a small chick; therefore, the ibises were not considered a central focus for species identification but used to demonstrate the application of studying animal mummies under an anthropological framework.

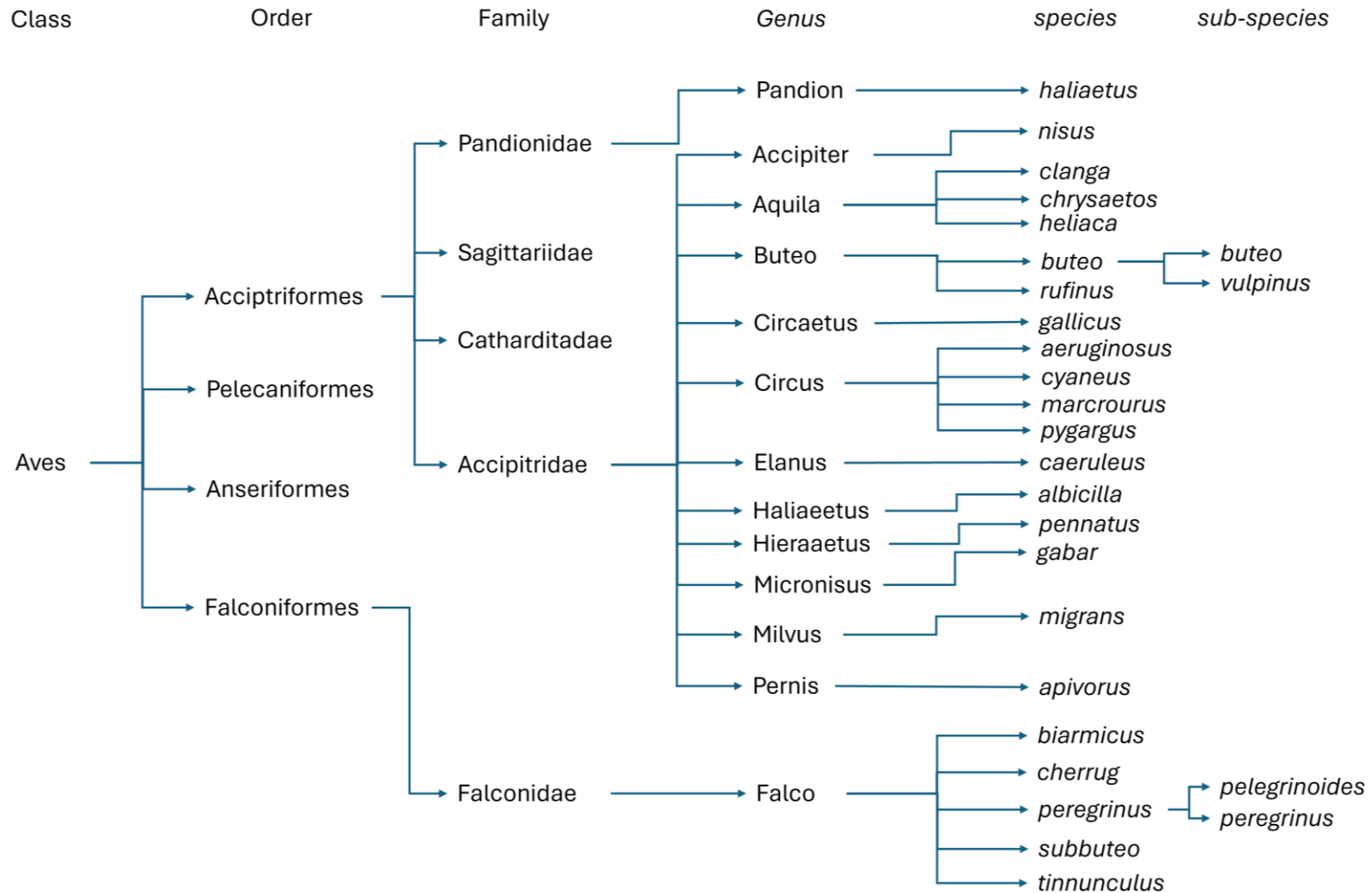


Figure 3.4 Taxonomic system for each mummified bird represented in Lortet and Gaillard (1905). Note, the names are listed as their current, valid taxonomic identification. The original names written by Lortet and Gaillard can be found in Appendix G. Image created by Maris Schneider.

### *Raptor anatomy: Accipitridae versus Falconidae*

Birds belonging to the Family Accipitridae and Falconidae are the most commonly mummified birds in ancient Egyptian bundles (Bailleul-LeSuer, 2019; von den Driesch et al., 2005). Accipitridae is a taxonomic Family that includes birds of prey with broad, rounded wings and relatively short tails, such as hawks, eagles, vultures, and buzzards. These birds are known for their powerful, soaring flight and sharp talons, which they use to catch and kill their prey. They are generally larger and more powerful than birds in the Falconidae Family (Sustaita, 2008). Conversely, Falconidae is a taxonomic Family that includes birds of prey with long, pointed wings and long tails, such as falcons, kestrels, and caracaras. These birds are known for their speed, agility, and ability to perform high-speed aerial maneuvers. They are generally smaller and more agile than the Accipitridae species (Sustaita, 2008). Both Families have distinguishable skeletal features that can aid species identification with non-destructive imaging techniques. This thesis uses the following osteological traits to examine Accipitridae versus Falconidae.

#### *The tomial tooth*

The tomial tooth is a specialized beak found in some birds of prey, which plays a critical role in their hunting and feeding behaviour. It is a small, pointed projection curved towards the inside of the beak, made of a keratinized epidermis (Bellairs & Jenkins, 1960) and serves as a sharp cutting surface that allows the bird to efficiently tear and slice through the flesh of its prey (Csermely & Rossi, 2006). It is a result of natural selection, wherein a specialized structure evolved to fit the specialized feeding habits of birds of prey (Csermely & Rossi, 2006). While the presence of the tomial tooth is not apomorphic for the Family Accipitridae or Falconidae, it is a critical feature in differentiating birds of prey from other commonly mummified birds in ancient Egypt, like the Sacred Ibis. Ibises have a straighter, crescent-shaped beak that is more versatile for searching through mud and weeds for prey (Ross, 2004).

### *Accessory pygostyle bones*

The accessory pygostyle bones are a unique anatomical feature found in the Genera *Falco* but are absent in *Buteo* and *Accipiter*. This bilateral pair of small bones is located in the tail of a bird, attached to the ventral surface and lateral edges of the pygostyle bone (Smith & Smith, 1990; 1992). Evidence suggests that sections of these accessory bones are responsible for strong muscle attachments, likely functioning to transmit the force of several major tail depressor and abductor muscles to the pygostyle (Richardson, 1972). The adaptive significance of these bones would be to afford a greater area for the tail depressor muscle attachments. The occurrence of accessory pygostyle bones in the tail in falcons allows for greater stress to act on the tail, notably for rapid maneuvering and forcing braking in flight, which these birds are known for (Richardson, 1972).

### *Strong species identifiers*

There are particular bones (or absence thereof) that can aid in narrowing down which Genus a bird belongs to. In this thesis, I looked for the following features.

In the wings of the Genus *Buteo* and *Accipiter* there is a unique bone which is absent in most other species of birds. *Buteos* and *Accipiters* have an additional bone at the cranial margin of the carpus, articulating with the distal radius and the carpometacarpus (Smith & Smith, 1992). This *os prominens* is interposed in the tensor propatagialis muscle tendon and presumably affects the action of the muscle as it passes over the carpal joint to the insertion of the distal radius (Smith & Smith, 1992). Smith and Smith (1992) report that the Genus *Falco* does not possess this additional bone, which is corroborated by Zucca and Cooper (2000).

The second identifying bone is the humeroscapular bone. This is a small bone dorsal to the shoulder joint on the deep surface of the major deltoid muscle (Smith & Smith, 1992a). This bone is commonly mistaken as a fracture fragment in veterinary practices, particularly on 2D radiographs. The humeroscapular bone is a distinct osseous structure present in several large Genera of hawks (*Buteos* and *Accipiters*). While similar



structures have been observed in other bird species, their structure is fibrocartilaginous rather than bony (Smith & Smith, 1992a).

Finally, sesamoid bones in the right and left distal wings at the metacarpophalangeal joint (Figure 3.5) have been described by Zucca & Cooper (2000) in raptors belonging to the Genus *Falco*. There are three identifiable sesamoid bones: two at the metacarpophalangeal joint and one articulating the proximal and distal phalange.

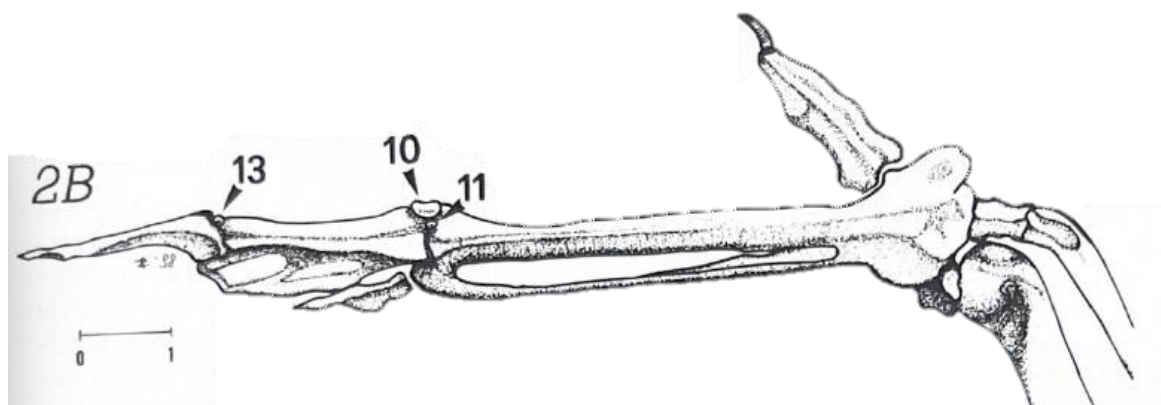


Figure 3.5 Depiction of the sesamoid bones in the distal wing, present in the Genus *Falco*. Each sesamoid bone is identified by markers 10, 11, and 13. Image retrieved from Zucca and Cooper (2000, p. 198).

#### *Cranial and long bone measurements*

Measurements were taken of the following skeletal elements (following the unpublished methods in Nelson et al. [2009]): length of the head (including the beak), breadth of head, length of the humerus, length of ulna, length of the metacarpus, length of the femur, length of the tibia, and length of the tarsometatarsus. All long bone measurements were taken on the anterior-posterior 2D slices, and cranial measurements were taken from the superior-inferior view of the 2D slices, following the standards of von den Driesch (1976). It should be noted that there may be slight variations in measurements, as these standards are for physical measurements, whereas the measurements here are taken on overlaid digital images (Appendix F). To help account for this issue, the slices are viewed in slab view, which joins a series of contiguous slices into one slab by displaying an average grayscale volume for each column of pixels in the slab, following Spake et al. (2020). These measurements are compared to the documented species published by Lortet and Gaillard (1905). The two researchers from Lyon's School of Medicine studied more than a thousand mummified birds stored in the collection in Lyon. The mummies

were gathered from various necropolises from Lower and Upper Egypt. To identify the species of birds within the mummies, Lortet and Gaillard dissected the mummies and removed the feathers and soft tissues to reveal the skeletal elements for osteological analyses<sup>3</sup> (Lortet & Gaillard, 1905). The systematic analysis of Lortet and Gaillard allowed them to identify 26 species of diurnal birds of prey (Baillel-LeSuer, 2019). The birds documented in Lortet and Gaillard's work do not make an extensive list of all the birds that existed in ancient Egypt, and the skeletal measurement data is only presented as a species mean value (without measurements of variability); but, it is currently the only working literature with skeletal documentation from mummified birds, and it is used as the standard of comparison for Egyptologists (e.g., Baillel-LeSuer, 2019; Johnston et al., 2020; von den Driesch et al, 2005). The standards used for long bone measurements are not disclosed by Lortet and Gaillard (1905). Consequently, their standards could differ from those published in 1976 by von den Driesch. This could lead to discrepancies in measurement comparisons; however, von den Driesch (1976) are the current zooarchaeological standards and will be used in tandem with the digital standards of Spake et al. (2020) for this thesis. An extensive list of the documented birds and their associated skeletal elements from Lortet and Gaillard (1905) can be found in Appendix G.

All skeletal measurements are taken on the lowest resolution micro-CT scans for each bundle to ensure the long bones are captured in their entirety. While the stitched mid-resolution scans would be *more* ideal for measurement accuracy (Conlogue et al., 2020), there is a chance of distortion or loss of data by applying the image registration and stitching algorithm; therefore, to ensure the most accuracy, the low-resolution scans were used for measurements. These measurements are input into Microsoft Excel (v.2403-17425.20146). The acquired measurements for each skeletal feature, for each specimen, are then subtracted from all recorded measurements (presented as species means) in Lortet and Gaillard (1905) to calculate the difference. These differences were plotted in a

---

<sup>3</sup> One of the unwrapped mummies analyzed by Lortet and Gaillard was so well preserved they were able to identify a female kestrel based solely on the feathers alone! (Baillel-LeSuer, 2019).

line graph in Excel, and the least difference in measurements for the entirety of the skeleton was considered in determining the range of possible taxa the mummified bird could belong to.

Measurements of the greatest diaphyseal length of the long bones (humerus, femur, and tibia) were taken for Ibis 2727.01, following the same protocol listed above, and compared to the reported Sacred Ibis measurements reported in von den Driesch et al. (2005).

*A note about Lortet and Gaillard (1905)*

A major limiting factor in current avian mummy research is the lack of comprehensive data regarding species variation and skeletal measurements of birds from ancient Egypt. The foundational work by Lortet and Gaillard (1905) is heavily relied upon by researchers examining animal mummies. This reliance on historical data presents several challenges. Firstly, there is a significant gap in the species catalogue, potentially omitting some species that were present in ancient Egypt but not documented by Lortet and Gaillard (1905). This incomplete record can lead to gaps in our understanding and potential misidentifications. Secondly, the methodologies for measuring skeletal elements may have evolved over the past century, so the standards and techniques used in this thesis may differ from those employed by Lortet and Gaillard (1905). These potential differences in measurement standards could lead to inconsistencies and affect the accuracy of comparative analyses. Additionally, the lack of detailed methodology in the historical records means that it is challenging to replicate Lortet and Gaillard's (1905) measurements or understand the context in which they were taken. This lack of reproducibility further complicates efforts to build on their work or validate their findings with modern techniques.

### *Scleral ossicle*

Considering the previously mentioned skeletal features and the long bone measurements, the species identification was narrowed further using the scleral ossicle (Figure 3.6), which shows high interspecies variation, as discussed in Chapter 2. Lemmrich (1931) provides a systematic overview regarding the relationship between ring form and species type. He describes three identification factors: type, scale count, and arrangement. Type refers to either Type A or Type B. Type A is described as having two or more pairs of distinguished scales, and Type B is described as having one pair of distinguished scales. According to Lemmrich (1931), a distinguished scale is a single-ringed bone which either overlaps the two neighbouring scales or is overlapped by the two neighbouring scales. This gives the scales the appearance of being larger or smaller than the other scales, respectively.

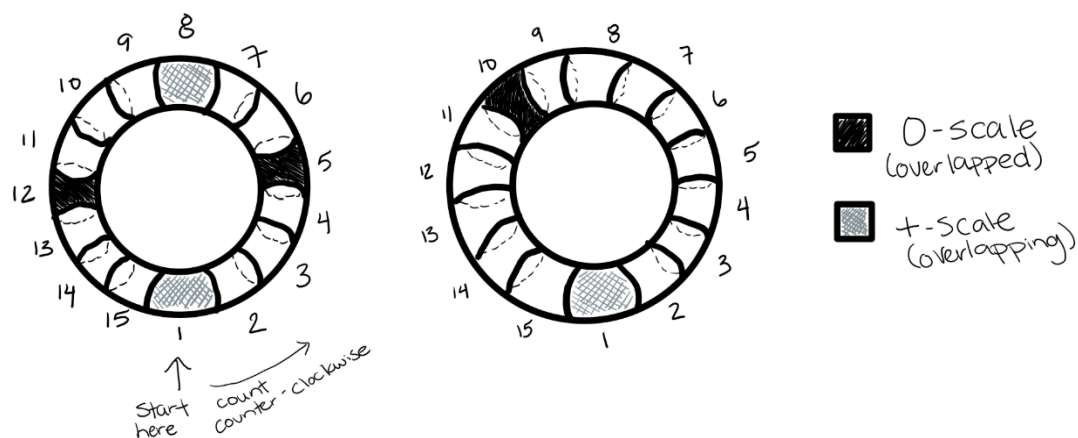


Figure 3.6 Example of scleral ossicle ring type and arrangement. Type A arrangement (2+ distinguished pairs) shown on the right. Type B arrangement (1 distinguished pair) shown in middle. Legend for distinguished scale reference on right. Reference drawing provided in Lemmrich (1931, p. 518). Image drawn by Maris Schneider.

Scale count refers to the number of single-ringed bones comprising the entire ossicle. Finally, the arrangement relates to how these scales overlap. Lemmrich (1931) describes scale arrangement as +-scale and O-scales. +-scales refers to a scale that covers both of the neighbouring rings. O-scales refer to a scale that is covered by the neighbouring rings. Lemmrich (1931) identifies where the overlapping or overlapped scales are on the ring by beginning with the bottommost scale and moving counterclockwise, noting which scale in the ring are distinguished scales (i.e., the bottommost scale is 1, the second scale

moving counterclockwise is scale 2 and so on). For example, the drawings provided in Figure 3.6, would be recorded as follows: (1a) Type A, 15 scales, +-scales 1, 8; O-scales 5, 12 (1b) Type B, 15 scales, +-scales 1; O-scales 10. In this thesis, I identify where and how the scales overlap and use Lemmrich's (1931) detailed species documentation to identify further possible species presented in the studied mummy bundles.

### 3.2.5.1 Challenges in taxonomy

Taxonomy, the science of classifying and naming living organisms, provides a structured framework for understanding and categorizing the diversity of life on Earth. However, taxonomic nomenclature systems have been around since the early 1700s, when *Systema Naturae* was first published by Carl Linnaeus, and as a result, there is an inherent non-uniformity in naming systems and descriptions throughout the literature. Many taxonomic descriptions published in the early nineteenth century lack adequate details or are poorly preserved (Godfray, 2002). Traditionally, taxonomic descriptions are based on the Linnaean system, which relies on morphology. However, within the last 20 years, DNA sequencing has become a prominent method of studying species and their evolutionary relationships. Relationships and lineages that used to be based on phenotypic observations are now being redefined, incorporating both phenotypes and genotypes (Godfray, 2002). Creating a taxonomic system based solely on DNA has been advocated; however, the reality of the associated costs and infrastructure have so far prevented such a project (Godfray, 2002). Therefore, we end up with systems combining historical, phenotypic, genetic data, and/or cladistic grouping, leaving us with temporal inconsistencies and discrepancies within literature and between disciplines (Godfray, 2002).

For example, the seminal work of Lortet and Gaillard (1905), is invaluable to current researchers examining bird mummies. However, 100 years after Lortet and Gaillard's publication, the MAHES project re-examined the Lyon collection and provided an updated taxonomic list, including input from naturalists, Egyptologists, chemists, and radiologists (Baillel-LeSuer, 2019). What was once identified as *Cerchneis tinnunculus* has now been corrected to *Falco tinnunculus*. Due to these inconsistencies and inaccuracies in nomenclature, this thesis will follow the skeletal measurements laid out

by Lortet and Gaillard (1905) but use the updated nomenclature provided by Baillel-LeSuer (2019) and the Integrated Taxonomic Information System (ITIS). The ITIS global database collaborates with the Smithsonian Institute to provide comprehensive and validated taxonomic classifications (Integrated Taxonomic Information System, 2023).

### 3.2.6 Effects of resolution

Qualitative analyses were examined on the scans at varying resolutions to discuss the effect of different resolutions in visualizing fine skeletal features. Specifically, I am looking for clarity within the scans, the ability to differentiate between skeletal features, define borders of features during the deep learning training, and the contrast difference between skeletal and desiccated tissue. Additionally, as long bone measurements are possible for the Redpath birds and the Chatham falcon with a clinical CT scan and micro-CT scans, the percent error (Perini et al., 2005) will be calculated between the measurements with the two scanning mediums using the following formula:

$$\text{Percent error} = \left( \frac{\text{Real value} - \text{Estimated value}}{\text{Real Value}} \right) \times 100$$

The micro-CT value is treated as the real value in the formula because the accuracy of measurements is determined by the effective spatial resolution, which is superior in micro-CTs (Conlogue et al., 2020; Nelson et al., 2009). Comparative error values under 5% were considered accurate, following results in other statistical and osteometric analyses (e.g., Bland & Altman, 1996; Curate et al., 2019; Langley et al., 2018). To minimize potential bias from taking intra-observer measurements, clinical CT scan measurements were taken three weeks after analyzing the micro-CT scans and documented in a separate Excel spreadsheet.

Additionally, linear regression models of the micro-CT (x-axis) and clinical CT (y-axis) and  $R^2$  values were graphed and calculated, respectively, in Excel to examine the variance in the estimated variable compared to the real value (Frost, 2024) for the Chatham Falcon, Faucon 2726.02, and Faucon 5731. A high  $R^2$  indicates small differences between the two values, suggesting the regression model is a good fit, so long

as the data is not biased. Residual plots were used to look for bias in the models (Appendix K).

## Chapter 4

### 4 Results

This chapter will summarize the anatomical features used to identify the birds mummified in the bundles examined here. The first bird presented will be the Chatham Falcon, followed by the two falcons from the Redpath Museum, then the two Redpath ibises, and will conclude with observations regarding the CMH Falcon 1 from the IMPACT database (Wade & Nelson, 2015). Alongside the CMH Falcon 1 results, there is an examination of the cranial and long bone measurements on clinical CT versus micro-CT scans. In tandem with the results presented for the osteological traits, the effect of differing resolutions or X-ray targets (where applicable) on the visualization of various skeletal features is presented. All image segmentation data processing was done using the same deep learning algorithm, initially trained using manually segmented data from the low-resolution micro-CT (110  $\mu\text{m}$ ) Chatham Falcon dataset (2% of the dataset was segmented). Three slices from every other dataset were also included in new training iterations to optimize output on each dataset. All raw data regarding cranial and long bone measurements and deviation calculations from documented species can be found in Appendix H. 3D renderings derived from the clinical CT scans of all mummified raptors can be found in Appendix I, as they did not yield identifiable results. Any additional observations (e.g., cause of death, foodstuff placement) identifiable on the micro-CT scans can be found in Appendix J. All images included in this Chapter were rendered on Dragonfly 3D World (v. 2024.1-1579, Comet Technologies) by Maris Schneider.

#### 4.1 Chatham Falcon

##### *Osteological analysis with resolution comparison*

The tomial tooth was visible on the clinical CT scan, the 110  $\mu\text{m}$  micro-CT, the 50  $\mu\text{m}$  stitched micro-CT set, and the physical mummy itself (Figure 3.1 and Appendix A). In scanning at the highest resolution (25  $\mu\text{m}$  with the tungsten and molybdenum targets), I purposely cut the tomial tooth from the scan to increase the resolution on different cranial features. The presence of the tomial tooth confirms that the bird within a bundle is a bird



of prey belonging to one of the genera *Falco* (falcons), *Elanus*, *Milvus*, and *Pernis* (kites), or *Platylophus*, *Lanius*, and *Eurocephalus* (shrikes) (Csermely et al., 1998; Fowler et al., 2009; Lacesse, 2015). The Chatham falcon also displayed accessory pygostyle bones (Figure 4.1), confirming the bird belongs to the Genus *Falco*.

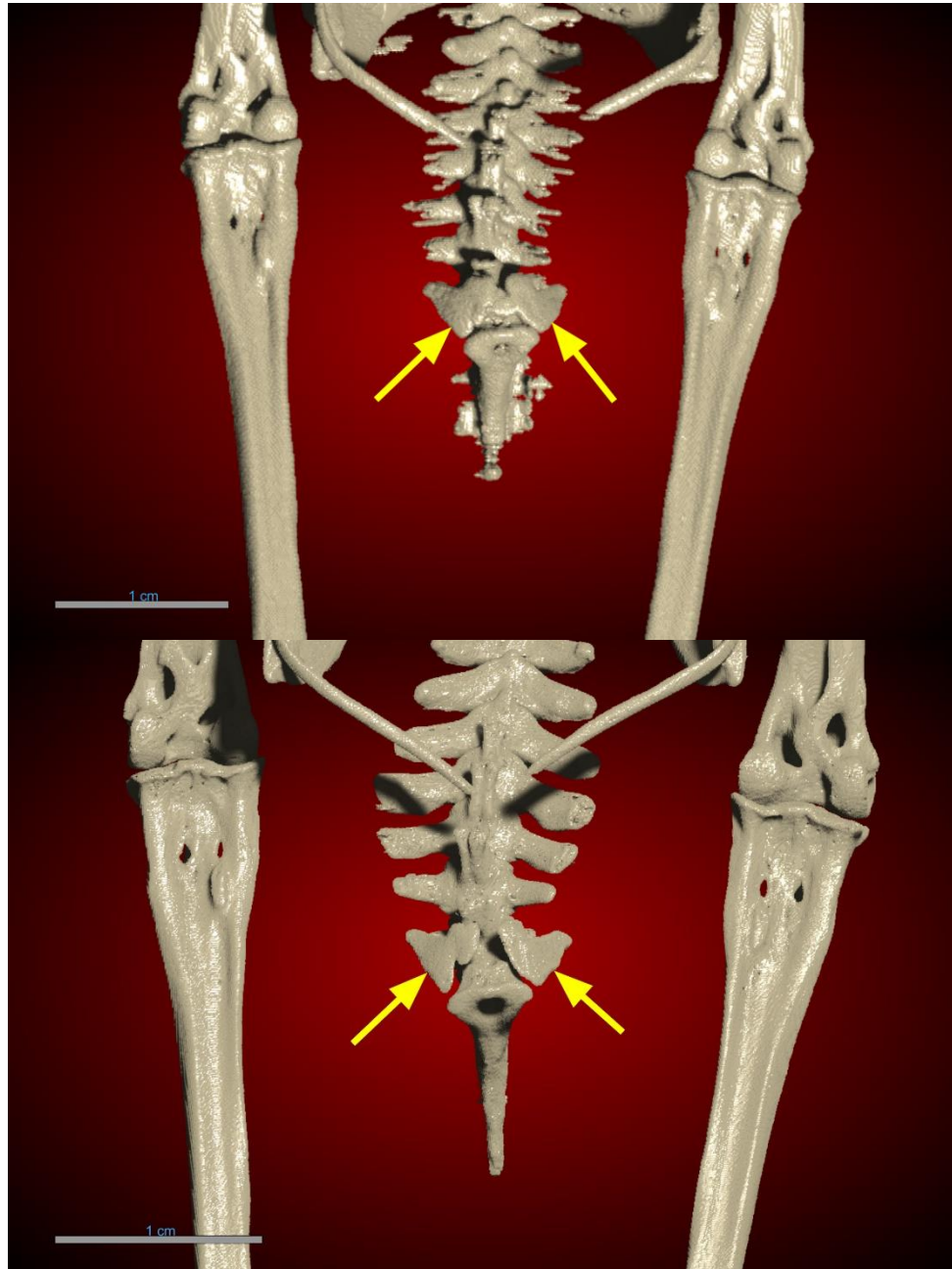
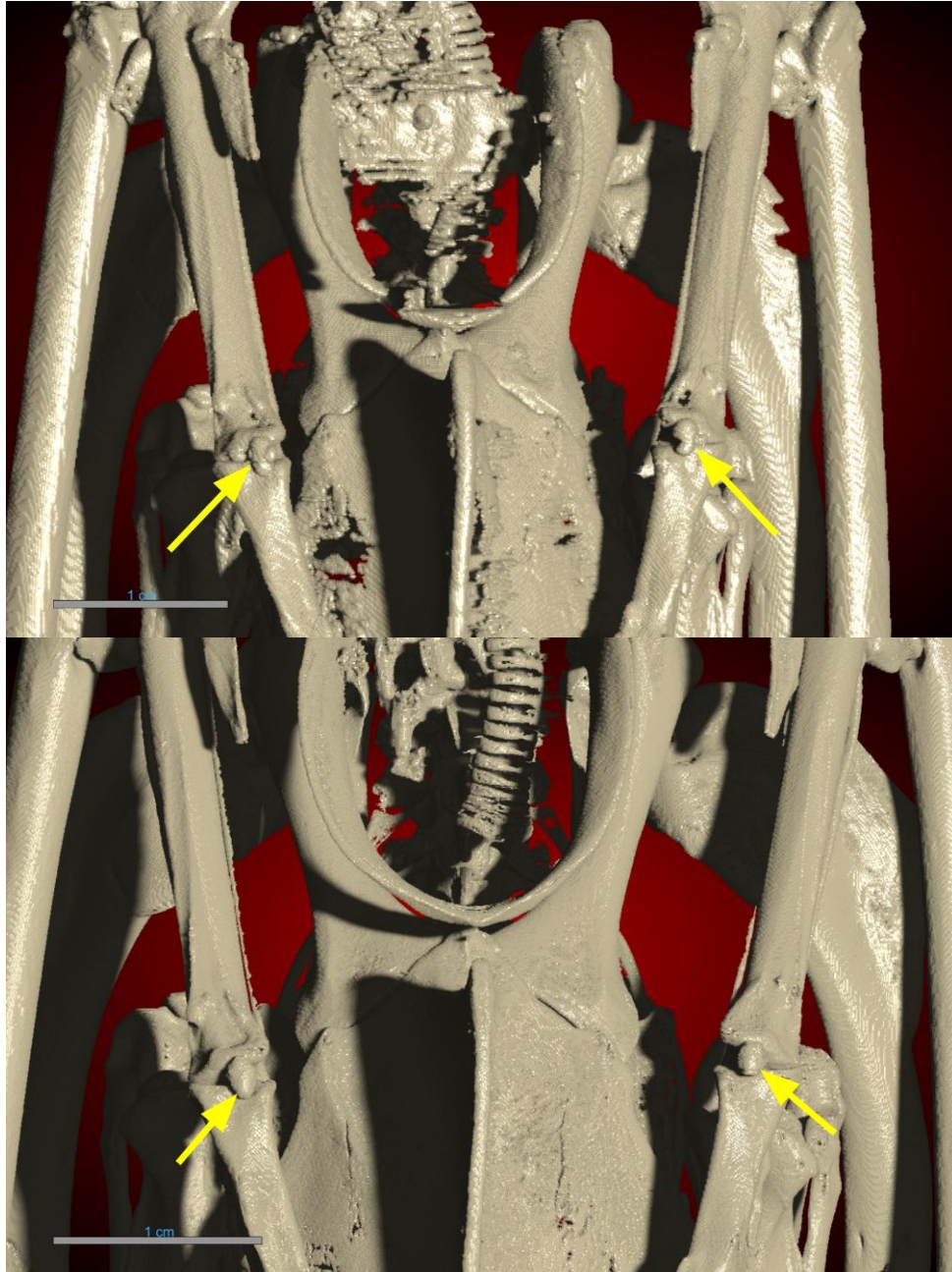


Figure 4.1 Presence of the accessory pygostyle bones, ventral to the pygostyle bone, in the Chatham Falcon. Top image at 110  $\mu\text{m}$ ; bottom image at 50  $\mu\text{m}$ .

Additionally, sesamoid bones were observed at the metacarpophalangeal joints (Figure 4.2) on 3D deep learning renderings on the 50  $\mu\text{m}$  and 110  $\mu\text{m}$  micro-CT scans. While

the clarity of the bone is greater on the 50  $\mu\text{m}$  micro-CT scan, the 110  $\mu\text{m}$  provides sufficient visualization of these small bones. An added benefit, however, of the higher resolution (50  $\mu\text{m}$ ) micro-CT scan, were the more clearly defined borders in the automatic image segmentation (see the difference in the segmentation of the sternum and tracheal area in Figure 4.2). This could prove more beneficial for future researchers employing differing osteological analyses than those presented in this thesis.



*Figure 4.2 Identification of left and right sesamoid bones at metacarpophalangeal joints in the distal wing of the Chatham Falcon. Top image at 110  $\mu\text{m}$ ; bottom image at 50  $\mu\text{m}$ .*

The resolution on the clinical scan was not great enough to visualize the distal sesamoid bones. These sesamoid bones confirm that the Chatham Falcon belongs to the Genus *Falco*. Additionally, an absence of *os prominens* (Smith & Smith, 1992b; Zucca & Cooper, 2000) articulating the radius and carpometacarpus and the absence of the humeroscapular bone (Smith & Smith, 1992a) confirm this identification. The absence of these bones was also confirmed by examining the 2D slices, ensuring they were not missing in the 3D reconstructions due to an error in the image processing techniques employed here.

Based on the above skeletal features, measurements of the Chatham Falcon were compared to other documented falcon species in Lortet and Gaillard (1905). All measurements of skeletal features presented in this Chapter are done using feature numbers to represent a skeletal element.

*Table 4.1 Reference of feature number to measured skeletal element in avian skeletons.*

| Feature number | Avian osteological element                   |
|----------------|--|
| 1              | Length of head (tip of beak to occiput bone) |
| 2              | Breadth of head                              |
| 3              | Length of humerus                            |
| 4              | Length of ulna                               |
| 5              | Length of metacarpus                         |
| 6              | Length of femur                              |
| 7              | Length of tibia                              |
| 8              | Length of tarsometatarsus                    |

The results of the skeletal measurements (Figure 4.3) indicate that the Chatham Falcon is most similar in size and linear proportion to *F. subbuteo* and *F. tinnunculus*.

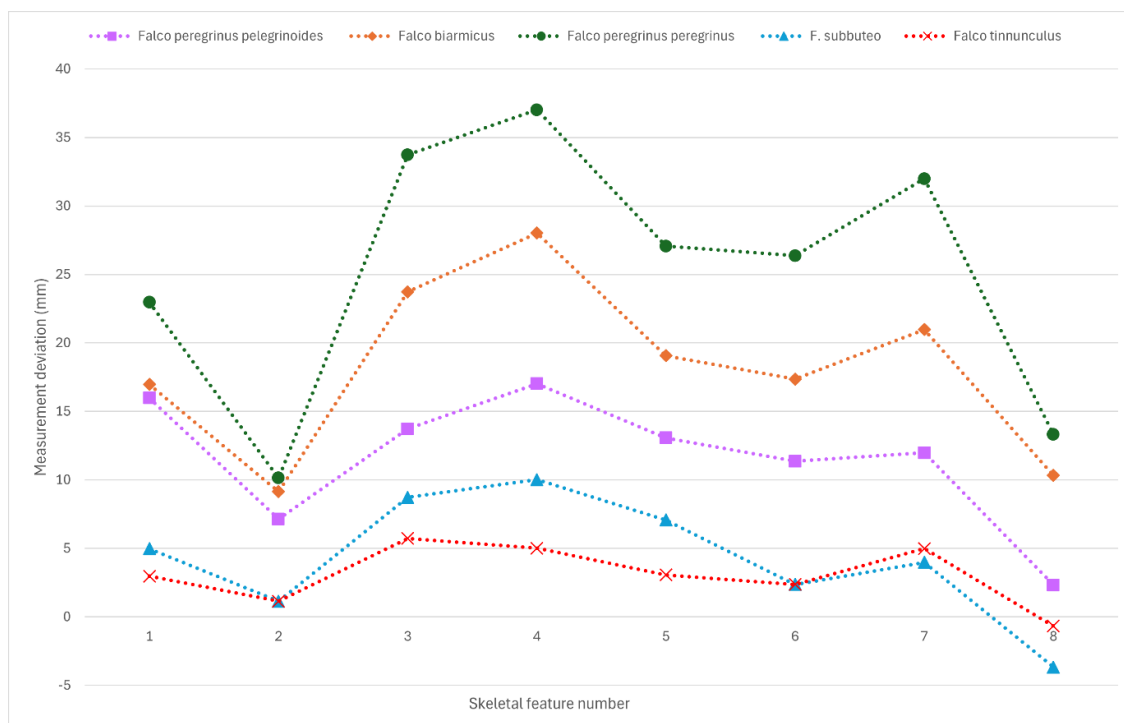


Figure 4.3 Measurement deviation of skeletal features (Table 4.1) of known falcon species (Lortet & Gaillard, 1905) compared to the Chatham Falcon. Species with the least amount of deviation in skeletal trait measurements have a line running closest to 0 on the y-axis.

A key benefit of the micro-CT scans was the visualization of the scleral ossicle. The 110  $\mu\text{m}$  (Figure 4.4) had the poorest visualization of the scleral ring of the micro-CT scans. The individual scleral bones are extremely small and not very dense. In the lowest resolution micro-CT scan, the contrast resolution was insufficient to differentiate between the surrounding desiccated tissue and the scleral ring. This produces a “globular” effect on the 3D rendering, as the deep learning algorithm cannot clearly distinguish between bone and desiccated tissue.

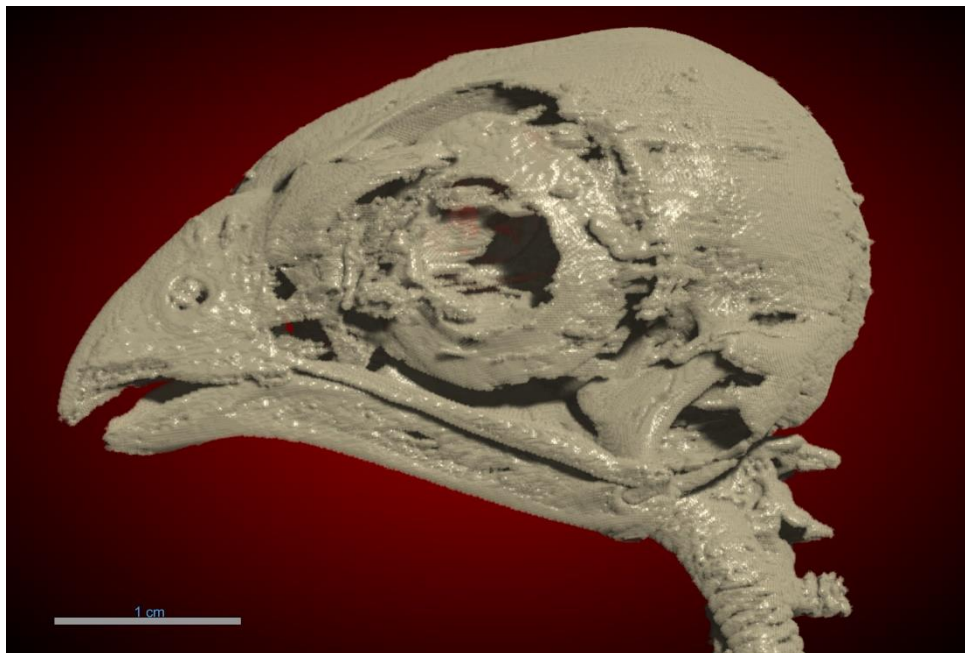


Figure 4.4 110  $\mu\text{m}$  3D deep learning segmentation rendering of the skull of the Chatham Falcon, showcasing the poor differentiation between bone and surrounding noise, thus obscuring the view of the individual scleral bones.

The scleral ring is visible in the 50  $\mu\text{m}$  deep learning segmented image. However, the individual ossicles are not (Figure 4.5). There are some indications of the shape of the individual ossicle bones, but not enough differentiation to discern the scleral arrangement. The 25  $\mu\text{m}$  scan with a tungsten target had excellent visualization of the ossicle bones (Figures 4.5, 4.6), and the arrangement of the bones is evident. According to Lemmrich (1931), all species in the Genus *Falco* have Type B arrangements (one pair of distinguished scales), whereas accipiters have Type A and Type B (Lemmrich, 1931). The Chatham falcon has a Type B arrangement of 14 ossicles in a 1:7 configuration. This arrangement is indicative of the species *F. tinnuculus*<sup>4</sup>, not *F. subbuteo*.

---

<sup>4</sup> According to Lemmrich (1931), *F. peregrinus* also has 14 ossicles with a 1:7 arrangement. However, based on the skeletal measurements, this species of bird is much larger than the Chatham Falcon and, therefore, not a plausible species identification.

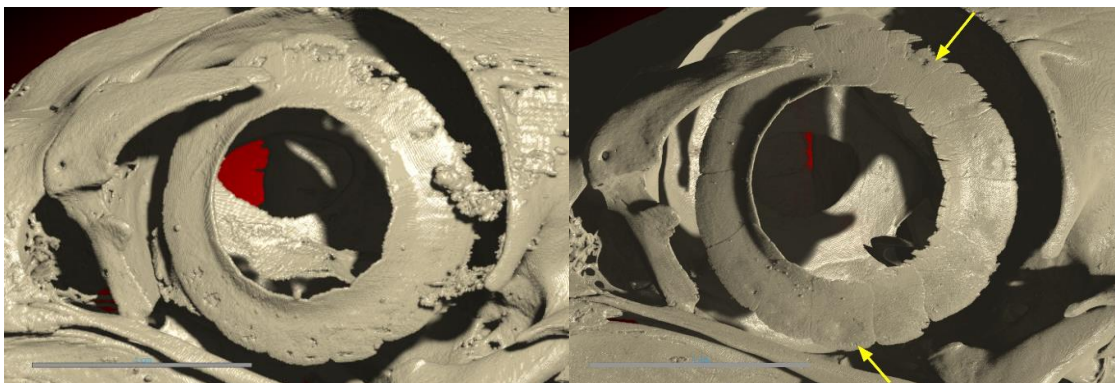


Figure 4.5 Visualization of the scleral ring in the Chatham Falcon. At 50  $\mu\text{m}$  (left) there is good visualization of the entire ring structure, and the shape of the individual scales can almost be discerned. At 25  $\mu\text{m}$  (right) individual ossicles are fully visible. Bottom yellow arrow indicates the first overlapping distinguished scale, and the topmost yellow arrow indicates the overlapped distinguished scale, confirming the 1:7 arrangement.

Moreover, a scan at 25  $\mu\text{m}$  with a molybdenum target was acquired to determine if a tungsten versus molybdenum target significantly impacted resolution and visualization. The target type did not affect 3D deep learning renderings of the scleral ossicle at this resolution, as the ossicle arrangement was evident in both images (Figure 4.6).

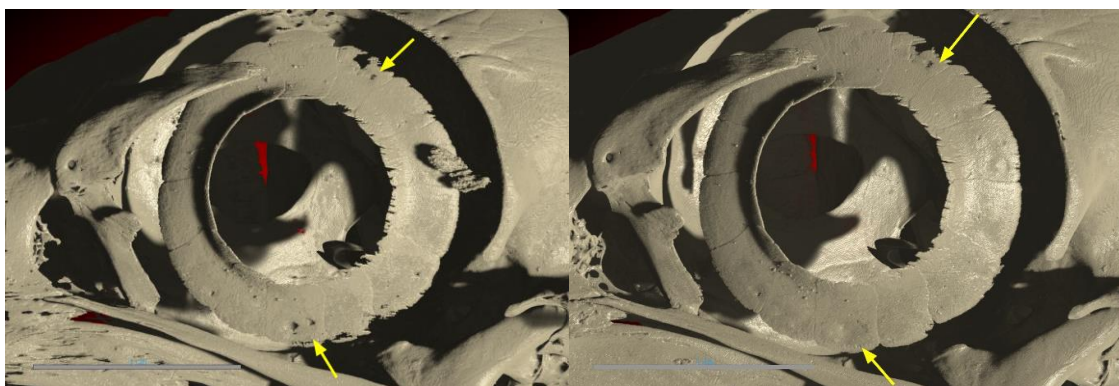


Figure 4.6 Scleral ossicle arrangement of the Chatham Falcon at 25  $\mu\text{m}$  using the molybdenum (left) target and the tungsten (right) target. No discernable differences between the targets were noted.

In his seminal work, Lemmrich (1931) only references *F. tinnunculus* using text annotations (e.g., B, 14, 1:7). Following his visual documenting style (Lemmrich, 1931) and the observations of the scleral ossicle in the scans of the Chatham Falcon, I have created a diagram of the scleral arrangement for *F. tinnunculus*, explicitly highlighting the location of the distinguished scales (Figure 4.7).

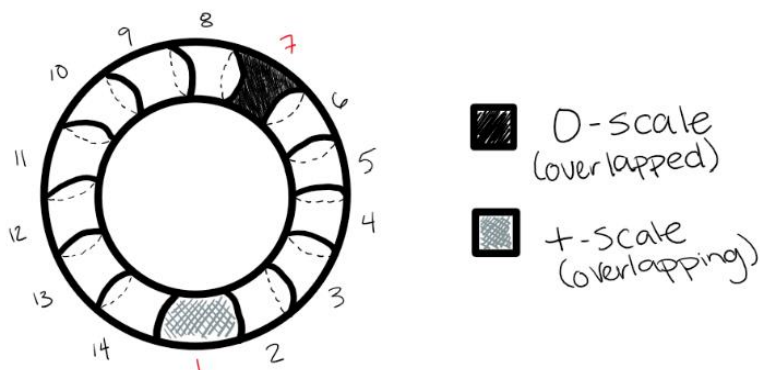


Figure 4.7 Diagram of the scleral scale arrangement for *Falco tinnunculus*, in accordance with the documenting style from Lemmrich (1931). Image drawn by Maris Schneider.

Deep learning segmentation of the 25  $\mu\text{m}$  micro-CT dataset was optimal and produced excellent visualization of the scleral ring. However, according to a previous, unpublished study of the Chatham Falcon (Nelson et al., 2009), the scleral ring and ossicle arrangement *should* have been visible on the 50  $\mu\text{m}$  micro-CT scan. A quick examination of the 2D slice view (Figure 4.8) of the 50  $\mu\text{m}$  data set confirmed that the individual ossicles are visible, although the differentiation between the ossicles is minuscule. Therefore, I manually segmented the ossicle ring (Figure 4.9) to determine if the deep learning algorithm was responsible for the poor visualization. Manual segmentation<sup>5</sup> yielded no better

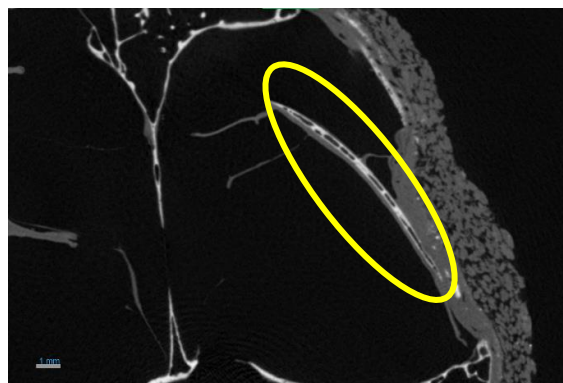


Figure 4.8 A 2D slice view of three scleral bones in the 50  $\mu\text{m}$  dataset of the Chatham Falcon.

visualization of the scleral ossicles at 50  $\mu\text{m}$  than the deep learning rendered 3D image. A final image was rendered by manipulating the 2D slices to view the entire ossicle on one slice in 2D (Figure 4.10). After that, the 50  $\mu\text{m}$  volumetric dataset was set to slab mode

---

<sup>5</sup> For perspective, training a deep learning algorithm takes a few days to create good input data and can be applied to multiple datasets. Manual segmentation of the one scleral ring takes 4 hours, as the ring spans across approximately 300 2D slices of the dataset and can only be used once on a singular dataset. This is only one structure of the entire skeleton. Imagine using this method to segment the entire micro-CT dataset. This is why deep learning is the preferred method, despite the challenges that come along with it.

(maximum intensity project), which displays the highest intensity values for each voxel in the slice integration (Dragonfly, 2020d). This view depicts the individual ossicles. The ossicle arrangement can be discerned, however, not as clearly as the 3D rendering at 25  $\mu\text{m}$ . This is because the more dense areas seen on the 2D slab image are radiopaque areas where the ossicle scales overlap, not the true borders of the bone, like those seen on the 25  $\mu\text{m}$  image (Figure 4.6). From this brief tangential analysis, it can be confirmed that visualizing the scleral ossicle at a lower resolution is possible with different visualization methods other than 3D image segmentation.



Figure 4.9 Manually segmented left scleral ossicle of the Chatham Falcon at 50  $\mu\text{m}$ .

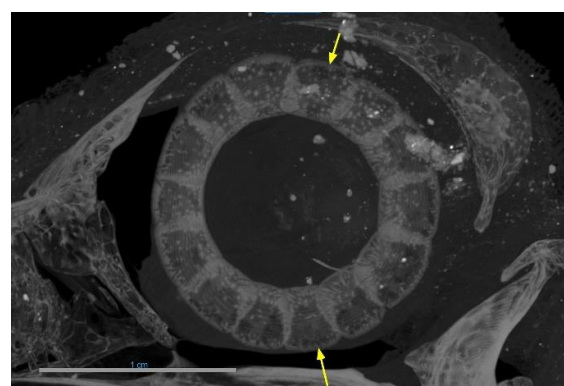
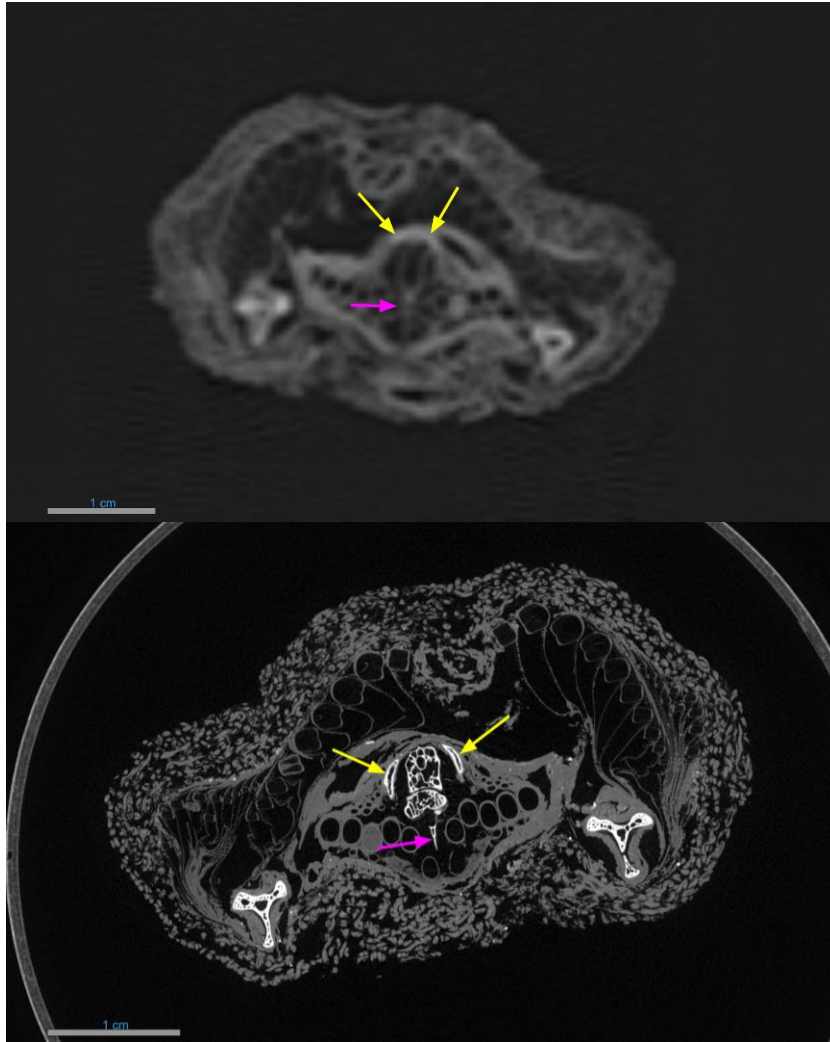


Figure 4.10 2D maximum intensity project view of a scleral ossicle in the Chatham Falcon at 50  $\mu\text{m}$ .

The clinical CT scans of the Chatham Falcon did not yield any identifiable skeletal markers. Figure 4.11 shows the visualization of skeletal elements on a clinical CT compared to a mid-resolution (50  $\mu\text{m}$ ) micro-CT of the Chatham Falcon. Both images compare the 2D slices looking at the accessory pygostyle bones. These images demonstrate the difference in resolution between the two types of scans and show how poor resolution can inhibit image processing and feature visualization. Specifically, the clinical CT scan has poor contrast and spatial resolution, which creates a blurring effect between the borders of bone and desiccated tissue. While it may be clear what skeletal structures are and are not to a human observer (although I would argue that even human-made distinctions of bones are difficult on the clinical CT scan), it is essential to recall that image processing relies on *what a computer can see*. An image is just a matrix of pixels, and a computer only processes aspects like pixel brightness/intensity (Bezryadin et al., 2007), which is more definable with high spatial



and contrast resolution images. This is one of the most significant challenges in relying on non-human guided segmentation.



*Figure 4.11 Identification of the accessory pygostyle bones in the Chatham Falcon on a 2D slice of a clinical CT scan (top) and the 50  $\mu\text{m}$  micro-CT scan (bottom) (yellow arrow indicating the pygostyle bone; pink arrows indicating the accessory bones). See figure 4.1 for 3D rendering of these bones.*

### *Dental CBCT*

A dental CBCT was acquired with the hope of providing usable results, which could mitigate the need to have access to a micro-CT scanner or supercomputers capable of processing extremely large files. Unfortunately, upon retrieval of the dental CBCT scan, we realized the data had been improperly acquired, improperly processed, or improperly

transferred<sup>6</sup> (or any combination thereof). This resulted in the following dataset (Figure 4.12).

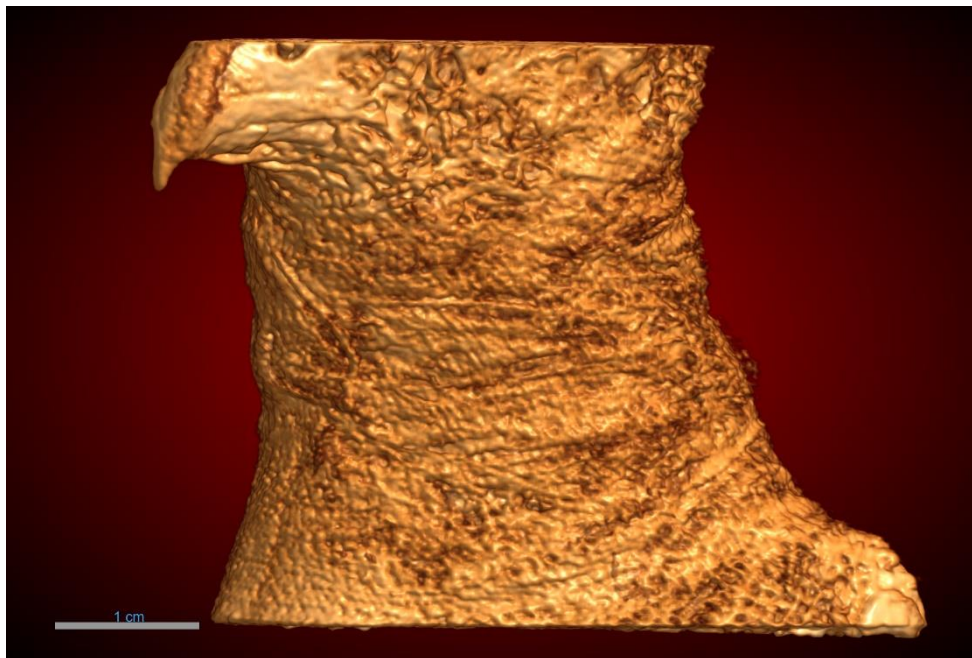


*Figure 4.12 Full dataset acquired of the Chatham Falcon using at dental CBCT scanner.*

Despite the unfavourably cropped dataset we acquired, I will provide brief remarks regarding the quality of the dental CBCT scan. Viewing the 2D slices, it is clear that the long bones create good contrast on a dental CBCT scan. The less dense features, like the cranium and scleral ossicle, have poor contrast resolution (Figure 4.13).

---

<sup>6</sup> During our time at the Schulich School of Medicine and Dentistry, we noted many challenges in scanning the Chatham Falcon. The most notable is that the software designed to help align the scanning medium is designed to align a patient's mouth properly – not a mummy. Clearly, despite our best efforts, we could not create a sufficient picture.

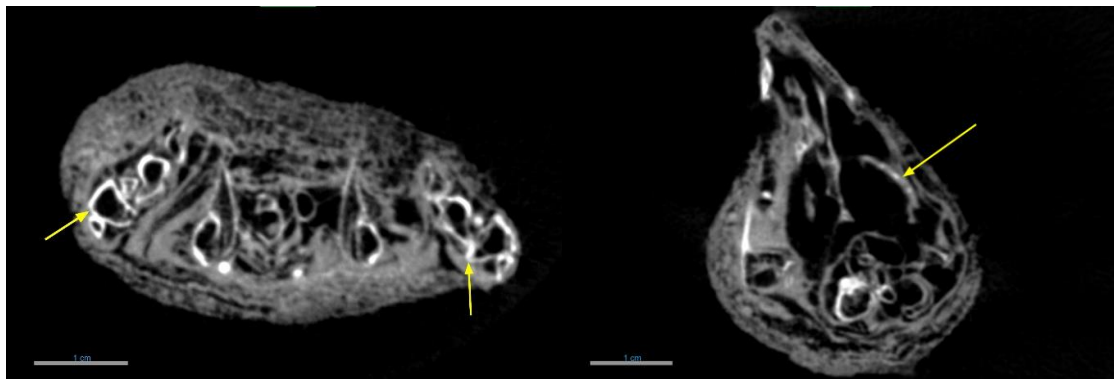


Figure 4.13 2D slice of the Chatham Falcon from a dental CBCT. Image on left shows the clear distinction between dense long bones and surrounding tissue/bandages. Image on the right identifies the scleral ossicle, which shows poor definition compared to the surrounding background noise.

The high contrast in the long bones leads me to believe that a dental CBCT scan *could* be used in species identification, particularly in examining structures such as the accessory pygostyle or sesamoid bones. Furthermore, I propose that examining the dense talons of mummified birds, which have high X-ray attenuation properties<sup>7</sup>, could provide valuable insights through the utilization of dental CBCT scanners. Talons have been used previously by other researchers studying mummified birds, particularly looking at curvature on radiographs (Morgan & McGovern-Huffman, 2008; Morgan et al., 2011).

Expectedly, dental CBCT cannot be used to examine the scleral ossicle arrangement, as even the low-resolution micro-CT scans do not produce a clear enough image. At this stage, I can neither definitively reject nor endorse the utilization of dental CBCT scanners for non-destructive examinations of mummified animals, but further investigation is warranted.

In sum, the Chatham Falcon is strongly believed to belong to the species *Falco tinnuculus* based on the presence of the tomial tooth, sesamoid bones at the metacarpophalangeal joint, the accessory pygostyle bones, the long bone measurements, and the scleral ossicle arrangement. Most traits needed for species identification were visible on the lowest resolution micro-CT scan (110 $\mu$ m), and the highest resolution scan

---

<sup>7</sup> Similar to teeth, for which dental CBCT scanners are optimized.

(25  $\mu\text{m}$ ) was only necessary to visualize the scleral ossicle arrangement. Unfortunately, the contrast between desiccated tissue/wrappings and bone on the clinical CT could not yield 3D renderings sufficient to visualize diagnostic skeletal elements. The long bones on the clinical CT scan were measured and compared to the measurements taken on the micro-CT scan. Surprisingly, the results of these measurements were relatively accurate and are discussed in more detail below (Chapter 4.4).

## 4.2 Redpath Museum raptors

### 4.2.1 Faucon 2726.02

#### *Osteological analysis with resolution comparison*

Faucon 2726.02 presents with similar skeletal elements to the Chatham Falcon. The beak is damaged (Figure 3.2 and Appendix A); therefore, no comments can be made regarding the tomial tooth.

Like the Chatham Falcon, Faucon 2726.02 displayed accessory pygostyle bones (Richardson, 1972; Smith & Smith, 1990) as identified in Figure 4.14 with the 50  $\mu\text{m}$  and

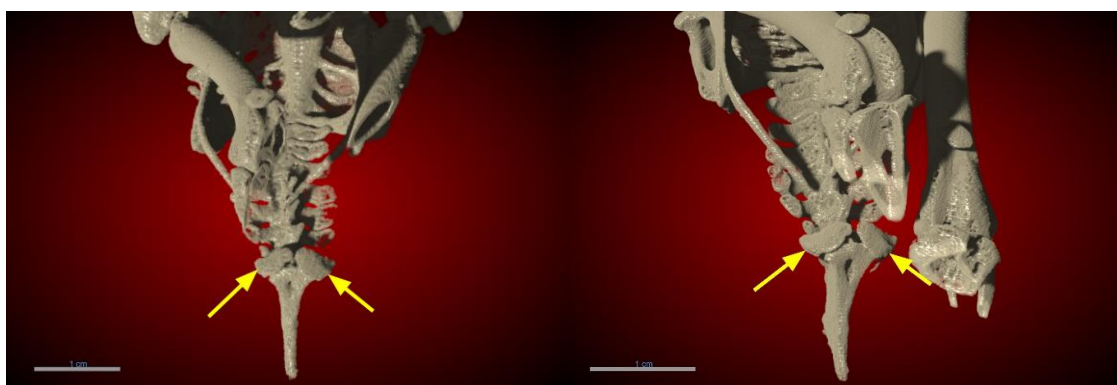


Figure 4.14 Presence of the accessory pygostyle bones, ventral to the pygostyle bone, in Faucon 2726.02. Left image at 100  $\mu\text{m}$ ; right image at 50  $\mu\text{m}$ . Note, the datasets have been cropped, as the position the falcon is mummified in obstructs the view of the accessory bones.

100  $\mu\text{m}$  micro-CT scans. Furthermore, the 50  $\mu\text{m}$  and 100  $\mu\text{m}$  micro-CT scans of Faucon 2726.02 revealed the presence of distal sesamoid bones at the metacarpophalangeal joint (Zucca & Cooper, 2000) in the right and left wings, shown in Figure 4.15. Moreover, the lack of *os prominens* articulating the radius and carpometacarpus (Smith & Smith, 1992a; Zucca & Cooper, 2000) and the humeroscapular bone (Smith & Smith, 1992a) serves as

additional confirmation that the mummified Faucon 2726.02 is a member of the *Falco* Genus. Again, the absence of these traits was also confirmed with a the 2D slice analysis. The clinical CT scan of Faucon 2726.02 retrieved from the IMPACT database (Wade & Nelson, 2015) similarly did not have a high enough resolution to visualize these small, identifying skeletal features.

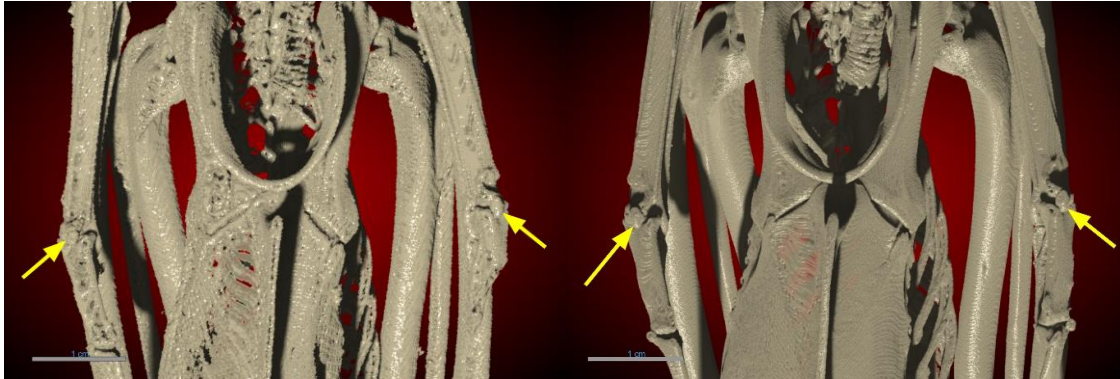


Figure 4.15 Identification of left and right sesamoid bones at the metacarpophalangeal joint in the distal wing of Faucon 2726.02. Left image at 100 µm; right image at 50 µm.

Similar to the Chatham Falcon, the skeletal measurements of Faucon 2726.02 were compared to those of other documented species in the Genus *Falco* (Lortet & Gaillard, 1905). The total length of the head (from occiput to beak) was not included, as the tomial

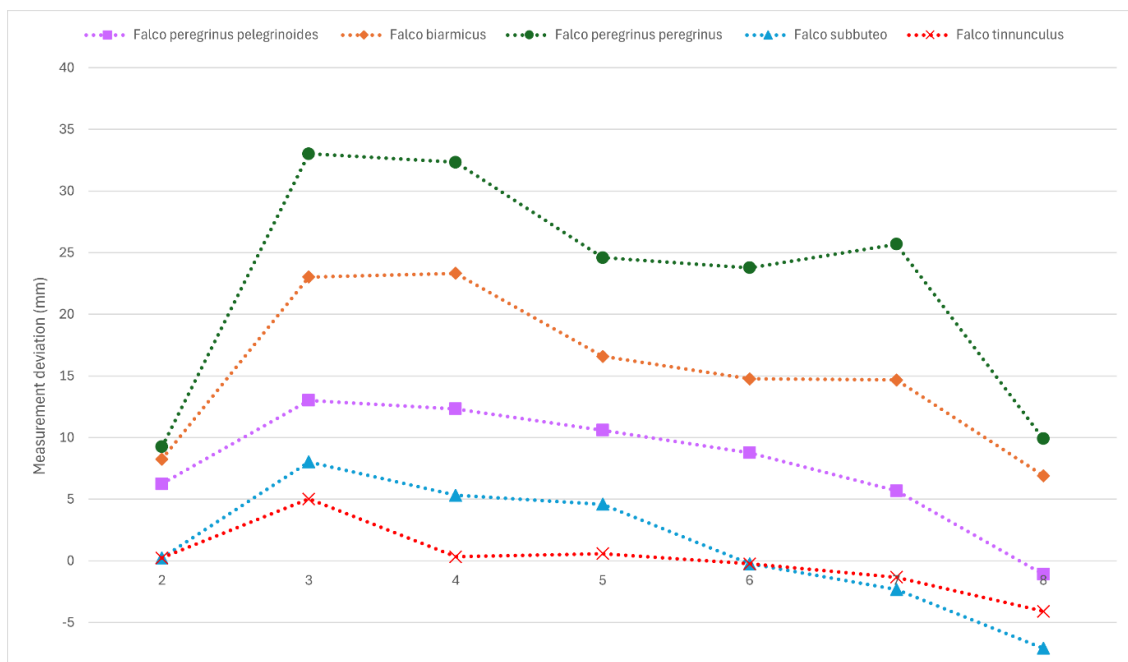


Figure 4.16 Measurement deviation of skeletal features (Table 4.1) of known falcon species (Lortet & Gaillard, 1905) compared to Faucon 2726.02. Species with the least amount of deviation in skeletal trait measurements have a line running closest to 0 on the y-axis.

tooth of Faucon 2726.02 is broken and missing. Skeletal measurements and linear proportions (Figure 4.16) suggest that Faucon 2726.02 is closest in size to *F. subbuteo* and *F. tinnunculus*.

Once again, the scleral ring was visible on all three micro-CT scans 3D image renderings (Figures 4.17, 4.19). However, only in the 25  $\mu\text{m}$  scan were the individual ossicles clear enough to discern the arrangement pattern (Figure 4.19).

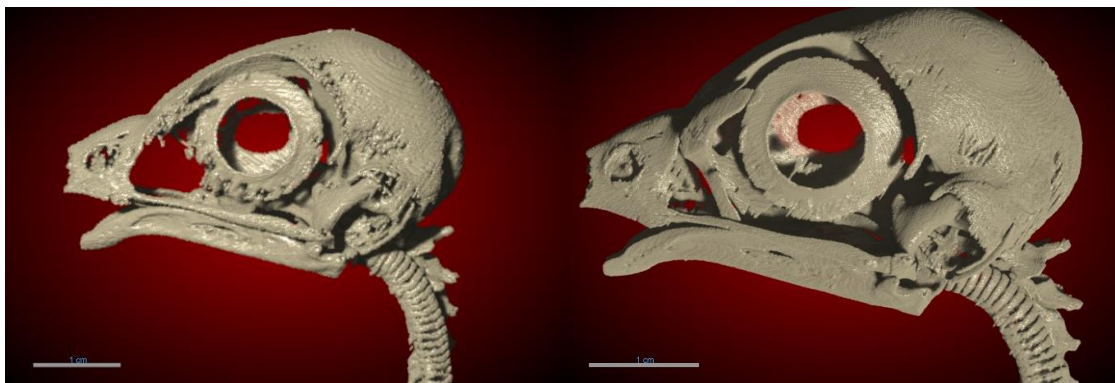


Figure 4.17 100  $\mu\text{m}$  (left) and 50  $\mu\text{m}$  (right) 3D rendering of the skull of Faucon 2726.02, showcasing the scleral ring. While the bone is clearly present, there is no significant differentiation between the individual ossicles to determine ossicular arrangement.

It should be noted that on the 100  $\mu\text{m}$  scan (Figure 4.17), there is “missing” bone directly under the nasal bone. The low density nature of the cranial bones in avian species is likely the cause of the deep learning algorithm misinterpreting the border between bone and desiccated tissue. Although these are high-resolution scans (compared to a clinical CT or dental CBCT scan), less dense structures still have poor contrast resolution compared to the surrounding desiccated tissue, making segmentation challenging. In this instance, the deep learning algorithm underestimated the border of the skeletal structures,

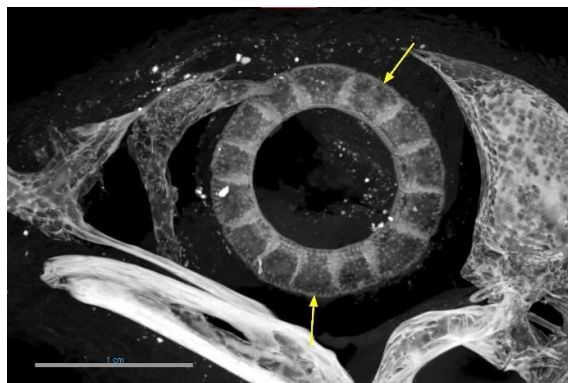


Figure 4.18 2D maximum intensity project view of a scleral ossicle in Faucon 2726.02 at 50  $\mu\text{m}$ .

whereas the algorithm overestimated the borders in the 110  $\mu\text{m}$  of the Chatham Falcon (Figure 4.4).

A 2D maximum intensity projection image (Figure 4.18) was created to examine the ossicles at 50  $\mu\text{m}$  for Faucon 2726.02. This image confirms the number of ossicles and

arrangement presented below in the 25  $\mu\text{m}$  image renderings (Figure 4.18).

Faucon 2726.02 presents a Type B arrangement of 14 ossicles in a 1:7 configuration, like the Chatham Falcon and the documented arrangement for *F. tinnuculus* (Lemmrich, 1931). If the bird belonged to the species *F. subbuteo*, we would see a scleral ring with 15 individual ossicles and a 1:7 configuration (Lemmrich, 1931). The individual ossicles in the 3D rendering of Faucon 2726.02 at 25  $\mu\text{m}$  are not as clear as the high-resolution scan of the Chatham Falcon (see Figures 4.5 and 4.19). Therefore, the overlapping/overlapped structures of the distinguished scales were confirmed on the 2D slab view of the dataset (Figures 4.20, 4.21).

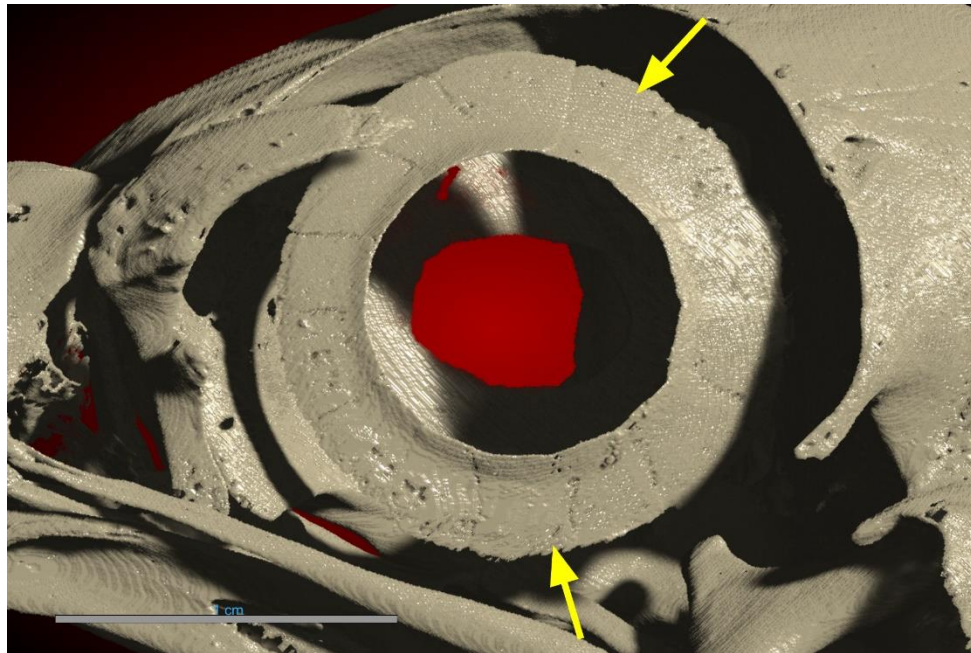


Figure 4.19 Visualization of the scleral ring in Faucon 2726.02 at 25  $\mu\text{m}$ . Bottommost yellow arrow indicates the first overlapping distinguished scale, and the topmost yellow arrow indicates the overlapped distinguished scale, confirming the 1:7 arrangement.

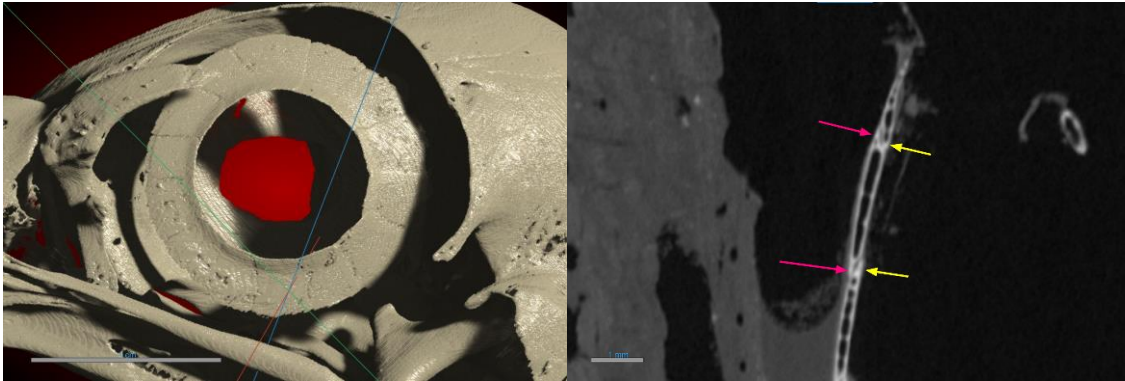


Figure 4.20 2D confirmation of the overlapping structure of ossicle 1 in Faucon 2726.02. 3D view (left) confirms which ossicle is being examined in 2D (right), with the placement of a 3D marker. Image on right shows the individual ossicle in question. Pink arrows indicate where the individual scale overlaps both of the neighbouring scales. Yellow arrows indicate where both of the neighbouring scales are overlapped by scale 1.

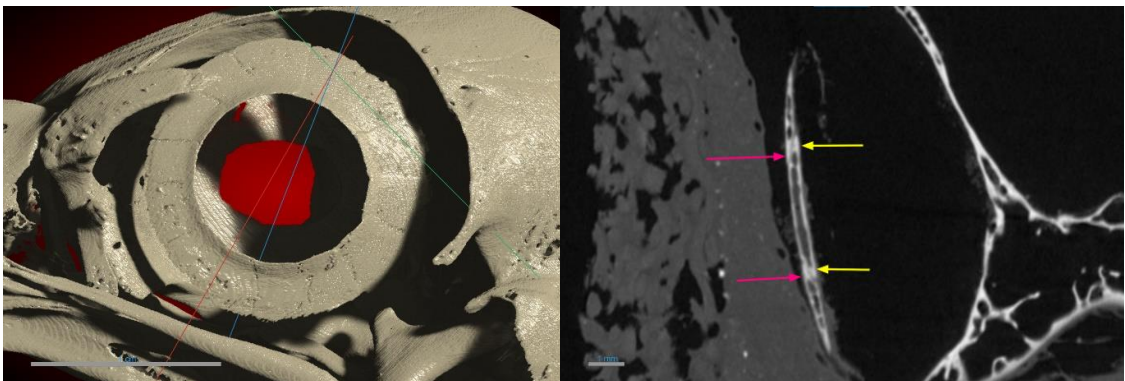


Figure 4.21 2D confirmation of the overlapped structure of ossicle 7 in Faucon 2726.02. 3D view (left) confirms which ossicle is being examined in 2D (right), with the placement of a 3D marker. Image on right shows the individual ossicle in question. Pink arrows indicate where the neighbouring scales overlap the middle scale. Yellow arrows indicate where the middle scale is overlapped by the neighbouring scales, confirming that scale 7 is a distinguished scale.

Comparable to the clinical CT of the Chatham Falcon, the scan acquired from the IMPACT database (Wade & Nelson, 2015) of Faucon 2726.02 did not provide sufficient visualization of skeletal traits, including the scleral ossicle arrangement, the accessory pygostyle bones, and the sesamoid bones. The algorithm again overestimated borders with low contrast (such as the long bones) compared to the neighbouring desiccated tissue and underestimated features with low bone density, such as the skull.

To summarize, Faucon 2726.02 is strongly believed to belong to the species *Falco tinnuculus* based on the presence of sesamoid bones at the metacarpophalangeal joint,



accessory pygostyle bones ventral to the pygostyle bone, the long bone measurements, and the scleral ossicle arrangement. These traits are all shared with the Chatham Falcon, suggesting both mummified birds belong to the same species. Although the visualization of skeletal characteristics was not as clear as the scans taken of the Chatham Falcon (discussed more in Chapter 5), the appendicular traits necessary for species identification were visible on the lowest resolution micro-CT scan. The highest resolution scan was only necessary to visualize the scleral ossicle arrangement. Additionally, the 2D maximum intensity projection is useful for visualizing the individual scleral scales at  $50\mu\text{m}$ .

#### 4.2.2 Faucon 5731

##### *Osteological analysis with resolution comparison*

The tomial tooth was clearly observed on the clinical CT scan, all micro-CT scans, and the physical examination of the mummy (Figure 3.2 and Appendix A), corroborating that Faucon 5731 belongs to a Genus within falcons, kites, or shrikes. (Csermely et al., 1998; Fowler et al., 2009; Lacesse, 2015).

Upon initial observations of the  $88\mu\text{m}$  deep learning segmentation 3D rendering, it appeared that Faucon 5731 did not possess accessory pygostyle bones (Figure 4.22).

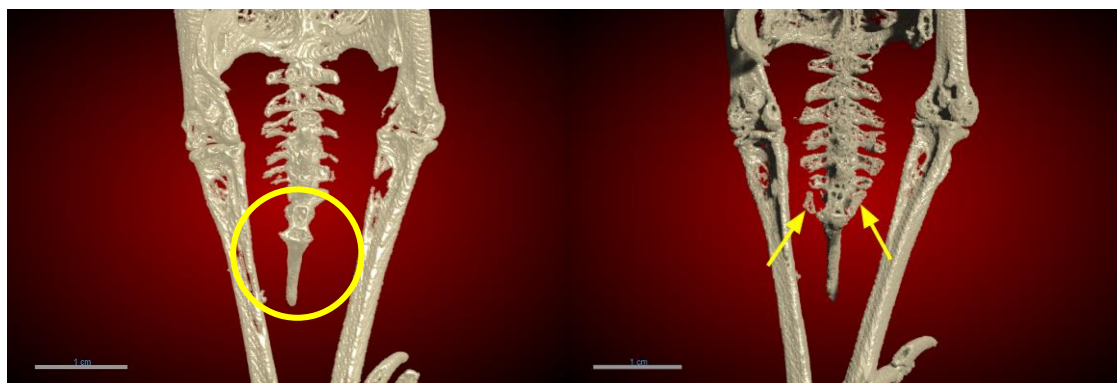


Figure 4.22 Depiction of the pygostyle bone showing the lost data due to poor image segmentation. The image on the left shows a pygostyle bone with no articulating accessory bones, whereas the image on the right shows the clear presence of accessory pygostyle bones, following new iterations of training to the deep learning algorithm. Both images are shown at  $88\mu\text{m}$ .

However, after checking on the original micro-CT dataset slice views and the  $44\mu\text{m}$  3D rendering (Figure 4.23), it was confirmed that Faucon 5731 does have accessory

pygostyle bones, and the lack of visualization in the 3D rendering was due to a processing error when applying the deep learning image segmentation algorithm. To improve the output image, the algorithm underwent five iterations of additional training, with manually segmented data from the low resolution (88  $\mu\text{m}$ ) Faucon 5731 dataset. Despite the multiple training rounds, the output renderings were still less than ideal. However, segments of the accessory pygostyle bones could be visualized at 88  $\mu\text{m}$  (Figure 4.22). The failure of the deep learning algorithm, in this case, emphasizes the need to confirm the presence and absence of skeletal features using multiple image analysis techniques, specifically the slice view.

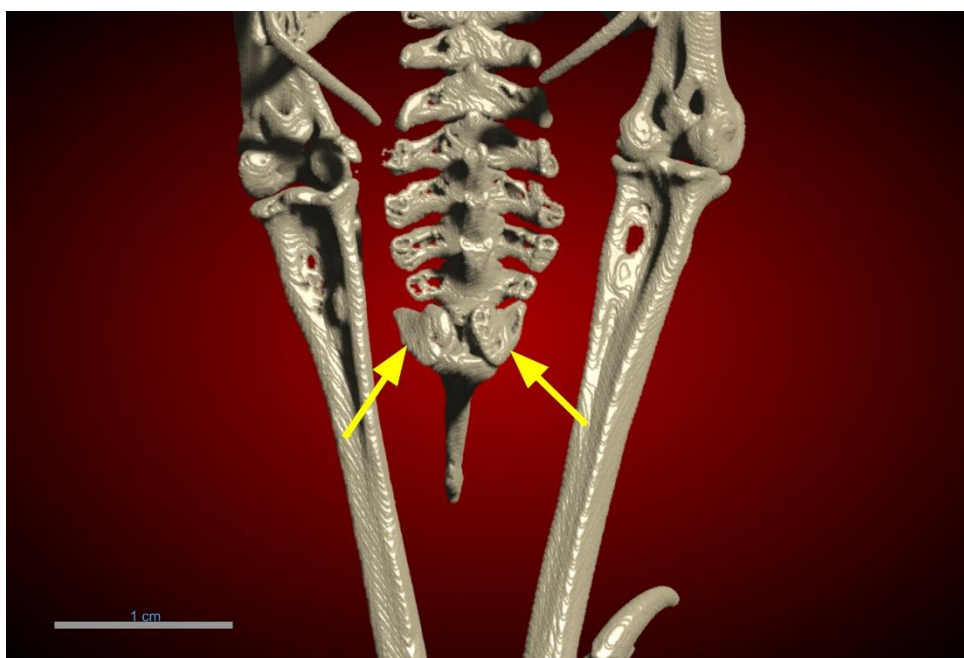


Figure 4.23 Confirmation of the presence of the accessory pygostyle bones in Faucon 5731 at 44  $\mu\text{m}$ .

Despite the numerous training iterations, the metacarpophalangeal sesamoid bones were never visualized on the 88  $\mu\text{m}$  scan (Figure 4.24). Still, their presence was confirmed on the 88  $\mu\text{m}$  2D slice view (Figure 4.25) and the 44  $\mu\text{m}$  segmented 3D image (Figure 4.24), and the slice view.

Due to the challenges in visualization with the 88 $\mu\text{m}$  scan of Faucon 5731, the absence of the *os prominens* (Smith & Smith, 1992a; Zucca & Cooper, 2000) and humeroscapular bone (Smith & Smith, 1992a) was confirmed on the stitched 44  $\mu\text{m}$  scan. These skeletal traits indicate that Faucon 5731 belongs to the Genus *Falco*.

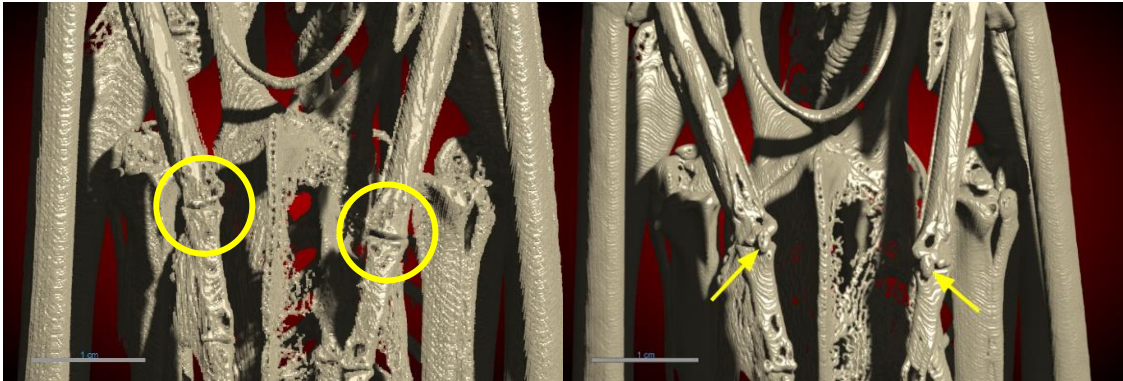


Figure 4.24 Difference in visualization of the metacarpophalangeal sesamoid bone between 88  $\mu\text{m}$  (left) and 44  $\mu\text{m}$  (right) micro-CT scans of Faucon 5731.

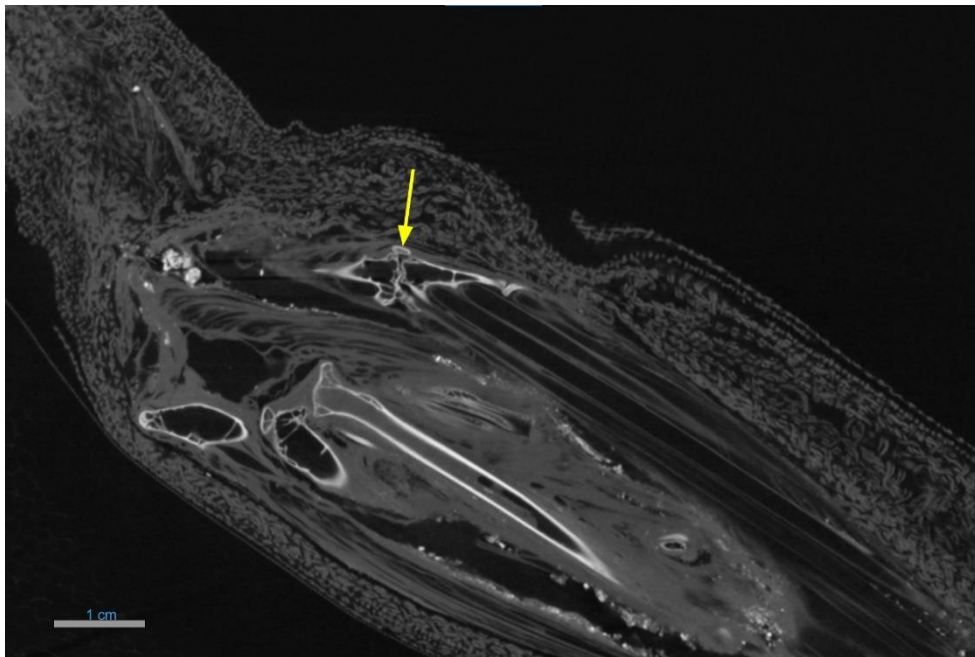


Figure 4.25 Identification of a metacarpophalangeal sesamoid bone on a 2D slice of Faucon 5731, at 88  $\mu\text{m}$ .

Cranial and long bone measurements from Faucon 5731 were compared to the documented falcons in Lortet and Gaillard (1905). Based on the calculated differences, Faucon 5731 is most similar in size to *F. subbuteo* and *F. tinnunculus* (Figure 4.26).

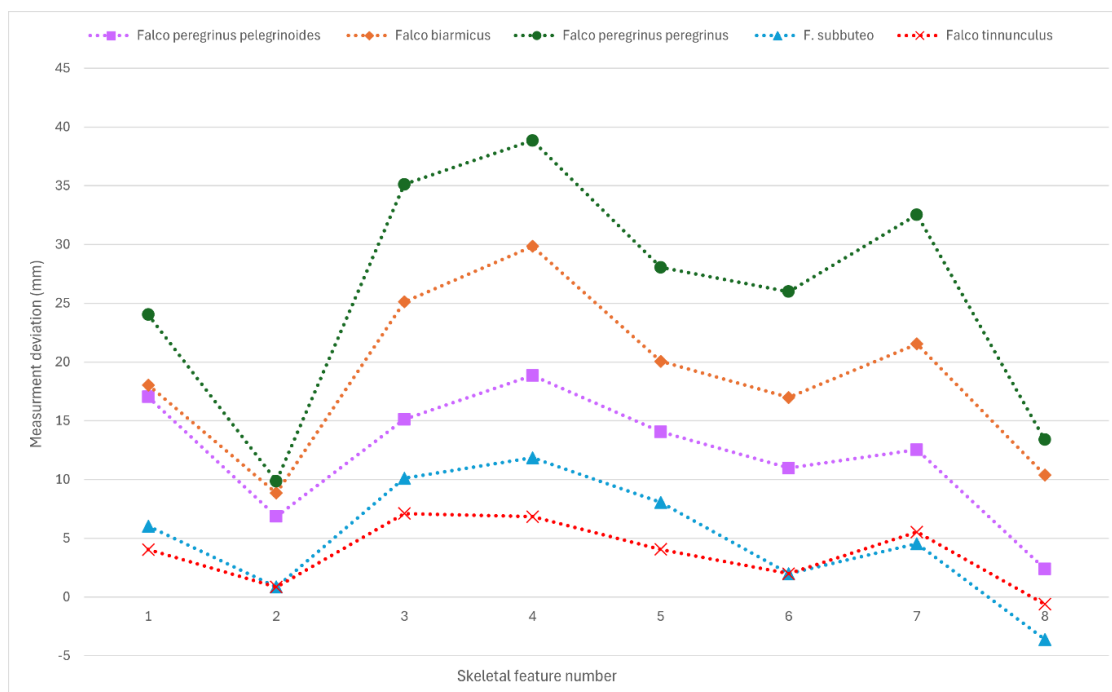


Figure 4.26 Measurement deviation of skeletal features (Table 4.1) of known falcon species (Lortet & Gaillard, 1905) compared to Faucon 5731. Species with the least amount of deviation in skeletal trait measurements have a line running closest to 0 on the y-axis.

Despite the multiple iterations of deep learning algorithm training, the scleral ring had extremely poor visualization on the 88  $\mu\text{m}$  and 44  $\mu\text{m}$  datasets (Figure 4.27). Although identifiable results were not expected at these resolutions (based on the semi-automatically rendered images at low- and middle-resolutions for the Chatham Falcon and Faucon 2726.02), it was expected that we would obtain clear images of the scleral ring structure. This was not the case for Faucon 5731.

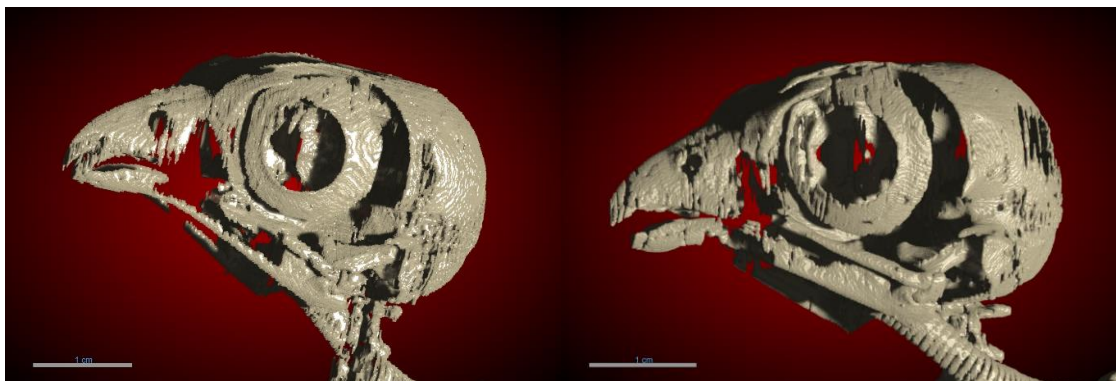


Figure 4.27 3D visualization of the scleral ring for Faucon 5731 at 88  $\mu\text{m}$  (left) and 44  $\mu\text{m}$  (right).

Based on the results from the Chatham Falcon and Faucon 2726.02, there should have been no difficulty in analyzing the scleral ossicle arrangement on the 22  $\mu\text{m}$  scan of Faucon 5731, which should have led to an identification of Faucon 5731 down to the taxonomic *species* level. Once more, the initial algorithm failed to segment a significant piece of the scleral ring (Figure 4.28), and even following multiple iterations of training, the deep learning algorithm could not output a usable image at 22  $\mu\text{m}$  to adequately visualize the number and arrangement of the ossicular scales (Figure 4.28).

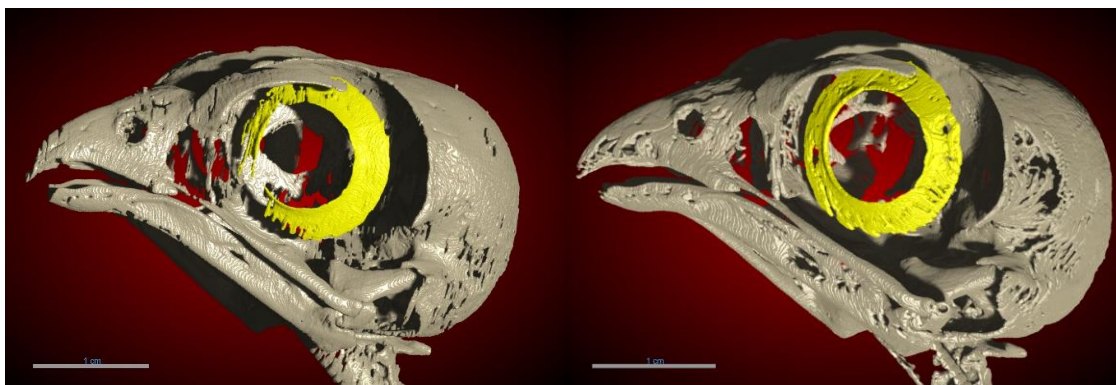


Figure 4.28 Image on the left highlights the scleral ring segmentation prior to retraining of the deep learning algorithm. Image on the right highlights the scleral ring at multiple additional iterations of deep learning training. Despite the more accurately segmented image, the arrangement of ossicles cannot be visualized.

Due to the poor quality of the micro-CT 3D deep learning renderings at all resolutions of Faucon 5731, the 2D image with the maximum intensity projection was created with the highest resolution (22  $\mu\text{m}$ ) scan (Figure 4.29), not the middle resolution (44  $\mu\text{m}$ ), as with the other two falcons. This image confirmed that Faucon 5731 has 14 ossicles, as shown in Figure 4.29. The arrangement was not evident. Based on the size of the mummified

falcon and the presence of 14 ossicles (Lemmrich, 1931), this bird likely also belongs to the species *F. tinnunculus*. In contrast, a bird of similar size with 15 ossicles would belong to *F. subbuteo* (Lemmrich, 1931). Furthermore, while the overlapping arrangement was able to be confirmed on the 2D slices for Faucon 2726.02, there is not enough distinction between the individual ossicle scales to do the same for Faucon 5731 (Figure 4.30).

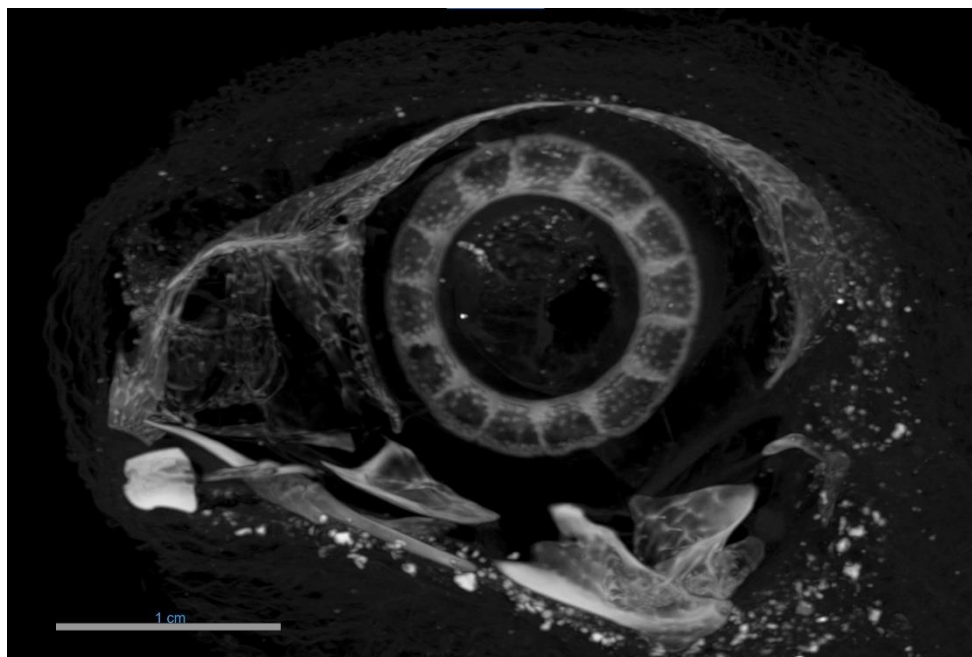


Figure 4.29 2D maximum intensity project view of a scleral ossicle in Faucon 5731 at 22  $\mu\text{m}$ .

Like the other mummified raptors, the clinical CT scan of Faucon 5731, from the IMPACT database (Wade & Nelson, 2015) yielded no usable results regarding the visualization of the accessory pygostyle bones, the metacarpophalangeal sesamoid bones, or the scleral ossicles.

*Such high-resolution scans but poorer visualization – what happened to Faucon 5731?*

Despite obtaining the highest resolution scans of all the falcons in this thesis, the deep learning segmentation was highly challenged in outputting high quality images capable of visualizing intricate skeletal features for Faucon 5731. Despite having a smaller voxel (22  $\mu\text{m}$  versus 25  $\mu\text{m}$ ) size than the other raptor's scans, the quality of the micro-CT scans for Faucon 5731, especially the highest resolution scan, is actually much worse. Figure

4.30 shows a 2D slice of the scleral ossicle for Faucon 5731 and the Chatham Falcon, markedly where the individual ossicles overlap. There is a clear distinction between the

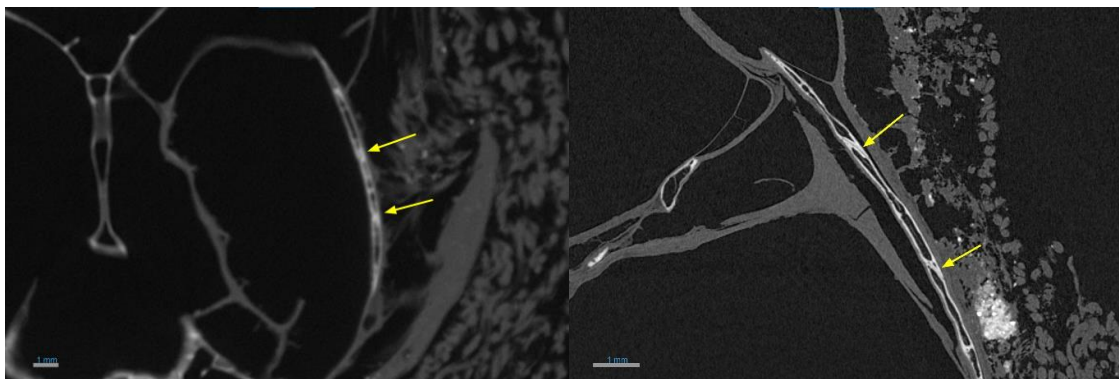


Figure 4.30 Examination of the scleral ossicles at 22  $\mu\text{m}$  in Faucon 5731 (right) and at 25  $\mu\text{m}$  in the Chatham Falcon (left).

ossicles in the scan of the Chatham falcon (good spatial and contrast resolution). In contrast, the distinction between the ossicles in the scan of Faucon 5731 is very poor, almost indistinguishable (poor spatial and contrast resolution). The 2D image of Faucon 5731 looks blurry, while the image of the Chatham Falcon has clean, definable borders despite having a slightly larger voxel size. These clearly defined borders allow for superior image segmentation, whereas the blurry borders in Faucon 5731 scans make differentiating minute features almost impossible. Despite the multiple iterations of training, the deep learning algorithm struggled with the scan, reminding us that a good quality low-resolution scan is better than a bad quality high-resolution scan—comments regarding *why* the quality of scans for Faucon 5731 is so poor will be addressed in Chapter 5.

Due to the poor quality scans of Faucon 5731, a definitive species identification cannot currently be provided, although the bird is part of the Genus *Falco*, likely belonging to the species *tinnunculus*. Congruent with the other mummified raptors present, the presence of the accessory pygostyle bones and the metacarpophalangeal sesamoid bones confirms the Genus; skeletal measurements confirm the bird belongs to the smaller falcons, and the number of ossicles places the bird within the *tinnunculus* species. Unfortunately, the arrangement of the distinguished ossicles cannot be determined at this point to confirm the species level identification further.

### 4.3 Additional observations with micro-CT scans

In addition to the excellent visualization of the skeletal elements for species identification of the Chatham Falcon, Faucon 2726.02, and Faucon 5731 with the micro-CT scans, the ossified tracheal rings for each bird were well visualized (image of each falcon' trachea can be found in Appendix J). Both the Chatham Falcon (Figure J.1) and Faucon 5731 (Figure J.3) present with a twisted trachea and a slight tilt in the position of the cranium, indicative of a twist motion of the neck, prior to death. Comparatively, Faucon 2726.02 (Figure J.2) shows no tracheal twisting.

### 4.4 Redpath Museum ibises

Species identification was not carried out on the ibis mummy bundles, as micro-CT scans revealed the presence of a baby bird (not yet hatched) and no bird at all. Therefore, presented here are some brief results pertaining to the internal contents of the two bundles, which will be used to interpret their cultural and religious significance.

#### 4.4.1 Ibis 2727.01

Micro-CT scanning confirmed the presence of a baby mummified ibis (similar to observations made by Wade et al. [2012] using clinical CT) in bundle 2727.01. The low



Figure 4.31 3D rendering of Ibis 2727.01 at 27  $\mu\text{m}$  with indication of which bones were measured for aging. The bill is also identified, as it clearly differentiates between birds of prey and wading birds, such as ibises.



bone density of the chick hindered the deep learning algorithm in segmenting the skeleton from the desiccated tissue. As a result, the algorithm consistently over- or underestimated the borders of the skeletal features. Nevertheless, the bird's skeleton is visible, particularly the long bones (Figure 4.31). These bones were measured and compared to standards from von den Driesch et al. (2005) in an attempt to age the chick. Results are presented in Table 4.2. The metacarpals were not measured on the chick, as they could not be visualized with enough confidence to ensure the correct bones were being measured (in both 3D and 2D views).

*Table 4.2 The long bone measurement standards and age classification of the Sacred Ibis (retrieved from von den Driesch et al., 2005) are compared to the long bone measurements of Ibis 2727.01.*

| Standards from von den Driesch et al. (2005) | Greatest diaphyseal length (mm) |       |        |                  | Age in days (since hatching) | Age classification |
|--|---------------------------------|-------|--------|------------------|------------------------------|--------------------|
|  | Humerus                         | Femur | Tibia  | Metatarsus II-IV |                              |                    |
|  | 27-30                           | 27-30 | 32-50  | 21-25            | 1-2                          | Neonate            |
|  | 30-50                           | 30-35 | 50-75  | 25-35            | 2-14                         | Infantile          |
|  | 50-70                           | 35-50 | 75-90  | 35-60            | 15-35                        | Infantile-Juvenile |
|  | 70-100                          | 50-60 | 90-120 | 60-85            | 36-50                        | Juvenile           |
|  | > 100                           | > 60  | > 120  | > 85             | 50-70 (90)                   | Subadult           |
|  | > 113                           | > 63  | > 133  | > 90             | > 90                         | Adult              |
|  |                                 |       |        |                  |                              |                    |
| Ibis 2727.02                                 | 17.17                           | 21.10 | 28.30  | N/A              | ?                            | ?                  |

Skeletal measurements of Ibis 2727.01 demonstrate that the chick is smaller than a neonate, suggesting the bird wrapped in the bundle had not yet hatched. There is no evidence of an eggshell on the micro-CT scan, which would appear as a bright white structure due to the similar X-ray attenuation of eggshells and bone (both made primarily of calcium). The tibia is longer than the humerus and femur, similar to the proportional growth trends presented by von den Driesch et al. (2005).

#### 4.4.2 Ibis 2727.02

During the initial scanning process, it was noted that Ibis 2727.02 produced a flat histogram when setting up the scan parameters. This indicated that the density of any object(s) within the bundle was uniform. This was confirmed when examining the initial 2D X-ray when no visible internal elements could be identified. The skeletal elements

were also extremely difficult to see on the initial projections of Ibis 2727.01. Therefore, we (Shumeng Jia, Dr. Salah Brika, and I) continued scanning despite the poor initial results. 3D renderings and a slice analysis revealed no skeletal elements from any animal inside the wrapped bundle (Figure 4.32). Instead, a clay- or mud-like substance is

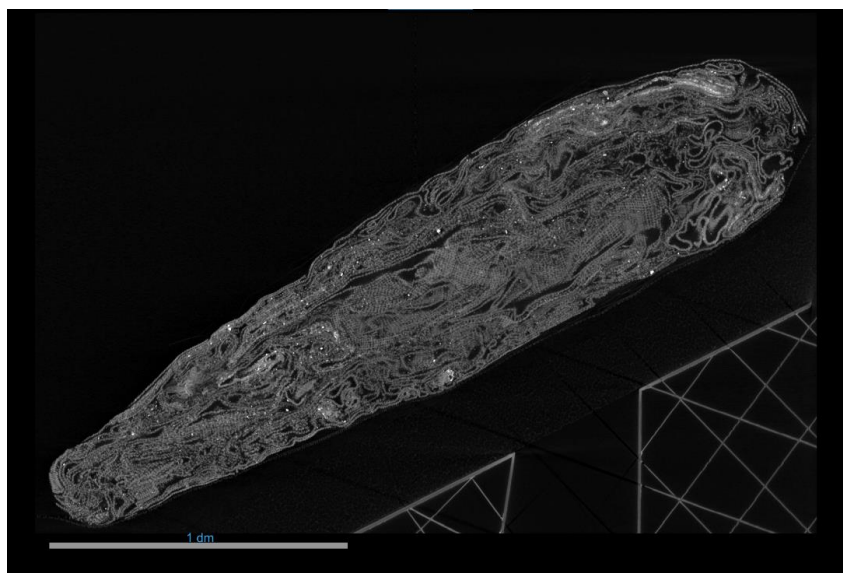


*Figure 4.32 Lateral slice view of Ibis 2727.02 revealing intricately wrapped linens but no avian skeletal elements.*

wrapped around the linens used for mummification and shaped into a conical bundle. The conical shape is representative of a mummified ibis (cf. Atherton-Woolham et al., 2019; McKnight, 2020). At this point, I cannot determine if the clay/mud was intentionally added to maintain the conical shape of the bundle or picked up from the surrounding environment in the embalming house. It does appear that the clay/mud is more highly concentrated at the “head” end of the bundle, possibly indicating an intent to maintain shape. This could be confirmed with additional testing, such as volume thickness mapping analyses, which is unfortunately outside the scope of this thesis.

## 4.5 IMPACT and the CMH Falcon 1

Similar to the clinical CT scans examined of the other mummified falcons, the resolution was not great enough on the clinical CT scan of the CMH Falcon 1 to visualize minute skeletal details that could have been used for species identification. This was the case for the 2D slice analysis and the 3D rendering. However, comparing the cranial and long bone measurements taken on low-resolution micro-CT scans and the clinical CT reveals a

low percentage error between the *real* (micro-CT) and *estimated* (clinical CT) measurements. Including all but one measurement, the comparative differences had an error rate of less than 5% for all skeletal elements (Table 4.3).

Table 4.3 Calculations of the percent error of long bone measurements taken on low resolution micro-CT scans compared to clinical CT scans for the Chatham Falcon, Faucon 2726.02, and Faucon 5731.

| Species           | Skeletal Element | Micro-CT measurement (mm) | Clinical CT measurements (mm) | Percentage error (%) |
|-------------------|------------------|---------------------------|-------------------------------|----------------------|
| Chatham Falcon    | Length of head   | 45.03                     | 43.11                         | 4.26                 |
|                   | Breadth of head  | 28.86                     | 28.81                         | 0.17                 |
|                   | Humerus          | 50.27                     | 49.72                         | 1.09                 |
|                   | Ulna             | 57.98                     | 57.43                         | 0.95                 |
|                   | Metacarpus       | 31.93                     | 32.10                         | -0.53                |
|                   | Femur            | 42.64                     | 41.37                         | 2.98                 |
|                   | Tibiotarsus      | 55.02                     | 54.50                         | 0.95                 |
|                   | Tarsometatarsus  | 38.67                     | 37.96                         | 1.84                 |
| RP Faucon 2726.02 | Length of head   |                           |                               |                      |
|                   | Breadth of head  | 31.77                     | 29.75                         | -6.79*               |
|                   | Humerus          | 52.96                     | 50.98                         | -3.88                |
|                   | Ulna             | 62.77                     | 62.67                         | -0.16                |
|                   | Metacarpus       | 33.84                     | 34.41                         | 1.66                 |
|                   | Femur            | 44.71                     | 45.23                         | 1.15                 |
|                   | Tibiotarsus      | 61.66                     | 61.32                         | -0.55                |
|                   | Tarsometatarsus  | 41.16                     | 42.09                         | 2.21                 |
| RP Faucon 5731    | Length of head   | 45.25                     | 43.97                         | -2.91                |
|                   | Breadth of head  | 29.92                     | 29.15                         | -2.64                |
|                   | Humerus          | 48.16                     | 48.89                         | 1.49                 |
|                   | Ulna             | 58.55                     | 56.16                         | -4.26                |
|                   | Metacarpus       | 30.68                     | 30.95                         | 0.87                 |
|                   | Femur            | 43.24                     | 43.02                         | -0.51                |
|                   | Tibiotarsus      | 56.52                     | 54.47                         | -3.76                |
|                   | Tarsometatarsus  | 37.53                     | 38.61                         | 2.80                 |

\*Indicates the singular measurement with an error rate greater than 5%.

In addition to the error measurement, least squares linear regression graphs (Figure 4.33) and  $R^2$  values were used to interpret the goodness of fit of the data to a regression model. Differences between the estimated and real values should be small and unbiased. Linear regression models for the Chatham Falcon, Faucon 2726.02, and Faucon 5731 were all

unbiased (Appendix K) and had high  $R^2$  values, with slope values close to 1.0 (Figure 4.33), reflecting a strong correlation between the two datasets for each observed bird.

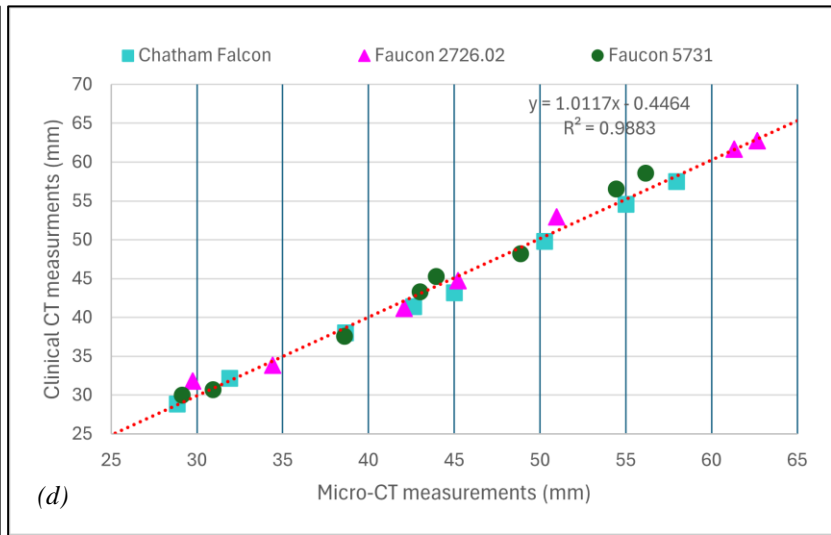
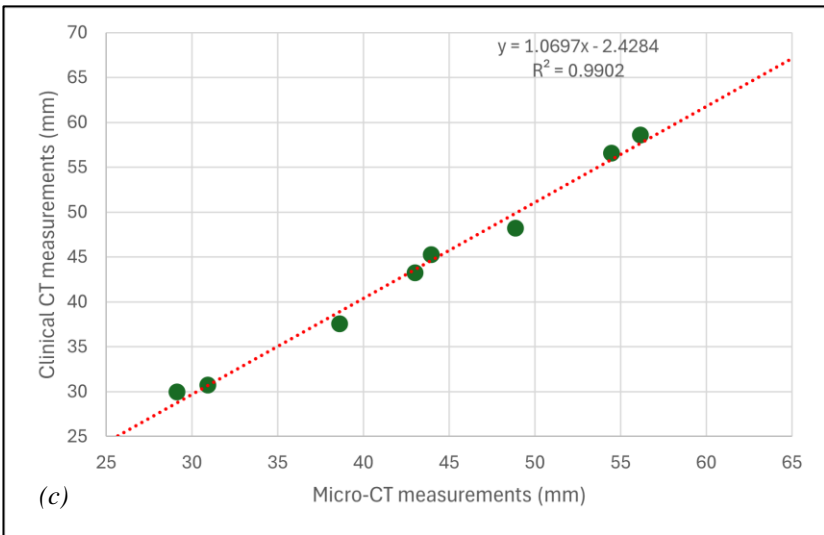
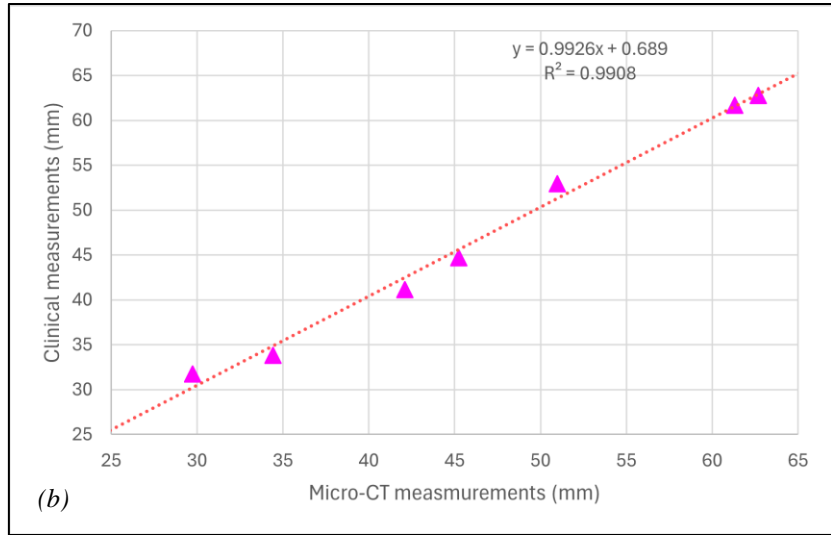
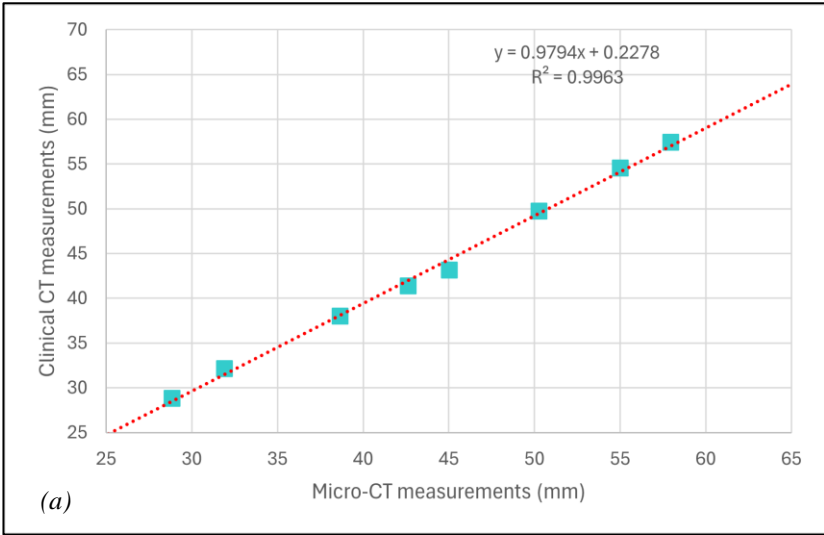


Figure 4.33 Linear regression comparing micro-CT measurements to clinical CT measurements of the Chatham Falcon (a), Faucon 2726.02 (b), and Faucon 5731 (c). Graph D presents all falcon data combined.

Working under the assumption that the measurements taken from the clinical CT scans are reasonably accurate, the same cranial and long bone measurements were taken of the CMH Falcon 1, and differences compared to documented raptors from Lortet and Gaillard (1905) were plotted in Figure 4.34.

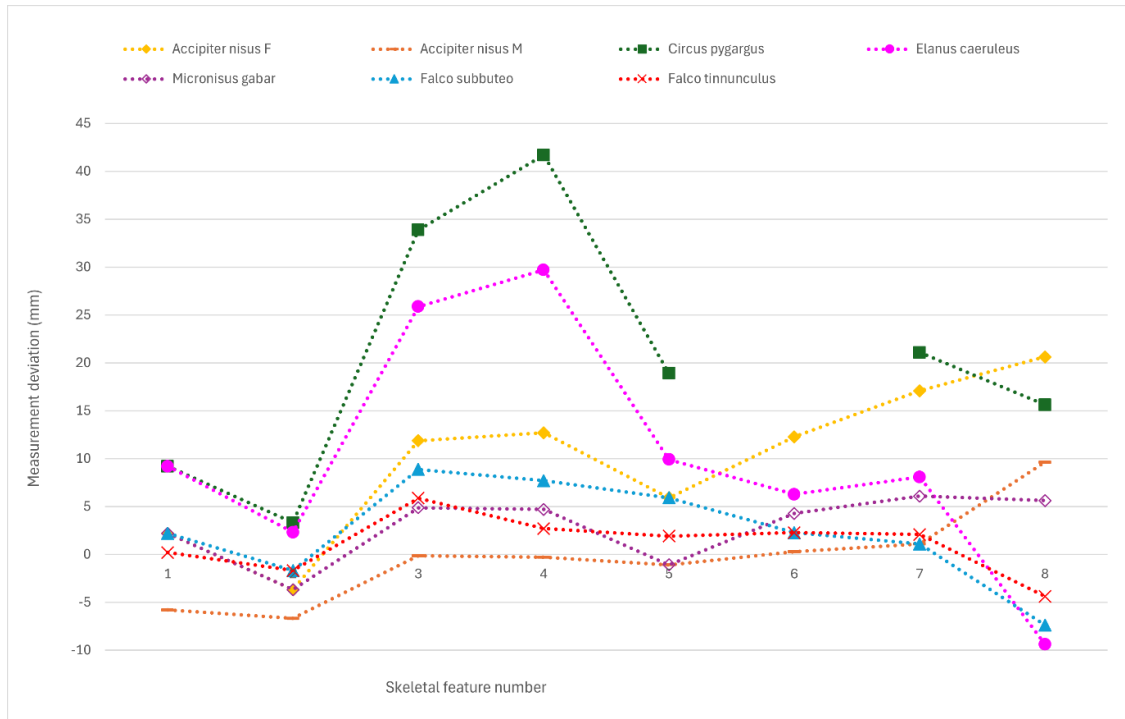
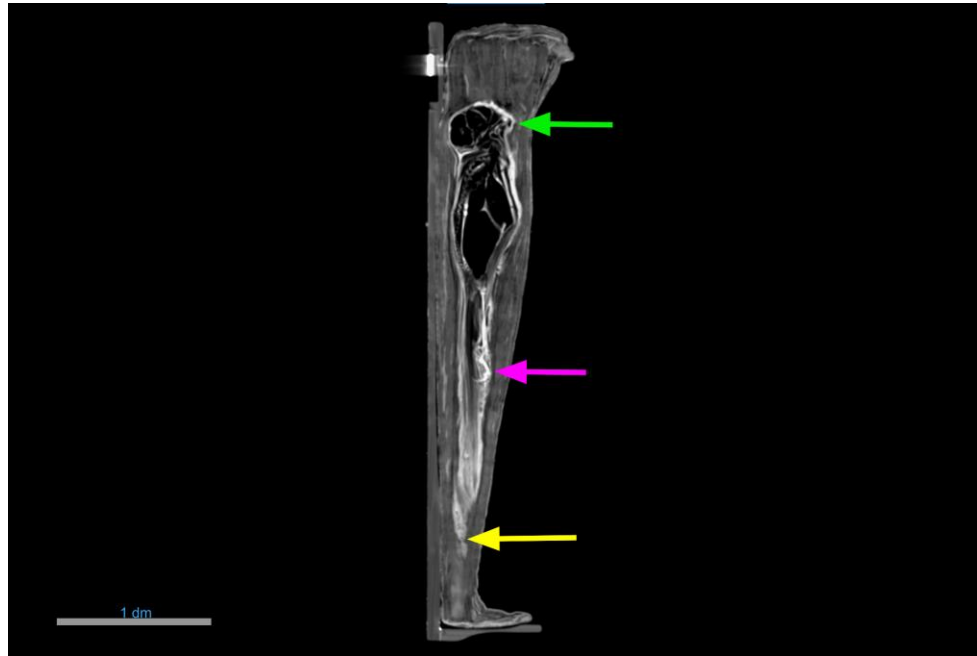


Figure 4.34 Measurement deviation of known raptor species (Lortet & Gaillard, 1905) compared to CMH Falcon 1. Species with the least deviation in skeletal trait measurements have a line running closest to the y-axis.

Figure 4.34 showcases one of the greatest challenges in working with avian skeletal remains, using only skeletal measurements and proportions. From the above graph, CMH Falcon 1 may belong to any of the following species: *Accipiter nisus* (male), *Micronisus gabar*, *Falco subbuteo*, or *Falco tinnunculus*. If we could visualize certain features (or the lack thereof) like metacarpophalangeal sesamoid bones or accessory pygostyle bones, the likely species identification could be cut in half. Yet, with the currently available data, there is a mess of similarly sized species that cannot be untangled.

It is also noteworthy that there is a significant size discrepancy between the mummified bird and the coffin in which it is encased. The CMH Falcon 1 is considerably smaller

than its coffin; specifically, the bird's physical head does not reach the head of the coffin, nor do its feet and tail feathers extend to the foot of the coffin (Figure 4.35).



*Figure 4.35 2D sagittal slice view of CMH Falcon 1 showing the size difference between the mummified bird and its coffin. Green arrow indicates the head of the bird; pink arrow indicates the talons; yellow arrow indicates tail feathers and mummification linens.*

## 4.6 Summary

This thesis explores the applicability of various resolution CT scans to studying mummified birds from ancient Egypt. Deep learning image segmentation, in combination with 2D image modalities (when necessary), was used to examine the internal skeletal remains at multiple resolutions to determine the species of bird each bundle belonged to. While there were significant challenges with the deep learning segmentation, the results indicate that a significant portion species identification can be completed using low-resolution micro-CT scans ( $\sim 110\text{-}100\ \mu\text{m}$ ), and high-resolution micro-CT scans ( $\sim 25\ \mu\text{m}$ ), are only necessary for visualizing the scleral ossicle. Surprisingly, although clinical CT scans do not have good 3D visualization, it was determined they are relatively reliable for cranial and long bone measurements, which can be used to narrow down possible candidate species. The following chapter will discuss the species identification results, placing them within the broader context of ancient Egyptian religion. It will also

comment on the methodological applications of CT scanning and deep learning image processing to the non-destructive study of mummified birds.



## Chapter 5

### 5 Discussion

This thesis sought to answer the following questions: (1) Using Computed Tomography scans, what is the minimal resolution required to effectively visualize diagnostic skeletal traits for the most precise taxa identification of birds within ancient Egyptian mummy bundles?; (2) To what level of specificity can taxa be identified within an avian bundle?; and (3) What comments can be made regarding the exploitation of certain birds in ancient Egypt and their religious importance?

This chapter will discuss the findings presented in Chapter 4 in relation to the posed research questions. It will begin with the skeletal observations and measurements of the mummified birds of prey (Chatham Falcon, Faucon 2726.02, Faucon 5731, and the CMH Falcon 1) and placing the proposed species identification within the larger context of ancient Egyptian religion and society, thus addressing question 3. Next, this chapter will comment on the findings from the mummified ibis bundles, placing them in the greater context and also addressing question 3. Finally, this discussion will conclude with an examination of the pros and cons of using various resolution CT scans in the non-destructive study of avian mummy bundles, referring to the primary research questions in this thesis, questions 1 and 2. The Chapter will conclude with some thoughts on deep learning image segmentation. Although deep learning was not a central theme of this investigation, the method both hindered and aided the research, thus meriting a brief discussion.

#### 5.1 Chatham Falcon, Faucon 2726.02, and Faucon 5731

From the examination of the skeletal features and measurements, the mummified bird from the Chatham-Kent Museum and Faucon 2726.02 from the Redpath Museum (and likely Faucon 5731 from the Redpath Museum) have been identified as most probably belonging to the species *Falco tinnuculus*. Colloquially referred to as the common kestrel, this bird played a significant role in ancient Egyptian mythology as a symbol of the goddess Isis (Houlihan & Goodman, 1986). Isis, one of the most important deities in

the Egyptian pantheon, was worshipped as a goddess of fertility, motherhood, healing, and magic (Hart, 2005; Shorter, 1978). Isis is also the symbolic mother of the king, as her genealogy depicts her as the Mother of Horus (Hart, 2005; Shorter, 1978). The goddess was seen as the essential link between deities and royalty, with the pharaoh/king regarded as the living embodiment of Horus on Egypt's throne (Hart, 2005). The Pyramid Texts describe the ruler drinking divine milk from the breasts of his mother, Isis. This imagery is depicted in numerous statuettes of Isis seated on a throne, nursing the young Horus on her lap (Hart, 2005).

Isis intended to raise her son Horus in secret so he could eventually avenge his father's (Osiris) assassination (Hart, 2005). This protection of Horus from danger is often referenced in magical texts for curing children's ailments, such as scorpion bites or burns. Isis' great magic was invoked to aid children as if they were Horus themselves (Hart, 2005). For example, a spell against burns was recited over a mixture of human milk, gum, and cat hairs to be applied to the injured child. The spell invoked to Isis assured that power from her saliva and urine would relieve the pain (Hart, 2005).

Additionally, Isis was a principal mourner in the Osiris myth (see Mojsov, 2005) and, by extension, became a principal mourner for the deceased. The piercing shrieks of birds of prey were believed to represent her wailing cries – she is even referred to as a “screecher” (along with goddess Nephthys) in Pyramid Texts (Scalf, 2012). As protectors of the deceased, Isis and Nephthys were often depicted as women with outstretched bird wings on the corners of the New Kingdom royal sarcophagi (Scalf., 2012), such as those seen on the inner coffin of

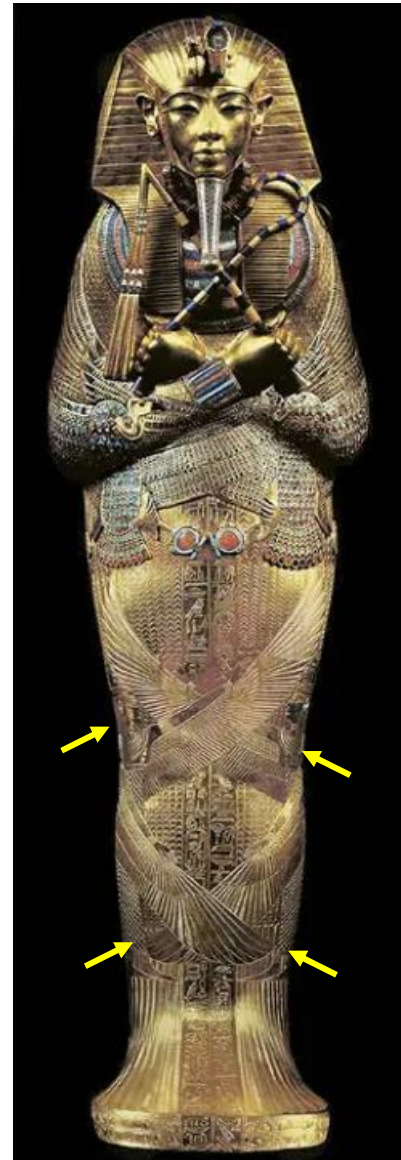


*Figure 5.1 Arrows indicate the wings of Nephthys and Isis wrapped around the inner coffin of Tutankhamun. Image retrieved from <https://www.thecollector.com/ancient-egyptian-goddess-isis/>.*

King Tutankhamun (Figure 5.1), pharaoh during the 18<sup>th</sup> Dynasty Egypt in the New Kingdom (Redford, 2001).

While the birds of ancient Egypt, especially falcons and hawks, are typically associated with solar gods like Ra and Horus, Isis also played an important role in Egyptian society and was revered for her abilities to cast spells, protect from harm and ill fortune, invoke fertility, both for humans and the Nile flood plains, and in assisting Egyptians in their journey to the afterlife (Pinch, 2004). It is unsurprising that falcon remains, particularly those of *F. tinnunculus*, are reportedly the most commonly mummified birds of prey in various catacombs throughout Egypt (Baillel-LeSeur, 2019; Rowland et al., 2013; von den Driesch et al., 2005).

Rowland et al. (2013) report that 84% of the skeletal elements recovered at the Sacred Falcon Necropolis of Djedhor at Quensa belong to the Family Falconidae, with 30% of those remains belonging to the Genus *Falco*. Although 30% may not seem significant, it is notable considering the next most commonly represented Genus within the Falconidae Family, Accipiter, accounts for only 3% of the faunal assemblage at this site (Rowland et al., 2013).

Similarly, von den Driesch et al. (2005) and Baillel-LeSuer (2019) report that *F. tinnunculus* accounts for the majority of the diurnal birds of prey recovered from the Tuna el-Gebel site in Egypt, making up approximately 43% of the avian remains. Once again, the next most commonly mummified species at this site was *A. nisus*, accounting for only 8% of the avian faunal assemblage. The bias toward *F. tinnunculus* could be explained through access to the animal, as the common kestrel was and still is a common breeding resident throughout the Nile Delta and Valley (Goodman & Meininger, 1989), whereas *A. nisus* was a migratory bird, found in Egypt during the winter months (Goodman & Meininger, 1989), thus not accessible for hunting and husbandry year-round.

By far, the most commonly depicted falcon in Egyptian art is the Horus Falcon. The artwork suggests possible species associated with the Horus deity, *F. eleonora*, *F. biarmicus*, and *F. peregrinus* (Houlihan & Goodman, 1986). Important to note is artwork

depicting the Horus Falcon and the goddess Isis in kestrel form is so detailed the species can be differentiated in hieroglyphic inscriptions and artwork. Kestrel falcons are painted light brown with a reddish tint (characteristics of female kestrels). Detailed markings on the upper part of the tail are painted in dark brown (Houlihan & Goodman, 1986). Horus Falcons were also painted in a much wider range of colours, with a white underbelly and an emphasis on the moustachial streak (Houlihan & Goodman, 1986). This makes it difficult to associate Horus with a particular species of bird, while Isis is clearly associated with a specific species, the kestrel, as seen in the hieroglyphic depictions.



*Figure 5.2 Comparison of modern common kestrels (female – right; male – left) to hieroglyph from the tomb of Sennedjem, Deir el-Medina, showing the goddess Isis in kestrel form (middle). Modern bird images retrieved from [https://en.wikipedia.org/wiki/Common\\_kestrel](https://en.wikipedia.org/wiki/Common_kestrel); hieroglyphic image retrieved from Houlihan & Goodman (1989, p. 45).*

Additionally, hieroglyphic depictions of Isis even include the correct colouring for female kestrels (brown head), whereas a male would have a lighter brown/grey head (Figure 5.2). This is appropriate as Isis is a goddess, not a god. Detailed and accurate bird artwork demonstrates ancient Egyptians' intense observations of the natural world, down to the sex of specific bird species. It allows for modern-day conclusions regarding their ability to differentiate between species and actively mummify specific bird species as offerings to specific deities.

The Chatham Falcon and Faucon 5731 both presented with broken necks (Appendix J), which supports the notion that these mummified birds were votive offerings, as opposed to being pets or sacred animals, which were generally mummified after dying of natural

causes (Ikram, 2015b). While there is no evidence of neck-snapping or cranial trauma in Faucon 2726.02, it is possible that Faucon 2726.02 died of natural causes or was dipped, alive, directly into hot resin. However, if the bird were placed directly in hot resin, we would expect to see black powder (disintegrated flesh) and skeletal disarticulation (cf. Ikram, 2015b), which are not present in any of the mummified birds studied here. Additionally, evidence of dense natron artifacts on the 3D renderings confirms that the birds were desiccated prior to burial. It is probable that remnants of natron were accidentally included in the bundle simply through contact with mummification materials in the embalming houses. However, the micro-CT scans show clear evidence of desiccated tissue, further suggesting the use of natron for mummification. These findings, along with the radiocarbon date for Faucon 2726.02 (52BC-24AD), confirm that these mummies were votive offerings produced during the late Ptolemaic to early Roman periods, during the height of the animal mummy industry.

## 5.2 CMH Falcon 1

The clinical CT scan of the CMH Falcon 1 clearly showcased the challenge of working with clinical CTs and avian remains. The poor spatial and contrast resolution of the original data makes for poor visualization all around, in turn, creating inadequate 3D deep learning segmented images, which cannot be used for clear skeletal visualization. However, by comparing the skeletal measurements on micro-CT and clinical CT scans, this thesis found that long bone and cranial measurements from clinical CTs are accurate. Therefore, based on the size of the bird and the respective skeletal elements, the CMH Falcon 1 is believed to belong to one of the smaller diurnal raptor species, possibly *Accipiter nisus* (male), *Micronisus gabar*, *Falco subbuteo*, or *Falco tinnunculus*.

Unlike the other raptors studied here, the CMH Falcon 1 is encased in a detailed coffin (Appendix A). In Chapter 4, it was noted that the interred bird is significantly smaller than the coffin in which it is encased. This is particularly important as the bird's coffin is carved and painted to resemble the sky god Horus. However, Houlihan and Goodman (1986) document that the larger falcon species, *F. eleonora*, *F. biarmicus*, or *F. peregrinus*, were typically depicted in artwork and hieroglyphic inscriptions representing the god Horus. The coffin provides a unique insight into the cultural significance of the

votive mummy; however, its large size would also hinder future investigations with a micro-CT scanner. A low-resolution micro-CT scan would be required to narrow down species identification. Although capturing the coffin in such a scan is unnecessary, the likelihood of fitting it into a micro-CT scanner and would require careful consideration of positioning (possibly mounting the mummy on an angle) within the scanner, as was the case with the Redpath Museum mummies in this study.

Based on the literature review, coffins encasing mummified birds seem to be quite rare, as I could find no mention of a studied avian mummy similar to the CMH Falcon 1. Elaborate coffins representing falcon deities such as Osiris, Sokar, and Horus have been discovered, but they typically contain mummified grains and sand. “Corn mummies” are believed to have been offerings to the god Osiris, as he represented rebirth and life after death, and the mummified corn symbolized germination and the possibility of new life (The Metropolitan Museum of Art, n.d.). Wooden coffins for animals were seen more commonly associated with mummified pets, like the mummified gazelle found in the tomb of Isetemkheb D, from the Third Intermediate Period (Ikram, 2005). Perhaps the wooden coffin suggests that CMH Falcon 1 dates to an older period in ancient Egypt or is representative of a more cherished animal rather than a strictly votive offering. However, it is also important to consider that a broad range of decorative features was employed when creating avian mummies (see Atherton-Woolham et al., 2019), and perhaps the wooden coffin is simply indicative of economic differences in votive mummy production.

The CMH Falcon 1 highlights the need for improved methods of species identification. Without identifying the bird species, even down to the Genus level, we can offer minimal social, cultural, and religious commentary regarding this bird's role in ancient Egypt. This particular mummy, however, may offer insights into an internal versus external dichotomy, where the internal elements may not accurately represent the external appearance. The external coffin is significantly larger compared to the interred bird, and this discrepancy would not be visible to a local or pilgrim purchasing the mummy. It is intriguing to consider that a votive offering, created with such detail and care, could contain remains that do not match its outward image. Alternatively, the interred bird

might have had another purpose in Egyptian society, one that remains unknown due to the limitations of our current 3D imaging methods and lack of original context.

### 5.3 Ibis 2727.01

Skeletal measurements of Ibis 2727.01 indicate that the bird had not yet hatched. At many famous sites in Egypt, it is common to recover eggs and nest material, suggesting that ancient Egyptians had regular access to nesting and breeding birds. von den Driesch et al. (2005) suggest that the servants of the ibis cult were responsible for collecting any and all dead birds and any part of them from the sacred lands before bringing the remains to the embalmers. What is interesting about Ibis 2727.01 is that this bird does not seem to be at an age where it has hatched, yet there is no evidence of an eggshell anywhere in the bundle. I propose two interpretations of these results. The first is that the species of bird encased inside the bundle does not belong to the Sacred Ibis (*Threskiornis aethiopicus*) species and belongs to a much smaller species of ibis, the Glossy Ibis (*Plegadis falcinellus*). This interpretation would be difficult to prove, as the contrast is lacking within the scan of such a tiny chick (due to the uncalcified bones), thus making 3D visualization extremely difficult. Therefore, rendering a 3D image adequate enough to carry out species identification is near impossible. The cartonnage on the front of the bundle (Figure 3.3) depicts a Sacred Ibis; therefore, an investigation of the true internal contents versus the external representation would yield valuable insights into votive religious practices in ancient Egypt.

The second interpretation suggests that this chick was removed from its egg prior to hatching. The height of the animal mummy industry created such a high demand for faunal remains for mummification that the industry likely outpaced the natural breeding habits of all animals, particularly birds (Cornelius et al., 2012). From the large abundance of eggshell and nest remains found in catacombs, it is clear that cult farmers had regular access to chicks and eggs (von den Driesch et al., 2005), meaning this unhatched egg could have been easily taken from a nest for mummification. Moreover, reports of ibis remains in different embryonic stages have been uncovered at sites such as Hermopolis Magna (von den Driesch et al., 2005). Therefore, it is highly probable that this chick was taken from a nest, removed from its shell, and mummified. The young age of the bird and

lack of skeletal development would also account for the lack of density in the skeletal structures and, therefore, the poor resolution contrast between skeleton, tissue, wrappings, and background noise.

In a study of this mummified ibis, Wade et al. (2012) observed on a clinical CT scan that Ibis 2727.01 appeared to have some form of grain placed within its eviscerated body cavity (Wade et al., 2012). Placing foodstuffs in mummified birds was considered a provision for the afterlife (Wade et al., 2012), similar to victual offerings for humans (Ikram, 2005a). However, the micro-CT scan of Ibis 2727.01 reveals that the bird is packed with an unknown substance (Appendix K), which is clearly not grains, as previously thought. It is possible that this substance was intended to represent food in the afterlife. Alternatively, the material may have been used to help maintain the shape of the small chick throughout the mummification process and to help maintain the shape of the conical bundle.

#### 5.4 Ibis 2727.02

Micro-CT scanning of Ibis 2727.02 revealed no internal skeletal elements, confirming that this votive offering is, in fact, a pseudo-mummy. Pseudo-mummies are votive offerings that externally look like they contain animals (i.e. correct shape, markings on the bandages). Upon investigation of the literature, it has been revealed that the internal contents of many pseudo mummies contain rags, twigs, plant material, mud, pottery, bones from a completely different animal, or human bones (Cornelius et al., 2012). Ibis 2727.02, for example, only contains mummified linens, carefully folded and wrapped to create a conical shaped bundle. Other examples of these pseudo-mummies include a mummy bundle at the Sunderland Museum, appearing to be an offering of a jackal to the god Anubis. In reality, radiographic images revealed the internal contents to be a human humerus (McKnight et al., 2015). Another example is a votive mummy with falcon decorations dedicated to the god Horus, which was found to contain an ibis, not a falcon (Cornelius et al., 2012). Pseudo-mummies were extremely common; some research projects revealed that one-third of studied animal mummy collections are pseudo (McKnight & Atherton-Woolham, 2016), and others revealed that half of the studied mummies are pseudo (McKnight, 2020). Notably, the study by McKnight (2020)



revealed that *true* votive mummies—those containing *any* animal remains—account for only half of the mummies studied. Among these true mummies, only half contained a complete skeleton, while the other half had partial remains or co-mingled skeletons. Thus, it can be estimated that only a quarter of votive offerings contained complete skeletal remains (McKnight, 2020).

While the reason for creating these pseudo-mummies is unknown, it has been attributed to a few factors, including the inability to catch wild animals, over-exploitation of animals, scarce resources, or simply creating cheaper votive offerings (Cornelius et al., 2012). Overexploitation of resources seems particularly plausible, as millions of mummified birds have been and continue to be recovered from catacombs all over Egypt (Houlihan & Goodman, 1986; Wade et al., 2011; Wasef et al., 2019). Modern DNA data (Wasef et al., 2019) and insights from raptor behavioural specialists (Enderson et al., 1998; Holland, 2007) reveal that breeding raptors in captivity was unsuccessful and that bird husbandry in ancient Egypt likely involved herding migratory, wild birds (Baillel-LeSeur, 2019). Consequently, to meet the increasing demand from growing animal cults and religious instabilities, pseudo mummies were produced to supplement the true ones. A systematic undertaking of radiocarbon dating, and chronological ordering of true and pseudo mummies could contribute to the discussion regarding resource exploitation over time, however, this has yet to occur.

## 5.5 The effects of resolution

The significance of resolution in 3D imaging cannot be overstated, as it directly impacts the quality and usability of acquired data. Yet, higher resolution scans generate larger datasets, which require more storage and processing power. Balancing resolution with available resources is often a key consideration and challenge when applying 3D imaging techniques in bioarchaeology. Therefore, this thesis sought to examine the usability of lower resolution 3D imaging techniques in identifying avian species. It would be redundant to say that high-resolution micro-CT scans are better for species identification. In an ideal world, we would only work with high-resolution, or stitched mid-resolution micro-CT scans. Although, a poor quality, high-resolution scan is not better than a good quality low-resolution scan, as evidenced by the data from Faucon 5731.

### 5.5.1 Why were the scans of Faucon 5731 so poor?

The high-resolution micro-CT scans of Faucon 5731 yielded the poorest spatial resolution of all the datasets acquired for this research. Several compounding factors likely contributed to these poor quality scans. Firstly, Faucon 5731 was the first animal mummy scanned by a new team of researchers and me in Montreal. Our loan with the Redpath Museum only allowed us access to each mummy for one day, which, combined with the inexperience of the new team and the unfamiliar equipment, likely resulted in a high rate of human error during the scan acquisition.

Additionally, the sliding stage on which the Redpath Museum mummies were mounted likely contributed to some scanning errors. A custom-made stage was created to scan the mummies at the required angle, allowing the object to slide in and out of the micro-CT mount to adjust the center of rotation (Figures A.1, A.12, A.7, and A.17). While the stand was reasonably stable, even the slightest movement at high resolutions can significantly impact the scan. In addition, all scans taken on the Yxlon FF35 CT scanner, including those of Faucon 5731, were reconstructed automatically, with the Yxlon Reconstruction Workspace 2206.4.0. While time saving, the automatic reconstruction does not allow for human inspection of the acquired data prior to generating a 3D image. For this reason, we opted for manual reconstructions with the Nikon scanner to provide an extra "check" before the 3D image was reconstructed, specifically ensuring no movement occurred during the scan, therefore ensuring that the quality of the 3D rendering was not compromised. While this manual check does not correct for any movement, it does allow for researchers to decide whether or not the specimen should be remounted and rescanned, prior to 3D reconstruction, therefore, ensuring a good quality scan is acquired.

### 5.5.2 Micro-CT scans

Before processing this thesis data, I hypothesized that the stitched mid-resolution (~50-40  $\mu\text{m}$ ) micro-CT scans would be the most beneficial for species identification. These scans combine multiple smaller scans to create a detailed composite image, theoretically providing a balance between resolution and field of view. However, the stitching protocol requires significant time and computing power, which might not be necessary for

effective species identification. If mid-resolution micro-CT scans were the sole scans acquired for analysis, the scans can be examined independently, without stitching, to look for specific skeletal features, however, they would require the stitching and image recognition protocol to accurately measure some skeletal elements. In this thesis, I opted to complete measurements on the low-resolution ( $\sim 110\text{-}85\ \mu\text{m}$ ) micro-CT scans, as the stitched scans occasionally had misalignments, which could impact the already flawed measurement methods employed.

Upon analyzing the data, I found that low-resolution ( $\sim 110\text{-}85\ \mu\text{m}$ ) micro-CT scans of the Chatham Falcon and Faucon 2726.02 offered satisfactory visualization of almost all skeletal elements, with the exception of the scleral ossicles. These low-resolution scans were able to capture the overall morphology and structure of the skeletons, providing a clear view of the major and minor bones and their configurations. This level of detail is typically sufficient for identifying the species of the bird. Further, using low-resolution micro-CT scans to train the deep learning algorithm proved efficient when applying the trained algorithm to higher resolution ( $\sim 30\text{-}20\ \mu\text{m}$ ) scans. The low-resolution micro-CT scans were purposely used for the training protocol because they had the poorest resolution compared to the higher resolution scans, meaning that, the algorithm was able to differentiate between different identified data classes at the lowest resolution, and easily able to extrapolate this learning to higher resolution scans. Training the algorithm in this manner allowed for good image segmentation on the low-resolution scans and even better on the higher resolution scans.

To enhance the accuracy of species identification, incorporating a single high-resolution ( $\sim 20\ \mu\text{m}$ ) scan of the cranium would be highly effective. The cranium contains many distinguishing features used in avian taxonomy, such as the shape and structure of the beak and scleral ossicle. High-resolution scans can capture these fine details more clearly than low-resolution scans, ensuring that critical traits are not missed.

Therefore, micro-CT scanning should be employed using a combined approach—low-resolution scans for the whole skeleton and high-resolution scans for the cranium—thus allowing for the most efficient and effective strategy in analyzing mummified avian

bundles. This method minimizes the need for extensive stitching and reduces computational demands while still providing sufficient detail for accurate species identification. By obtaining both low-resolution and high-resolution micro-CT<sup>8</sup> scans, avian skeletal remains can be studied using advanced 3D imaging processing alongside 2D slice views for optimal skeletal analysis. This approach saves time and resources while ensuring accurate visualization of all necessary skeletal traits, thereby enhancing the reliability of the identification process.

It is worth noting, however, that certain micro-CT scanners may not be able to capture both the low-resolution volume of the entire mummy, and the high-resolution volume of the head. The Nikon and Yxlon scanners used here are large cabinet-style scanners that have a great deal of flexibility in terms of the size of the object that can be captured. Our research team was initially going to acquire high-resolution scans of the mummified animals with the Zeiss Xradia Versa 250 at McGill University. This machine captures extremely high-resolution (voxel size <25  $\mu\text{m}$ ), but small volume scans, so we quickly realized that scanning the mummies in this unit would require extensive data acquisition time (a single scan can take upwards of 16 hours to complete) and processing to stitch together multiple scans to capture any area of the mummified animal. Thus, the specific scanning protocol chosen for future scans will, in part, depend on the configuration of the available scanner.

### 5.5.3 Clinical CT

The greatest challenge in employing clinical CT scanners for studying avian bundles is poor spatial resolution. With clinical CT scanners, the resolution is set to balance the need for quick scanning (to reduce X-ray exposure to a patient) and the level of detail required for a medical diagnosis. Clinical CT scanners typically have a spatial resolution

---

<sup>8</sup> This project was part of a larger research grant on image processing with AI technology. Obtaining one low-resolution and one high-resolution scan enables new forms of image processing, such as training a CNN to resolve high-resolution details from a low-resolution scan. This technique helps mitigate the need for multiple micro-CT scans and would enable possible species identification at lower resolutions by applying the trained CNN to upsample high-resolution data from the low-resolution scan.

of approximately 0.5-1.0mm, meaning they can distinguish between features at least 0.5mm large and 0.5mm apart (Kalender, 2006). For smaller objects, which many of the bird bones are (specifically the cranial and sesamoid bones), the resolution on a clinical CT scan is insufficient to capture small details, leading to a loss of critical details. Moreover, lower spatial resolution results in blurred edges and poor definitions of boundaries. Large voxels representing small objects create an averaging partial volume effect on the fine details, meaning that the scanner essentially blends adjacent small structures into a single voxel. This significantly hinders employing an image segmentation technique such as deep learning. This is why structures like the sesamoid bones, the accessory pygostyle bones, and the scleral bones all appear to be blended with the surrounding bones and desiccated tissues.

That said, not all hope is lost for clinical CT scans. Results from this thesis show that skeletal measurements are still remarkably accurate on the 2D slice projections, as evidenced by the low error rate between measurements taken on the micro-CT and clinical CT scans. The high  $R^2$  value found when comparing clinical and low-resolution micro-CT scans indicates that the variability between measurements is minimal. Therefore, clinical CT scans can serve as a good starting point for species identification. At the very least, they can help narrow down the size of a mummified bird. The tomial tooth is also visible on clinical CTs and could be used to help narrow down the genera of a mummified bird in future studies. Other features seen on the micro-CT scans, such as the twisting of the trachea, were not visible on the clinical CT scans. Therefore, these scans have a limited ability to be used in discussing aspects such as cause of death.

#### 5.5.4 Dental CBCT

The dental CBCT scan results for the Chatham Falcon were among the most disappointing. This disappointment is not due to the lack of commentary on the applicability of dental CBCT scans for species identification but rather the significant challenges faced in acquiring the scan. The goal of including a dental CBCT scan was to assess the visualization of small skeletal elements with a resolution lower than micro-CTs but significantly higher than clinical CTs. Given the unfavourable results from clinical CT scans, it was hoped that the dental CBCT would provide a high enough resolution 3D

rendering that could still be useful to zooarchaeologists for species identification. Dental and clinical CT scanners are more accessible and cost-effective than micro-CTs. However, a significant challenge was mounting the Chatham Falcon within the dental CBCT scanner and aligning it with the pre-programmed software designed to align teeth. Unlike micro-CT or clinical scans, where the initial X-ray projection is a clear image of the object, the Sirona Orthophos XG 3D scanner used in this thesis included an overlay of a human mouth (which helps radiologists align a patient's face properly). The reality is that medical imaging equipment is designed and built to make the lives of clinicians and medical professionals easier and to make medical diagnoses more accurate and time-efficient. These tools are typically not designed with research purposes in mind. Eventually, we were able to adequately mount the Chatham Falcon, therefore, the cropped nature of the dataset must have resulted during the data processing and storage process. A final challenge worth noting regarding dental CBCT scanners is the small volume ( $\sim 8\text{cm}^3$ ) they are able to capture. A fair amount of avian mummies are smaller in size, however, this small field of view would make capturing images of mummies such as the CMH Falcon 1 difficult (possibly impossible), even if researchers were to combine dental CBCT scanning with the image stitching protocol.

With these challenges in mind, dental CBCT can still provide helpful information, as there is a clear distinction between long bones and background noise on our acquired scan. Other preliminary multi-resolution studies on *tsantsa* (shrunken heads) and medieval manuscripts show promise using this modality of imaging (A. Nelson, personal communication, March 14, 2024) therefore, its application in studying mummified animals should show promise too. The question remains: To what extent can we see skeletal variation on these scans? If sufficient visualization can be achieved with dental CBCT scanners, perhaps more traditional methods of identifying avian remains can be employed on long bone and cranial analysis. Using the scleral ossicle will no doubt not be feasible with dental CBCT; however, other methods should be explored with this scanning technique. If dental CBCT scans yield good visualization, researchers will not have to consistently rely on high-resolution scanners and supercomputers to store and process raw data.

## 5.6 Tangential thoughts on deep learning

Deep learning image processing is an extremely powerful tool, though it is not without its faults. Like all machine learning tools, deep learning relies heavily on human input for training. The human provided training data is processed through multiple layers of convolution, ultimately creating a “black box” effect. This means that what is being learned from the manually segmented data becomes unclear. This effect makes it difficult to pinpoint what exactly went wrong with the segmentations of Faucon 5731. In this thesis, the deep learning algorithm repeatedly missed data for Faucon 5731, necessitating multiple training iterations to produce better images. Although the missing data was verified using the 2D slice views, the primary goal of a trained deep learning algorithm is to expedite the data processing component of research, thereby providing more time for analysis.

We might not have noticed their absence following segmentation if we had not been specifically looking for small features such as the sesamoid bones. This raises concerns about other potential data omissions that could hinder future analysis or lead to misidentifications, as initially happened when I mistakenly believed Faucon 5731 belonged to *A. nisus* due to the absence of *Falco* skeletal elements. I remain a strong advocate for deep learning methods, particularly for projects involving extensive data processing over extended periods. However, using multiple image processing methods as checks is crucial to ensure data is processed efficiently and accurately. In clinical radiology, examining 2D and 3D views of CT data is standard practice and should, therefore, be employed in all CT data processing.

## Chapter 6

### 6 Conclusion

This chapter will summarize the key research findings presented in this thesis and provide some closing thoughts regarding the posed research questions. Additionally, it will address some limitations of this study and broader studies of mummified animals and suggest potential avenues for future research.

#### 6.1 Summary

This thesis undertook an examination of mummified avian bundles through multi-resolution computed tomographic techniques. The results demonstrate the applicability of studying avian bundles with 3D imaging techniques. Specifically, low-resolution (~110-80  $\mu\text{m}$ ) micro-CT scans coupled with deep learning image segmentation had good visualization of identifiable, post cranial skeletal elements for the Chatham Falcon, Faucon 2726.02, and Faucon 5731. If the scleral ossicle method is needed to narrow down a species identification, a high-resolution (~30-20  $\mu\text{m}$ ) micro-CT scan is needed to accurately visualize the overlapping structure of scales with deep learning, although alternative 2D visualization at 50  $\mu\text{m}$  could be sufficient for visualizing the number of ossicular scales, just not necessarily the arrangement. Therefore, micro-CT scanning can be effectively used in species identification with one low resolution and one high resolution scan of a single bundle. The middle resolution and 3D image stitching protocol is not necessary when employing only deep learning methods of image segmentation. However, if the object cannot be captured fully in the micro-CT scanners' lowest resolution field of view, two middle-resolution scans stitched together, should suffice for species identification, provided that multiple image processing modalities are employed. The middle-resolution scans and stitching are by far the most time consuming, as they require more time setting up the initial scan to ensure clear overlap features are present for stitching, additional time aligning the scans to be stitched, and a significant amount of processing power to combine the multiple datasets. As previously noted, the size of the micro-CT scanner can greatly limit the ability to obtain low-resolution, full-body scans and is a crucial factor in determining the appropriate resolution for scans needed for



analysis. When possible, for micro-CT scanning, I would recommend one low-resolution (110-85  $\mu\text{m}$ ) and one high-resolution ( $\sim 25 \mu\text{m}$ ) scan, as they provide sufficient information for species identification.

Unfortunately, the clinical and dental CBCT scans did not yield results capable of identifying birds to a specific taxonomic designation. While clinical CT scans can measure long bones and provide some useful data, they fall short in visualizing detailed skeletal elements necessary for precise species identification. Clinical CT scans lack the resolution needed to identify avian remains down to the species or even Genus level. Therefore, while they are a helpful starting point, they cannot replace the detailed analysis provided by micro-CT scans for accurate species identification.

The goal of this thesis was not to provide a universal method for identifying avian remains in mummified bundles. The reality is that identifying osteological elements from birds, even with the highest resolution scans and the best zooarchaeologists, will always remain a challenge because our current methods, relying on a handling the physical remains, cannot be easily translated to the digital world. Instead, identifying digital avian remains relies on creative and innovative methods that likely are not used by practicing zooarchaeologists. There is no single answer to how to identify avian skeletons – each scan is case specific – using a combination of traditional zooarchaeological techniques and veterinary literature, this thesis shows species identification is possible with micro-CT scans.

With the osteological methods used in this thesis, three of the raptors studied were identified as belonging to the species *F. tinnunculus* based on the presence of the metacarpophalangeal sesamoid bones, accessory pygostyle bones, skeletal measurements, and the scleral ossicle arrangement. Using this identification, the three falcons were discussed regarding their importance to the goddess Isis, who represented power, magic, fertility, and healing in ancient Egypt.

In addition to the studied falcons, two conical bundles were briefly studied, expected to reveal the remains of mummified ibises. Micro-CT scanning revealed that one bundle possessed a young chick, likely unhatched, and one was a pseudo mummy, containing no

skeletal elements. The presence of an unhatched chick indicates the inclusion of even the smallest and least developed specimens, while the pseudo mummy underscores the lengths to which embalmers would go to meet the pilgrim demand, including the creation of mummies without any skeletal elements.

In summary, the results of this thesis underscore the viability of studying avian mummies through non-destructive imaging techniques. The study not only reaffirmed the challenges associated with using clinical CT scans, as previously identified by McKnight et al. (2022) but also showcased the feasibility of employing low-resolution (~110-80  $\mu\text{m}$ ) micro-CT scanning for species identification purposes. By successfully identifying the avian species, this research was able to contextualize the studied mummies within the broader cultural and religious landscape from which they originated. These findings highlight the potential of non-destructive imaging methods in unravelling the mysteries surrounding ancient avian husbandry and mummification practices, shedding light on their significance in ancient civilizations.

## 6.2 Limitations

As with any research, this project has limitations that must be acknowledged. A central limitation of this thesis pertains to the mounting procedures for the Redpath Museum mummies. The challenges with the mounting procedure and subsequent scanning was highlighted with the micro-CT scans of Faucon 5731. Ideally, the mummies would have been mounted vertically, ensuring that the X-rays penetrated the object uniformly as it rotated. This vertical alignment would have provided a more consistent and accurate scan by maintaining equal penetration across all angles. The use of a moving stand permitted the required positioning but introduced potential for movement during scanning. Even the slightest movement can significantly impact the quality of high-resolution scans. In a perfect setup, a fixed stand that did not require adjustments to align the mummy with the beam path would have been used. This would have minimized the risk of movement, thereby enhancing the clarity and precision of the scans. By eliminating the need for a moving stand, we could have achieved greater stability during the scanning process. This stability is crucial, as any movement, however minimal, can cause blurring and distortions in the final images, compromising the accuracy of the data. To mitigate these

issues in future research, it is essential to use equipment and mounting techniques that ensure maximum stability and uniform X-ray penetration. This approach will improve the overall quality and reliability of high-resolution scans, leading to more accurate analyses and interpretations.

The zoo-osteological methods employed in this thesis have limitations when applied to new studies of avian bundles. These methods assumed fully intact skeletons, but the reality is that many bundles contain missing elements, co-mingled elements, different species, or no elements whatsoever (Atherton-Woolham & McKnight, 2014). This significantly hinders the effectiveness of species identification methods and digital imaging techniques. Many avian bundles from archaeological contexts are incomplete, with key skeletal parts absent due to preservation conditions, past handling, or ancient mummification practices. This absence of crucial bones can prevent accurate identification, as osteological methods often rely on the presence of specific skeletal features unique to particular species. Secondly, the presence of co-mingled elements will complicate the identification process. Bundles may contain bones from multiple individuals or even different species, adding additional challenges to digital species identification, possibly leading to the misidentification of skeletal elements or no identification at all.

### 6.3 Future directions

The study and application of 3D imaging methods to identify species of animal mummies is still very much in its infancy. There are only a select few studies that have undertaken mass studies of animal mummies (e.g., McKnight & Atherton-Woolham, 2016). Therefore, the future directions this research could take are endless. Species identification, with non-destructive methods, remains at the forefront of animal mummy studies as research seeks to understand the relationships between animals and the ancient Egyptian worldview. Recognizing that this area will remain a significant focus in the future, I will instead present a few innovative research ideas that have the potential to yield noteworthy discoveries, while contributing to new methods of species identification.

A unique aspect of avian morphology that warrants investigation is long bone ratios in relation to flight styles. The use of long bone measurements alone for species identification is problematic due to significant overlap in the size of different species and sexual dimorphism within species. However, studies of wing element proportions (i.e., feather length compared to total arm length [humerus, ulna, and manus summed]) can help discriminate between flight styles of living birds and be used to categorize specific species of birds (Wang et al., 2011). In the scans of our mummified birds, both micro-CT and clinical CT, the feathers could be visualized, as they were completely preserved. Therefore, there is a unique opportunity to study feathers and limb-bone proportions with mummified birds and discuss species identification in relation to flight style. Intra-limb proportional differences are also clearly comparable using clinical and micro-CT scans (as seen in Figures 4.3, 4.16, 4.26, and 4.34), and could be another avenue of exploration, without including an analysis of feathers, in discussing flight and movement styles. This approach could be particularly advantageous when using lower resolution scans, as only measurements are required, and this thesis demonstrates that such measurements are relatively accurate. This research would, of course, require bundles that contain complete remains (no partial or co-mingled); regardless, it is still worth exploring.

Another avenue worth exploring would be incorporating eggshells and embryonic development studies into animal mummy analyses. This thesis suggests that Ibis 2727.01 was removed from its shell, prior to hatching, possibly demonstrating the overexploitation of resources to sustain the high demand for animal mummies. These observations could only be confirmed through a comparative study with embryonic studies, preferably with multiple bird species. Additionally, during my time in Montreal, Dr. Reznikov and I discussed the possibility of studying the pore structure of interred and mummified eggshells as a source of species identification. Microscopic analyses of eggshells using high-resolution micro-CT scans and a scanning electron microscope have the potential to reveal unique results regarding the microscopic, calcified structures responsible for eggshell formation (Buss et al., 2023). Dr. Reznikov proposes that these structures are species-specific, and therefore, eggshells could be used to understand species selection in ancient Egypt. As previously mentioned, the study of animal

mummies necessitates innovative approaches that are not typically used by zooarchaeologists, and these methods could offer a promising solution.

Finally, the application of deep learning image segmentation should be explored in greater detail. While the algorithm used in this thesis had some challenges, the push towards computer-guided data processing significantly decreases the time required to process scans, thus allowing for more time dedicated to interpreting results. Imagine a study like the *Ancient Egyptian Animal Bio Bank* project, where over 800 animals were studied through various non-destructive techniques (McKnight & Atherton-Woolham, 2016), where 3D images could be semi-automatically rendered, with minimal human intervention. The applications of those 3D images would be endless, from the creation of a digital skeletal database to 3D printing of avian remains for teaching and museums to research projects that could comment on broader interpretations, owing to the large quantity of data available. Perhaps *F. tinnunculus* was the most commonly mummified bird during the height of the animal cults (Baillet-LeSeur, 2019; Rowland et al., 2013; von den Driesch et al., 2005), but this could only be confirmed through the study of massive amounts of bundles. Although high-resolution scans and deep learning training require large computing and processing power, the creation of smaller ROIs (i.e., of just the skeletal objects) through segmentation results in smaller datasets that can be more easily transferred and shared between researchers and public education institutions.

## 6.4 Conclusion

The use of 3D scanning techniques, particularly micro-CT scans, allows for species identification down to the taxonomic level of species. In identifying the species of birds, mummified bundles can be placed back within their original religious context.

Additionally, observations regarding the role animals played in society and how they were exploited can be made. The birds studied in this thesis show just a small insight into what can be accomplished through non-destructive imaging studies, and although we got lucky with complete skeletal remains, using similar methods to study co-mingled and partial skeletal bundles has the potential to also contribute to ideas regarding religious significance, cultural implications, resource exploitation, and economic factors. As the species identification of animal mummies is still very much in its infancy, and the use of

3D imaging technology has only recently been employed, there is a plethora of information yet to come from studying these avian bundles.

## References

- Adams, J., 2015. Imaging animal mummies: history and techniques. In McKnight, L., & Atherton-Woolham, S. (Eds.), *Gifts for the Gods: Ancient Egyptian Animal Mummies and the British* (pp.68-71). Liverpool University Press.
- Alaica, A. K. (2018). Partial and complete deposits and depictions: Social zooarchaeology, iconography and the role of animals in Late Moche Peru. *Journal of Archaeological Science: Reports*, 20, 864–872.  
<https://doi.org/10.1016/j.jasrep.2018.02.002>
- Allen, J., & Hill, M. (2018, January). *Egypt in the Late Period (ca. 664–332 B.C.)* The Met’s Heilbrunn Timeline of Art History.  
[https://www.metmuseum.org/toah/hd/lapd/hd\\_lapd.htm](https://www.metmuseum.org/toah/hd/lapd/hd_lapd.htm)
- Assmann, J. (2005). *Death and Salvation in Ancient Egypt*. Cornell University Press.
- Atherton-Woolham, S. D., & McKnight, L. M. (2014). Post-mortem restorations in ancient Egyptian animal mummies using imaging. *Papers on Anthropology*, 23, 9–18.  
<https://doi.org/10.12697/poa.2014.23.1.01>
- Atherton-Woolham, S. D., McKnight, L. M., Price, C., & Adams, J. (2019). Imaging the gods: Animal mummies from Tomb 3508, North Saqqara, Egypt. *Antiquity*, 93(367), 128–143. <https://doi.org/10.15184/aqy.2018.189>
- Backus, S. B., Sustaita, D., Odhner, L. U., & Dollar, A. M. (2015). Mechanical analysis of avian feet: Multiarticular muscles in grasping and perching. *Royal Society Open Science*, 2(2), 140350. <https://doi.org/10.1098/rsos.140350>
- Bailleul-LeSuer, R. (2019). From Egyptology to Ornithology The Cults of Sacred Falcons and The Musee des Confluences’ Raptor Mummies. In S. Porcier, S. Ikram, & S. Pasquali (Eds.), *Creatures of Earth, Water, and Sky Essays on Animals in Ancient Egypt and Nubia*. Sidestone Press.
- Bartosiewicz, L., & Gal, E. (2007). Sample size and taxonomic richness in mammalian and avian bone assemblages from archaeological sites. *Archeometriai Műhely*, 37–44.
- Beason, C. (2021). *Evaluating Cranial Nonmetric Traits in Mummies from Pachacamac, Peru: The Utility of Semi-Automated Image Segmentation in Paleoradiography* (Publication No. 8221) [Master’s thesis, University of Western Ontario]. Electronic Thesis and Dissertation Repository. <https://ir.lib.uwo.ca/etd/8221>
- Bellairs, A., & Jenkin, C. (1960). The Skeleton of Birds. In A. Marshal (Ed.), *Biology and Comparative Physiology of Birds I* (Vol. 1, pp. 241–300). Academic Press.
- Beucher, S. (1992). The Watershed Transformation Applied to Image Segmentation. *Scanning Microscopy*, (1992)6, 299-314.

Bezryadin, S., Bourov, P., & Ilinih, D. (2007). Brightness calculation in digital image processing. *International symposium on technologies for digital photo fulfillment, 1*, 10-15. Society for Imaging Science and Technology.

Bodziony-Szweda, K. (2010). The Great Hunt. Some remarks on symbolic and ritual significance of the hunt and chase motifs in Egyptian art. *Studies in Ancient Art and Civilization, 14*, 55–66.

Bommas, M. (2012). Isis, Osiris, and Serapis. In C. Riggs (Ed.), *The Oxford Handbook of Roman Egypt*. Oxford University Press. (pp. 419–435).

Botelho, J. G., Smith-Paredes, D., & Vargas, A. O. (2015). Altriciality and the Evolution of Toe Orientation in Birds. *Evolutionary Biology, 42*, 502-510.  
<https://doi.org/10.1007/s11692-015-9334-7>

Brevick, P. (2019). *Feeding the Pharaohs: A Discussion and Object Study of Fowl Victual Mummies from Ancient Egypt*. [Master's thesis, University of Memphis]. Electronic Theses and Dissertations. <https://digitalcommons.memphis.edu/etd/1998>

Budge, E. A. W. (2013). *From Fetish To God Ancient Egypt*. Routledge.  
<https://doi.org/10.4324/9781315810539>

Burghardt, A. J., Link, T. M., & Majumdar, S. (2011). High-resolution Computed Tomography for Clinical Imaging of Bone Microarchitecture. *Clinical Orthopaedics and Related Research®*, 469(8), 2179–2193. <https://doi.org/10.1007/s11999-010-1766-x>

Buss, D. J., Reznikov, N., & McKee, M. D. (2023). Attaching organic fibers to mineral: The case of the avian eggshell. *iScience*, 26(12), 108425.  
<https://doi.org/10.1016/j.isci.2023.108425>

Capponi, L. (2016). *Augustan Egypt the creation of a Roman province*. Routledge.

Carnegie Museum of Natural History. (n.d.). *Egypt and the Nile*. Carnegie Museum of Natural History. <https://carnegiemnh.org/egypt-and-the-nile/>

Chatham-Kent Museum. (2024). provenance\_943\_5. [Unpublished document]. Chatham-Kent Museum.

Choy, G., Khalilzadeh, O., Michalski, M., Do, S., Samir, A. E., Pinykh, O. S., Geis, J. R., Pandharipande, P. V., Brink, J. A., & Dreyer, K. J. (2018). Current applications and future impact of machine learning in Radiology. *Radiology*, 288(2), 318–328.  
<https://doi.org/10.1148/radiol.2018171820>

Ciliberti, R., Tosi, A., & Licata, M. (2020). Feline mummies as a fertilizer: Criticisms on the destruction of archaeozoological remains during the 19th century. *Archaeofauna*, 29, 129–135.



Clark, D. P., & Badea, C. T. (2021). Advances in micro-CT imaging of small animals. *Physica Medica*, 88, 175–192. <https://doi.org/10.1016/j.ejmp.2021.07.005>

Cohen, A., & Serjeantson, D. (1996). *A manual for the identification of bird bones from archaeological sites revised edition*. Archetype Publications Ltd.

Comet Technologies Canada. (2024). *About Us*. Dragonfly – a brand of Comet. <https://www.theobjects.com/company/index.html>

Comet Yxlon. (n.d.). *FF35 CT*. Comet Yxlon. <https://yxlon.comet.tech/en/products/ff35-ct>

Conlogue, G. J., Nelson, A. J., & Lurie, A. G. (2020). Computed Tomography (CT), Multi-Detector Computed Tomography (MDCT), Micro-CT, and Cone Beam Computed Tomography (CBCT). In R. G. Beckett & G. J. Conlogue (Eds.), *Advances in Paleoimaging Applications for Paleoanthropology, Bioarchaeology, Forensics, and Cultural Artifacts* (pp. 111–275). CRC Press.

Cornelius, I., Swanepoel, L. C., Plessis, A. du, & Slabbert, R. (2012). Looking inside votive creatures: Computed tomography (CT) scanning of ancient Egyptian mummified animals in Iziko Museums of South Africa: a preliminary report. *Akroterion*, 57, 129–149.

Csermely, D., & Rossi, O. (2006). Bird claws and bird of prey talons: Where is the difference? *Italian Journal of Zoology*, 73(1), 43–53. <https://doi.org/10.1080/11250000500502368>

de Vartavan, C. (1990). Contaminated plant-foods from the tomb of Tutankhamun: A new interpretive system. *Journal of Archaeological Science*, 17(5), 473–494. [https://doi.org/10.1016/0305-4403\(90\)90029-5](https://doi.org/10.1016/0305-4403(90)90029-5)

Dragonfly. (2020a). *Analyzing Connected Components*. <https://www.theobjects.com/dragonfly/dfhelp/2022-1/Content/Specialized%20Workflows/Connected%20Components%20Analysis/Analyzing%20Connected%20Components.htm>

Dragonfly. (2020b). *Dragonfly Daily 17 Image Segmentation with Deep Learning in Dragonfly (2020)*. [Video file]. YouTube. <https://www.youtube.com/watch?v=8g7uT7ZiOjk>

Dragonfly. (2020c). *Stitching of multiple data sets in Dragonfly*. [Video file]. YouTube. <https://www.youtube.com/watch?v=WdFavt2rjVA>

Dragonfly. (2020d). *Working in Slab Mode*. [https://www.theobjects.com/dragonfly/dfhelp/3-5/Content/04\\_Working%20with%20Image%20Data/Working%20in%20Slab%20Mode.htm](https://www.theobjects.com/dragonfly/dfhelp/3-5/Content/04_Working%20with%20Image%20Data/Working%20in%20Slab%20Mode.htm)

Dragonfly. (2024). *Deep Learning FAQs*. <https://www.theobjects.com/dragonfly/deep-learningfaq.html>

du Plessis, A., Broeckhoven, C., Guelpa, A., & le Roux, S. G. (2017). Laboratory x-ray micro-computed tomography: A user guideline for biological samples. *GigaScience*, 6(6), gix027. <https://doi.org/10.1093/gigascience/gix027>

du Toit, C. J., Chinsamy, A., & Cunningham, S. J. (2022). Comparative morphology and soft tissue histology of the remote-touch bill-tip organ in three ibis species of differing foraging ecology. *Journal of Anatomy*, 241(4), 966–980. <https://doi.org/10.1111/joa.13734>

Ejsmond, W., & Przewłocki, Ł. (2014). Some Remarks on Cat Mummies in Light of the Examination of Artefacts from the National Museum in Warsaw Collection. *Studies in Ancient Art and Civilisation*, 18, 239–258. <https://doi.org/10.12797/SAAC.18.2014.18.15>

Enderson, J.H., C.M. White & U. Banasch. (1998). Captive Breeding and Release of Peregrines (*Falco peregrinus*) in North America. In R.D. Chancellor, B.U. Meyburg & J.J. Ferrero (Eds), *Holarctic Birds of Prey. Proceedings of an International Conference* (pp. 437-444). ADENEX & WWGBP.

*Falcon-form case containing a corn mummy: Ptolemaic period*. The Metropolitan Museum of Art. (n.d.). <https://www.metmuseum.org/art/collection/search/551556>

Farmelo, G. (1995). The Discovery of X-rays. *Scientific American*, 273(5), 86–91.

Fowler, D. W., Freedman, E. A., & Scannella, J. B. (2009). Predatory functional morphology in Raptors: Interdigital variation in talon size is related to prey restraint and immobilisation technique. *PLoS ONE*, 4(11). <https://doi.org/10.1371/journal.pone.0007999>

Franzmeier, H. (2022). The End of New Kingdom Egypt. In M. Gehler, R. Rollinger, & P. Strobl (Eds.), *The End of Empires* (pp. 97–120). Springer Fachmedien. [https://doi.org/10.1007/978-3-658-36876-0\\_5](https://doi.org/10.1007/978-3-658-36876-0_5)

Franz-Odendaal, T. A. (2008). Toward understanding the development of scleral ossicles in the chicken, *Gallus gallus*. *Developmental Dynamics*, 237(11), 3240-3251. <https://doi.org/10.1002/dvdy.21754>

Franz-Odendaal, T. A. (2018). Skeletons of the Eye: An Evolutionary and Developmental Perspective. *The Anatomical Record*. 303(1), 100-109. <https://doi.org/10.1002/ar.24043>

Franz-Odendaal, T. A., & Hall, B. K. (2006). Skeletal elements within teleost eyes and a discussion of their homology. *Journal of Morphology*, 267(11), 1326–1337. <https://doi.org/10.1002/jmor.10479>

Frey, G. D. (2014). Basic CT parameters. *American Journal of Roentgenology*, 203(2), 126–127. <https://doi.org/10.2214/AJR.13.10994>

Friedman, S. N., Nguyen, N., Nelson, A. J., Granton, P. V., MacDonald, D. B., Hibbert, R., Holdsworth, D. W., & Cunningham, I. A. (2012). Computed Tomography (CT) bone segmentation of an Ancient Egyptian mummy a comparison of automated and semiautomated threshold and dual-energy techniques. *Journal of Computer Assisted Tomography*, 36(5), 616–622.

Frost, J. (2024, February 26). *How to interpret R-squared in regression analysis*. Statistics By Jim. <https://statisticsbyjim.com/regression/interpret-r-squared-regression/>

Gardner, J. C., Garvin, G., Nelson, A. J., Vascotto, G., & Conlogue, G. (2004). Paleoradiology in mummy studies: the Sulman Mummy Project. *Canadian Association of Radiologists Journal*, 55(4), 228-34.

Godfray, H. (2002). Challenges for taxonomy. *Nature*, (417), 17-19. <https://doi.org/10.1038/417017a>

Goh, T. Y., Basah, S. N., Yazid, H., Aziz Safar, M. J., & Ahmad Saad, F. S. (2018). Performance analysis of image thresholding: Otsu technique. *Measurement*, 114, 298–307. <https://doi.org/10.1016/j.measurement.2017.09.052>

González García, C., Núñez-Valdez, E., García-Díaz, V., Pelayo G-Bustelo, C., & Cueva-Lovelle, J. M. (2019). A Review of Artificial Intelligence in the Internet of Things. *International Journal of Interactive Multimedia and Artificial Intelligence*, 5(4), 9. <https://doi.org/10.9781/ijimai.2018.03.004>

Goodman, S.M. & Meininger, P.L. *The Birds of Egypt*. Oxford University Press.

Graham, L. (2020). From Isis-kite to Nekhbet-vulture and Horus-falcon: Changes in the identification of the bird above Osiris’s phallus in temple “conception of Horus” scenes. *Birmingham Egyptology Journal*, 8, 1–32.

Hall, M. I. (2008). The anatomical relationships between the avian eye, orbit and sclerotic ring: Implications for inferring activity patterns in extinct birds. *Journal of Anatomy*, 212(6), 781–794. <https://doi.org/10.1111/j.1469-7580.2008.00897.x>

Hamwood, J., Alonso-Caneiro, D., Read, S. A., Vincent, S. J., & Collins, M. J. (2018). Effect of patch size and network architecture on a convolutional neural network approach for automatic segmentation of OCT retinal layers. *Biomedical Optics Express*, 9(7), 3049. <https://doi.org/10.1364/boe.9.003049>

Hart, G. (2005). *The Routledge Dictionary of Egyptian Gods and goddesses* (2nd ed.). Routledge.

Hekkala, E. R., Aardema, M. L., Narechania, A., Amato, G., Ikram, S., Shirley, M. H., Vliet, K. A., Cunningham, S. W., Gilbert, M. T., & Smith, O. (2020). The secrets of Sobek – a crocodile mummy mitogenome from ancient Egypt. *Journal of Archaeological Science: Reports*, 33, 102483. <https://doi.org/10.1016/j.jasrep.2020.102483>

- Hekkala, E. R., Colten, R., Cunningham, S. W., Smith, O., & Ikram, S. (2022). Using Mitogenomes to Explore the Social and Ecological Contexts of Crocodile Mummification in Ancient Egypt. *Bulletin of the Peabody Museum of Natural History*, 63(1), 3–14. <https://doi.org/10.3374/014.063.0101>
- Hermena, S., & Young, M. (2023). CT-scan Image Production Procedures. In *StatPearls*. StatPearls Publishing. <http://www.ncbi.nlm.nih.gov/books/NBK574548/>
- Heyndrickx, M., Bultreys, T., Goethals, W., Van Hoorebeke, L., & Boone, M. N. (2020). Improving image quality in fast, time-resolved micro-CT by weighted back projection. *Scientific Reports*, 10(1). <https://doi.org/10.1038/s41598-020-74827-x>
- Holland, G. (2007). Falconidae – Falcons and Kestrels. In G. Holland (Ed.) *Encyclopedia of Aviculture* (pp. 525-531). Hancock House Publishers.
- Houlihan, P. F., & Goodman, S. M. (1986). *The Birds of Ancient Egypt* (Vol. 1). Aris Phillips.
- Hussain, J. (2019). *Deep Learning Black Box Problem*. [Master's Thesis, Uppsala University]. Digitala Vetenskapliga Arkivet.
- Ikram, S. (1995). *Choice Cuts: Meat Production in Ancient Egypt*. Peeters Press & Department Oriental Studies.
- Ikram, S. (2005a). Divine Creatures Animal Mummies. In S. Ikram (Ed.), *Divine Creatures: Animal Mummies in Ancient Egypt* (pp. 1–15). The American University in Cairo press.
- Ikram, S. (2005b). Manufacturing Divinity The Technology of Mummification. In S. Ikram (Ed.), *Divine Creatures: Animal Mummies in Ancient Egypt* (pp. 16–43). The American University in Cairo press.
- Ikram, S. (2005c). The Loved Ones: Egyptian Animal Mummies as Cultural and Environmental Indicators. In H. Buitenhuis, A.M. Choyke, L. Martin, L. Bartosiewicz, & M. Mashkour (Eds.), *Archaeology of the New East* (pp. 240-248). Groningen: ARC.
- Ikram, S. (2007). Animals in the Ritual Landscape at Abydos: A Synopsis. In Z. Hawass & J. Richards (Eds.), *The Archaeology and Art of Ancient Egypt: Essays in Honor of David B. O'Connor* (Vol. 1, pp. 417–432). Supreme Council of Antiquities Press.
- Ikram, S. (2010). Mummification. *UCLA Encyclopedia of Egyptology*, 1(1). <https://escholarship.org/uc/item/0gn7x3ff>
- Ikram, S. (2012). An Eternal Aviary: Bird Mummies from Ancient Egypt. In R. Bailleul-LeSuer (Ed.), *Between Heaven and Earth: Birds in Ancient Egypt* (pp. 43-49). The Oriental Institute of the University of Chicago.

- Ikram, S. (2013). Man's Best Friend For Eternity: Dog And Human burials In Ancient Egypt. *Anthropozoologica*, 48(2), 299–307. <https://doi.org/10.5252/az2013n2a8>
- Ikram, S. (2015a). Experimental Archaeology: From Meadow to Em-baa-lming Table. In C. Grave-Brown (Ed.), *Egyptology in the Present: Experiential and Experimental Methods of Archaeology* (pp. 53–74). The Classical Press of Whale.
- Ikram, S. (2015b). Speculations on the Role of Animal Cults in the Economy of Ancient Egypt. In M. Massiera, B. Mathieu, & F. Rouffet (Eds.), *Apprivoiser le sauvage / Taming the Wild* (pp. 211–228). Universite Paul Valery Montpellier 3 - CNRS.
- Ikram, S. (2019a). An Eternal Aviary: Bird Mummies From Ancient Egypt. In S. Porcier, S. Ikram, & S. Pasquali (Eds.), *Creatures of Earth, Water, and Sky Essays on Animals in Ancient Egypt and Nubia* (pp. 43–49). Sidestone Press.
- Ikram, S. (2019b). Shedding New Light on Old Corpses Developments in the Field of Animal Mummy Studies. In S. Porcier, S. Ikram, & S. Pasquali (Eds.), *Creatures of earth, water, and sky: Essays on animals in Ancient Egypt and Nubia* (pp. 179–191). Sidestone Press.
- Ikram, S., & Nicholson, P. T. (2015). The Sacred Animal Necropolis at North Saqqara: The Cults and Their Catacombs. In S. Ikram (Ed.), *Divine Creatures: Animal Mummies in Ancient Egypt* (pp. 44–71). The American University in Cairo press.
- Ikram, S., Nicholson, P., Bertini, L., & Hurley, D. (2013). Killing Man's best friend? In K. Boulden & S. Musselwhite (Eds.), *Archaeological Review from Cambridge Humans and Animals: Vol. 28.2* (pp. 48–66).
- Integrated Taxonomic Information System. (2023). <https://www.itis.gov>
- Ji, C. (2010). Accurate 3D data stitching in circular cone-beam micro-CT. *Journal of X-Ray Science and Technology*, 18(2), 99–110. <https://doi.org/10.3233/xst-2010-0246>
- Johnston, R., Thomas, R., Jones, R., Graves-Brown, C., Goodridge, W., & North, L. (2020). Evidence of diet, deification, and death within ancient Egyptian mummified animals. *Scientific Reports*, 10(1). <https://doi.org/10.1038/s41598-020-69726-0>
- Kachelrieß, M. (2004). Micro-CT. In W. Semmler & M. Schwaiger (Eds.), *Handbook of Experimental Pharmacology Molecular Imaging I* (Vol. 185/1, pp. 23–52). Springer.
- Kalender, W. A. (2006). X-ray computed tomography. *Physics in Medicine & Biology*, 51(13), 29–43. <https://doi.org/10.1088/0031-9155/51/13/R03>
- Kandel, I., & Castelli, M. (2020). The effect of batch size on the generalizability of the Convolutional Neural Networks on a histopathology dataset. *ICT Express*, 6(4), 312–315. <https://doi.org/10.1016/j.icte.2020.04.010>

- Kiljunen, T., Kaasalainen, T., Suomalainen, A., & Kortensniemi, M. (2015). Dental cone beam CT: A review. *Physica Medica*, *31*(8), 844–860. <https://doi.org/10.1016/j.ejmp.2015.09.004>
- Kitchen, K. A. (1991). The Chronology of Ancient Egypt. *World Archaeology*, *23*(2), 201–208.
- Lacese, C. (2015). Falconiformes (Falcons, Hawks, Eagles, Kites, Harriers, Buzzards, Ospreys, Caracaras, Secretary Birds, Old World and New World Vultures). In R. E. Miller & M. E. Fowler (Eds.), *Fowler's Zoo and Wild Animal Medicine* (Vol. 8, pp. 127–142). Elsevier Saunders.
- Lawson, B. (2016). Egyptian mummies at the Redpath Museum: Unravelling The History of McGill University's collection. *Fontanus*, *14*, 1–37. <https://doi.org/10.26443/fo.v14i.281>
- Lechuga, L., & Weidlich, G. A. (2016). Cone Beam CT vs. Fan Beam CT: A Comparison of Image Quality and Dose Delivered Between Two Differing CT Imaging Modalities. *Cureus*, *8*(9), e778. <https://doi.org/10.7759/cureus.778>
- LeCun, Y., Bengio, Y., & Hinton, G. (2015). Deep learning. *Nature*, *521*(7553), Article 7553. <https://doi.org/10.1038/nature14539>
- Lemrich, W. (1931). Der skeralring der vögel. *Naturwss*, *65*, 513–586.
- Lima, FC., Vieira, LG., Santos, ALQ., De Simone, SBS., Hirano, LQL., Silva, JMM., & Romão, MF. (2009). Anatomy of the scleral ossicles in brazilian birds. *Brazilian Journal of Morphological Science*, *26*, 165-169.
- Lin, E., & Alessio, A. (2009). What are the basic concepts of temporal, contrast, and spatial resolution in cardiac CT? *Journal of Cardiovascular Computed Tomography*, *3*(6), 403–408. <https://doi.org/10.1016/j.jcct.2009.07.003>
- Linglin, M., Amiot, R., Richardin, P., Porcier, S., Antheaume, I., Berthet, D., Grossi, V., Fourel, F., Flandrois, J.-P., Louchart, A., Martin, J. E., & Lécuyer, C. (2020). Isotopic systematics point to wild origin of mummified birds in Ancient Egypt. *Scientific Reports*, *10*(1), Article 1. <https://doi.org/10.1038/s41598-020-72326-7>
- Lorenzoni, D. C., Bolognese, A. M., Garib, D. G., Guedes, F. R., & Sant'Anna, E. F. (2012). Cone-Beam Computed Tomography and Radiographs in Dentistry: Aspects Related to Radiation Dose. *International Journal of Dentistry*, *2012*, e813768. <https://doi.org/10.1155/2012/813768>
- Lortet, D., & Gaillard, C. (1905). La faune momifiée de l'ancienne Égypt. Archives due Muséum d'Histoire Naturelle de Lyon, série 2, No 9, 1-130.

MacLeod, R. (2012) *Theban mummy, male (332-30 BCE) - 1859*. Quebec Anglophone Heritage Network. <https://100objects.qahn.org/content/theban-mummy-male-332-30-bce-1859>

Makovetsky, R., Piche, N., & Marsh, M. (2018). Dragonfly as a Platform for Easy Image-based Deep Learning Applications. *Microscopy and Microanalysis*, 24(S1), 532–533. <https://doi.org/10.1017/S143192761800315X>

Mark, J. J. (2017). *The Soul in Ancient Egypt*. World History Encyclopedia. <https://www.worldhistory.org/article/1023/the-soul-in-ancient-egypt/>

Marković, M., Mezzatesta, E., Porcier, S., Vieillescazes, C., & Mathe, C. (2022). Rethinking the Process of Animal Mummification in Ancient Egypt: Molecular Characterization of Embalming Material and the Use of Brassicaceae Seed Oil in the Mummification of Gazelle Mummies from Kom Mereh, Egypt. *Molecules (Basel, Switzerland)*, 27(5), 1532. <https://doi.org/10.3390/molecules27051532>

McKnight, L. (2020). On a Wing and a Prayer: Ibis Mummies in Material Culture at Abydos. *Arts*, 9(4), Article 4. <https://doi.org/10.3390/arts9040128>

McKnight, L. M., Adams, J. E., Chamberlain, A., Atherton-Woolham, S. D., & Bibb, R. (2015). Application of clinical imaging and 3D printing to the identification of anomalies in an ancient Egyptian animal mummy. *Journal of Archaeological Science: Reports*, 3, 328–332.

McKnight, L., & Atherton-Woolham, S. (2016). The evolution of imaging ancient Egyptian animal mummies at the University of Manchester, 1972–2014. In C. Price, R. Forshaw, A. Chamberlain, & P. T. Nicholson (Eds.), *Mummies, magic and medicine in ancient Egypt: Multidisciplinary essays for Rosalie David* (pp. 345-354). Manchester University Press.

McKnight, L., Bibb, R., Mazza, R., & Chamberlain, A. (2018). Appearance and Reality in Ancient Egyptian Votive Animal Mummies. *Journal of Ancient Egyptian Interconnections*, 20, 52–57.

McKnight, L., White, J., Rosier, A., Cooper, J., & Bibb, R. (2022). Identification of avian remains contained within wrapped ancient Egyptian mummies: Part 1, A critical assessment of identification techniques. *Journal of Archaeological Science: Reports*, 45, 103585. <https://doi.org/10.1016/j.jasrep.2022.103585>

Metwaly, A. M., Ghoneim, M. M., Eissa, Ibrahim. H., Elsehemy, I. A., Mostafa, A. E., Hegazy, M. M., Afifi, W. M., & Dou, D. (2021). Traditional ancient Egyptian medicine: A review. *Saudi Journal of Biological Sciences*, 28(10), 5823–5832. <https://doi.org/10.1016/j.sjbs.2021.06.044>

Millet, N. B., Hart, G. D., Reyman, T. A., Zimmerman, M. R., & Lewin, P. K. (1998). ROM I: mummification for the common people. In A. Cockburn, E. Cockburn, & T. A.

- Reyman (Eds.), *Mummies, disease and ancient culture* (pp. 71–84). Cambridge University.
- Mohamed, M. H. (2017). The Celestial Cow Goddess Mehet-Weret. *Journal of Association of Arab Universities for Tourism and Hospitality*, 14(2), 55–66. <https://doi.org/10.21608/jaauth.2017.48142>
- Mojsov, B. (2005). *Osiris: Death and afterlife of a god*. Blackwell Pub.
- Morgan, L. W., & McGovern-Hoffman, S. (2008). Noninvasive radiographic analysis of an Egyptian falcon mummy from the late period 664–332 BC. *Journal of Avian Biology*, 39(5), 584–587. <https://doi.org/10.1111/j.0908-8857.2008.04269.x>
- Morgan, L., McGovern-Huffman, S., & French-Kreigh, P. (2011). Comparison of two Falconid mummies from the late period of ancient Egypt using noninvasive techniques. *Journal of Raptor Research*, 45(4), 357–361. <https://doi.org/10.3356/jrr-11-21.1>
- Nelson, A. J., & Wade, A. D. (2015). Impact: Development of a radiological mummy database. *The Anatomical Record*, 298(6), 941–948. <https://doi.org/10.1002/ar.23130>
- Nelson, A. J., Granton, P. V., Friedman, S. N., Ikram, S., Cunningham, I. A., & Holdworth, D. W. (2009). *The use of non-destructive clinical and micro-CT imaging in the analysis of an Ancient Egyptian raptor mummy*. Unpublished manuscript.
- Nemtoi, A., Czink, C., Haba, D., Gahleitner, A. (2013). Cone beam CT: a current overview of devices. *Dentomaxillofac Radiology* 24(8), 20120443. <https://doi.org/10.1259/dmfr.20120443>
- Nicholson, P. T. (2005). The Sacred Animal Necropolis at North Saqqara. In S. Ikram (Ed.), *Divine Creatures: Animal Mummies in Ancient Egypt* (pp. 44–71). The American University in Cairo press.
- Nicholson, P. T. (2016). The Sacred Animal Necropolis at North Saqqara: Narrative of a ritual landscape. In C. Price, R. Forshaw, A. Chamberlain, & P. T. Nicholson (Eds.), *Mummies, magic and medicine in ancient Egypt: Multidisciplinary essays for Rosalie David* (pp. 19–31). Manchester University Press.
- Nicholson, P. T. (2022). Sacred Animals at Saqqara. *Heritage*, 5(2), 1240–1252. <https://doi.org/10.3390/heritage5020064>
- Nikon. (2021, March). *Nikon introduces the X-ray CT system “XT H 225 ST 2x.”* Nikon: About Us. [https://www.nikon.com/company/news/2021/0316\\_x-ray\\_01.html](https://www.nikon.com/company/news/2021/0316_x-ray_01.html)
- O’Brien, J. (2011, November 17). Unwrapping the ancient Egyptian animal mummy industry. *BBC News*. <https://www.bbc.com/news/magazine-15780427>



- Oesterdiekhoff, G. W. (2008). Magic and animism in old religions: the relevance of sun cults in the world-view of traditional societies. *Narodna Umjetnost: Croatian Journal of Ethnology and Folklore Research*, 45(1).
- Orta, J., Boesman, P. F. D., Kirwan, G. M., & Marks, J. S. (2020, March 4). *Long-legged buzzard (Buteo rufinus)*, version 1.0. Birds of the World. <https://birdsoftheworld.org/bow/species/lolbuz1/cur/introduction>
- Otte, C. (2013). *The (Bird) Eyes Have It*. California Academy of Sciences. <https://www.calacademy.org/blogs/project-lab/the-bird-eyes-have-it>
- Overton, N. J., & Hamilakis, Y. (2013). A manifesto for a social zooarchaeology. Swans and other beings in the Mesolithic. *Archaeological Dialogues*, 20(2), 111–136. <https://doi.org/doi:10.1017/S1380203813000159>
- Pérez-Ramos, A., & Figueirido, B. (2020). Toward an “Ancient” Virtual World: Improvement Methods on X-ray CT Data Processing and Virtual Reconstruction of Fossil Skulls. *Frontiers in Earth Science*, 8. <https://www.frontiersin.org/articles/10.3389/feart.2020.00345>
- Piche, N., Bouchard, I., & Marsh, M. (2017). Dragonfly SegmentationTrainer—A General and User-Friendly Machine Learning Image Segmentation Solution. *Microscopy and Microanalysis*, 23(S1), 132–133. <https://doi.org/10.1017/S1431927617001349>
- Pinch, G. (2004). *Egyptian mythology: a guide to the gods, goddesses, and traditions of ancient Egypt*. Oxford University Press.
- Rageot, M., Hussein, R. B., Beck, S., Altmann-Wendling, V., Ibrahim, M. I. M., Bahgat, M. M., Yousef, A. M., Mittelstaedt, K., Filippi, J.-J., Buckley, S., Spiteri, C., & Stockhammer, P. W. (2023). Biomolecular analyses enable new insights into ancient Egyptian embalming. *Nature*, 614(7947), Article 7947. <https://doi.org/10.1038/s41586-022-05663-4>
- Ramesh, K. K. D., Kumar, G. K., Swapna, K., Datta, D., & Rajest, S. S. (2021). A Review of Medical Image Segmentation Algorithms. *EAI Endorsed Transactions on Pervasive Health and Technology*, 7(27). <https://doi.org/10.4108/eai.12-4-2021.169184>
- Redford, D. B. (2001). *The Oxford Encyclopedia of ancient Egypt* (Vol. 1). Oxford Univ. Press.
- Redler, G., Jones, K. C., Templeton, A., Bernard, D., Turian, J., & Chu, J. C. H. (2018). Compton scatter imaging: A promising modality for image guidance in lung stereotactic body radiation therapy. *Medical Physics*, 45(3), 1233–1240. <https://doi.org/10.1002/mp.12755>
- Redpath Museum. (2023). McGill University. World Cultures Collections, Database. [Unpublished document]. Redpath Museum.

- Reedy, C. L. (2006). Multiple Functions and Multiple Histories of Tibetan Tsha-Tshas (votive Clay Images). *Studies in Conservation*, 51(sup2), 144–150. <https://doi.org/10.1179/sic.2006.51.Supplement-2.144>
- ReFaey, K., Quinones, G. C., Clifton, W., Tripathi, S., Quiñones-Hinojosa, A., ReFaey, K., Quinones, G. C., Clifton, W., Tripathi, S., & Quiñones-Hinojosa, A. (2019). The Eye of Horus: The Connection Between Art, Medicine, and Mythology in Ancient Egypt. *Cureus*, 11(5). <https://doi.org/10.7759/cureus.4731>
- Reimer, P. J., Austin, W. E., Bard, E., Bayliss, A., Blackwell, P. G., Bronk Ramsey, C., Butzin, M., Cheng, H., Edwards, R. L., Friedrich, M., Grootes, P. M., Guilderson, T. P., Hajdas, I., Heaton, T. J., Hogg, A. G., Hughen, K. A., Kromer, B., Manning, S. W., Muscheler, R., ... Talamo, S. (2020). The intcal20 Northern Hemisphere radiocarbon age calibration curve (0–55 cal KBP). *Radiocarbon*, 62(4), 725–757. <https://doi.org/10.1017/rdc.2020.41>
- Reznikov, N., Buss, D. J., Provencher, B., McKee, M. D., & Piché, N. (2020). Deep learning for 3D imaging and image analysis in biomineralization research. *Journal of Structural Biology*, 212(1), 107598. <https://doi.org/10.1016/j.jsb.2020.107598>
- Richardin, P., Porcier, S., Ikram, S., Louarn, G., & Berthet, D. (2017). Cats, crocodiles, cattle, and more: Initial steps toward establishing a chronology of ancient Egyptian animal mummies. *Radiocarbon*, 59(2), 595–607.
- Richardson, F. (1972). Accessory Pygostyle Bones of Falconidae. *The Condor*, 74(3), 350–351. <https://doi.org/10.2307/1366597>
- Ronneberger, O., Fischer, P., & Brox, T. (2015). U-Net: Convolutional Networks for Biomedical Image Segmentation. In N. Navab, J. Hornegger, W. M. Wells, & A. F. Frangi (Eds.), *Medical Image Computing and Computer-Assisted Intervention - MICCAI 2015* (pp. 234–241). Springer Cham Heidelberg New York Dordrecht London.
- Ross, G. A. (2004). Ibis in urban Sydney: A gift from Ra or a pharaoh's curse? *Urban Wildlife*, 148–152. <https://doi.org/10.7882/fs.2004.091>
- Rowland, J., Ikram, S., Tassie, G. J., & Yeomans, L. (2013). The Sacred Falcon Necropolis of Djedhor(?) at Quesna: Recent Investigations from 2006–2012. *The Journal of Egyptian Archaeology*, 99, 53–84.
- Rudin, C., & Radin, J. (2019). Why Are We Using Black Box Models in AI When We Don't Need To? A Lesson From an Explainable AI Competition. *Harvard Data Science Review*, 1(2). <https://doi.org/10.1162/99608f92.5a8a3a3d>
- Scalf, F. (2012). The Role of Birds within the Religious Landscape of Ancient Egypt. In R. Bailleul-LeSuer (Ed.), *Between Heaven and Earth: Birds in Ancient Egypt* (pp. 33–40). The Oriental Institute of the University of Chicago.

- Scanes, C. G. (2018). Chapter 6—The Neolithic Revolution, Animal Domestication, and Early Forms of Animal Agriculture. In C. G. Scanes & S. R. Toukhsati (Eds.), *Animals and Human Society* (pp. 103–131). Academic Press. <https://doi.org/10.1016/B978-0-12-805247-1.00006-X>
- Schiødt, S. (2020). *Medical science in ancient Egypt: A translation and interpretation of Papyrus Louvre-Carlsberg (pLouvre E 32847 + pCarlsberg 917)* [PhD dissertation, University of Copenhagen].
- Seibert, J. A. (2004). X-ray imaging physics for nuclear medicine technologists. Part 1: Basic principles of x-ray production. *Journal of Nuclear Medicine Technology*, *32*(3), 139–147.
- Seibert, J. A., & Boone, J. M. (2005). X-ray imaging physics for nuclear medicine technologists. Part 2: X-ray interactions and image formation. *Journal of Nuclear Medicine Technology*, *33*(1), 3–18.
- Shaw, I. (2004). *Ancient Egypt: A Very Short Introduction*. Oxford University Press.
- Shorter, A. W. (1978). *The Egyptian Gods A Handbook*. Routledge & Kegan Paul.
- Smith, B. D. (1990). Cone-beam tomography: Recent advances and a tutorial review. *Optical Engineering*, *29*(5), 524–534. <https://doi.org/10.1117/12.55621>
- Smith, B. J., & Smith, S. A. (1992a). The Humeroscapular Bone of the Great Horned Owl (*Bubo virginianus*) and other Raptors. *Anatomia, Histologia, Embryologia*, *21*(1), 3239. <https://doi.org/10.1111/j.1439-0264.1992.tb00316.x>
- Smith, S. A., & Smith, B. J. (1990). Normal xeroradiographic and radiographic anatomy of the red-tailed hawk (*Buteo jamaicensis*) refers to other diurnal raptors. *Veterinary Radiology*, *31*(6), 301–312. <https://doi.org/10.1111/j.1740-8261.1990.tb00805.x>
- Smith, S. A., & Smith, B. J. (1992b). *Atlas of avian radiographic anatomy*. W.B Saunders Company.
- Spake, L., Meyers, J., Blau, S., Cardoso, H. F. V., & Lottering, N. (2020). A simple and software-independent protocol for the measurement of post-cranial bones in anthropological contexts using thin slab maximum intensity projection. *Forensic Imaging*, *20*, 200354. <https://doi.org/10.1016/j.fri.2020.200354>
- Spin-Neto, R., Gotfredsen, E., & Wenzel, A. (2013). Impact of Voxel Size Variation on CBCT-Based Diagnostic Outcome in Dentistry: A Systematic Review. *Journal of Digital Imaging*, *26*(4), 813–820. <https://doi.org/10.1007/s10278-012-9562-7>
- Storer, R. (1960). Adaptive Radiation in Birds. In A. Marshal (Ed.), *Biology and Comparative Physiology of Birds I* (Vol. 1, pp. 15–55). Academic Press.

Su, Q.-H., Zhang, Y., Shen, B., Li, Y.-C., & Tan, J. (2020). Application of molybdenum target X-ray photography in imaging analysis of caudal intervertebral disc degeneration in rats. *World Journal of Clinical Cases*, 8(16), 3431–3439. <https://doi.org/10.12998/wjcc.v8.i16.3431>

Sundararajan, B. (2024,). *Stride in cnns: Stepping towards efficient image processing*. Medium. <https://medium.com/@bragadeeshs/stride-in-cnns-stepping-towards-efficient-image-processing-e58a34b02ff0>

Sustaita, D. (2008). Musculoskeletal underpinnings to differences in killing behavior between North American accipiters (Falconiformes: Accipitridae) and falcons (Falconidae). *Journal of Morphology*, 269(3), 283–301. <https://doi.org/10.1002/jmor.10577>

Swinton, W. (1960). The Origin of Birds. In A. Marshal (Ed.), *Biology and Comparative Physiology of Birds I* (Vol. 1, pp. 1–14). Academic Press.

Tabikha, K. (2023, May 27). *Embalming rooms for humans and animals among latest finds at Egypt's Saqqara necropolis*. The National. <https://www.thenationalnews.com/mena/egypt/2023/05/27/embalming-rooms-for-humans-and-animals-among-latest-finds-at-egypts-saqqara-necropolis/>

Tafti, D., & Maani, C. V. (2023). X-ray Production. In *StatPearls*. StatPearls Publishing. <http://www.ncbi.nlm.nih.gov/books/NBK537046/>

te Velde, H. (1980). A Few Remarks upon the Religious Significance of Animals in Ancient Egypt. *Numen*, 27(1), 76–82. <https://doi.org/10.2307/3269982>

The British Museum. (n.d.). *Stela: British museum*. The British Museum. [https://www.britishmuseum.org/collection/object/Y\\_EA27332](https://www.britishmuseum.org/collection/object/Y_EA27332)

Tokita, M., Matsushita, H., & Asakura, Y. (2020). Developmental mechanisms underlying webbed foot morphological diversity in waterbirds. *Scientific Reports*, 10, 8020. <https://doi.org/10.1038/s41598-020-64786-8>

Tsang, L. R., & McDonald, P. G. (2019). A comparative study of avian pes morphotypes, and the functional implications of Australian raptor pedal flexibility. *Emu – Austral Ornithology*, 119(1), 14-23. <https://doi.org.proxy1.lib.uwo.ca/10.1080/01584197.2018.1483203>

Tuschel, D. (2020). Spectral Resolution and Dispersion in Raman Spectroscopy. *Spectroscopy*, 35(9), 9–15.

Vandrope, K. (2010). The Ptolemaic Period. In A. B. Lloyd (Ed.), *A Companion to Ancient Egypt* (Vol. 1, pp. 159–179). Blackwell Publishing Ltd.

- von den Driesch, A. (1976). Part Three: Measurement of the Bird Skeleton. In *A guide to the measurement of animal bones from archaeological sites* (pp. 103–131). essay, Peabody Museum of Archaeology and Ethnology, Harvard University.
- von den Driesch, A., Kessler, D., Steinmann, F., Peters, J., & Berteaux, V. (2005). Mummified, deified and buried at Hermopolis Magna - the sacred birds from Tuna El-Gebel, Middle Egypt. *Ägypten und Levante – Egypt and the Levant*, *1*, 203–244. <https://doi.org/10.1553/aeundl15s203>
- Vos, R. L. (1993). Death, embalming and burial of an Apis Bull. In *The Apis Embalming Ritual* (pp. 30–42). Peeters Press.
- Wade, A. D., Ikram, S., Conlogue, G., Beckett, R., Nelson, A. J., Colten, R., Lawson, B., & Tampieri, D. (2012). Foodstuff placement in ibis mummies and the role of viscera in embalming. *Journal of Archaeological Science*, *39*(5), 1642–1647. <https://doi.org/10.1016/j.jas.2012.01.003>
- Wade, A. D., Ikram, S., Conlogue, G., Beckett, R., Nelson, A. J., & Colten, R. (2011). Backroom Treasures: CT Scanning of Two Ibis Mummies from the Peabody Museum Collection. *Anthropology Presentations*. 2. <https://ir.lib.uwo.ca/anthropres/2>
- Wade, A., Nelson, A., Garvin, G., & Holdsworth, D. W. (2010). Preliminary Radiological Assessment of Age-related Change in the Trabecular Structure of the Human Os Pubis\*. *Journal of Forensic Sciences*, *56*(2), 312–319. <https://doi.org/10.1111/j.1556-4029.2010.01643.x>
- Walls, GL. (1942). *The vertebrate eye and its adaptive radiation*. Cranbrook Institute of Science.
- Wang, X., McGowan, A. J., & Dyke, G. J. (2011). Avian wing proportions and flight styles: First step towards predicting the flight modes of Mesozoic birds. *PLoS ONE*, *6*(12). <https://doi.org/10.1371/journal.pone.0028672>
- Wasef, S., Subramanian, S., O’Rorke, R., Huynen, L., El-Marghani, S., Curtis, C., Poppinga, A., Holland, B., Ikram, S., Millar, C., Willerslev, E., & Lambert, D. (2019). Mitogenomic diversity in Sacred Ibis Mummies sheds light on early Egyptian practices. *PLOS ONE*, *14*(11), e0223964. <https://doi.org/10.1371/journal.pone.0223964>
- Wasson, D. L. (2016, August 2). *Roman Egypt*. World History Encyclopedia. [https://www.worldhistory.org/Roman\\_Egypt/](https://www.worldhistory.org/Roman_Egypt/)
- Wetterstrom, W., & Murray, M. A. (2001). Agriculture. In D. Redford (Ed.), *The Oxford Encyclopedia of Ancient Egypt* (Vol. 1). Oxford University Press.
- Whiting, B. R., Massoumzadeh, P., Earl, O. A., O’Sullivan, J. A., Snyder, D. L., & Williamson, J. F. (2006). Properties of preprocessed sinogram data in x-ray computed tomography. *Medical Physics*, *33*(9), 3290–3303. <https://doi.org/10.1118/1.2230762>

- Willemink, M. J., & Noël, P. B. (2019). The evolution of image reconstruction for CT— from filtered back projection to artificial intelligence. *European Radiology*, 29(5), 2185–2195. <https://doi.org/10.1007/s00330-018-5810-7>
- Willemink, M. J., Takx, R. A. P., de Jong, P. A., Budde, R. P. J., Bleyers, R. L. A. W., Das, M., Wildberger, J. E., Prokop, M., Bult, N., de Mey, J., Leiner, T., & Schilham, A. M. R. (2014). Computed tomography radiation dose reduction. *Journal of Computer Assisted Tomography*, 38(6), 815–823. <https://doi.org/10.1097/rct.0000000000000128>
- Woodman, N., Ikram, S., & Rowland, J. (2021). A new addition to the embalmed fauna of Ancient Egypt: Güldenstaedt’s white-toothed shrew, *Crocidura gueldenstaedtii* (pallas, 1811) (mammalia: Eulipotyphla: Soricidae). *PLOS ONE*, 16(4).
- Yamanaka, D., Ohtake, Y., & Suzuki, H. (2013). The Sinogram Polygonizer for Reconstructing 3D Shapes. *IEEE Transactions on Visualization and Computer Graphics*, 19(11), 1911–1922. <https://doi.org/10.1109/TVCG.2013.87>
- Zelazko, A. (2023, October 21). *Osiris / Description, Myth, Symbols, & Facts /*. Britannica. <https://www.britannica.com/topic/Osiris-Egyptian-god>
- Zivie-Coche, C. (2008). Late Period Temples. In W. Wendrich, J. Dieleman, E. Ffrench-Dodd, & J. Bahnes (Eds.), *UCLA Encyclopedia of Egyptology*, 1(1). <https://escholarship.org/uc/item/30k472wh>
- Zucca, P., & Cooper, J. E. (2000). Osteological Aspects of the Falcon Wing. In J. T. Lumeij, P.T. Redig, M. Lierz, & J. E. Cooper (Eds.), *Raptor Biomedicine III including Bibliography of Diseases of Birds of Prey* (pp. 195–199). Zoological Education Network.

## Appendices

*Note: Unless otherwise specified, all appendices regarding Dragonfly are based on Dragonfly Version 2022.2 Build 1409 (Comet Technologies Canada Inc). Dragonfly's technologies are continuously updated, so some information may be outdated. The most current version is Version 2024.1 Build 1579.*

### **Appendix A: Additional images of mummified birds**

Throughout the research process, all mummies (not including those studied from the IMPACT database) were documented with detailed photographs for later reference. All photos were taken by Maris Schneider and presented here in chronological order of pictures and scans. Additionally, Andrew Nelson provided photographs of the CMH Falcon 1, which are included at the end of this appendix.

*Faucon 5731 (photographed and scanned 2023-05-23, Montreal, Quebec)*



*Figure A.1 Demonstrates the mounting and positioning of faucon 5731 in the Yxlon FF25 CT scanner.*



*Figure A.2 The left profile perspective mummified falcon 5731's mummified head, highlighting the diverse wrapping orientations of linen wrappings alongside the distinctive morphology of the falcon's tomial tooth.*



*Figure A.3 Top-down view of falcon 5731 mummy, providing a comprehensive view of the entire mummy from head to toe.*





*Figure A.5 The right lateral aspect of the faucon 5731's mummified torso is shown, emphasizing a segment of linen slightly detached from the mummy's body.*



*Figure A.4 The left lateral aspect of the faucon 5731's mummified torso is presented, delineating the diverse orientations of linen wrappings and highlighting the well-preserved pattern characteristic of mummification linen materials.*



*Figure A.6 The distal end, where the feet and feathers are wrapped, of faucon 5731 is documented, wherein minor damage at the lower portion of the mummy is discernible. This damage reveals internal layers of wrapping that exhibit a slightly lighter hue compared to the outer layers, indicative of the outer layer's potential alteration over time or application of resin or oils during the mummification process.*

*Ibis 2727.02 (photographed and scanned 2023-06-01, Montreal, Quebec)*



*Figure A.7 Depiction of the mounting and positioning of ibis 2727.02 within the Yxlon FF25 CT scanner.*



*Figure A.9 A close-up examination is presented, focusing on the anterior superior region of ibis specimen 2727.02 mummy. The visual inspection reveals evident damage to the external wrappings, likely due to taphonomic processes.*



*Figure A.8 The distal end of ibis 2727.02 mummy is portrayed, specifically emphasizing the damage evident at the lowermost point of the mummified bundle. Note the diverse orientation of linen wrappings, indicative of the intricate wrapping technique employed during the mummification process.*



*Figure A.10 The upper right segment of ibis specimen 2727.02 exhibits notable damage, characterized by the absence of external linen layers, thereby exposing the majority of internal wrappings. Note that, during the manipulation of the mummy bundle, whether for transportation or transfer into and out of the scanner, slight shifting of the internal wrappings occurred.*



*Figure A.10 A fragment of linen wrapping from ibis 2727.02 was detached during handling at the Redpath Museum and was sent to the Radiochronology Laboratory at Laval University (Quebec City, Quebec) for carbon dating analysis.*

*Ibis 2727.01 (photographed and scanned 2023-06-02, Montreal, Quebec)*



*Figure A.12 The photograph shows the mounting and positioning of ibis 2727.01 within the Xylon FF25 CT scanner. Concurrently, the door of the scanning apparatus is opened, exposing the X-ray tube.*



*Figure A.11 The left lateral aspect of the mummified bundle of ibis 2727.01 is shown here, delineating minor damage to the external layer of the linen along its side.*



*Figure A.13 The feet of the ibis 2727.01 bundle are showcased, revealing slight damage to the mummified bundle, accompanied by the unravelling of the woven linen wrapping.*



*Figure A.14 The magnified image captures a distinctive knot formed by the interlacing threads within the linen wrapping at the feet of the ibis 2727.02 bundle. The knot is revealed due to the damage sustained by the external layers of the bundle. This photograph was referenced by Dr. Reznikov during the Yxlon Webinar on September 12<sup>th</sup>, 2023, as part of the discussion regarding the collaborative research initiative between Western's Anthropology Department and McGill's Biological Engineering Department.*



*Figure A.16 The image showcases the ibis cartonnage positioned on the anterior-superior surface of the ibis 2727.01 mummy bundle. It portrays an adult ibis in a water environment.*



*Figure A.15 The right lateral aspect of ibis 2727.01 is portrayed, highlighting the presence of small perforations in the external layer of linen. Surrounding these “punctures,” slight unravelling of the linen material is discernable. Such damage is presumably attributed to taphonomic alterations.*



*Faucon 2726.02 (photographed and scanned 2023-06-09, Montreal, Quebec)*

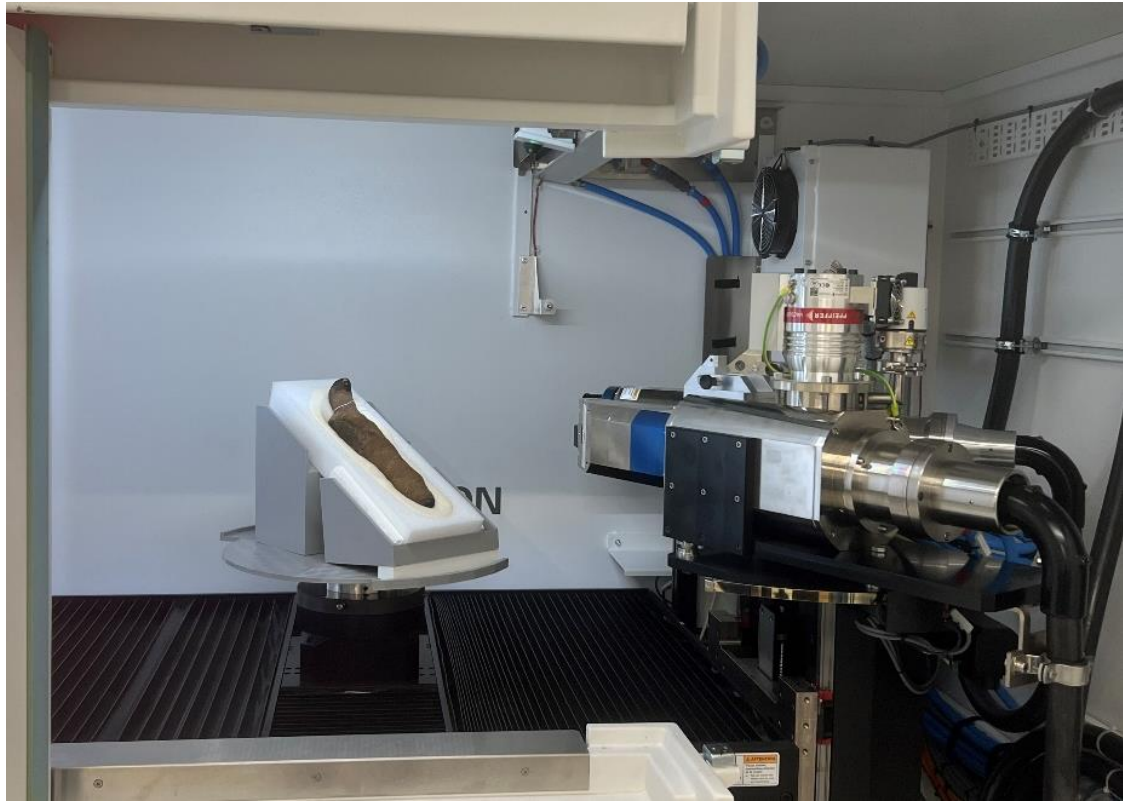


*Figure A.17 The photograph shows the mounting and positioning of faucon 2726.02 within the Xylon FF25 CT scanner. Concurrently, the door of the scanning apparatus is opened, exposing the X-ray tube.*



*Figure A.18 The frontal view captures the head of falcon 2726.02, highlighting damage to the tip of the beak, which has led to the exposure of the trabecular structure with the nasal bone, indicative of extensive damage to the entire premaxilla. Furthermore, the observed darker hue of the mummy's head compared to the rest of the bundle suggests oxidative breakdown subsequent to burial (Abdel-Maksouda & El-Amin, 2013) or differing techniques employed during the mummification process (Ikram, 2005b)., possibly the internal wrappings were covered in resin, and a new wrapping was placed around the torso with no resin, leaving the more internal layers exposed at the head and feet.*



*Figure A.20 The right lateral aspect of faucon 2726.02's head is depicted.*



*Figure A.19 The left lateral aspect of faucon 2726.02's head is depicted.*



*Figure A.22 The left lateral aspect of faucon 2726.02's torso is presented, revealing a uniform orientation of linen wrapping. Noteworthy is the tightness of the wrapping on this side of the bundle, which appears smooth, likely because resin has filled in the gaps within the woven linen, securing the external wrappings firmly in place. Furthermore, it is notable that no damage is evident on this side of the mummy.*



*Figure A.21 The right lateral aspect of faucon 2726.02's torso is showcased, showing a discernible variation in the orientation of linen wrappings. Additionally, slight lifting of the external linens is observed in this region, indicating resin presented in the same way as the left lateral side, thus not sealing the linens down on this side.*



*Figure A.24 The region encompassing the feet and feathers of faucon 2726.02 is presented with no observable damage to the linen wrappings. A comparable darkened hue, akin to that observed at the head of the bundle, is evident in this area. Similar discussions accounting for discolouration are presented in Figure A.19.*



*Figure A.23 A fragment of linen wrapping from faucon 2726.02 was detached during handling at the Redpath Museum and was sent to the Radiochronology Laboratory at Laval University (Quebec City, Quebec) for carbon dating analysis.*

*Chatham Falcon (photographed 2024-01-26; scanned 2024-02-03, London Ontario)*



*Figure A.25 The upper portion of the Chatham falcon is shown, revealing the exposed tomial tooth along with remnants of linen wrapping around the tooth. Additionally, the anterior wrappings are damaged, leading to the exposure of internal skeletal elements.*



*Figure A.27 The lower portion of the Chatham falcon is highlighted. A significant portion of the linen wrappings has been lost/damaged, thereby exposing the right foot, talons, and preserved feathers.*



*Figure A.26 A left lateral profile of the Chatham, drawing attention to the differing directions of the linen wrappings.*

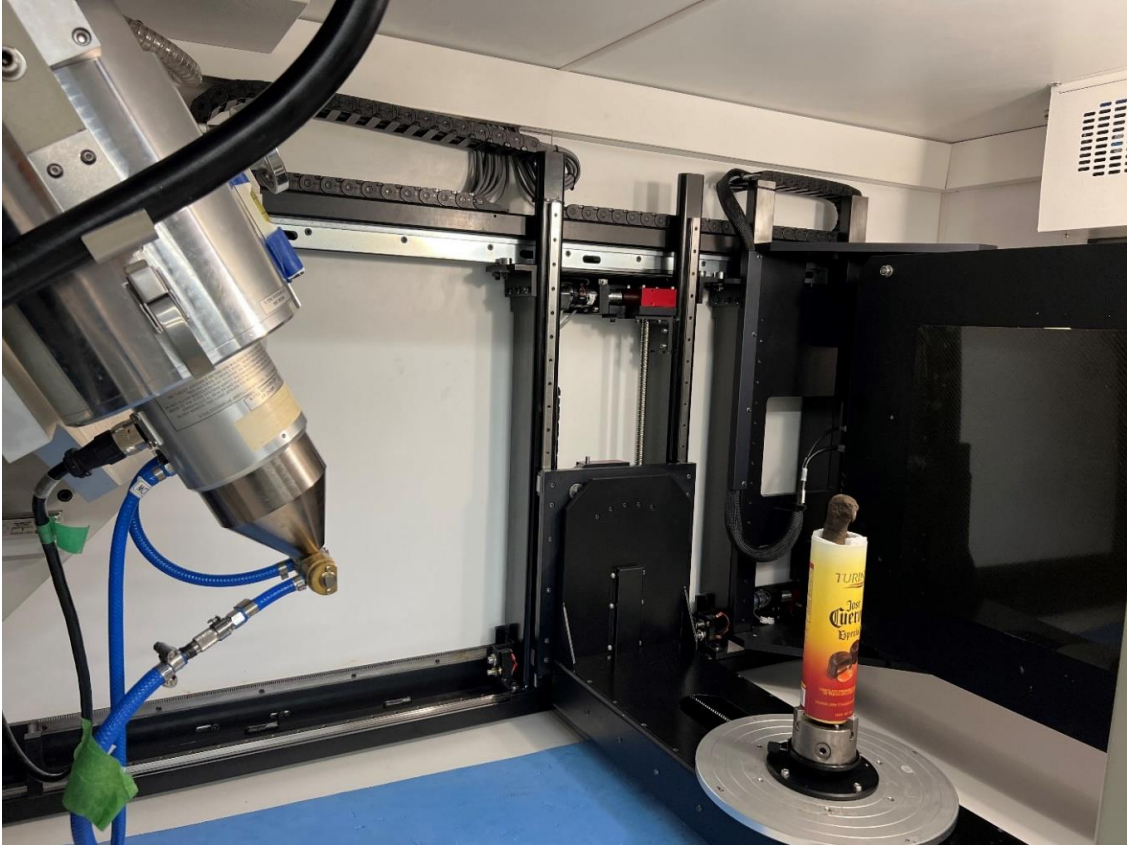


*Figure A.28 The photograph shows the mounting and positioning of the Chatham falcon within the Nikon Metris XT H 225 ST cabinet scanner. The different mounting procedures employed for the Chatham falcon compared to those specimens on loan from the Redpath Museums stem from variances in conservation protocols between the respective institutions. The mounting approach adopted from the Chatham falcon is more optimal for 3D imaging procedures.*



*Canadian Museum of History Falcon 1 (photographed and scanned 2009-08-30, Ottawa, Ontario)*

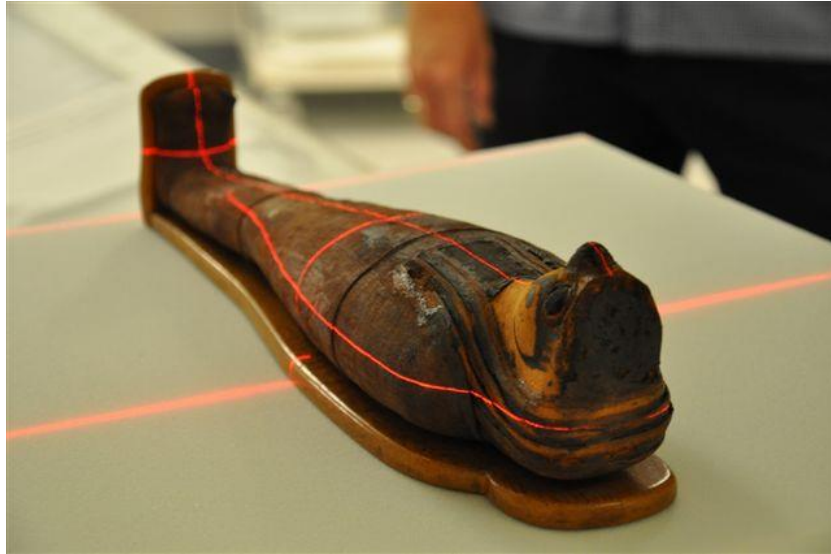


*Figure A.30 CMH Falcon 1 being aligned in the LightSpeed VCT Scanner.*



*Figure A.31 CMH Falcon 1 packaged for transport.*

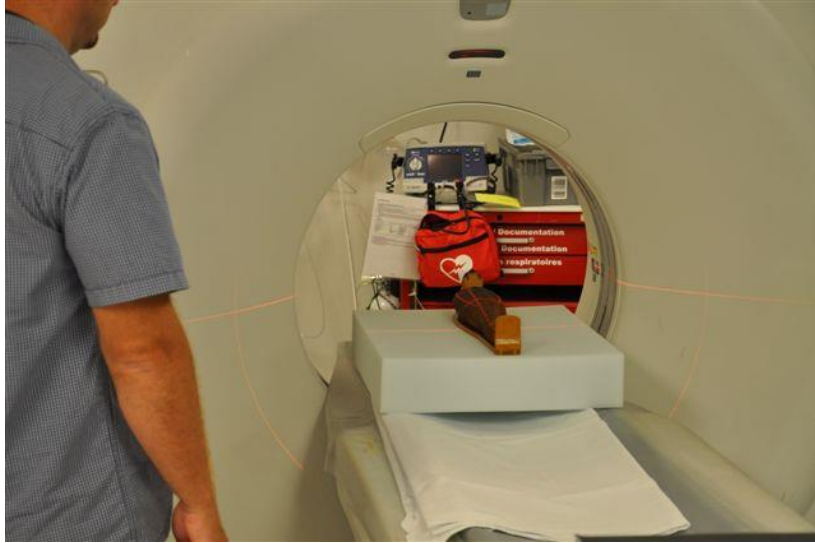


*Figure A.32 CMH Falcon 1 positioning in LightSpeed VCT scanner.*

## Appendix B: Procedural guide for multi-image registration stitching in Dragonfly

This three-part procedural guide walks the reader through the step-by-step process of stitching multiple micro-CT scans together in Dragonfly. I demonstrate this process using three scans of the Chatham Falcon at 45  $\mu\text{m}$ , taken on the Nikon Metris XT H 225 CT cabinet microCT scanner. The following explanations can also be found in Mike Marsh's (Senior Director of Product Management at Dragonfly) stitching tutorial:

<https://www.youtube.com/watch?v=WdFavt2rjVA>.

### Part 1: Set Up

Dragonfly is capable of processing multiple file types. Please refer to the following tutorials (<https://www.theobjects.com/dragonfly/tutorials.html>) on how to upload different image file types.

Note: The process can be completed with as many input scans as desired.

- 1) After uploading the image files into Dragonfly, select the 4-panel view (red box, Figure B.1) under the layout tab on the left-hand side.

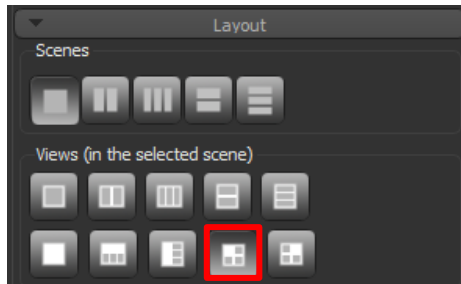


Figure B.1 Image demonstrating the 4-panel view selection on Dragonfly.

- 2) On the right-hand side, under properties, change each data set to a different colour (lookup table). Be sure that these are solid colours (i.e., blue, cyan, yellow, or magenta). You can do this by clicking on the box next to the eye (red box, Figure B.2). be sure to do this for the 2D and 3D views.

Note: These colours will not be permanent. They are to help visualize the separate scans.

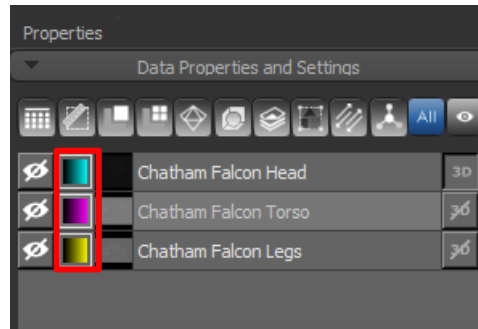


Figure B.2 Image indicating where the colour lookup tables are on Dragonfly to change colour of datasets.

- 3) The images must be manipulated with the histogram on the right-hand side, under the window leveling tab. Adjust the histogram's min and max range by dragging the yellow bars until the scanned images show the desired contrast. This process needs to be repeated for all of the datasets being stitched

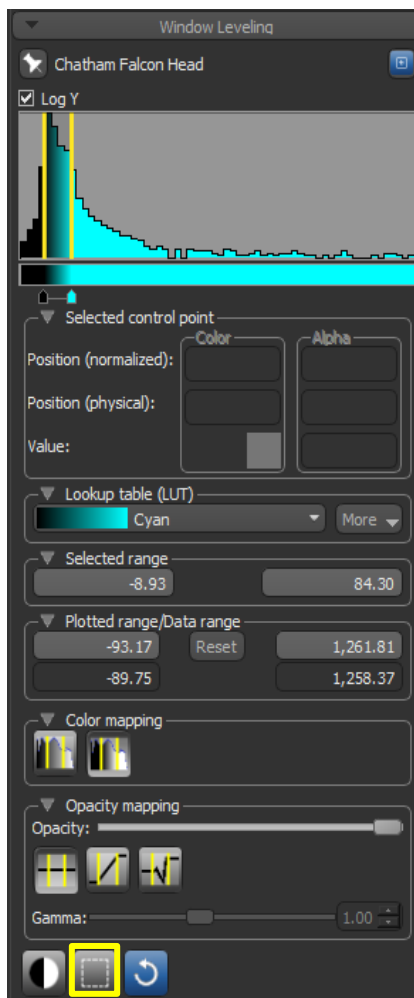


Figure B.3 Image showcasing the window leveling function in Dragonfly.

Tip: If you have selected the 3D image plane, the histogram will only adjust that plane. Be sure to adjust the 2D planes by selecting any of the three orientations before adjusting the leveling bars.

Tip: For a quick adjustment, based on Dragonfly's pre-trained image recognition, auto-adjust the contrast with the button highlighted (yellow box, Figure B.3), press CTRL, and drag a square across the slice. This only works on 2D planes.

- 4) Ensure that all 2D image planes are oriented as desired. Use the flip/rotate buttons on the right-hand side of Dragonfly to adjust all datasets. Ensure that all scans are oriented the same way so that overlapping features line up. Once the images are correctly oriented and set to the desired colour, the individual scans are ready to be aligned.

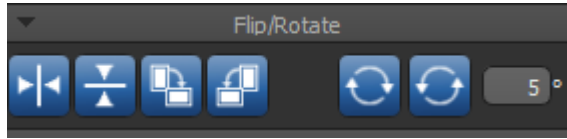



Figure B.4 Image showing the flip/rotate buttons to adjust the 2D views of datasets.

## Part 2: Aligning Images

- 1) Turn off all but one uploaded scan by clicking the  button. For ease in stitching, it is best to visualize the middlemost scan while leaving the outermost scans hidden.
- 2) Zoom out on the image by holding down the scroll wheel on the mouse and moving the mouse towards the computer. Click and hold the left and right mouse buttons simultaneously to move the 2D scan within the image panel. Situate the scanned image within the centre of the image plane.

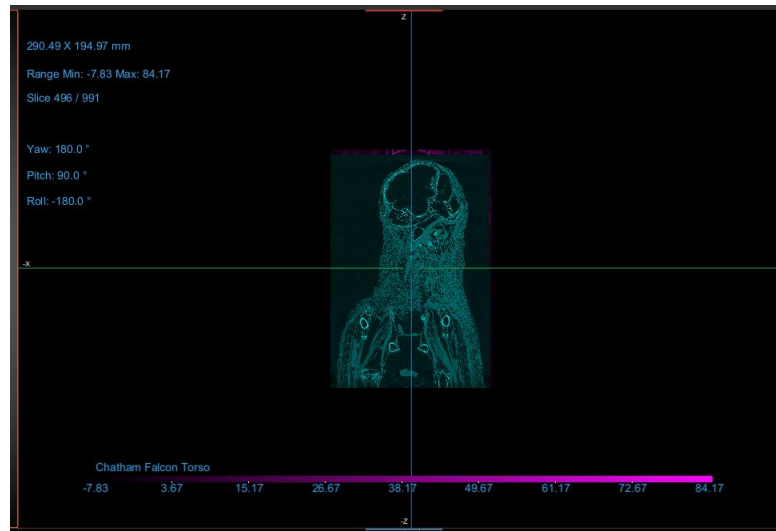


Figure B.5 One 2D view of the scanned image, zoomed out and centred within the image panel.

- 3) Now turn on only one of the other scans (again by selecting the eye button). This should overlay the two scans. Note: one of the scans will be covered. You can confirm that both scans are visible by looking at the 3D image.

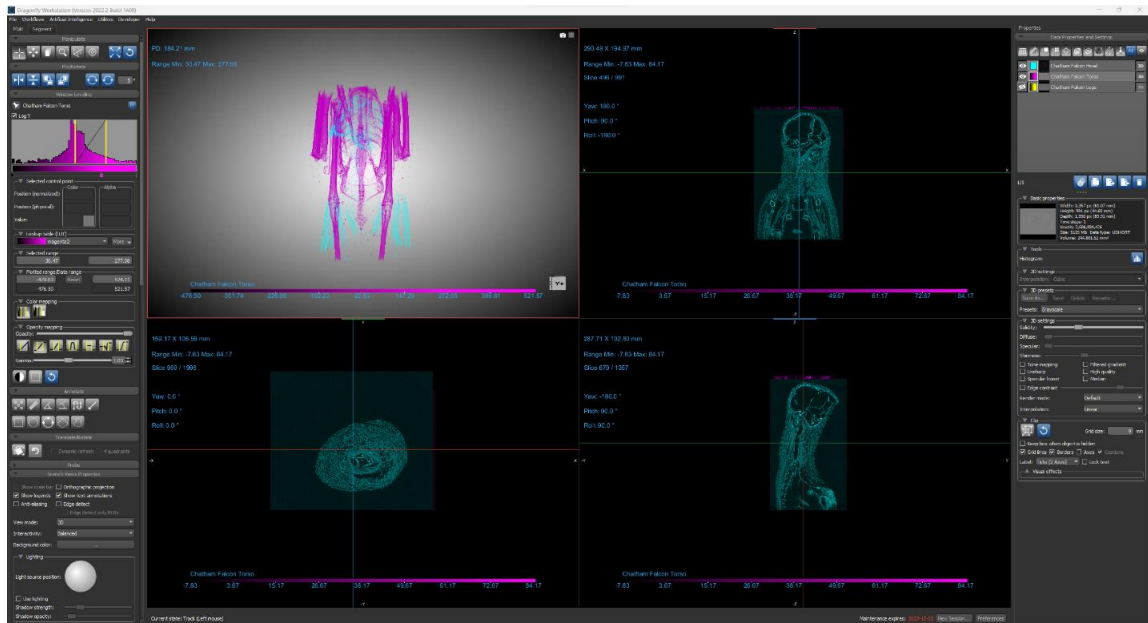


Figure B.6 Image showing 2 overlaid scans prior to adjustment to align anatomical features. Note the overlay of the features in 3D, showing that both scans are, in fact, visible, despite the pink scan (the torso) not being visible (yet) in 2D.

- 4) Select the displace button (yellow box, Figure B.7) under the translate/rotate tab.

This feature allows the user to move the images in each scan separately.

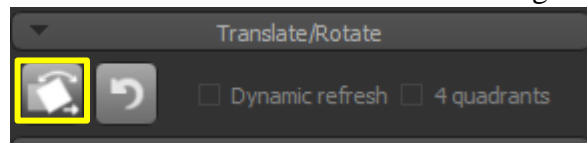


Figure B.7 The displace button in Dragonfly.

- 5) Select the desired data set. Left-click on the displace box that appears once the displace buttons (yellow arrow, Figure B.8) have been turned on, and move the upper data set to the top of the middle dataset. It helps to have the 3D image visible while working through the alignment to visualize how the 2D planes are moving in 3D space.

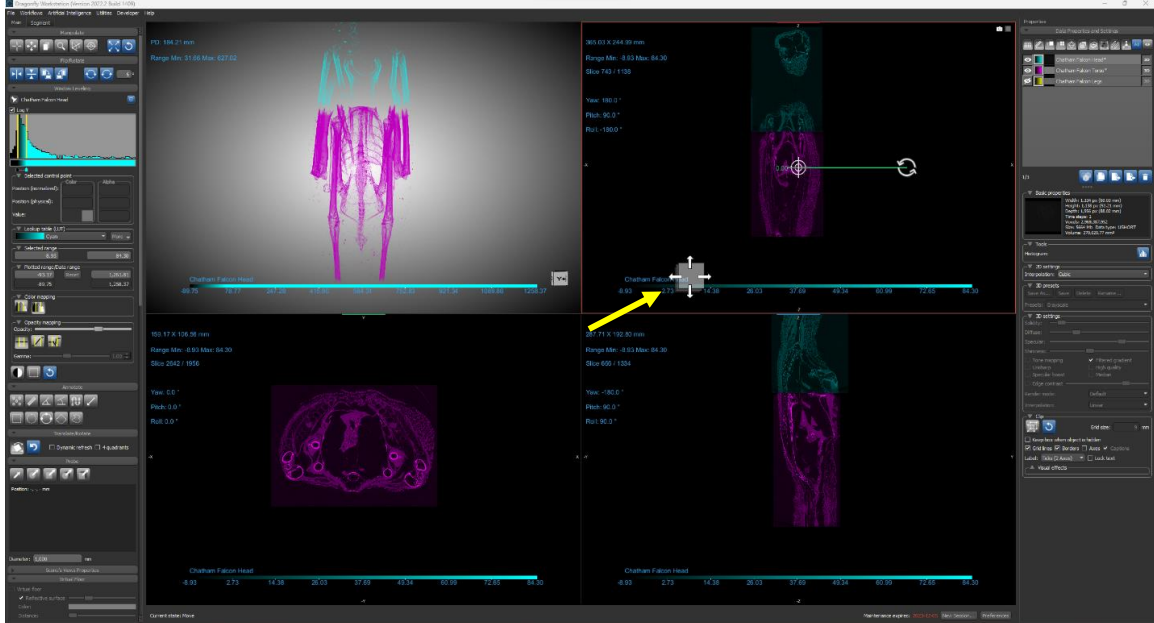


Figure B.8 Screen view of Dragonfly when working with the image displacement feature. The red arrow indicates the box which must be clicked in order to move one scan to a new location to overlap the neighbouring scan. In this case, the blue scan (the bird's head) has been moved above the pink scan (the bird's torso) to begin overlapping the anatomical features.

- 6) Adjust the opacity of the uppermost scan. Select the uppermost scan on the right-hand side. Adjust the opacity by sliding the opacity mapping bar left (found under the Windows Leveling tab). Lower the opacity to a point where the other scan can be seen underneath the adjusted scan.
- 7) Use the displace square to move the upper scan so that the anatomical features in both scans overlap. Moving the mouse up and down moves the slices up and down within the image panel. Moving the mouse left to right moves through the slices (of the selected scan), which allows you to find the proper anatomical features.

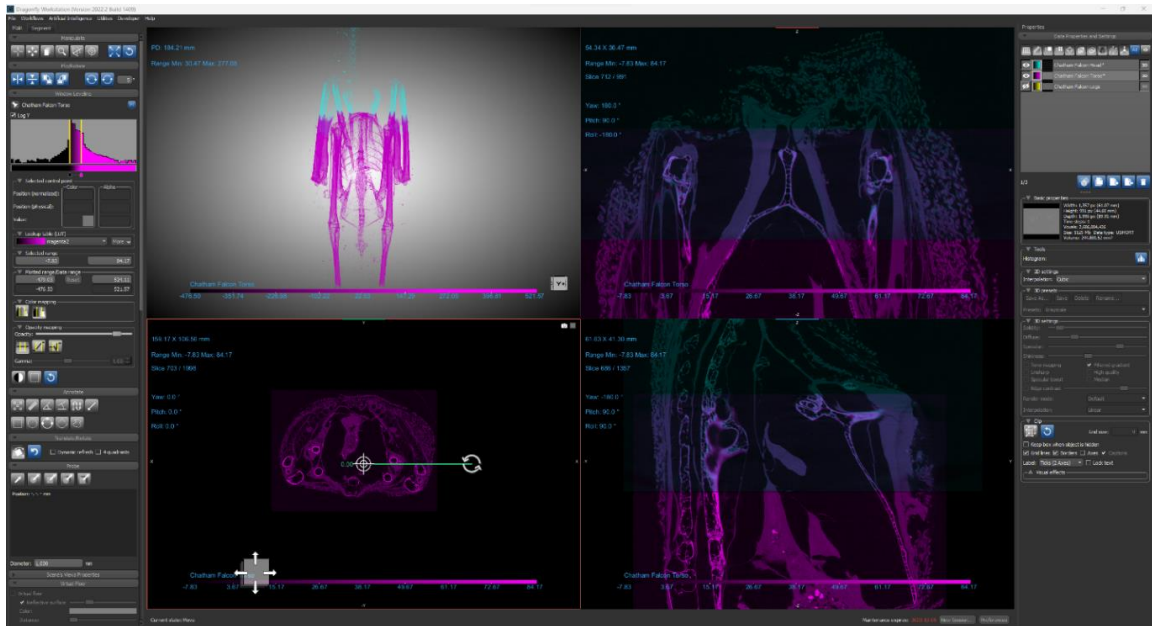


Figure B.9 Zoomed in image, showing how the uppermost and middlemost scans have been overlapped. Note how the anatomical features in both scans are perfectly aligned.

- 8) Scroll through the entire slice volume in all three planes to ensure all the features are aligned correctly. This can be done with the scroll wheel on the mouse or by hovering the mouse over the slice # in the upper left corner, holding the left mouse button down, and dragging the mouse.
- 9) Once the first scans have been correctly and accurately aligned, hide the topmost scan and turn on the bottommost scan (with the eye button). Leave the middlemost scan visible.



- 10) Repeat steps 4-8 in Part 2 of this procedural guide on the bottommost scan. (Note: this process can be repeated as many times as necessary, depending on how many scans need to be registered.)

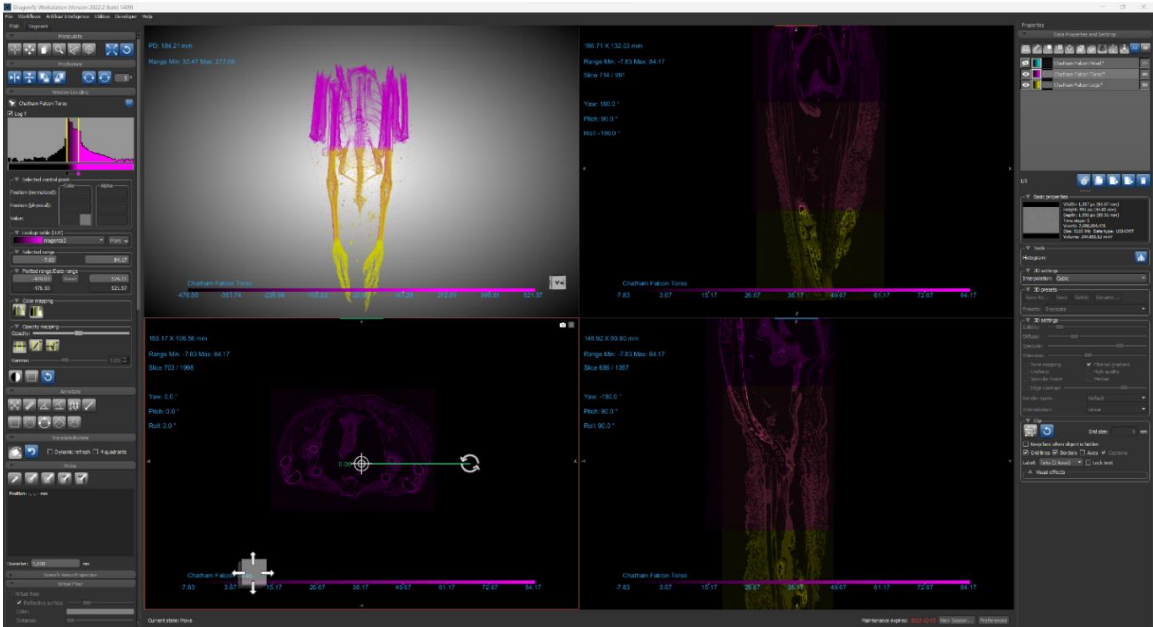


Figure B.10 Image showing the alignment of the bottommost and middlemost scan aligned following the protocol in Part 2 of this procedural guide.

- 11) After all your scans have been aligned, turn on all scans (eye button) and do one final check to ensure everything is correctly aligned.

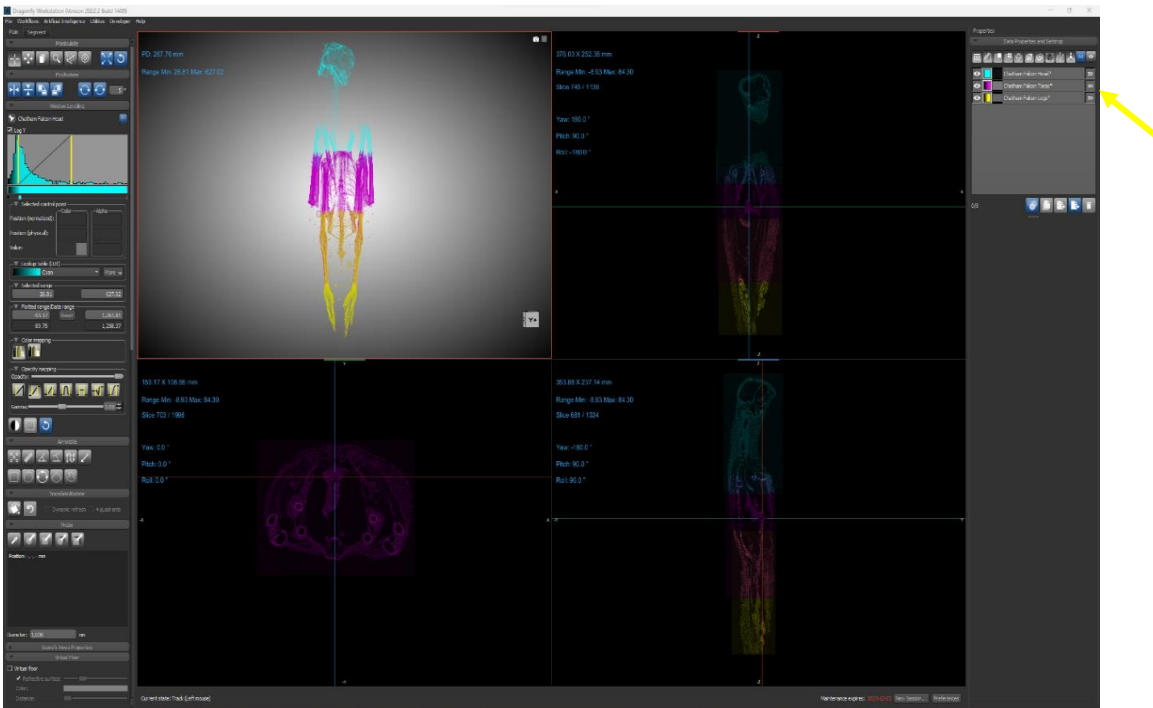


Figure B.11 Image showing the final alignment of all microCT datasets, prior to the final stitching.

## Part 2b: Auto-Alignment

In some instances, the manual alignment will fail to align the images perfectly. Once the scans have been aligned to the best of your ability (note the double borders in Figure B.12).

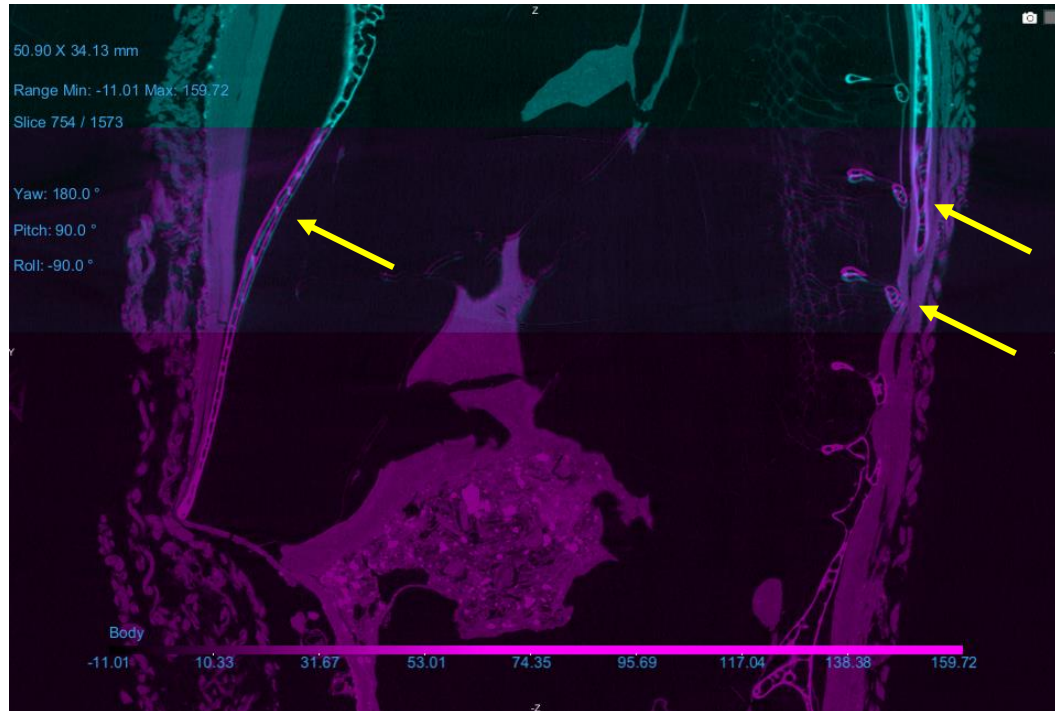


Figure B.12 Double border effect owing to improper alignment of two scans - note the areas the red arrows are pointing to.

- 1) Once the scans have aligned as best as possible, right-click on one of the datasets and select *Image Registration* (Figure B.13).
- 2) In the image registration pop-up, set one dataset as fixed (typically the one you are not moving) and the other as moving. Note that you can only do image recognition on two datasets at a time. If you are processing more, make sure the fixed dataset always stays the same. Once the datasets are selected, click apply.
- 3) Once the image registration is complete, the datasets should be accurately aligned. You can now complete the steps in Part 3 to finish stitching.

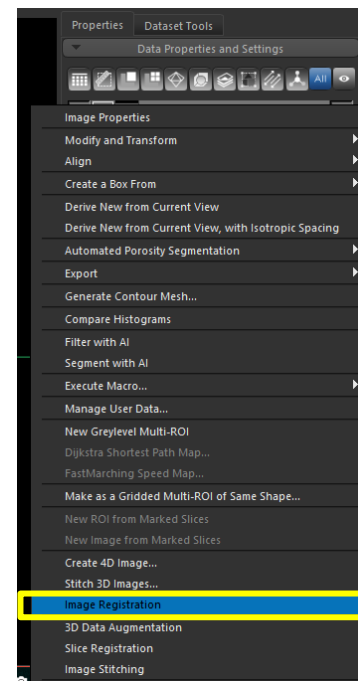


Figure B.13 Image registration for auto-alignment.

### Part 3: Stitching

- 1) While holding down the CTRL button, click on all of the datasets that have been aligned on the right-hand side of Dragonfly (red arrow in Figure B.11).
- 2) Right-click on one of the datasets and select *Stitch 3D Images...*
- 3) In the pop-up window, ensure all the datasets are present. Click *Stitch* (yellow box, Figure B.12).

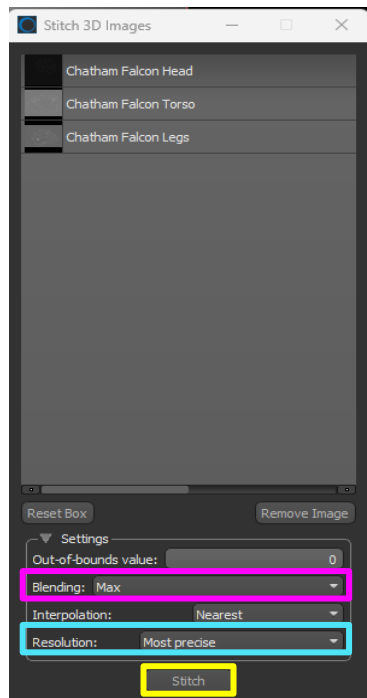


Figure B.14 Pop-up window for stitching 3D images in Dragonfly.

Tip: After stitching, if you find the image quality/resolution seems reduced or “fuzzier” than the original image quality, try to merge the images without blending (pink box, Figure B.14). This will overlap the scans, without losing any resolution – **but** it’s important that your scans are perfectly aligned for this because the image recognition algorithm will make no changes to the image alignment when it combines the volumes. And always make sure the resolution is set to *most precise*! (blue box, Figure B.14). Additional information on stitching settings can be found here: <https://www.theobjects.com/dragonfly/df/help/2024-1/Default.htm#Post-Processing/Stitch%203D%20Images/Settings%20for%20Stitching%203D%20Images.htm#output-parametersfor>

- 4) Once the stitching is complete, a new dataset (red arrow, Figure B.13) will appear in the original Dragonfly window, consisting of all the stitched scans, which can be used for all future analyses in Dragonfly. Note that the colours you set for the alignment will not be present in the stitched image; it will revert back to the original grayscale.

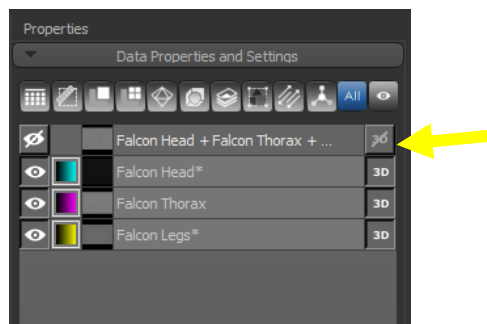


Figure B.15 New dataset in Dragonfly, resulting from stitching together multiple datasets.

## Appendix C: Procedural guide for training and applying a deep learning algorithm for 3D image segmentation

This three-part procedural guide walks the reader through the step-by-step process for training and applying a deep learning algorithm to micro-CT scans. I demonstrate this process with a scan of a frozen Cooper's Hawk from the Natural History collection at the Redpath Museum (Montreal, Quebec). The scan was acquired at 13.96  $\mu\text{m}$  on the Yxlon FF25 CT scanner. The following explanations can also be found in Mike Marsh's (Senior Director of Product Management at Dragonfly) deep learning tutorial:

<https://www.youtube.com/watch?v=8g7uT7ZiOjk>.

### Part 1: Set Up

Dragonfly is capable of processing multiple file types. Please refer to the following tutorials (<https://www.theobjects.com/dragonfly/tutorials.html>) on how to upload different image file types.

- 1) The user must identify the “ground truth” for algorithm training before beginning any segmentations. Right-click on any 2D image plane and select *Image Plane* to show you which 2D plane is the current ground truth. If this view can be used for segmentation, then no further steps are required to set ground truth. If you desire a different orientation for segmentation, click on the desired image plane (pink box, Figure C.1), then right-click on the data set on the left-hand side and click *Derive New From Current View* (yellow box, Figure C.1). A new dataset will appear on the left-hand side – this will be the dataset that will be used for segmentation.

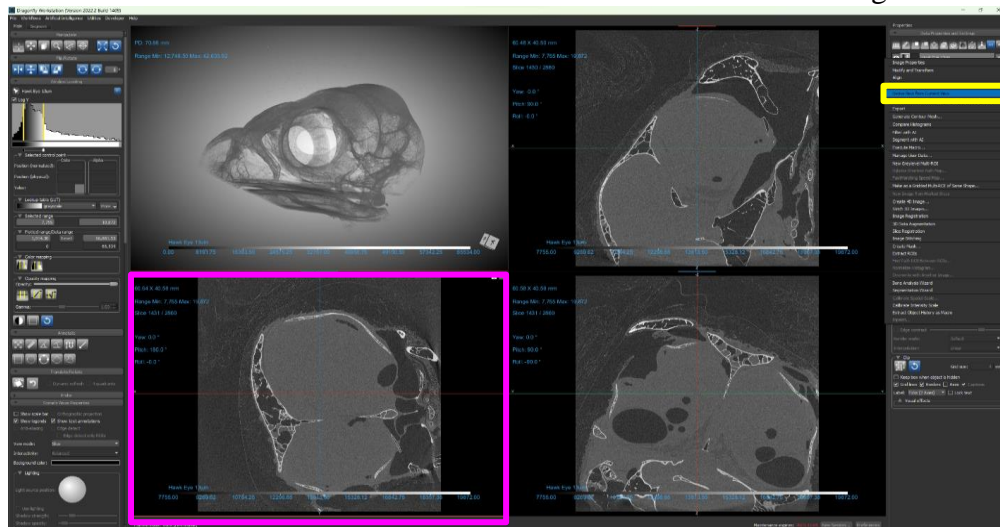


Figure C.1 Setting ground truth from desired image plane.

## Part 2: Segmentation and Training

- 1) Click on the *Artificial Intelligence* drop-down tab and select *Segmentation Wizard* (yellow box, Figure C.2). A pop-up window (Figure C.3) will appear, where all segmentations will be conducted.

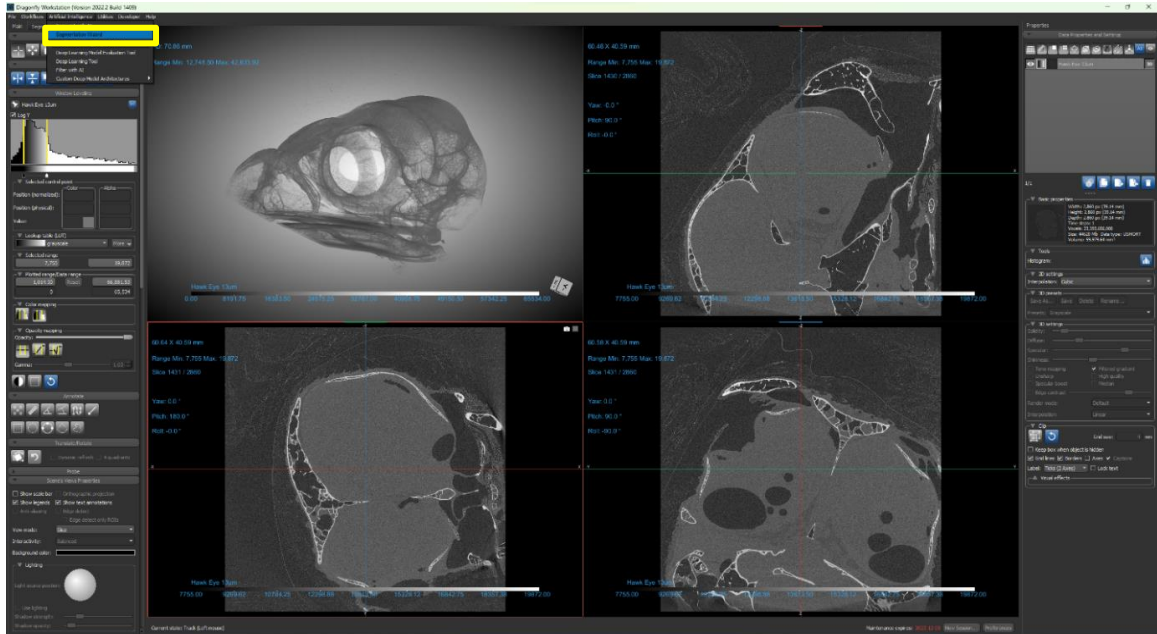


Figure C.2 Pop-up menu to open Segmentation Wizard.

- 2) Find the desired slice for segmentation. Click the new frame button (yellow box, Figure C.3). Decide how many data classes are being segmented (e.g., two classes – bone and background; 3 classes – bone, tissue, and background; etc.). To add more data classes, select the add button in the segmentation wizard (pink box, Figure C.3). Note that these classes can be renamed by double-clicking on the class.

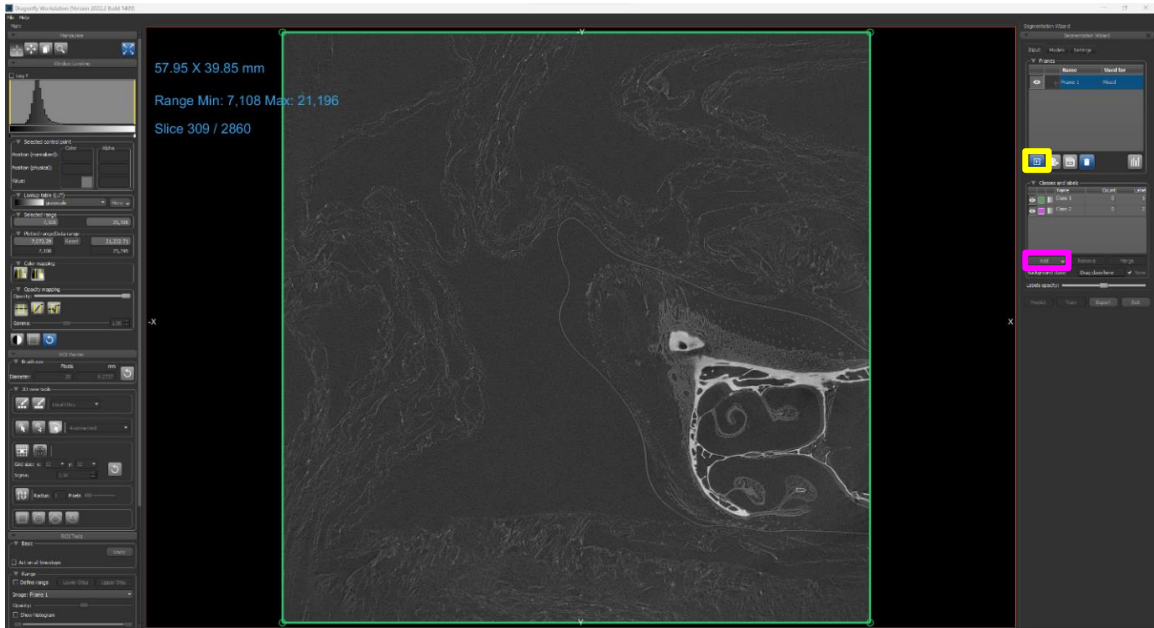


Figure C.3 Set up of data classes and frames in segmentation wizard, prior to segmentation.

- 3) To begin manual segmentations, click on the data class you will identify first. Use the ROI tools (Figure C.4) on the right-hand side to complete the segmentation.

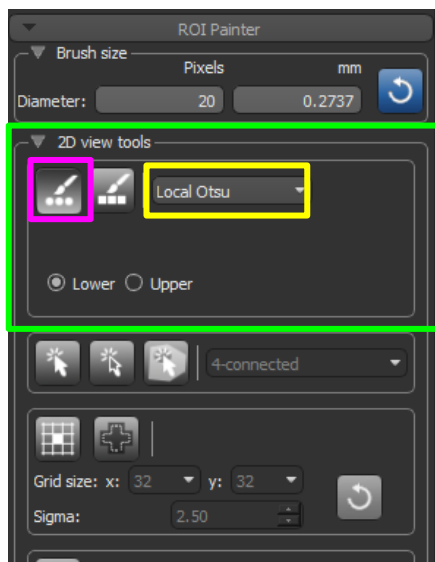


Figure C.4 ROI tools used for manual image segmentation.

The 2D view tools are used for image segmentation (green box, Figure C.4). Select 2D painter (pink box, Figure C.4), hold CTRL and the left clicker on the mouse to manually highlight the desired ROI. To erase, hold SHIFT and the left clicker on the mouse. The size of the paint brush can be adjusted by holding down CTRL and spinning the scroll wheel on the mouse.

Tip: The drop-down menu next to the painter tool (yellow box, Figure C.4) can be used to adjust which pixels are highlighted by the tool. E.g., the Local Otsu highlights pixels based on brightness.

### Tips: Manipulations in Dragonfly

- The slice can be moved by holding both the left and right clicker on the mouse and dragging the mouse.
- The slice can be zoomed in on by holding down the scroll wheel on the mouse and moving the mouse towards the computer (zoom out) and away from the computer (zoom in)
- To check the borders on a segmentation, adjust the opacity of the data class to reveal the true features on the image slice

- 4) Repeat the process in the next class (not including the background class) once the first class is segmented.
- 5) After segmenting the data classes, right-click on the background data class and select *Add All Unlabeled Voxels to Class*. This will automatically create the background class.

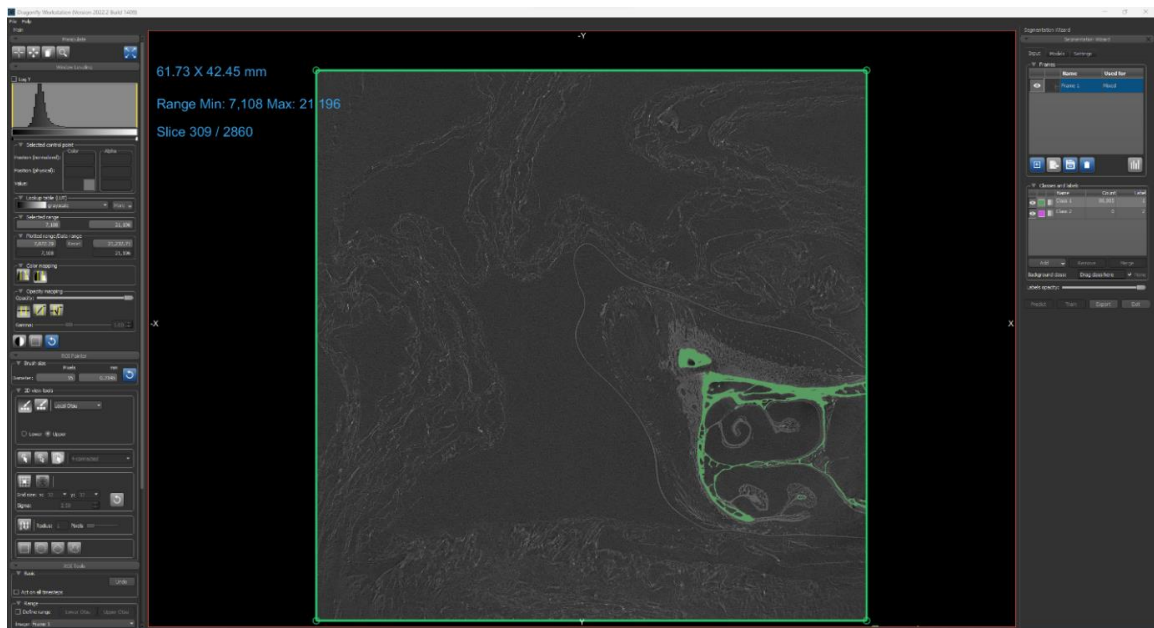


Figure C.5 Example of frame, with one segmented class of data.

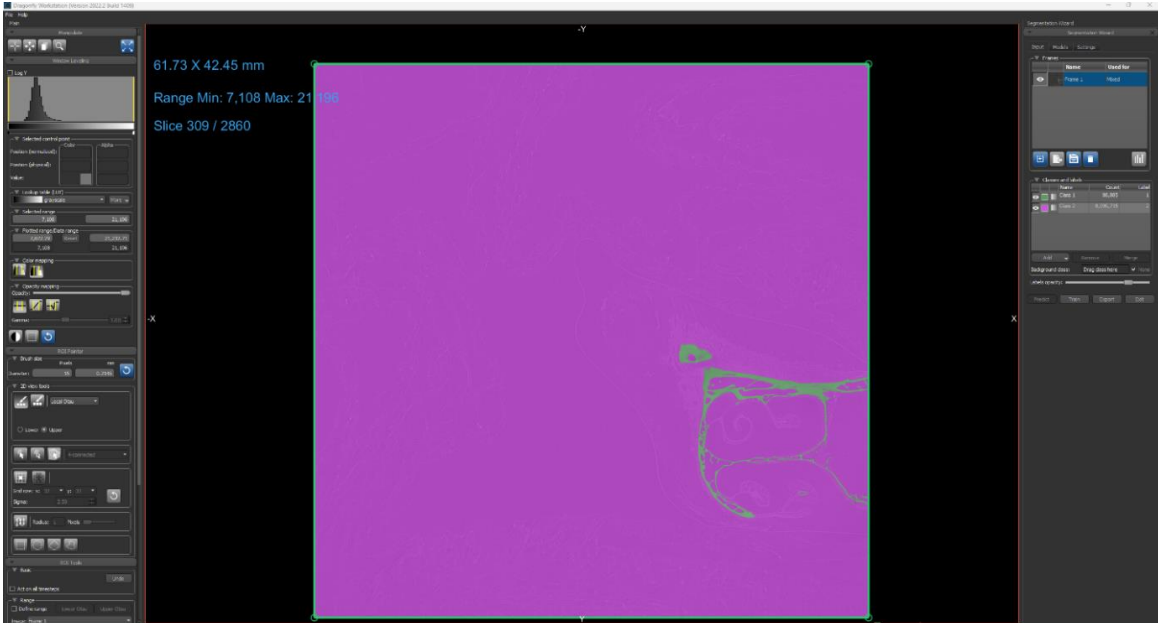


Figure C.6 Example of frame with segmented class and all background pixels labeled for the background class.

- 6) Repeat steps 2-5 in Part 2 of this procedure to segment multiple frames manually. For optimal results, 20% of the data set should be manually segmented before training the deep learning algorithm (e.g., 20 slices out of a 2000-slice data set). It is crucial to record the slice number of each segmented slice!
- 7) After all the slices have been segmented, export the multi-ROI from the segmentation wizard. Select the *Export all frames as a single multi-ROI* (yellow box, Figure C.7). Exit the segmentation wizard. This session will be saved in the segmentation wizard and can be returned at any time to fix segmentations or add more frames.

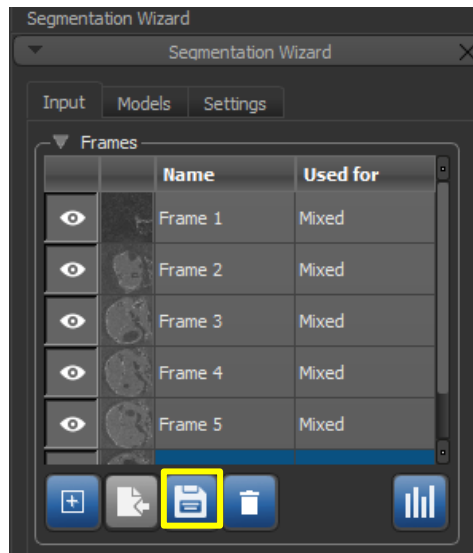


Figure C.7 Exporting a multi-ROI from segmentation wizard.



- 8) Once the multi-ROI has been exported, a mask must be created. A mask tells the deep learning training algorithm which slices in the data set have been segmented. Select the segment tab on the left-hand side to create a mask, click Create a new ROI, and label this ROI as a mask.
- 9) Find the first slice that was manually segmented. You can do this by scrolling through the dataset deck with the scroll wheel on your mouse or by right-clicking on the slice number in a panel and writing in the desired slice. Select the square ROI tool (yellow box, Figure C.8). Hold CTRL and drag the box across the entire segmented slice. Repeat this process with all the other manually segmented slices.

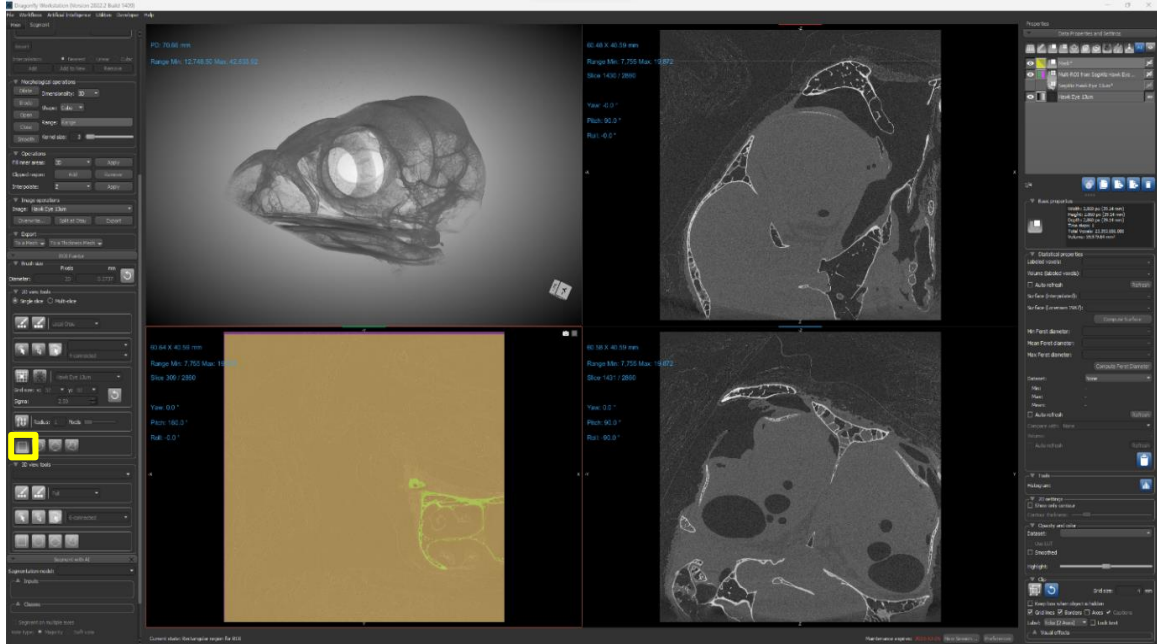


Figure C.8 Creating a mask ROI in Dragonfly for deep learning training.

- 10) The final step before training involves creating visual feedback. This allows the user to watch in real time as the algorithm adjusts its protocol during the training iterations. Select the main tab on the right-hand side. Scroll down to the annotate bar and select the square annotation (yellow box, Figure C.9). Drag a square across a new slice that has not been previously segmented and label the new dataset on the left-hand side as “visual feedback.”

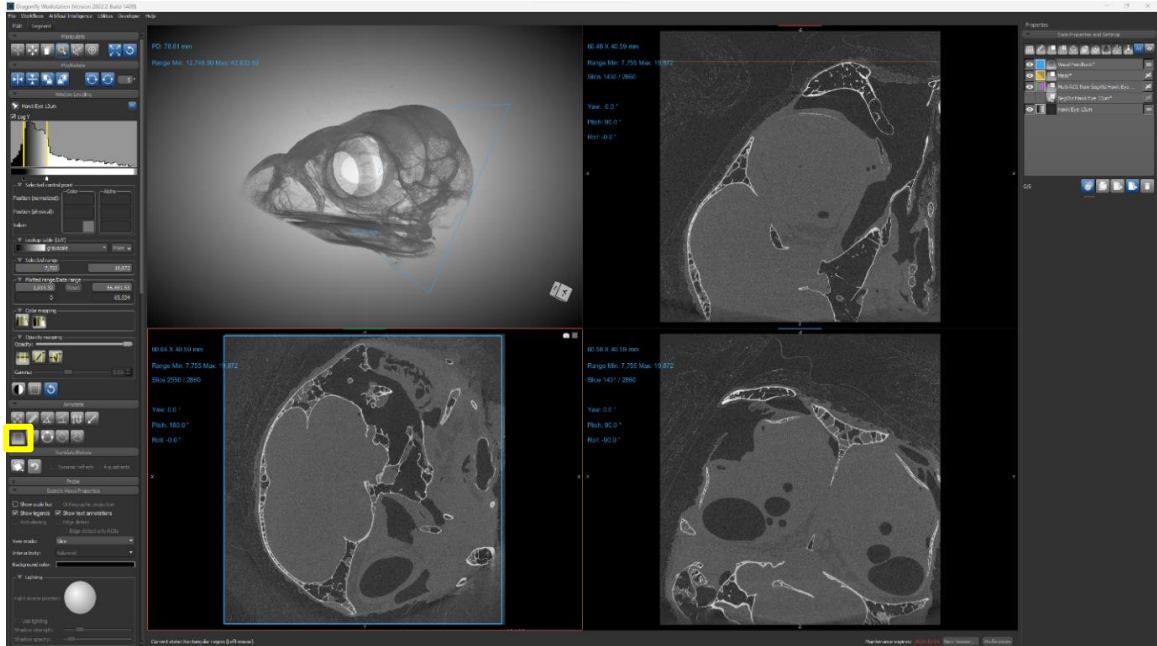


Figure C.9 Creating a visual feedback for deep learning training with a square annotation.

- 11) You should have the following datasets: the original CT scan (or a derived copy if ground truth had to be corrected), an exported multi-ROI, a mask ROI, and a visual feedback square. Open the *Deep Learning Tool* (yellow box, Figure C.10).

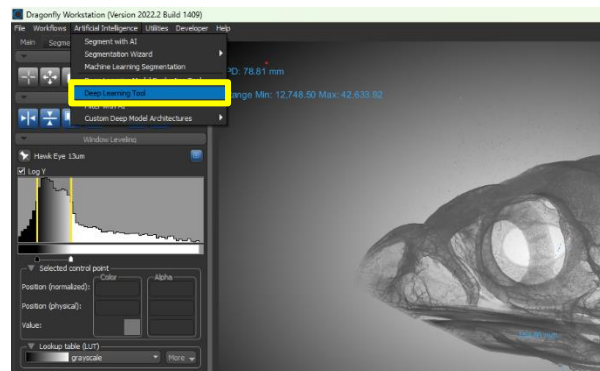


Figure C.10 Accessing the deep learning tool to input training data.

- 12) The model generator will appear. Select the desired model you wish to train (yellow box, Figure C.11). Be sure the class count (yellow arrow, Figure C.11) is set to the same number of classes you created in the manual training. Once you have selected your model and set the classes, click generate.

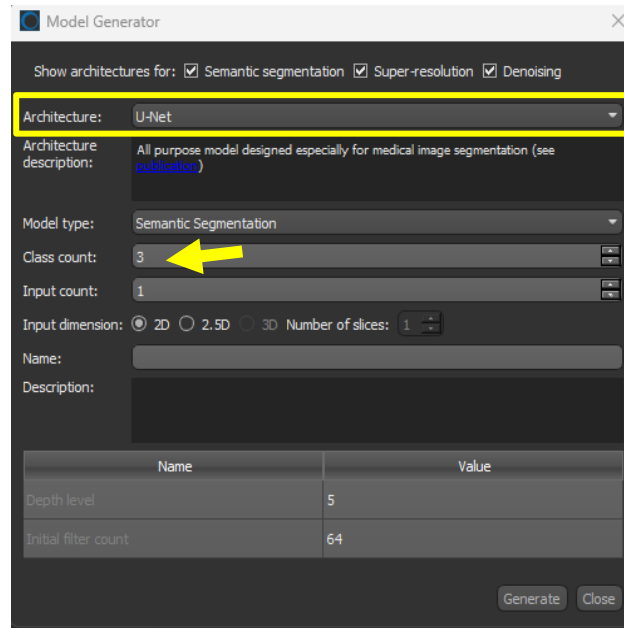


Figure C.11 Model generator in the deep learning tool.

Tip: In the Dragonfly architecture for deep learning, there is now a “pre-trained U-Net,” which has been trained by the Dragonfly engineers. This network can produce better output data, as there is already some training for image segmentation, and the network will not rely solely on your manually segmented slices. Instead, your input data will enhance the pre-trained parameters of the Dragonfly team. For details on the pre-trained algorithms visit <https://theobjects.com/dragonfly/deep-learning-pre-trained-models.html>.

Additional articles regarding the types of deep learning architectures can be found by clicking *see publications* in the architecture description box.

- 13) After generating the model, the deep learning tool opens the training parameters. Here, you need to tell the algorithm what data it will learn from. For additional deep learning parameters, see Appendix D. After everything is input, click train.

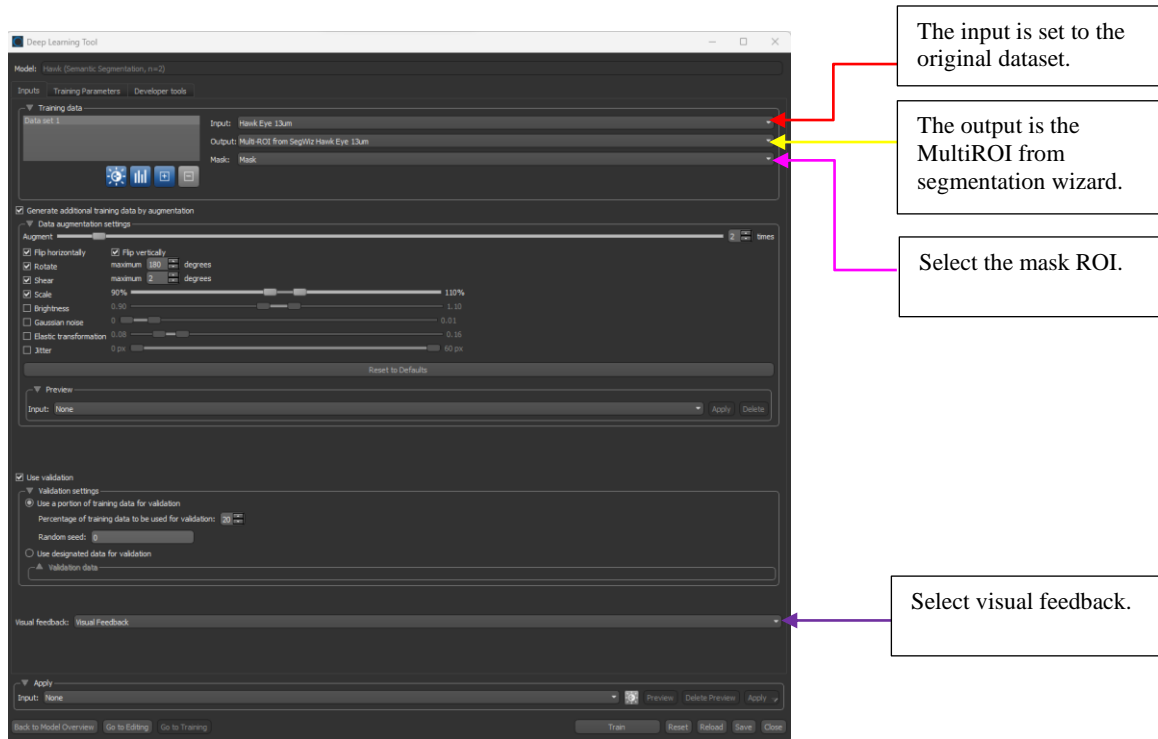


Figure C.12 Setting up the deep learning input data before training.

- 14) The training iterations will now begin (see Appendix D for details). Dragonfly can run a maximum of 100 epochs; however, it will automatically stop when the value of the loss function fails to decrease for ten consecutive epochs. Do not panic if your training does not reach 100 epochs—this is normal! During the iterations, you can observe real-time as the algorithm adjusts the data's boundaries with the image on the right-hand side.

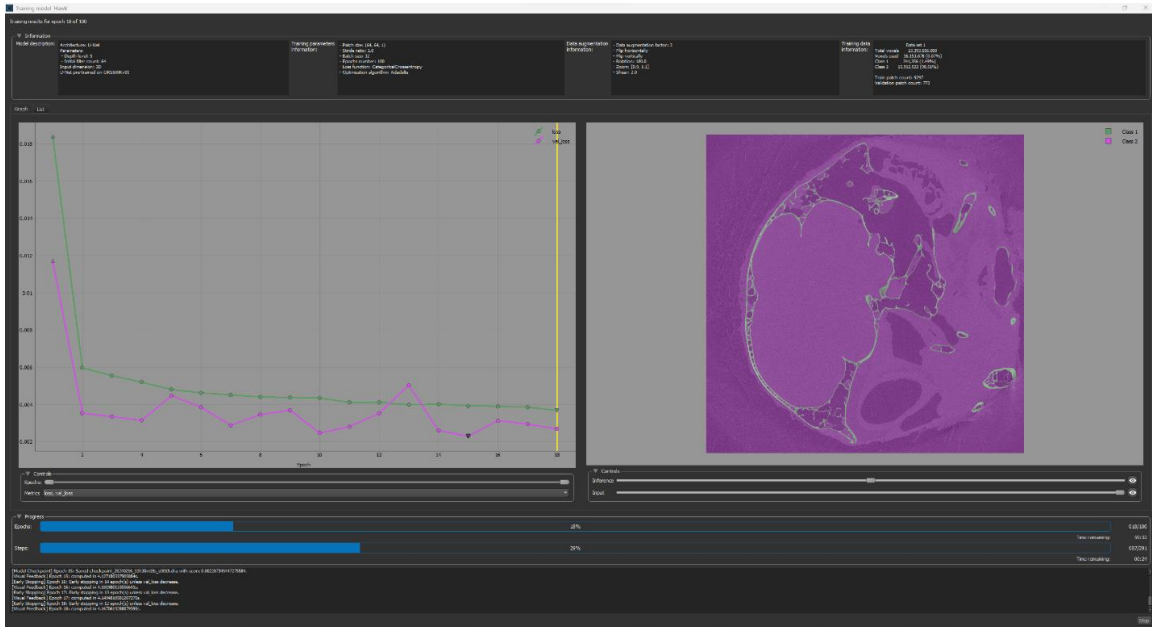


Figure C.13 Real-time training data. The green line represents the loss function of the training data, and the pink line represents the loss function of the validation. The image on the right-hand side shows real-time updates to the output data being produced as the algorithm is trained.

- 15) When the training is complete, the bottom right corner will have three options: export movie (this exports the real-time adjustments to the algorithm as seen in the visual feedback), export (this allows you to save your algorithm to your computer, which can then be transferred to other computers for use), and close (which saves all your data and closes the training pop-up).

### **Part 3: Application**

A trained deep learning algorithm can be applied immediately to a working dataset following training or saved for later use on new datasets.

- 1) To apply to the current working dataset, return to the deep learning pop-up after exiting the training session. At the bottom of the window, under apply, select the original raw dataset (yellow box, Figure C.14), and click preview. This will provide one slice segmented with the deep learning algorithm. If the algorithm did not output the desired results, re-start Part 2 of this appendix. If the results are desirable, proceed to click apply and apply to the entire dataset.

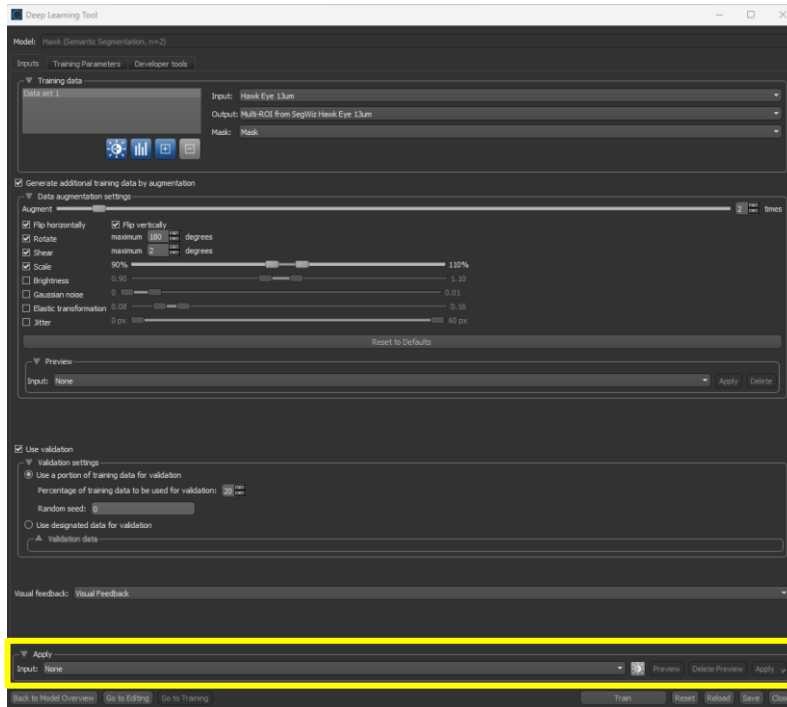


Figure C.14 Applying a trained deep learning algorithm to an entire dataset.

- 2) After the algorithm is applied to the dataset, close out of the deep learning tool. A new dataset called Segmentation will appear in Dragonfly. This is a multi-ROI with your separated data classes. This dataset can now be manipulated as desired.
- 3) To extract one class from the Multi-ROI, click on the segmentation dataset. Below, the individual ROIs will appear. Right-click on the desired ROI and select *Extract Class as an ROI* (yellow box, Figure C. 15).
- 4) To apply the trained deep learning algorithm to a new dataset, load the new dataset into Dragonfly. Open the segmentation wizard and segment a few slices (3 slices should do the trick at this point) of the new dataset. Export this (the same way as in Part 2, steps 2-7). Open the deep learning tab and select your trained algorithm. Go to training and set your input and output with your new data. Allow the training to run its iterations with the new data (this should be much faster than the original training process). Once the training is complete, click apply to all slices (Part 3, step 1).

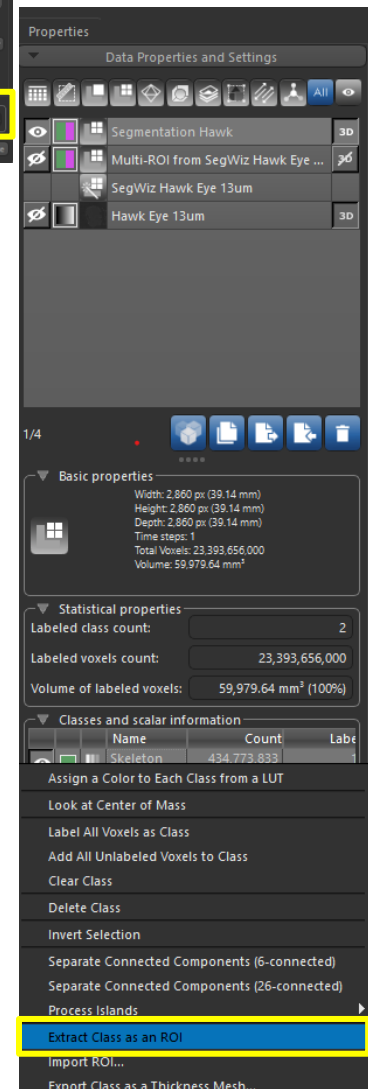


Figure C.15 Extracting a data class from a segmented Multi-ROI

**For a seminar I ran on Deep Learning, use the following link:**

**<https://youtu.be/PsWpxYV0DQg>**

## Appendix D: Understanding the deep learning parameters in Dragonfly

This appendix provides a more in-depth explanation of the training parameters that can be adjusted before training a deep learning algorithm. The following explanations can also be found in Mike Marsh's (Senior Director of Product Management at Dragonfly) deep learning tutorial: <https://www.youtube.com/watch?v=8g7uT7ZiOjk>.

When you do deep learning training, your input and output are decomposed into small patches (overlapping or non-overlapping).

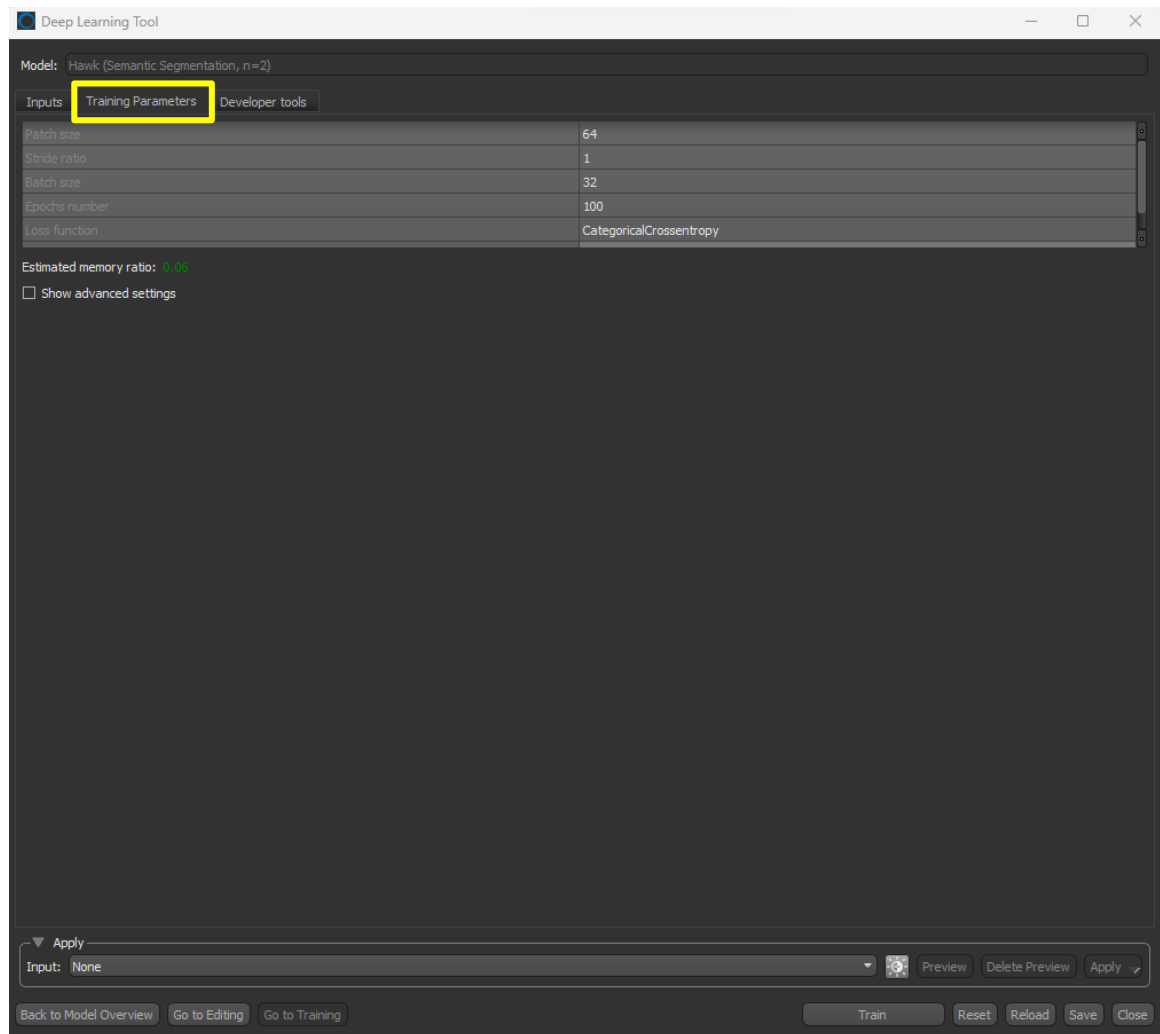


Figure D.1 Snapshot of the deep learning tool, showing the deep learning parameters which can be adjusted prior to a training iteration.



**Patch size:** For the large area where there is training data, the deep learning training will grab a  $n \times n$  ( $n$ =the number in the input size box) pixel patch, then move over and grab another patch. For each of those patches, you have the input and segmented images. For example, if you have a Patch Size of 64, the deep learning tool will divide the data set into sub-sections of 64x64 pixels. These subsections will be used as the training dataset. By dividing the images in such a way, each epoch should be faster and use less memory. Increasing the patch size can improve the performance of the CNNs classification and provide more reliable segmentation (Hamwood et al., 2018)

**Stride ratio:** The Stride ratio specifies the overlap between adjacent patches. A value of 1.0 = no overlap, where patches are not overlapping, and they are extracted sequentially. A value of 0.5 = a 50% overlap. Overlapping the input patches doubles the amount of training data, but it also means that the algorithm uses the training data twice. A value greater than 1.0 will result in gaps between the data patches. Increasing the stride ratio (i.e., no overlap) can decrease the time needed for training and reduce the computational load, but the model could lose some detailed information as it does not cover every pixel, resulting in reduced model accuracy (Sundararajan, 2024).

**Batch size:** In the deep learning training cycle, it will take a patch, push it through the network, get an output, compare that output to the ground truth output, and evaluate the cost function. Patches are randomly processed in batches, and the batch size determines the number of patches in one batch.

Hypothetically, suppose you have 100 patches and set **augmentation** to 2 (red arrow, Figure D.2); now you have 200 patches total. If you turn on **validation** (yellow arrow, Figure D.2) and set aside 20% of your data, it will set aside 20% of the non-augmented data for validation. Then, it will take the remainder of the data and put it through the network one patch at a time. After  $n$  patches (number set at the batch size) have gone through the network, it will look at the aggregate loss function from all  $n$  of those patches and then update the network weights. Then, it will repeat with the next batch of  $n$  patches. It will repeat this with every batch until it has done through the 80% of patches not being used for validation.

The network updates after every batch. A higher batch size will make for more computationally efficient training; a lower batch size will take much longer. A smaller batch size allows the model to learn from individual data that takes longer to train, whereas a larger batch size is faster to train but may not capture data nuances in the output model (Kandel & Castelli, 2020).

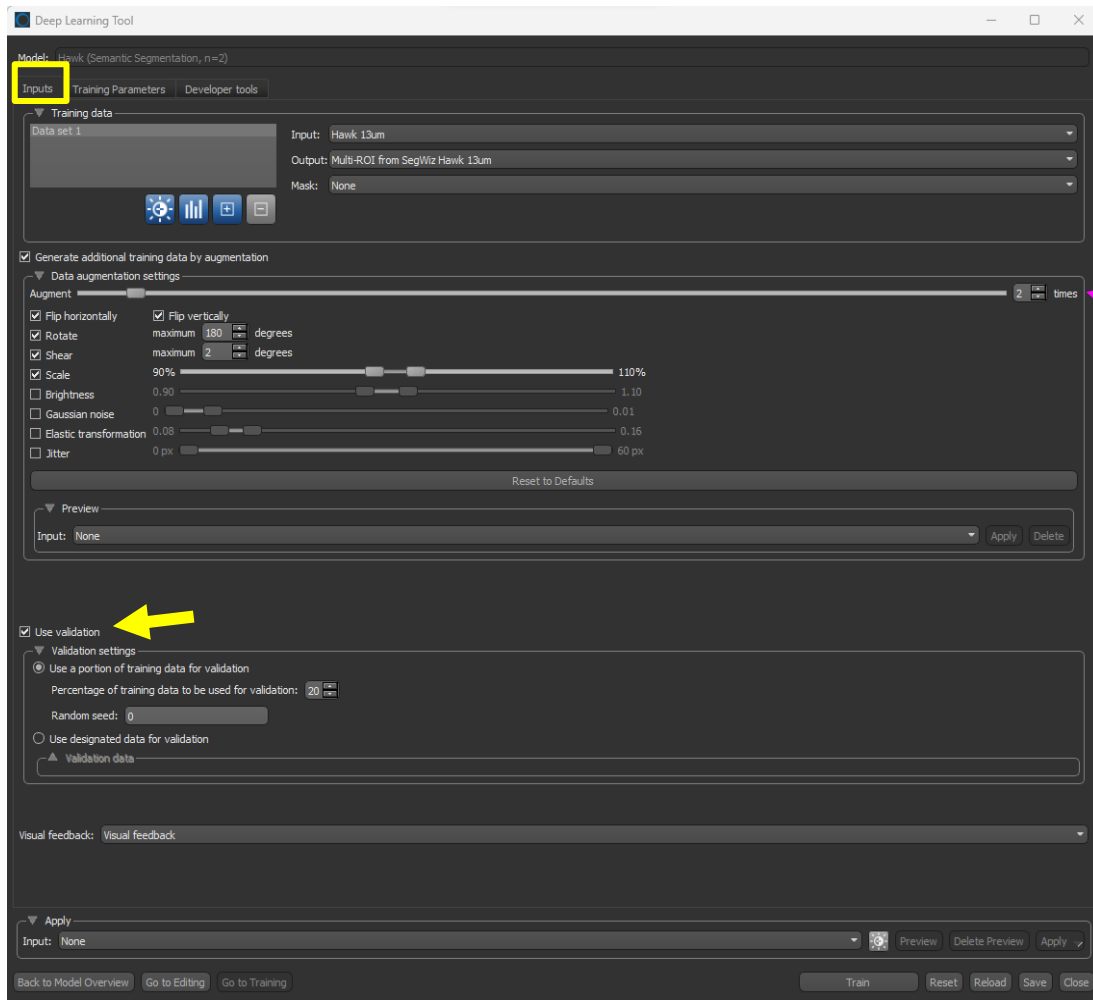


Figure D.2 Snapshot of deep learning parameters to set up augmentation and validation for training.

**Epochs:** A single pass over all the data patches is an epoch, including all patches not in validation. At that point, it will now push through all of the same training data again and give you a loss function for that batch of training data (green arrow, Figure D.3). It will report the loss function for the validation data (pink arrow Figure D.4) for the first epoch, and the whole cycle is repeated for a second epoch. You want to see the loss function fall and the accuracy increase.

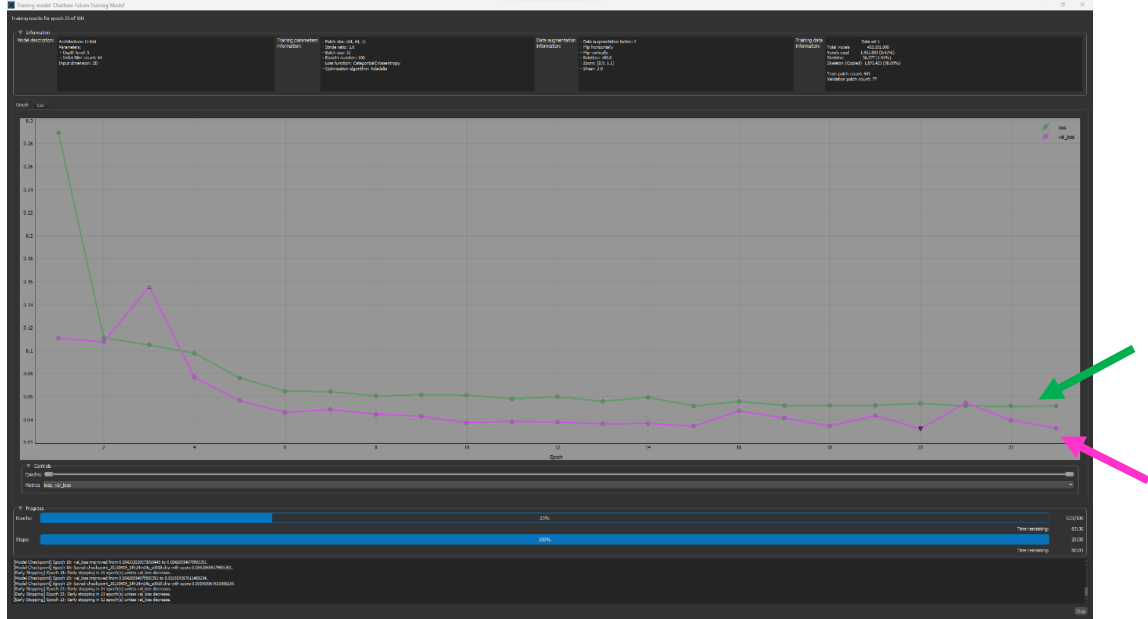


Figure D.3 Example of the loss function of training data and the loss function of the validation data during a U-Net training iteration.

Additional information on deep learning training can be found here:

[https://www.theobjects.com/dragonfly/dfhelp/2024-1/Default.htm#Artificial%20Intelligence/Artificial%20Intelligence.htm?TocPath=Artificial%2520Intelligence%257C\\_\\_\\_\\_\\_0](https://www.theobjects.com/dragonfly/dfhelp/2024-1/Default.htm#Artificial%20Intelligence/Artificial%20Intelligence.htm?TocPath=Artificial%2520Intelligence%257C_____0)

## Appendix E: Procedural guide for cleaning up segmented images using the Connected Components feature in Dragonfly

Some artifacts in a scan can be misidentified or need to be clarified for a deep learning algorithm when applied for image segmentation. In this thesis, a particularly challenging artifact was remnants of natron from the mummification process, which had a similar attenuation property compared to the skeletal remains of the birds. The connected components feature in Dragonfly can be used to remove these small artifacts following image segmentation with a deep learning algorithm. This is the procedural guide for using the connected components feature.

- 1) To begin, the ROI in need of cleaning up needs to be extracted from the segmented multi-ROI. To do so, click on the multi-ROI – on the left-hand side, the individual ROIs should appear. Right-click on the desired ROI (in this case, the skeleton) and select extract class as an ROI (yellow box, Figure E.1)

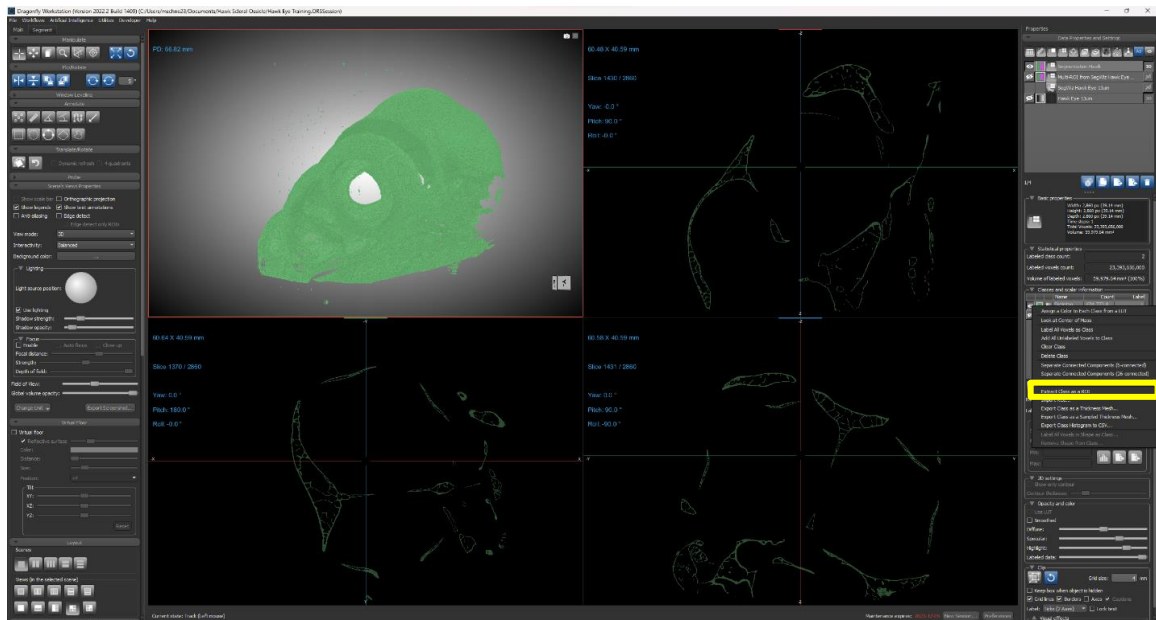


Figure E.1 Extracting a ROI from a segmented MultiROI.

- 2) The connected components in the extracted ROI need to be mapped. Right-click on the new ROI, hover over *Connected Components* (pink box, Figure E.2), and select *Multi-ROI analysis (#-connected...)* (yellow box, Figure E.2). Depending on the segmentation, there could be a few of the multi-ROI boxes, always selected the one with the highest number of connected components.

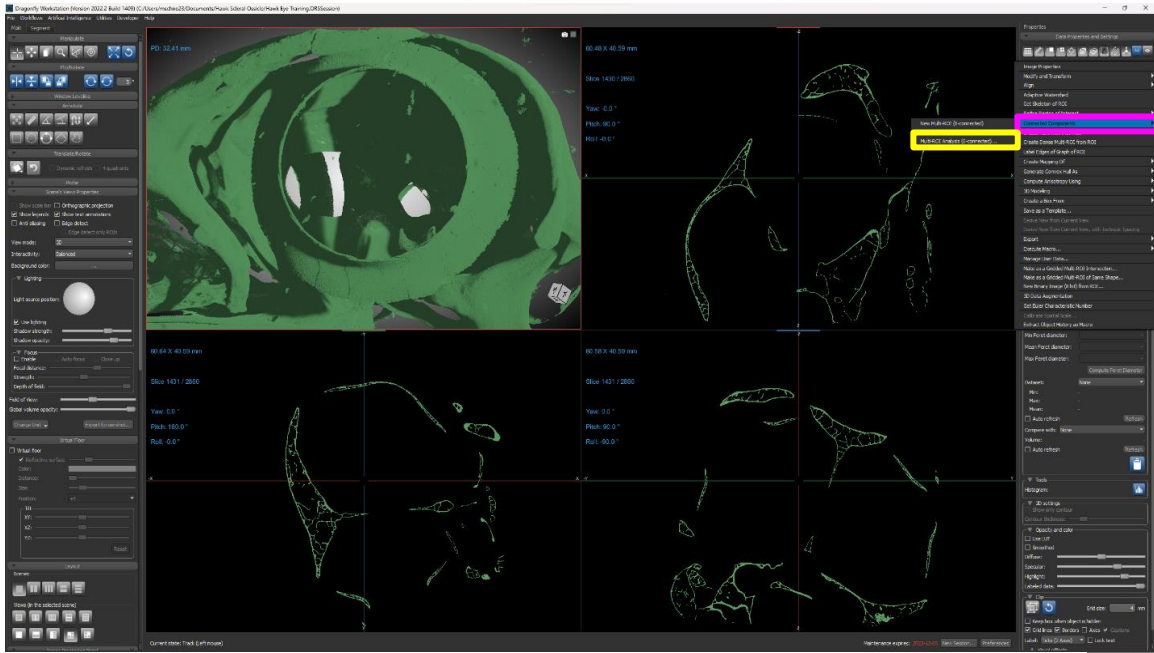


Figure E.2 Creating a MultiROI with the connected components feature.

- 3) After the connected components are mapped, an *Object Analysis* pop-up should appear. At this stage, the LUT needs to be set to as many colours as possible (e.g., discrete 32) (red box, Figure E.3). After the LUT has been set, select the hammer button (yellow box, Figure E.3).

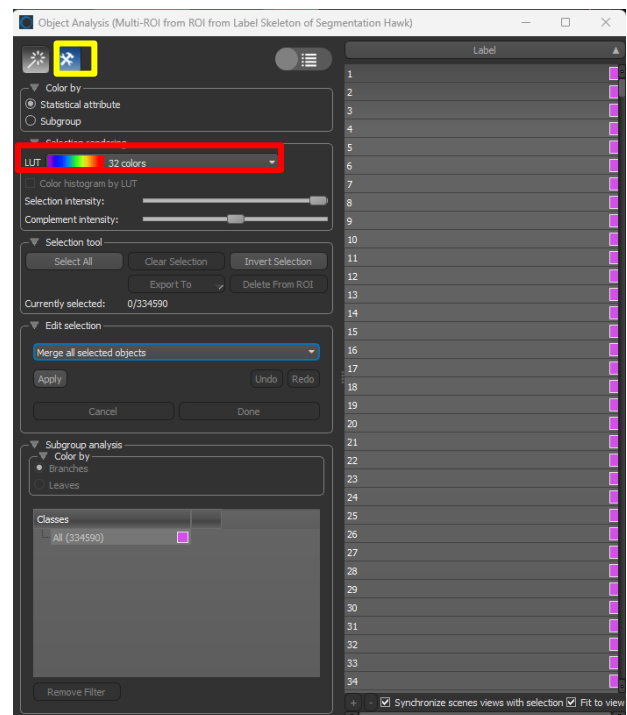
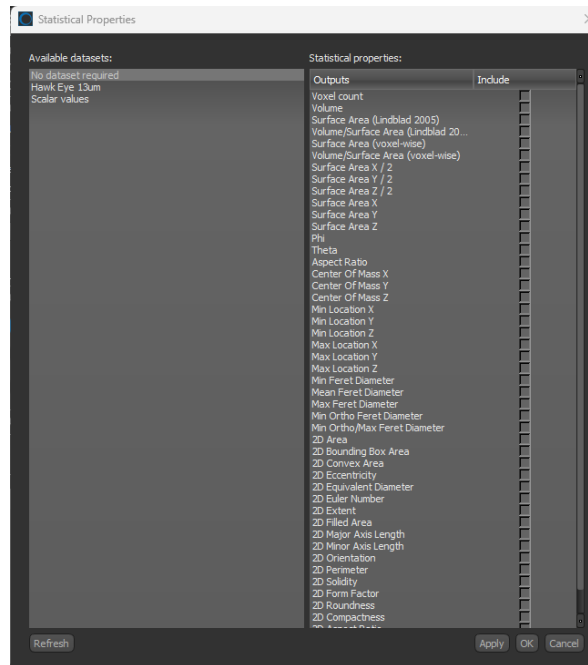


Figure E.3 Object Analysis pop-up in Dragonfly, following the creation of a Multi-ROI with the connected components feature.

- 4) This will open another pop-up tab with the statistical properties of the connected components multi-ROI. By selecting one of the options, all of the connected components will be sorted according to that statistical property. I recommend sorting the data by volume when dealing with small, drastically different sizes of artifacts (e.g., natron specs versus whole bones). Select your desired sorting mechanism and click OK. This will order all connected voxels from least to most.



*Figure E.4 Statistical properties of the connected components MultiROI.*

- 5) After mapping the connected components, your Dragonfly screen should look like Figure E.5. Note that the 3D model and the 2D planes are all mapped in varying colours—each colour represents a different volume size of connected components. On the right-hand side, there will also be a list of all the connected components, their colour, and their size (red box, Figure E.5).

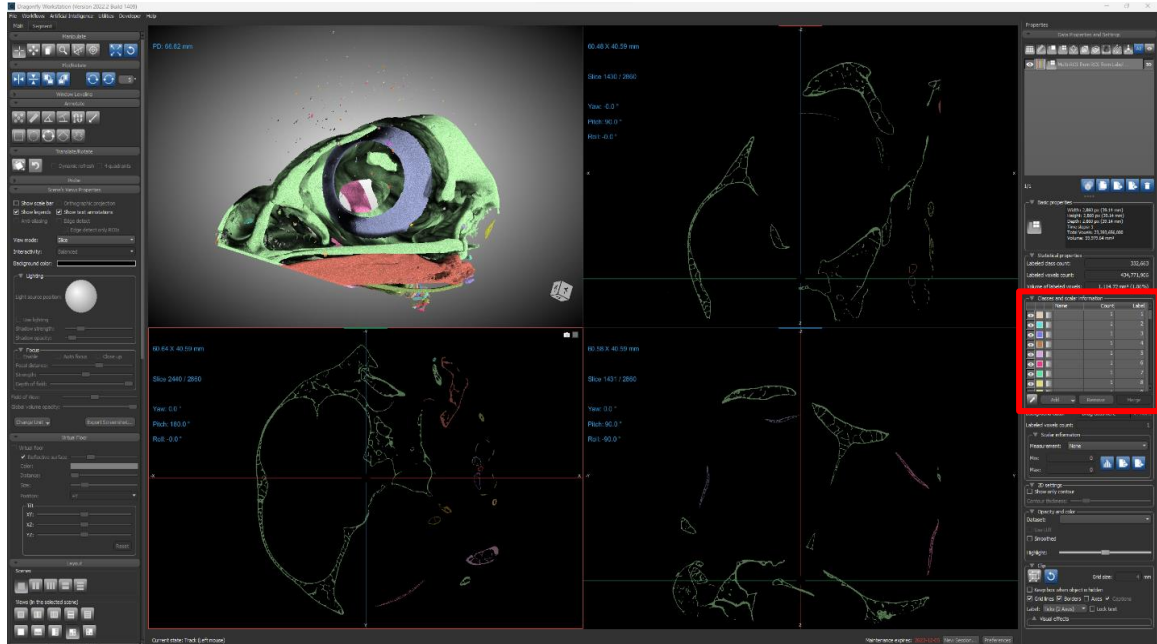
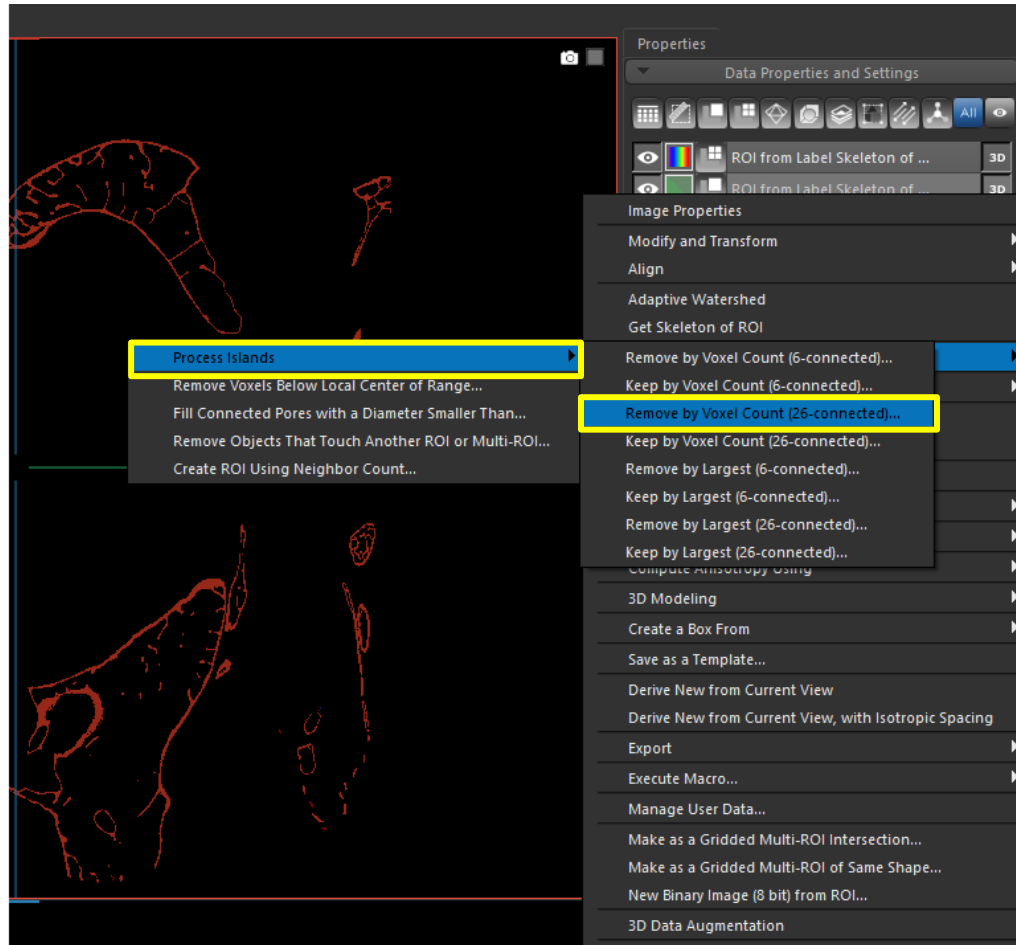


Figure E.5 Removing the smallest voxels from a connected components Multi-ROI.

- 6) Hold CTRL while highlighting the smallest voxels in the red box (Figure E.5). Once you have highlighted the desired voxels to remove, click remove. This process can be repeated until you achieve the desired resolution.

**Note:** If you are using a newer version of Dragonfly (i.e., Version 2024.1, Build 1579), this process has been significantly streamlined. The connected components analysis is no longer needed. To remove smaller connected voxels in this version, right-click on your segmented dataset, select connected components and click *New Multi-ROI (26-connected)*. In the new connected ROI, you must look at the voxel size and determine the smallest voxel (red box, Figure E.5) you want to include in your final image. Now, return to the original segmented data class. Right-click on the dataset, select *Refine Region of Interest*, select *Process Islands*, and click *Remove by Voxel Count (26-connected...)* (yellow boxes, Figure E.6). This will prompt you to input the smallest voxel you would like to include in the ROI, input the number you determined from looking at the connected components multi-ROI. Click OK; this will automatically remove all smaller voxels.



*Figure E.6 Removing small voxels with the process island feature in the updated version of Dragonfly.*



## Appendix F: Measuring bones in Dragonfly

This procedural guide demonstrates how the long bones of each bird were measured (following methods from Spake et al., 2020, modified in Dr. Nelson's lab). Shown here are the measurements of a humerus from the Chatham Falcon bundle, scanned at 110  $\mu\text{m}$  on the Nikon Metris XT H 225 ST cabinet scanner.

- 1) Find the bone you want to measure in the bottom right panel (XY view). Adjust the blue and red axis lines so they intersect with the bone (hover your cursor over the lines; small arrows should appear; use these arrows to manipulate the direction of the line).
- 2) Set the *View Mode* to *Slab average* (yellow box, Figure F.1).
- 3) Dotted lines should appear around the original axis lines. Drag these dotted lines out from the axis so that they match the diameter of the bone. This will bring an overlaid view of the 2D slices into view on the other 2D panels, enabling the view of the entire bone. Set the slab thickness to include the width of the whole bone. You can also right-click on one of the 2D scenes, click *Set Slab Thickness...*, and set the desired thickness.

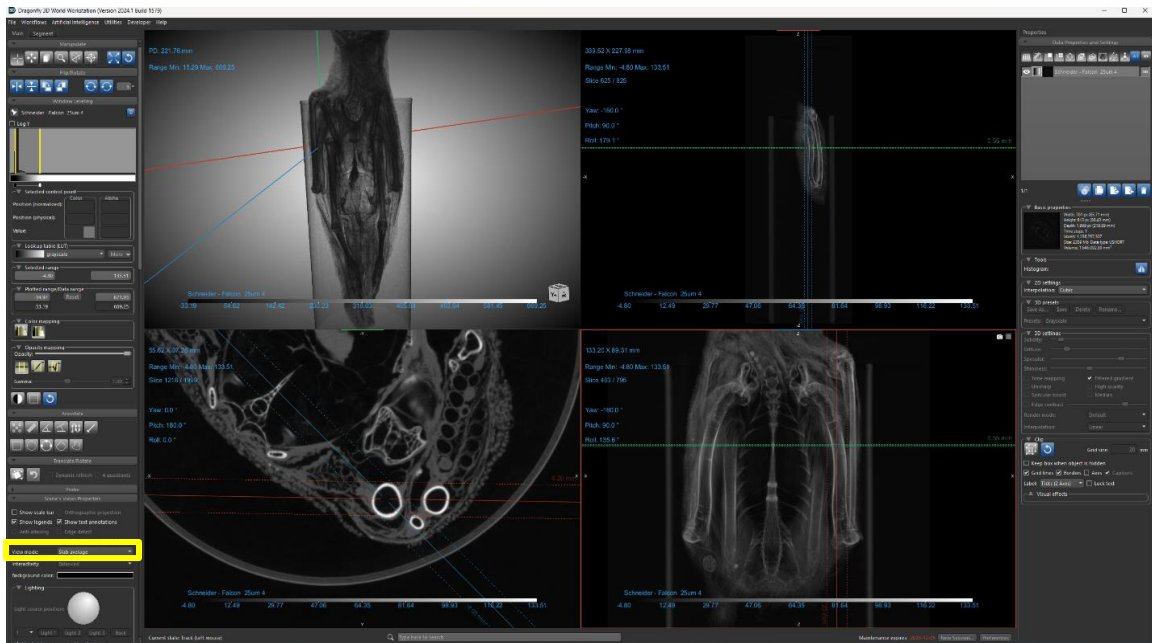


Figure F.1 Setting up slab view and axis orientation prior to measurements.

- 4) Once the bone is in full view, use the anterior-posterior view to take the measurements. First, the distal and proximal ends of the bone must be “capped” to measure the line of best fit. Use the arrow button (pink box, Figure F.2) to draw lines on the ends of the bone (Figure F.3).



Figure F.2 Annotation features for measurements in 2D.

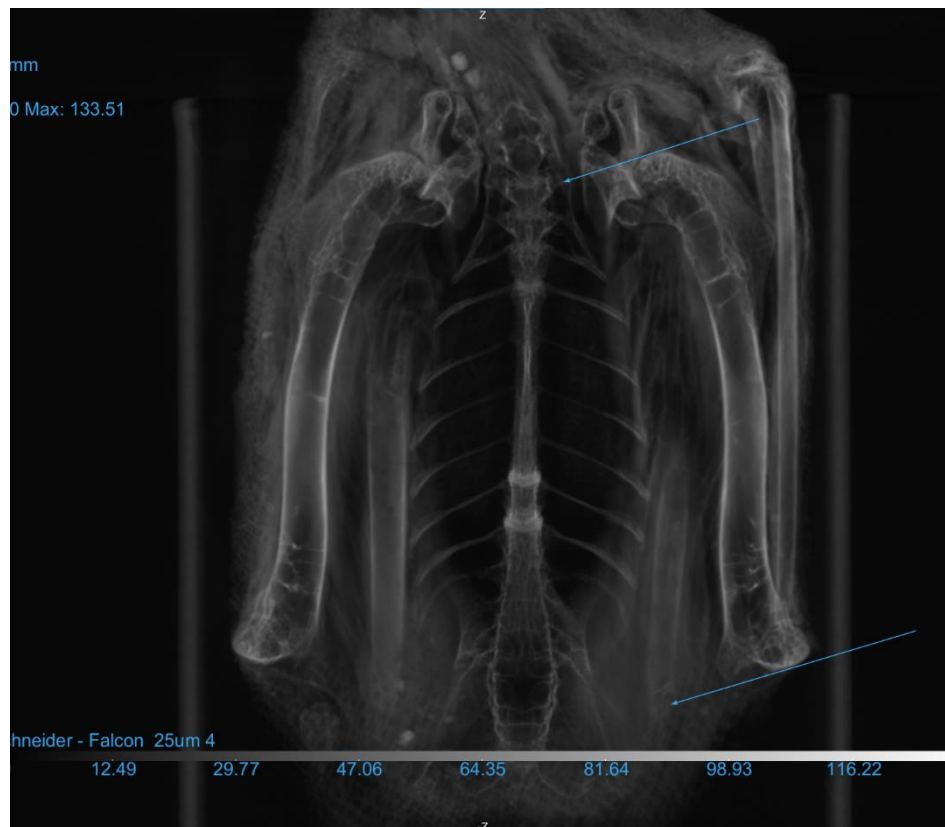
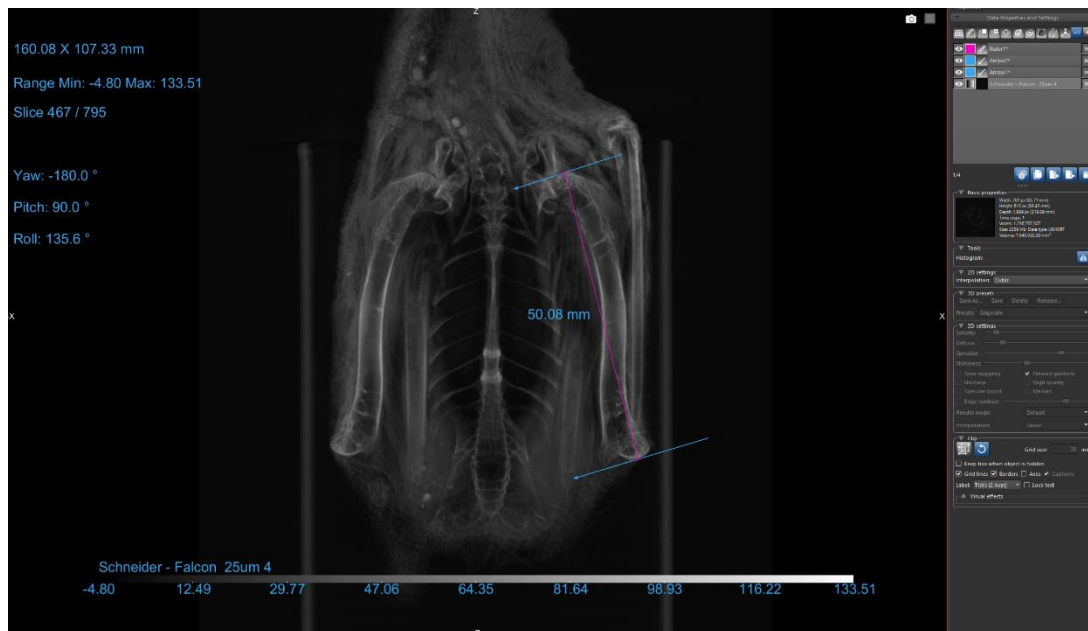


Figure F.3 Capping the distal and proximal end of the humerus to measure total length of the bone.

Use the ruler tool (yellow box, Figure F.2) to measure the median line of best fit between the proximal and distal end of the long bone. Be sure to zoom in on the lines and ensure



*Figure F.4 Measuring between the distal and proximal end of the humerus for total length measurement.*

### Appendix G: Raw measurements of known species of mummified birds

Table G.1 Measurements taken of mummified birds from *La faune momifiée de l'ancienne Égypte* (Lortet & Galliard 1905), with updated nomenclature from Baillel-Leseur (2012) and the ITIS. Species names are listed in order as they appear in the taxonomic tree from Chapter 3.

| Documented species        | Common name                     | Updated species name        | F1  | F2 | F3  | F4  | F5  | F6  | F7  | F8  |
|---------------------------|---------------------------------|-----------------------------|-----|----|-----|-----|-----|-----|-----|-----|
| <i>Pandion haliaetus</i>  | Osprey                          | -                           | 76  | 44 | 144 | 185 | 87  | 79  | 125 | 53  |
| <i>Accipiter nisus F</i>  | European sparrowhawk            | -                           | 50  | 28 | 62  | 73  | 39  | 55  | 75  | 63  |
| <i>Accipiter nisus M</i>  | European sparrowhawk            | -                           | 42  | 25 | 50  | 60  | 32  | 43  | 59  | 52  |
| <i>Aquila maculata</i>    | Greater spotted eagle           | <i>Aquila clanga</i>        | 92  | 50 | 137 | 168 | 72  | 83  | 127 | 90  |
| <i>Aquila fulva</i>       | Golden eagle                    | <i>Aquila chrysaetos</i>    | 114 | 63 | 183 | 211 | 100 | 124 | 168 | 104 |
| <i>Aquila imperialis</i>  | Imperial eagle                  | <i>Aquila heliaca</i>       | 115 | 62 | 188 | 219 | 99  | 113 | 150 | 92  |
| <i>Buteo vulgaris</i>     | Common buzzard                  | <i>Buteo buteo buteo</i>    | 79  | 45 | 108 | 120 | 60  | 76  | 103 | 75  |
| <i>Buteo desertorum</i>   | Common buzzard (Western steppe) | <i>Buteo buteo vulpinus</i> | 71  | 43 | 100 | 113 | 58  | 73  | 100 | 73  |
| <i>Buteo ferox</i>        | Long-legged buzzard             | <i>Buteo rufinus</i>        | 88  | 51 | 131 | 148 | 74  | 89  | 125 | 92  |
| <i>Circaetus gallicus</i> | Short-toed eagle                | -                           | 102 | 65 | 160 | 189 | 79  | 80  | 123 | 86  |
| <i>Circus aeruginosus</i> | Western marsh harrier           | -                           | 82  | 48 | 108 | 130 | 62  | 81  | 109 | 83  |
| <i>Circus cyaneus</i>     | Hen harrier                     | -                           | 63  | 37 | 89  | 108 | 57  | 68  | 98  | 74  |
| <i>Circus macrourus</i>   | Pallid harrier                  | -                           | 60  | 35 | 80  | 98  | 51  | 60  | 90  | 68  |
| <i>Circus pygargus</i>    | Montagu's harrier               | -                           | 57  | 35 | 84  | 102 | 52  | -   | 79  | 58  |

|                                |                              |                                       |     |    |     |     |    |    |     |     |
|--------------------------------|------------------------------|---------------------------------------|-----|----|-----|-----|----|----|-----|-----|
| <i>Elanus caeruleus</i>        | Black-winged/shouldered kite | -                                     | 57  | 34 | 76  | 90  | 43 | 49 | 66  | 33  |
| <i>Haliaeetus abielicillus</i> | White-tailed sea eagle       | <i>Haliaeetus albicilla</i>           | 97  | 49 | 167 | 201 | 84 | 97 | 142 | 80  |
| <i>Aquila pennata</i>          | Booted eagle                 | <i>Hieraaetus pennatus</i>            | 71  | 43 | 98  | 124 | 54 | 68 | 95  | 57  |
| <i>Melierax gabar</i>          | Gabar goshawk                | <i>Micronisus gabar</i>               | 50  | 28 | 55  | 65  | 32 | 47 | 64  | 48  |
| <i>Milvus aegyptius</i>        | Yellow-billed kite           | <i>Milvus migrans</i>                 | -   | 45 | 115 | 133 | 64 | 63 | 82  | 54  |
| <i>Pernis apivorus</i>         | European honey buzzard       | -                                     | 81  | 39 | 112 | 125 | 62 | 60 | 90  | 53  |
| <i>Falco feldeggi</i>          | Lanner falcon                | <i>Falco biarmicus</i>                | 62  | 38 | 74  | 86  | 51 | 60 | 76  | 49  |
| <i>Hierofalco saker</i>        | Saker falcon                 | <i>Falco cherrug</i>                  | 70  | 42 | 91  | 105 | 60 | 73 | 90  | 54  |
| <i>Falco barbarus</i>          | Barbary falcon               | <i>Falco peregrinus pelegrinoides</i> | 61  | 36 | 64  | 75  | 45 | 54 | 67  | 41  |
| <i>Falco peregrinus</i>        | Peregrine falcon             | <i>Falco peregrinus peregrinus</i>    | 68  | 39 | 84  | 95  | 59 | 69 | 87  | 52  |
| <i>Falco subbuteo</i>          | Eurasian hobby               | -                                     | 50  | 30 | 59  | 68  | 39 | 45 | 59  | 35  |
| <i>Cerchneis tinnunculus</i>   | European/common kestrel      | <i>Falco tinnunculus</i>              | 48  | 30 | 56  | 63  | 35 | 45 | 60  | 38  |
|                                |                              |                                       |     |    |     |     |    |    |     |     |
| <i>Ibis aethiopica</i>         | Sacred ibis                  | <i>Threskiornis aethiopicus</i>       | 250 | 33 | 127 | 146 | 71 | 77 | 163 | 114 |

F1 – Length of head (with beak)

F2 – Breadth of head

F3 – Length of humerus

F4 – Length of ulna

F5 – Length of metacarpus

F6 – Length of femur

F7 – Length of tibia

F8 – Length of tarsometatarsus

### Appendix H: Skeletal measurements and calculated differences from studied mummified birds

Table H.1 Cranial and long bone measurements of studied mummified birds (bolded) and calculated differences from documented, known species, skeletal measurements in Lortet and Gaillard (1905) (see Table G.1 for raw data regarding documented species).

| Studied bird   | Documented species           | Updated species name                  | Length of head | Breadth of head | Humerus      | Ulna         | Metacarpus   | Femur        | Tibiotarsus  | Tarsometatarsus |
|----------------|------------------------------|---------------------------------------|----------------|-----------------|--------------|--------------|--------------|--------------|--------------|-----------------|
| Chatham Falcon |                              |                                       | <b>45.03</b>   | <b>28.86</b>    | <b>50.27</b> | <b>57.98</b> | <b>31.93</b> | <b>42.64</b> | <b>55.02</b> | <b>38.67</b>    |
|                | <i>Falco barbarus</i>        | <i>Falco peregrinus pelegrinoides</i> | 15.97          | 7.14            | 13.73        | 17.02        | 13.07        | 11.36        | 11.98        | 2.33            |
|                | <i>Falco feldeggi</i>        | <i>Falco biarmicus</i>                | 16.97          | 9.14            | 23.73        | 28.02        | 19.07        | 17.36        | 20.98        | 10.33           |
|                | <i>Falco peregrinus</i>      | <i>Falco peregrinus peregrinus</i>    | 22.97          | 10.14           | 33.73        | 37.02        | 27.07        | 26.36        | 31.98        | 13.33           |
|                | <i>Falco subbuteo</i>        | -                                     | 4.97           | 1.14            | 8.73         | 10.02        | 7.07         | 2.36         | 3.98         | -3.67           |
|                | <i>Cerchneis tinnunculus</i> | <i>Falco tinnunculus*</i>             | 2.97           | 1.14            | 5.73         | 5.02         | 3.07         | 2.36         | 4.98         | -0.67           |
| Faucon 2726.02 |                              |                                       | -              | <b>29.75</b>    | <b>50.98</b> | <b>62.67</b> | <b>34.41</b> | <b>45.23</b> | <b>61.32</b> | <b>42.09</b>    |
|                | <i>Falco barbarus</i>        | <i>Falco peregrinus pelegrinoides</i> | 61             | 6.25            | 13.02        | 12.33        | 10.59        | 8.77         | 5.68         | -1.09           |
|                | <i>Falco feldeggi</i>        | <i>Falco biarmicus</i>                | 62             | 8.25            | 23.02        | 23.33        | 16.59        | 14.77        | 14.68        | 6.91            |
|                | <i>Falco peregrinus</i>      | <i>Falco peregrinus peregrinus</i>    | 68             | 9.25            | 33.02        | 32.33        | 24.59        | 23.77        | 25.68        | 9.91            |

|                     |                              |                                       |              |              |              |              |              |              |              |              |
|---------------------|------------------------------|---------------------------------------|--------------|--------------|--------------|--------------|--------------|--------------|--------------|--------------|
|                     | <i>Falco subbuteo</i>        | -                                     | 50           | 0.25         | 8.02         | 5.33         | 4.59         | -0.23        | -2.32        | -7.09        |
|                     | <i>Cerchneis tinnunculus</i> | <i>Falco tinnunculus*</i>             | 48           | 0.25         | 5.02         | 0.33         | 0.59         | -0.23        | -1.32        | -4.09        |
| <b>Faucon 5731</b>  |                              |                                       | <b>43.97</b> | <b>29.15</b> | <b>48.89</b> | <b>56.16</b> | <b>30.95</b> | <b>43.02</b> | <b>54.47</b> | <b>38.61</b> |
|                     | <i>Falco barbarus</i>        | <i>Falco peregrinus pelegrinoides</i> | 17.03        | 6.85         | 15.11        | 18.84        | 14.05        | 10.98        |              | 2.39         |
|                     | <i>Falco feldeggi</i>        | <i>Falco biarmicus</i>                | 18.03        | 8.85         | 25.11        | 29.84        | 20.05        | 16.98        |              | 10.39        |
|                     | <i>Falco peregrinus</i>      | <i>Falco peregrinus peregrinus</i>    | 24.03        | 9.85         | 35.11        | 38.84        | 28.05        | 25.98        |              | 13.39        |
|                     | <i>Falco subbuteo</i>        | -*                                    | 6.03         | 0.85         | 10.11        | 11.84        | 8.05         | 1.98         |              | -3.61        |
|                     | <i>Cerchneis tinnunculus</i> | <i>Falco tinnunculus*</i>             | 4.03         | 0.85         | 7.11         | 6.84         | 4.05         | 1.98         |              | -0.61        |
| <b>CMH Falcon 1</b> |                              |                                       | <b>47.8</b>  | <b>31.68</b> | <b>50.14</b> | <b>60.31</b> | <b>33.1</b>  | <b>42.73</b> | <b>57.92</b> | <b>42.38</b> |
|                     | <i>Accipiter nisus F</i>     | -                                     | 2.20         | -3.68        | 11.86        | 12.69        | 5.90         | 12.27        | 17.08        | 20.62        |
|                     | <i>Accipiter nisus M</i>     | -*                                    | -5.80        | -6.68        | -0.14        | -0.31        | -1.10        | 0.27         | 1.08         | 9.62         |
|                     | <i>Cerchneis tinnunculus</i> | <i>Falco tinnunculus*</i>             | 0.20         | -1.68        | 5.86         | 2.69         | 1.90         | 2.27         | 12.53        | -4.38        |
|                     | <i>Circus pygargus</i>       | -                                     | 9.20         | 3.32         | 33.86        | 41.69        | 18.90        | -            | 21.53        | 15.62        |
|                     | <i>Elanus caeruleus</i>      | -                                     | 9.20         | 2.32         | 25.86        | 29.69        | 9.90         | 6.27         | 32.53        | -9.38        |



|  |                       |                          |      |       |      |      |       |      |      |       |
|--|-----------------------|--------------------------|------|-------|------|------|-------|------|------|-------|
|  | <i>Falco subbuteo</i> | -                        | 2.20 | -1.68 | 8.86 | 7.69 | 5.90  | 2.27 | 4.53 | -7.38 |
|  | <i>Melierax gabar</i> | <i>Micronisus gabar*</i> | 2.20 | -3.68 | 4.86 | 4.69 | -1.10 | 4.27 | 5.53 | 5.62  |

\* Likely species identification as determined in Chapter 4.

### Appendix I: 3D renderings of studied mummified birds using clinical CTs

This appendix contains the 3D renderings of the Chatham Falcon, Faucon 2726.02, Faucon 5731, and the CMH Falcon 1 using the clinical CT data. These images were all rendered using Dragonfly 3D World (v.2024.1-1579).



*Figure I.1 3D rendering of the Chatham Falcon using a clinical CT scan. Despite the “globular” visualization, we can visualization the position the bird was mummified in, the tomial tooth, and the shape of the scleral ossicle. Deep learning image processing failed to effectively segment bone from desiccated tissue, thus many defining features are not visible. Due to low bone density in birds, particularly in the cranium, the contrast and spatial resolution between bone and tissue are not sufficient on a clinical CT for ideal segmentation and visualization.*

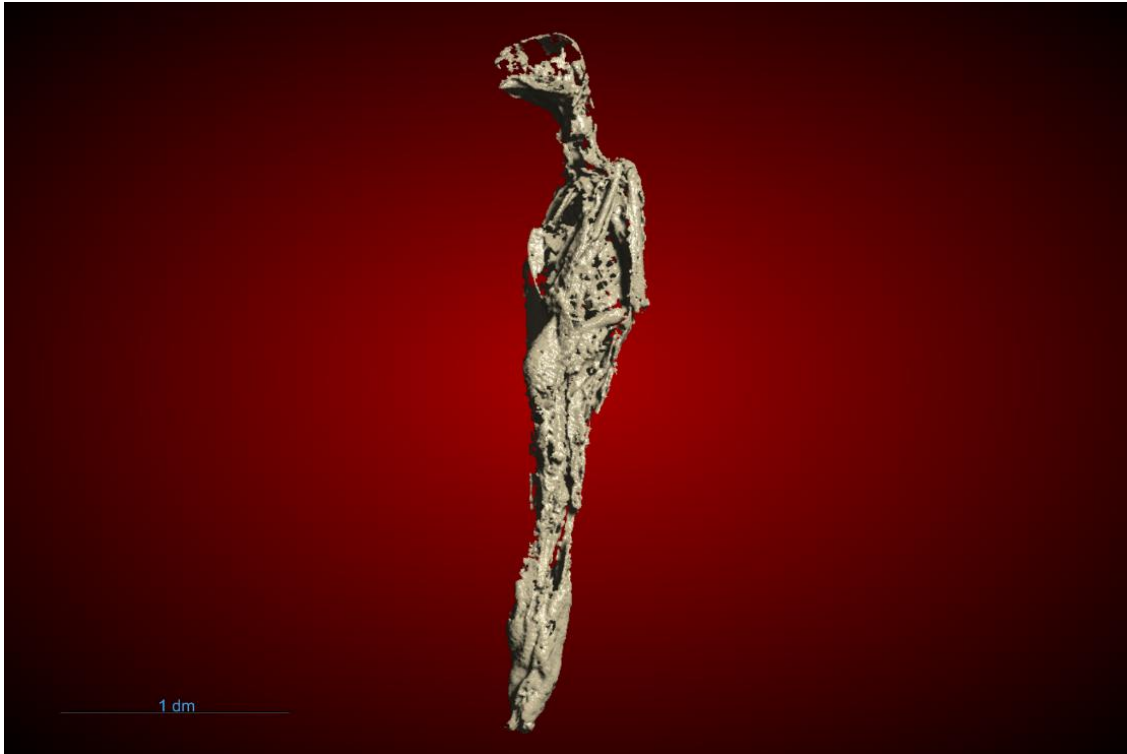


*Figure I.2 3D rendering of Faucon 2726.02 using a clinical CT scan. Similar to the Chatham Falcon, there is poor contrast and spatial resolution, leading to poor segmentation and visualization of finer skeletal traits, including the scleral ossicles, which are completely missing by the algorithm.*



*Figure I.3 3D rendering of Faucon 5731 using a clinical CT scan. The shape of the long bones is discernable, however, the less dense skeletal features, such as the cranium and scleral ossicle, could not be properly segmented.*

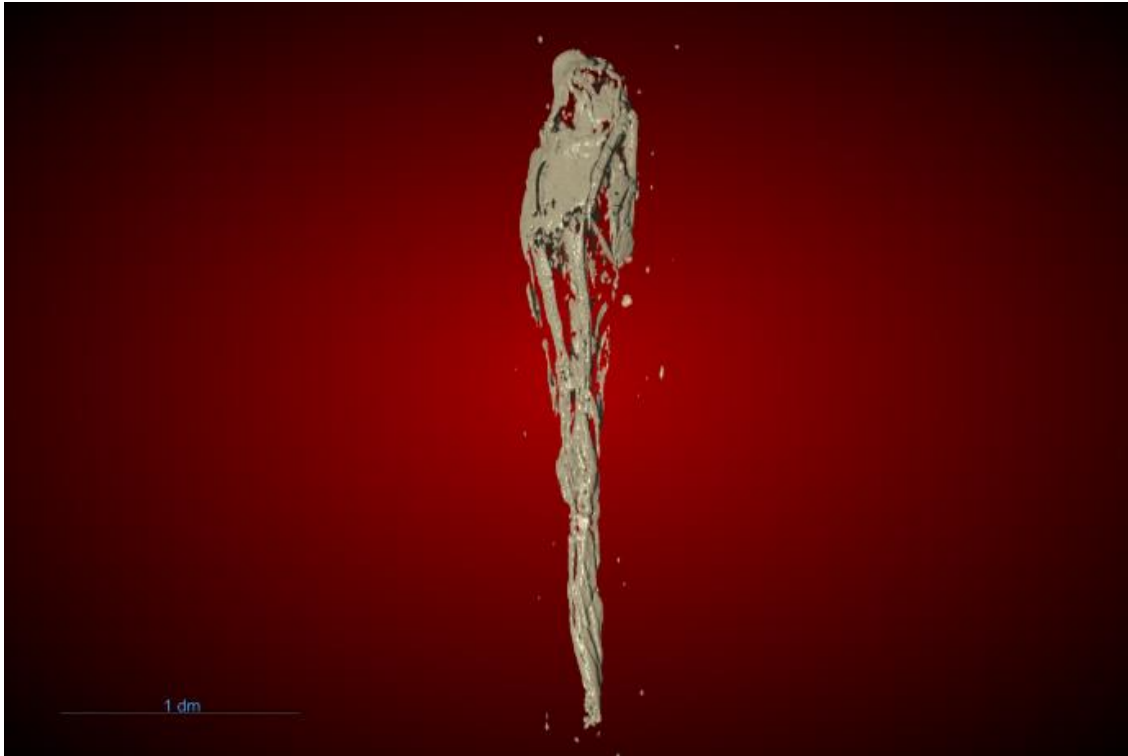


*Figure I.4 3D rendering of the CMH Falcon 1 using clinical CT data. Visualization of the skeletal elements is extremely poor.*

## Appendix J: Additional observations from mummified bundles

This appendix contains the 3D renderings of the necks of the Chatham Falcon, Faucon 2726.02, and Faucon 5731 in order to examine the cause of death. It also contains a 2D slice view of the torso of Ibis 2727.01, looking to corroborate findings from Wade et al. (2012). These images were all rendered using Dragonfly (v.2024.1-1579).

### *Chatham Falcon*

On the micro-CT scans, the ossified rings in the Chatham Falcon's trachea are visible. The bird's slightly angled head, and the twisting path of the trachea indicate that it met its demise by a sudden jerk of the head while the body remained stationary, resulting in a broken neck.

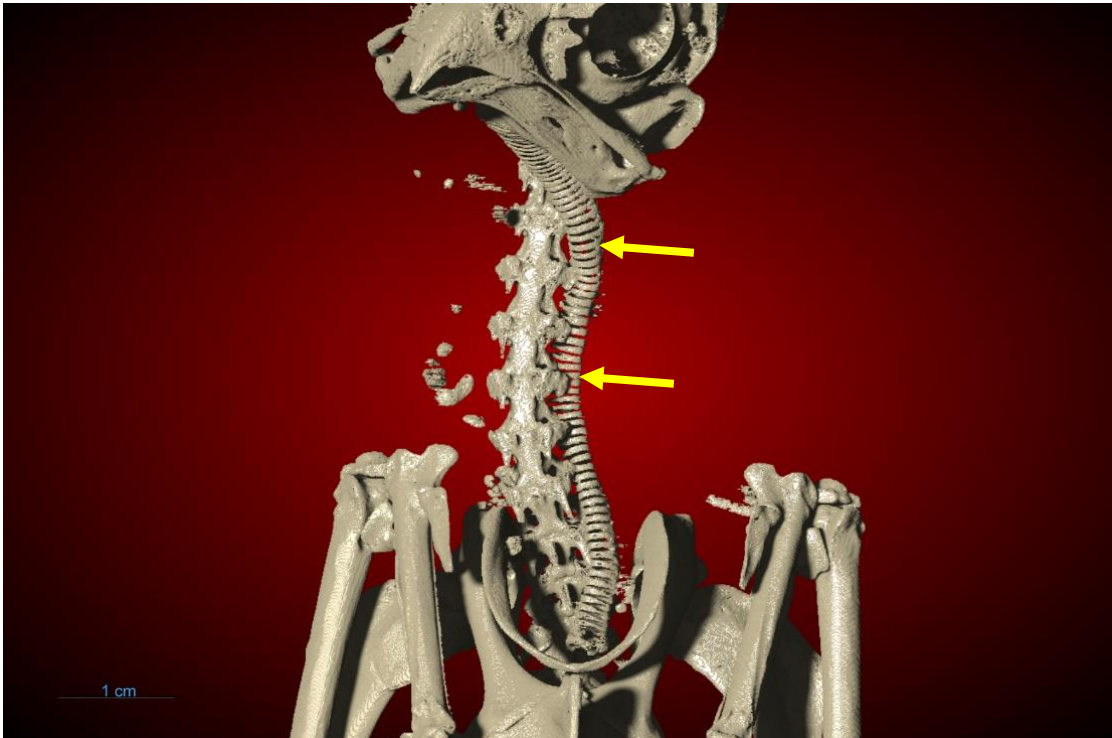


*Figure J.1 Twisting of the ossified rings of the trachea, indicating the Chatham Falcon's neck as twisted to kill the bird.*

*Faucon 2726.02*

Unlike the Chatham Falcon, Faucon 2726.02 has no twisting of the ossified tracheal rings. This suggests that the bird was not killed by the twisting of the neck, which was the preferred method for many avian votive mummies during the late Ptolemaic and early Roman periods (Ikram, 2005b).



*Figure J.2 Straight neck, as evidenced by the ossified trachea, suggests that Faucon 2726.02 did not die by its neck being twisted and broken.*

*Faucon 5731*

Faucon 5731 displayed a twisted trachea, even more severe than that of the Chatham Falcon. This confirms that Faucon 5731 similarly died by the twisting of its neck. This aligns with the method of killing most commonly employed in the production of votive avian mummies (Ikram, 2005b).

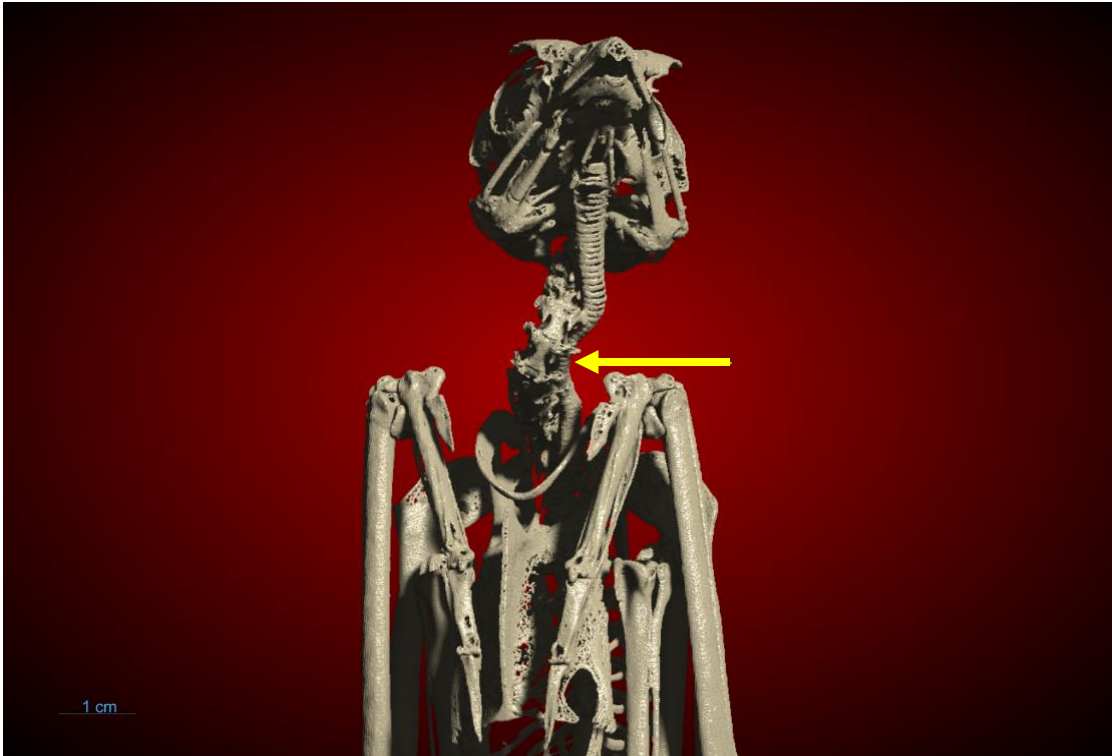


*Figure J.3 Twisting of the ossified rings of the trachea, indicating that Faucon 5731 was killed by twisting the cranium and neck while the body remained stationary.*



*Ibis 2727.01*

In a previous study (Wade et al., 2012), it was suggested that food (possibly grain) was placed inside *Ibis 2727.01*, as a food offering for the afterlife. The micro-CT data reveals the bird was filled with a substance, not grain.

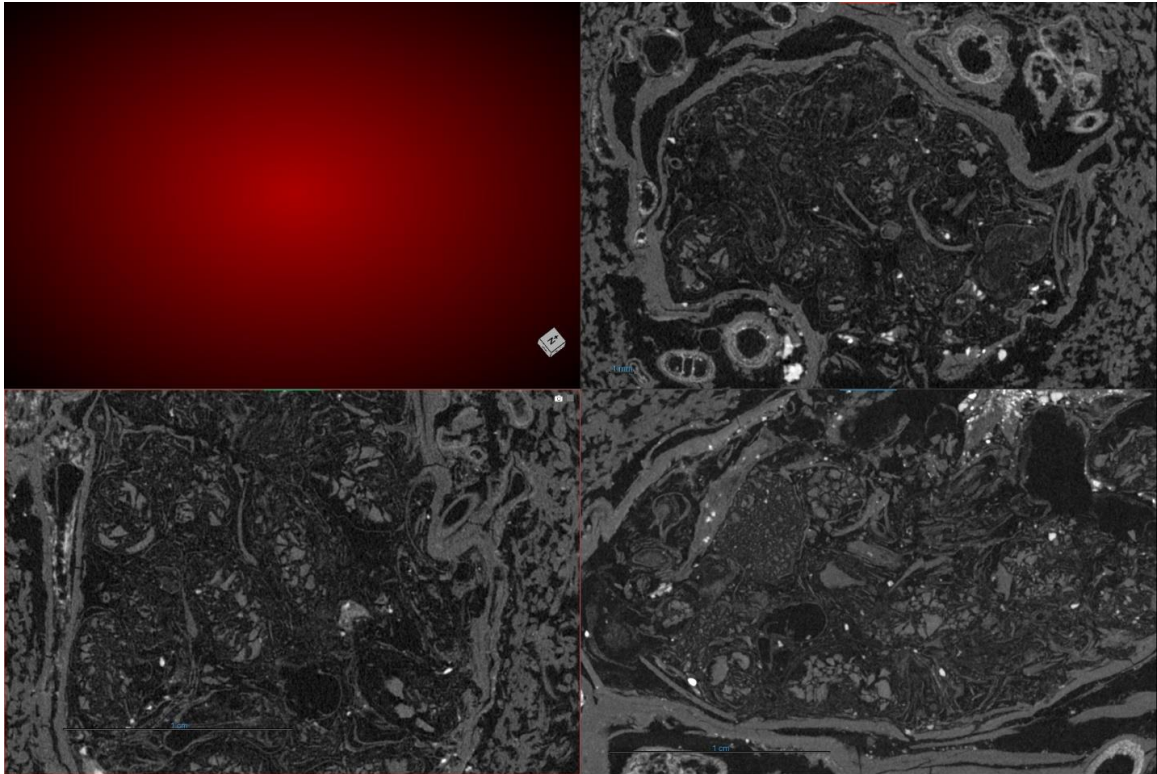


*Figure J. 4 2D slice view of Ibis 2727.01, cropped to examine the stomach. High resolution micro-CT scans reveal the bird is filled with multiple “pod” like structures, filled with an unknown substance.*

### Appendix K: Residual plots for clinical and micro-CT skeletal measurements

The following graphs look for bias in the linear regression models for the clinical and micro-CT datasets for the Chatham Falcon, Faucon 2726.02, and Faucon 5731. An unbiased model will have residuals which scatter randomly around zero; biased data will create residual patterns. All residual plots show unbiased linear models.

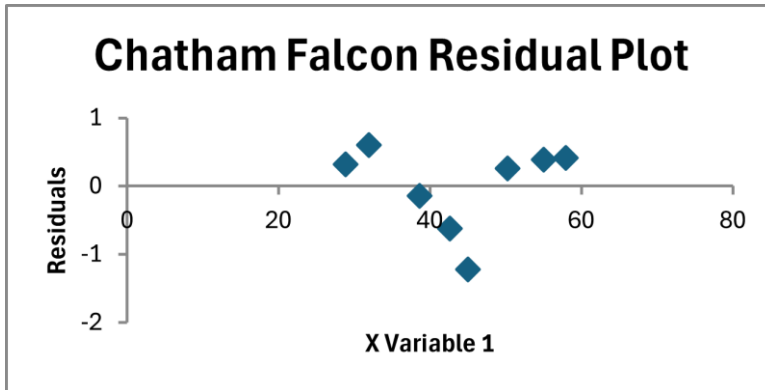


Figure K.1 Residual plot for the linear regression model of the Chatham Falcon clinical and micro-CT skeletal measurements.

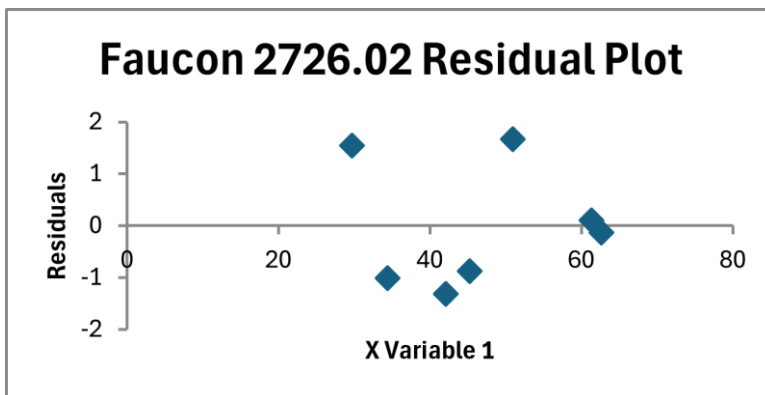
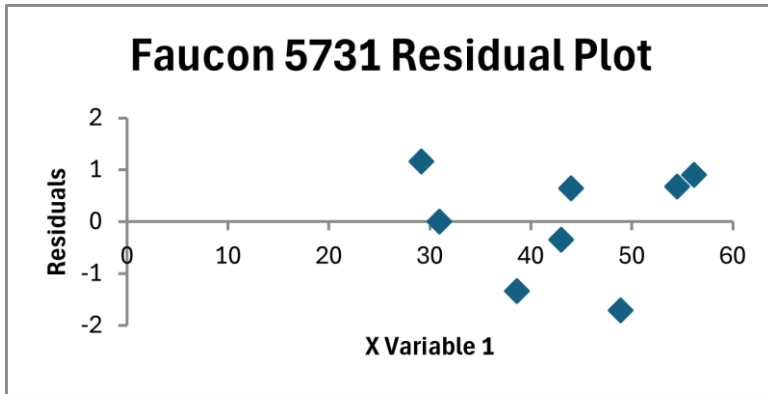


Figure K.2 Residual plot for the linear regression model of Faucon 2726.02 clinical and micro-CT skeletal measurements.



*Figure K.3 Residual plot for the linear regression model of Faucon 5731 clinical and micro-CT skeletal measurements.*

## Curriculum Vitae

**Name:** Maris Schneider

**Post-secondary Education and Degrees:** Mount Royal University  
Calgary, Alberta, Canada  
2019-2022 H.B.A.

Western University  
London, Ontario, Canada  
2022-2024 M.A.

**Honours and Awards:** Social Science and Humanities Research Council Canadian  
Graduate Scholarship – Masters  
2023-2024

Jason Lang Scholarship (Mount Royal University)  
2020-2022

**Related Work Experience:** Teaching Assistant  
The University of Western Ontario  
2022-2024

Graduate Research Assistance  
McGill University  
2023

### Publications:

Halgrain, M., **Schneider, M.**, Jia, S., Narcy, A., Gambier, E., Hincke, M., McKee, M., Rehault-Godbert, S., & Reznikov, N. (In submission). “3D micro-computed tomography study comparing embryonic skeletal development in layer versus broiler strains of the domestic chicken.” *Poultry Science*.

**Schneider, M. A.,** and Gilmour, R. J. (2023), Exploring radiogrammetry beyond the second metacarpal: Using the third, fourth, and fifth metacarpals to quantify cortical bone. *American Journal of Human Biology*, 35(3), e23831. <https://doi.org/10.1002/ajhb.23831>

**Conference Presentations:**

**Schneider, M.,** Nelson, A., Jia, S., Reznikov, N., & Brika, S. (2024). "Unveiling the Secrets of Pseudo Mummies: MicroCT Scanning Reveals Insights into Two Ibis Mummies from Ancient Egypt." (podium). Canadian Archaeological Association (May), Saskatoon, Saskatchewan, Canada.

**Schneider, M.,** Nelson, A., Jia, S., & Reznikov, N. (2023) "Digital Dissections: Deep Learning Image Segmentation of MicroCT Scans of Ancient Hands." (poster). Canadian Association of Biological Anthropology (October), Winnipeg, Manitoba, Canada.

**Schneider, M.,** & Nelson, A. (2023). "Animals in the ancient ritual landscape: A case study of species identification of an ancient Egyptian bird mummy, using stitched micro-Computed Tomography scans." (poster). 7<sup>th</sup> Microscopy Characterization of Organic-Inorganic Interfaces (June), Hamilton, Ontario, Canada.